Staying with the Hubble Trouble

CHRISTOPH BECKER

Staying with the Hubble Trouble

Christoph Becker

Abstract: This thesis investigates the tension between the expansion rate, also known as the Hubble-Lemaître constant, H_0, measurements by a number of independent early- and late-time observables.

In the first part, we consider an alternative to the standard theory of gravity, the generalised Proca (GP) theory, which can potentially alleviate the Hubble tension. Focusing on the GP Lagrangian at cubic order – the Cubic Vector Galilen (CVG) model – we derive the simplified equations for gravity and vector modes and implement them in a modified version of the `ECOSMOG` N-body code and augmented it further with ray-tracing modules taken from `Ray-RAMSES`. Accordingly, we conduct the first broad simulation study of a cosmologies based on the CVG theory. They explore the formation, evolution and clustering of dark matter based on matter, halo, weak lensing and voids statistics.

In the second part, we attempt to answer whether systematic errors in strong gravitational time delay measurements could partly explain the Hubble tension. We quantify the impact of line-of-sight structures on time-delay measurements and in turn, on the inferred value of H_0, and test the reliability of existing procedures for correcting for these line-of-sight effects. In that pursuit we create realistic lightcones using multiple lens plane ray-tracing to create a set of simulated strong lensing systems that are derived from the *CosmoDC2* semi-analytical extra-galactic catalogue.

Christoph Becker

Durham University

Staying with the Hubble Trouble

INSTITUTE FOR COMPUTATIONAL COSMOLOGY
DEPARTMENT OF PHYSICS
UNIVERSITY OF DURHAM
UNITED KINGDOM

DECEMBER 7, 2021

Contents

List of Tables

List of Figures

Acronyms

ΛCDM Lambda Cold Dark Matter. 6, 9, 11, 14, 18, 40, 46, 53, 55, 61, 66, 69, 72–74, 79, 88, 102, 107, 151

AMR Adaptive Mesh Refinement. 78, 80

BAO Baryon Acoustic Oscillations. 4, 24, 69, 76, 102

CDM Cold Dark Matter. 3–6

CMB Cosmic Microwave Background. 4, 9, 11, 24, 40, 69, 76, 151

csG Cubic Scalar Galileon. 10, 11, 40, 42–44, 46, 49–56, 62, 65, 67, 69–73, 95, 102, 103, 105, 109, 111, 121, 152, 154

cvG Cubic Vector Galileon. 11, 40–43, 45, 46, 49–57, 61–73, 77, 80–87, 89–103, 105–108, 110–112, 114–118, 120–122, 151–159

DGP Dvali-Gabadadze-Porrati gravity. 8–10, 23, 43, 75, 87, 91, 103, 106, 119

EOM Equation Of Motion. 9, 11, 18, 23, 28, 29, 33, 34, 36, 44, 46, 66, 67, 71, 75, 152

FLRW Friedmann-Lemaître-Robertson-Walker. 2, 25, 29

FOF Friend-of-Friend. 94, 120

FOV Field-of-View. 79

GP Generalised Proca. 6, 11, 12, 15, 18, 19, 21, 23–25, 56, 69, 72, 73, 75, 76, 118, 123, 151, 158

GR General Relativity. 1, 3, 6–9, 17, 22, 25, 26, 74, 88, 106

GSN Galaxy Shape Noise. 109, 110, 117

ICs Initial Conditions. 17, 18, 40, 51, 55, 61, 78

ISW Integrated Sachs-Wolfe Effect. 11, 24, 56, 69, 72, 76, 157

LOS Line-Of-Sight. 15, 16, 80

nDGP normal branch of the Dvali-Gabadadze-Porrati model. 9, 93, 112, 157

QCDM Quintessence Cold Dark Matter. 40, 54, 56, 61–63, 66, 67, 69–71, 77, 80–85, 87, 90–95, 97, 99–102, 105, 106, 109, 111, 115, 117, 118, 152, 154

QSA Quasi-Static Approximation. 30–32, 35, 36, 69

RSD Redshift Space Distortion. 24, 76, 87, 93, 100, 112

sDGP self-accelerating branch of the Dvali-Gabadadze-Porrati model. 8, 9, 40, 46, 47, 49–51, 53, 55, 70, 107, 152

SIE Singular Isothermal Ellipsoid. 135, 136, 140, 144, 149, 155, 158

SNR Signal-to-Noise Ratio. 82, 84, 92, 93, 95, 101, 103, 120, 154

WFL Weak-Field Limit. 31, 32, 34

WL Weak Lensing. 77, 80, 106, 109, 113, 114, 117

Declaration

THE WORK DESCRIBED in this thesis was undertaken between 2017 and 2021 while the author was a research student under the supervision of Prof. Baojiu Li and Prof. Richard Massey at the Institute for Computational Cosmology in the Department of Physics at the University of Durham. No part of this thesis has been submitted for any other degree at the University of Durham or any other university.

The contents of this work have appeared in the following papers:

- *Proca-stinated Cosmology I: A N-body code for the vector Galileon*
  Christoph Becker, Christian Arnold, Baojiu Li, Lavinia Heisenberg
  JCAP,10:055,2020. doi: 10.1088/1475-7516/2020/10/055

- *Proca-stinated Cosmology II: Matter, Halo, and Lensing Statistics in the vector Galileon*
  Christoph Becker, Alexander Eggemeier, Christopher T. Davies and Baojiu Li
  JCAP,06:014,2021. doi: 10.1088/1475-7516/2021/06/014

- *The impact of line-of-sight structures on measuring H_0 with strong lensing time-delays*
  Nan Li, Christoph Becker, Simon Dye
  Mon. Not. R. Astron. Soc. 504:2224-2234, 2020. doi: 10.1093/mnras/stab984

The generation of simulated images, as outlined in Sec. 4.3 in Chapter 4, was performed by Nan Li, but is included here for completeness.

A thesis submitted to the Department of Physics in partial fulfillment of the requirements for the degree of Doctor of Philosophy, Durham University

Acknowledgments

Durham can be characterized as a series of uniquely wonderful experiences of and encounters with many inspiring people and spaces I thought I would never do. Various awkward moments, materialities, affects, and *politics* have informed and shaped how I have perceived, felt, and negotiated the world and this work – so if I've had a coffee or too many beers with you — you're all crucial. I couldn't have done this without you.

First and foremost I thank my advisor Baojiu Li, whose kindness, vision, and insight have supported me throughout this work. Together we have worked and thought about so much more that could/should have been this thesis. I am also deeply thankful to Tessa Baker Kazuya Koyama, who ignited my first interest in studying the generalized Proca theory.

I've deeply enjoyed working with friends and colleagues Yan-Chuan Cai, Nan Li, Simon Dye, Lavinia Heisenberg, Alexander Eggemeier, Christian Arnold, and Christopher T. Davies. These endeavours would have been much harder without the guiding conversations, comments, and critiques by Richard Massey, Carlton Baugh, Cedric Lacey, Richard Bower, Masamune Oguri, Kenneth C. Wong, Andrew A. Robertson, Sownak Bose, Cesar Hernandez-Aguayo, Cristian Barrera-Hinojosa, Siavash Yasini, Xiangchong Li, Willem Elbers and many more.

This wouldn't have been possible without the efficiently running computing environment maintained and improved by the COSMA support team, especially Lydia Heck and Alastair Basden. A special mentioning also of the various public libraries with and on which this work was build:

Linux, RAMSES, Python, Zotero, LaTeX just to mention a few. Furthermore, the institute wouldn't have been functioning without the selfless dedication by Carlos Frenk, Shaun Cole, Shufei Rowe, Joanne Richardson, Emma Worden, and others.

Besides focusing on my research, I also enjoyed teaching, which wouldn't have been half as much fun without Lucy Budge, Sam Avis, and Stefan J. Spence. I also feel very lucky to have had the company of many who supported me throughout these years: Tyler, Maxime, Angelo, Matteo, Karan, Enrico, Yu-Shan, Pablo, Ida, Louise, Andrew, Niels, Seb, Nick, Giovanni, Paul, and the Durham University Concert Band Orchestra.

Most importantly, this thesis wouldn't be here without the continuous support of Tilly, a companion of multiple 'restarts' in many adventures. Thanks for this go also to my family. The word 'support' is not satisfactory to include their contributions.

1

Introduction

More than 100 years since Albert Einstein's elegant and elaborate theory of General Relativity (GR) was published, it is still the best theory to describe gravitational physics. A multitude of laboratory, ground-based and space-borne experiments have tested and verified GR on sub-mm and solar-system scales with intensifying scrutiny in the last decades. The year 2016 marked the centennial of Einstein's theory of gravity during which another milestone of its verification was reached by detecting the predicated existence of gravitational waves. However, for scales beyond the solar system we have simply extrapolated without rigorous testing. With increasing quantity and quality of observations on cosmological scales, we have found that the measurements of galaxy rotation curves and the late-time accelerated expansion might indicate the break down of GR. Cosmology is in a golden age of discovery and has entered the era of precision science, allowing to probe some of the fundamental concepts in physics. This thesis studies modifications to GR that could explain the late-time acceleration and how the expansion history of the Universe can be measured based on strong gravitational lensing. Before diving into the details, we will give a brief walk through the standard and alternative models of cosmology (Sec. 1.1), how they can be tested by using observations (Sec. 1.2) alongside computational simulations (Sec. 1.3).

1.1 Cosmological Models

The underlying physics on cosmological scales is described (within the inflationary paradigm) on the basis of two fundamental pillars:

- the cosmological principle, and

- the interpretation of General Relativity.

The cosmological principle – homogeneity and isotropy – is one of the most important features of the Universe. It stands for the fact, that observations made from one vantage point are representative of the Universe as a whole, allowing us to draw conclusions that are independent of our location within it. This principle has however a limited range of validity, as anyone who has looked at the night sky realizes that no direction looks like any other. But we have to understand, that what we can see with our own eyes is but a mere fraction of the whole. Seeing the agglomeration of luminous matter such as stars ($\sim$ 1 light year apart), galaxies ($\sim$ 10^6 light years apart) and clusters of galaxies ($\sim$ 3×10^7 light years apart) constitute only 'small' scales in a cosmological sense. Cosmology and its first principle, regard the large scales that span $\gtrsim 10^8$ light years (or $\gtrsim$ $100h^{-1}\mathrm{Mpc}$ [1] to use a more common unit system), where one starts to see little difference between elementary volumes of the Universe.

[1] One parsec ($1\mathrm{pc}$) is defined as the distance at which one astronomical unit (the distance from the Earth to the Sun) subtends an angle of one arcsecond ($1/3600$ of a degree). In the SI metric system: $1\mathrm{pc} = 3.0857 \times 10^{16}\mathrm{m}$ and $1\mathrm{Mpc} = 10^6\mathrm{pc}$.

Thus in cosmology, one takes the large-scale viewpoint as zeroth-order approximation, in which the underlying spacetime is described by the Friedmann-Lemaître-Robertson-Walker (FLRW) metric line element

$$\mathrm{d}s^2 = -\mathrm{d}t^2 + a^2(t)\delta_{ij}\mathrm{d}x^i\mathrm{d}x^j. \tag{1.1}$$

where t is the cosmic time, $a(t)$ is the scale factor, $\delta_{ij} = \mathrm{diag}[1,1,1]$ is the spatial sector of the metric (which here, and throughout this thesis is taken to be flat), and $\mathrm{d}x^2$ is the time-independent metric of the 3-dimensional space. As its first-order approximation, the smooth large-scale spacetime, Eq. 1.1, is perturbed by including the gravitational

potentials, Φ and Ψ, of the fine-scale structure leading to

$$\mathrm{d}s^2 = -(1+2\Psi)\mathrm{d}t^2 + a^2(t)(1-2\Phi)\delta_{ij}\mathrm{d}x^i\mathrm{d}x^j. \tag{1.2}$$

It is this perturbed metric in Newtonian gauge that we will return to throughout our work when we run cosmological N-bodysimulations.

The other fundamental pillar is the interpretation of GR. When Einstein constructed the theory of GR, he pursued it as a purely geometrical concept, ascribing gravitational interactions to the curvature of spacetime. Even though this interpretation is widely used nowadays, differential geometry affords much wider classes of geometric objects to represent the geometrical properties of manifolds. The two other possible geometrical objects are based on torsion (TEGR) and non-metricity (CGR), differing only by means of a boundary term and giving rise to the same field equations as the geometrical interpretation. In this work we will adapt Einstein's interpretation of GR and will therefore forego a description of the other two (for more details see, [e.g., 109]).

1.1.1 The Standard Model

In addition to the two fundamental pillars of cosmology, we name two[2] more that distinguish the standard model of cosmology from its variants:

- Einstein's interpretation of GR and his field equations are valid on all scales.
- The Universe is filled with a cosmological constant Λ, Cold Dark Matter (CDM), baryons and radiation.

To derive the field equations using the geometric interpretation of GR, we start with the Einstein-Hilbert action

$$S = \int \mathrm{d}^4x\sqrt{-g}\left[\frac{R}{16\pi G} + \mathcal{L}_M - \frac{\Lambda}{8\pi G}\right], \tag{1.3}$$

where g denotes the determinant of the metric tensor $g_{\mu\nu}$, R is the Ricci curvature scalar, G is the gravitational constant, $\mathcal{L}_M$ is the Lagrangian density[3], and Λ is the cosmological constant. Variation with respect to

[2] There are many more concepts and assumptions that go into constructing a working model of cosmology. But it is beyond this thesis to go into all of them.

[3] Here, we use the subscript "M" for both non- and relativistic matter. Later we shall make a distinction between dust (non-relativistic) and radiation (relativistic) by referring to them with "m" and "r" respectively.

$g_{\mu\nu}$ gives us the Einstein field equation [81],

$$R_{\mu\nu} - \frac{1}{2}g_{\mu\nu}R + \Lambda g_{\mu\nu} = 8\pi G T_{\mu\nu}, \tag{1.4}$$

where $R_{\mu\nu}$ is the Ricci curvature tensor, and $T_{\mu\nu}$ is the energy-momentum tensor. Applying the metric given by Eq. 1.1 to Eq. 1.4, we obtain the Friedmann equation [91],

$$H^2 = \frac{8\pi G}{3}\rho + \frac{\Lambda}{3}. \tag{1.5}$$

It is arguably one of the most important equations in cosmology. It relates the expansion rate of the Universe given by $H(t) \equiv \dot{a}/a$, the Hubble factor, to the density, ρ, and the cosmological constant, Λ. Taken together with the continuity equation and the equation of state, they provide a closed system which can be solved to determine the history and fate of the Universe.

While we derived Eq. 1.5, we have made use of the fourth pillar that defines what the content of the Universe is. Whatever it is, we have to realize that the cosmological principle guides us to consider each component as a homogeneous and isotropic perfect fluid[4]. If two or more components share the same equation of state we can, for cosmological purposes, just treat them as one. Therefore roughly speaking, in order to satisfy observational measurements of the Cosmic Microwave Background (CMB), supernovae, lensing and Baryon Acoustic Oscillations (BAO) the standard model of cosmology needs to contain the following: $\sim 70\%$ of Λ, 26% of CDM, and 5% of baryonic matter such as stars and gas that move on in a flat space ($K = 0$) [173]. As the main contribution of the radiation density comes from the CMB, its contribution is often negligible at late times. As our focus is on large scale structure growth at late times, we neglect any radiation in the cosmological simulations we have used.

[4] Meaning, that they are characterised by two quantities: the energy density, $\rho(t)$, and the pressure, $P(t)$.

To give a more nuanced account, modern cosmology parameterizes the source terms in the Friedmann equation, Eq. 1.5, through dimensionless density parameters Ω, for each component. It expresses the energy

densities in units of the critical density $\rho_{\rm crit} = 3H^2/(8\pi G)$, which represents the averaged cosmological density in the Universe today. Thus, the Ω-parameters for the different contents is given by

$$\Omega_m \equiv \frac{8\pi G\rho}{3H^2},\ \Omega_\Lambda \equiv \frac{\Lambda}{3Hr},\ \Omega_K \equiv -\frac{K}{(aH)^2} \tag{1.6}$$

Here, the matter energy density Ω_m corresponds to the sum of the contributions of CDM and baryons. Now, we can rewrite the Friedman equation as,

$$E(z)^2 = \Omega_{\rm m}(1+z)^3 + \Omega_\Lambda + \Omega_K(1+z)^2, \tag{1.7}$$

where we have used $E(z) \equiv H(z)/H_0$, with $H(z=0) \equiv H_0$ the Hubble-Lemaître constant and exchanged the scale factor a with the redshift z using their relation $a = 1/(1+z)$.

The relation between redshift and distance can be reconstructed through Eq. 1.7. For example, in a Euclidean universe ($\Omega_K = 0$), the angular-diameter distance, D_A (i.e. the distance reconstructed from knowing the physical size and measuring the angle it subtends in the sky) is given by

$$D_A(z) = \frac{1}{1+z}\int_0^z \frac{{\rm d}z}{H(z)} \tag{1.8}$$

and the corresponding luminosity distance is given by $D_L = (1+z)^2 D_A$. By measuring redshifts and distances of, e.g., stars, galaxies, supernovae and matching them to $D_A(z)$ and $D_L(z)$ at z close to 0 we can estimate H_0. Although these two cosmological distances are the most widely used in order to measure H_0, a third exists which will be introduced below and discussed in more detail in Sec. 4.

To study how the cosmological components form structures out of the initial density field and how these structures evolve, we need to go beyond a homogeneous and isotropic universe by including inhomogeneities. In other words, instead of using the line elements of Eq. 1.1 we need to consider Eq. 1.2. Linear perturbation theory allows us to relate

these inhomogeneities ($\rho(t, \boldsymbol{x})$) to small perturbations ($\delta(t, x)$) evolving on the background ($\bar{\rho}(t)$) Universe that have grown in time due to gravitational instabilities as

$$\rho(t, \boldsymbol{x}) = \bar{\rho}[1 + \delta(t, \boldsymbol{x})]. \tag{1.9}$$

The evolution of the perturbations, $\delta(t, x)$, can then be found through linear perturbation theory using Einstein's field equations along with the equations for conversation of mass and momentum. For example, by combining the (00) and $(0i)$ components of the Einstein field equations, we obtain the Poisson equation,

$$\partial^2\Phi = \frac{3}{2}\Omega_m a(\bar{\rho} - 1), \tag{1.10}$$

where ∂ is the partial derivative with respect to the comoving coordinate.

However, even though the Lambda Cold Dark Matter (ΛCDM) model is currently the most commonly used model of the Universe, it leaves many puzzles behind. The most prominent are the mysterious late-time acceleration and galactic rotation curves, which have motivated the introduction of dark energy (Λ) and CDM, which are both unidentified. Therefore, one of the key aims of modern cosmology is to reveal the identities of these two unknown components. Despite many years of research, their origin has not yet been identified.

1.1.2 Alternative Models

Chapters 2 and 3 investigate an alternative cosmological model to ΛCDM, based on the generalised form of the classical Proca action that describes a massive vector field with derivative self-interactions. To satisfy theoretical consistency, the modifications to the Einstein-Hilbert action (Eq. 1.3) suggested by the alternative theories to GR discussed here need to be treated as an effective theory, which is valid only at low energy scales. Thus, these gravity models alone remain difficult to reconcile with our current knowledge of quantum fields and further study is needed to extend them to higher energy scales. While exploring the Gen-

eralised Proca (GP) action, we compared it and found relations to other already well studied modified gravity theories which we briefly introduce here.

Starting from Einstein's theory of gravity, Eq. 1.4, there are basically two approaches to alter it such that it accounts for the late-time accelerated expansion: modifying the spacetime curvature terms ($R_{\mu\nu} - \frac{1}{2}g_{\mu\nu}R$) on the l.h.s., or by including an exotic matter source with a negative pressure in the energy-momentum tensor ($T_{\mu\nu}$) on the r.h.s[5]. Following the mathematical and conceptual framework for contemporary elementary particle physics, these modifications inevitably introduce either, e.g.,: a higher dimensional spacetime or extra degrees of freedom [109].

[5] However, it is important to realize that the two approaches – modifying left or right hand side of Eq. 1.4 – do not matter in GR, as we can always rephrase one into the other by defining a suitable conserved energy-momentum tensor that equals the Einstein tensor.

The first approach is to remove Λ and modify the right-hand side of the Einstein equations given in Eq. 1.4 by considering specific forms of the energy-momentum tensor, $T_{\mu\nu}$, with a negative pressure. Theories following this strategy are knwon as "modified matter models". One of the representative models that belongs to this class, are the so-called *quintessence*[6] models [232]. The term "quintessence" is used to denote a slowly evolving scalar field φ that interacts with all other components only through standard gravity. Generally, the gravitational interaction/coupling of matter with a scalar field gives rise to an additional force, that is felt by matter and different from the four known types of fundamental forces, referred to as *fifth force*. But in case of the quintessence field, its clustering on small scales is too small to leave any significant impact on the geodesic of matter and structure formation. This means that the Lagrangian density, $\mathcal{L}_M$, does not depend on φ. Neither directly, nor through the rescaling of the metric, which determines the geodesics of matter particles. For such models the modified Einstein-Hilbert action takes the form of

[6] According to ancient Greek science, the quintessence (from Latin "fifth element") denotes a fifth cosmic element after earth, fire, water, and air.

$$S = \int \mathrm{d}^4x\sqrt{-g}\left[\frac{R}{16\pi G} + \mathcal{L}_M + \frac{1}{2}\nabla^\mu\varphi\nabla_\mu\varphi + V(\varphi)\right]. \tag{1.11}$$

Quintessence models are generally portrayed as the simplest alternative to Λ, as they modify the expansion rate of the Universe while modifica-

tion of GR are insignificant. However, from a theoretical point of view, if one introduces a scalar field into a model, then one could expect it to couple to the remaining matter degrees of freedom directly. That is, standard quintessence models need to include an explanation for a vanishing coupling strength. These models are therefore somewhat less natural when compared to coupled quintessence models, where the scalar field interacts explicitly (that is, beyond the gravitational coupling) with ordinary matter.

The second approach is to modify the left-hand side of the Einstein equation, Eq. 1.4. Theories following this strategy are knwon as "modified gravity models". One representative model that belongs to this class is the Dvali-Gabadadze-Porrati gravity (DGP) model [78]. In this model the late-time acceleration of the Universe is realized by a scalar field φ, which can be understood geometrically as the perturbation of the position of a four-dimensional brane in a five-dimensional spacetime (the bulk). It follows the idea to dilute gravity by allowing gravitons to leak into the fifth dimension (on large scales), while confining ordinary matter onto the four-dimensional brane. The gravitational action of the model is given by

$$S = \int \mathrm{d}^4x\sqrt{-g}\left[\frac{R}{16\pi G} + \mathcal{L}_M\right] + \int \mathrm{d}^5x^{(5)}\sqrt{g^{(5)}}\left[\frac{R^{(5)}}{16\pi G^{(5)}}\right], \tag{1.12}$$

where g and R have the same meaning as before on the 4D brane, while $g^{(5)}$, $R^{(5)}$, and $G^{(5)}$ are respectively their equivalents in the 5D bulk. A characteristic parameter that can be defined for this model is the quantity

$$r_c \equiv \frac{1}{2}\frac{G^{(5)}}{G}, \tag{1.13}$$

known as the crossover scale/radius, which determines the distance scale on the brane above which the gravitational effects from the fifth dimension become important. This model is characterized by two branches of solutions. Firstly the self-accelerating branch of the Dvali-Gabadadze-Porrati model (sDGP), which has the advantage that it does

not require an additional dark energy field to explain the accelerated expansion, but is plagued by ghost instabilities (degrees of freedom whose energy is unbounded from below) and is ruled out by the CMB and SNIa data. Secondly the normal branch of the Dvali-Gabadadze-Porrati model (nDGP), which contains the same fifth force effects as the sDGP model but requires an explicit dark energy term to be added to the four-dimensional part of the action. In the DGP model, deviations from GR can be quantified by the parameter $H_0 r_c$. As $H_0 r_c \to \infty$ the expansion of the Universe is close to that of ΛCDM.

The reason that makes the DGP model interesting is that it features the Vainshtein mechanism. This mechanism leads to the suppression of the modifications on GR in regions where the second derivatives of the potential are large, such that the model can be made compatible with the stringent solar system tests [213]. This screening mechanism operates in models whose Equation Of Motion (EOM) for the scalar field φ contains nonlinear second order derivative terms, of which the DGP is just one example. The Vainshtein mechanism will be studied in greater detail in Sec. 2.3.3, but due to its importance we will briefly introduce it here. Consider a model whose scalar field EOM takes the following symbolic form:

$$A\left(\frac{\varphi_{,r}}{r}\right)^2 + B\left(\frac{\varphi_{,r}}{r}\right) = C\rho, \tag{1.14}$$

where A, B, and C are some model specific constants that can depend on time and $_{,r}$ denotes partial differentiation w.r.t. the radial coordinate r. If ρ is small, then the spatial gradient of φ should be small. In this case, the nonlinear term in Eq. 1.14 can be neglected compared with the other terms and one has that $\varphi_{,r}/r \sim \rho$. Recalling that for normal gravity we have that $\Phi_{,r}/r \sim \rho$, then the ratio of the fifth to the normal gravity force becomes

$$\frac{F_{\text{5th}}}{F_{\text{GR}}} \sim f(t), \tag{1.15}$$

i.e., a function of time alone and not space. On the other hand, when the

density gets high, the nonlinear term in Eq. 1.14 dominates, which results in $\varphi_{,r}/r \sim \sqrt{\rho}$. In this case, we have

$$\frac{F_{5\text{th}}}{F_{\text{GR}}} \sim \frac{1}{\sqrt{\rho}} \to 0, \; if \rho \to \infty, \tag{1.16}$$

and the fifth force is suppressed compared with standard gravity.

These derivative self-interactions that were introduced by the DGP model have furthermore the interesting property, that they are invariant under Galileon transformations of the scalar field

$$\partial_\mu \phi \to \partial_\mu \phi + b_\mu, \tag{1.17}$$

with c and b_μ being a constant scalar and four-vector respectively. Motivated by these findings, more general forms of derivative self-interactions that give rise to second order equations of motion were sought and led to the construction of the Galileon model, which is described by the following modified Einstein-Hilbet action

$$S = \int \mathrm{d}^4x\sqrt{-g}\left[\frac{R}{16\pi G} + \mathcal{L}_M - \frac{1}{2}\sum_{i=1}^{5} c_i\mathcal{L}\right] \tag{1.18}$$

in which $\mathcal{L}_i \; (i = 1, ..., 5)$ are the five allowed components of the Galileon Lagrangian density specified by the constant coefficients, c_i, which are free parameters of the model [160]. The first two Lagrangian densities, $\mathcal{L}_{1,2}$, are for the quintessence field with a linear potential. The remaining terms, $\mathcal{L}_{3,4,5}$, are characterised by their power of φ. In Sec. 2 we will encounter a simplified version of this model in which we have set $\mathcal{L}_{4,5} = 0$, giving it the name: Cubic Scalar Galileon (csG) model. Its Lagrangian density terms are

$$\sum_{i=1}^{3}\mathcal{L}_i = M^3\varphi + \nabla^\mu\varphi\nabla_\mu\varphi + \frac{2}{M^3}\Box\varphi\nabla^\mu\varphi\nabla_\mu\varphi, \tag{1.19}$$

where M is a new mass scale characterising the onset of the acceleration epoch, which is defined by $M^3 \equiv H_0^2 M_{\text{Pl}}$ with M_{Pl} the reduced Planck mass, and $\Box = \nabla^\mu\nabla_\mu$ is the d'Alambertian.

Besides the construction of viable theories of gravity that replace

the cosmological constant Λ with a dynamical scalar field φ, one can instead introduce an additional vector field, A_μ, into the gravity sector. This endeavour is motivated by the standard model of particle physics, as it relies on vector fields as force carriers. In contrast to scalars, the directionality of cosmic vector fields leads to large scale anisotropic expansion. According to CMB observations, these anisotropies are very faint, being at the order of 10^{-5}. By giving the vector field mass, the created anisotropy can be suppressed to the level of measurements. This novel model, known as the GP theory, opens up the possibility to construct vector-tensor theories with second order EOM, that include the Vainshtein screening mechanism and exclude ghost instabilities.

In this thesis, we study a sub-class of the GP theory that contains all Lagrangian densities up to cubic order [108]. Due to its similarity to the csG model we refer to it as the Cubic Vector Galileon (cvG) model. Both models are of great interest for this work, as each of them can resolve the Hubble tension (as shown by [20] for csG and [111] for cvG). One important difference between them is, that the cvG model can tune the strength of the fifth force while its background expansion history stays unchanged [26]. This opens up possibilities to overcome challenges faced by the csG model, such as void lensing and the Integrated Sachs-Wolfe Effect (ISW) [18, 14], while maintaining its ability fit early- and late-time measurements of H_0.

The implication of this vector theory of gravity for astrophysical objects is tremendous and rich in phenomenology, beyond the extensively studied scalar-tensor theories. The impact on the observations of large-scale structures and weak lensing makes it is possible to distinguish this model from ΛCDM according to both expansion history and growth of cosmic structures. Future galaxy surveys such as the DESI [71], Euclid [206], LSST [207], Nancy Grace Roman Space Telescope [6, formerly WFIRST] hold the potential to test the nature of gravity on cosmological scales; allowing us to put constraints on the parameter space of such modified gravity models or potentially to rule out deviations from the standard cosmological paradigm.

1.2 Cosmological Tests of Gravity

In the previous section we have seen that nonstandard gravity models can be obtained by modifying Einstein's field equation (Eq. 1.4), by introducing new degrees of freedom (via a scalar field φ or a vector field A_μ). They ultimately lead to modifications in the Friedmann equation (Eq. 1.5) and the Poisson equation (Eq. 1.10), which can be observed through measurements of, e.g., the rate of cosmic structure growth $D_+(t)$ and the background expansion history $H(t)$. However, the highly nonlinear nature of the evolution of large-scale structures can't be captured by linear perturbation theory. To complete our understanding of model behaviours in cosmology beyond linear perturbation theory, numerical simulations are quintessential. Such cosmological simulations provide the means to test gravity models beyond the well-established tests in the solar or other small systems, in that they probe completely different environments and much larger length scales. In this section, we will give a brief description of some of the most commonly used cosmological measurements.

1.2.1 Probes of the Density Field

The chapters 2 and 3 of this work test the GP model by studying its phenomenology in the nonlinear regime of large-scale structure formation and identify potential observables that can help to verify or falsify it. The focus of the study is kept on summary statistics of dark matter field, dark matter haloes, weak lensing maps, and void properties. A commonly used statistic to describe the distribution of, e.g., matter as a function of scale is the power spectrum $P(k)$. As most cosmological fields are approximately Gaussian random fields in the linear regime, $P(k)$ contains all the information to fully describe them. The power spectrum of matter distribution is obtained by Fourier transforming $\delta(\boldsymbol{x})$,

$$\delta(\boldsymbol{k}) = \int \delta(\boldsymbol{x}) \exp(i\boldsymbol{k}\cdot\boldsymbol{x}) \mathrm{d}^3x, \tag{1.20}$$

where $\boldsymbol{k}$ is the comoving wavevector of a given Fourier mode. The power spectrum is then given by

$$\langle \delta^*(\boldsymbol{k}')\delta(\boldsymbol{k})\rangle = (2\pi)^3 P(k)\delta^{(3)}(\boldsymbol{k}-\boldsymbol{k}'), \tag{1.21}$$

in which we have explicitly written the k-dependence of δ, δ^* is the complex conjugate of δ, $\delta^{(3)}$ is the 3D Dirac δ-function, and $\langle\cdot\rangle$ means the ensemble average over cosmological scales. We could of course stay in configuration space and instead use the two-point correlation function $\xi(r)$ – which is the inverse Fourier transform of $P(k)$ – given by

$$\xi(r) \equiv \langle \delta(\boldsymbol{x})\delta(\boldsymbol{x}+\boldsymbol{r})\rangle = (2\pi)^{-3}\int P(\boldsymbol{k})\exp(i\boldsymbol{k}\cdot\boldsymbol{r})\mathrm{d}^3k. \tag{1.22}$$

But using $P(k)$ is often preferred as it is faster to compute. Although $P(k)$ and $\xi(r)$ carry in principle the same information of $\delta(\boldsymbol{x})$, in practice this is not guaranteed since our analyses are restricted to a finite range of scales, and moreover, configuration and Fourier space statistics are impacted differently by systematic effects, which require slightly different analysis strategies (e.g. the treatment of shot noise).

In cosmological simulations, the continuous field $\delta(\boldsymbol{x})$ is accurately probed by tracer particles allowing the computation of $P(k)$ over a wide range of scales depending on the simulation box size and resolution. When dealing with observational data, one can only probe $\delta(\boldsymbol{x})$ with sparse "biased" tracers, such as dark matter haloes and galaxies. As these biased tracers do not follow the same clustering of the underlying matter field, various bias terms are needed to account for the differences. In the linear regime, i.e. large scales and $\delta \ll 1$, the bias factor is approximately scale independent and can relate the observed halo number density (δ_h) to the underlying matter fluctuations (δ) as

$$\delta_h(\boldsymbol{x}) = b\delta(\boldsymbol{x}), \tag{1.23}$$

where b is the linear bias factor. The halo number density is given by $\delta_h \equiv n_h/\bar{n}_h - 1$, where the subscript h denotes "halo" and $n_h(\boldsymbol{x})$, $\bar{n}_h$ are

the halo number density at x and the mean halo number density, respectively. Galaxies can be related to the underlying matter distribution in the same way.

A cosmological quantity that is of particular importance in the linear regime is the linear growth factor of cosmic structure $D_+(a)$. It determines the normalisation of the linear matter power spectrum relative to the initial density perturbation power spectrum as

$$\delta(k,a) = D_+(a)\delta(k,a_0), \tag{1.24}$$

where t_0 is the physical time today and $D_+(a=1)=1$. In the case of a matter dominated Universe, the linear growth factor is $D_+(t) \propto t^{2/3} \propto a(t)$. Its logarithmic derivative, the dimensionless linear growth rate

$$f = \frac{\mathrm{dln}\delta}{\mathrm{dln}a} = \frac{\mathrm{dln}D_+}{\mathrm{dln}a}, \tag{1.25}$$

determines the amplitude of peculiar velocity flows and redshift distortions [e.g., 167]. When the overdensity reaches a value of $\delta \sim 1$, the linear treatment of structure growth is no longer valid. In such case the nonlinear evolution is computed through numerical simulations.

1.2.2 Probes of the Expansion History

In the two decades since the discovery of the accelerated late-time expansion, distance measurements have improved steadily and led to the detection of a significant tension between the local distance ladder determination of the Hubble-Lemaître constant H_0 by Riess et al. [178] and that inferred by the Planck satellite assuming a flat ΛCDM model [173][7]. The tension could be due to an unknown source of systematic errors in the measurements, or it could be indicative of new physics, such as new degrees of freedom or a larger effective number of relativistic species. To find answers from an empirical standpoint will require further improvements in the precision of independent distance measurements.

[7] With 4σ to 6σ disagreement depending on the datasets considered.

Chapter 4 of this work discusses the relatively new approach to cosmic distance measurements that is independent of more traditional

methods, gravitational strong lensing time delays. This approach relies on the deflection of photons, that are emitted by a background source (such as a galaxy, quasar, supernova, or gravitational wave event), by a deep gravitational potential. If the background source appears to be stretched tangentially around a massive object, it is said to be weakly lensed (in Sec. 3.4.6 we study weak-lensing statistics in context of the GP theory). In rare occasions however, the Line-Of-Sight (LOS) of the source is suitably well aligned with an intervening object of sufficient mass that the deflection is strong enough for multiple images to appear for the observer. The arrival time of the images depends on the interplay of the geometric and gravitational delays specific to the configuration. Thus, if the emission from the gravitationally lensed source is variable in time (such as an active galactic nucleus or a supernova), the difference in arrival time is measurable. The time delay of image i, relative to the case of no lensing, is

$$t(\boldsymbol{\theta}_i;\boldsymbol{\beta}) = \frac{D_{\Delta t}}{c}\phi(\boldsymbol{\theta}_i;\boldsymbol{\beta}), \tag{1.26}$$

where $\boldsymbol{\theta}_i$ is the position of the lensed image i, $\boldsymbol{\beta}$ is the position of the source, $D_{\Delta t}$ is the so-called "time delay distance", and ϕ is the "Fermat potential" related to the lens mass distribution. The time-delay distance for a lens at redshift z_d and a source at redshift z_s is

$$D_{\Delta t} = (1+z_d)\frac{D_d D_s}{D_{ds}}, \tag{1.27}$$

where D_d, D_s, and D_{ds} are respectively the angular diameter distances of the lens, the source, and between the lens and the source. Through Eq. 1.27 $D_{\Delta t}$ is inversely proportional to H_0, and more weakly dependent on other cosmological parameters.

Initially, time delay cosmography was marred by controversies and systematic errors due to the low quality and incompleteness of data. With the beginning of modern monitoring campaigns at the turn of the millennium, these issues were overcome and the focuses shifted to the modeling of the lens mass distribution to constrain ϕ. As the available in-

formation on the lensing system was often limited to the multiple image positions, their time delays and flux ratios the best one could do was to assume a simple form for the lens mass distribution, such as a singular isothermal sphere [124], and to neglect the effects of structure along the LOS. These necessary but oversimplistic assumptions lead to grossly underestimated uncertainties on the obtained estimates of $D_{\Delta t}$ and significant inconsistencies between research groups and measurement techniques.

Since then, two methods have been pursued in order to obtain more realistic estimates of the uncertainties. One consists of using large samples of systems with relatively weak priors ([e.g., 163] and used in our work in Sec. 4). The other method consists of obtaining high quality data for each lens system, including high signal-to-noise ratio and high-resolution imaging of the host galaxy of the lensed object, spectroscopic measurement of the stellar velocity dispersion, and measurements to model the effect of mass inhomogeneities along the LOS and in the immediate neighborhood of the main deflector [e.g., 199, 211, 225].

With ever more strong lens time delays being measured and more ancillary data obtained, time delay cosmography is becoming equally precise to the more traditional techniques. Ultimately its advantage is, that it yields an *absolute* measurement of distance without relying on Cepheids or any other local rung of the distance ladder. Furthermore, unlike luminosity distance measurements, it is insensitive to dust or other photometric errors.

1.3 Cosmological simulations

Cosmological large-scale structure formation is an inherently complex process, which simple analytical methods are unable to describe down to small, nonlinear scales. The situation is exacerbated by many modified gravity models that rely on screening mechanisms, which are a nonlinear phenomena to evade the constraints imposed by the observed solar system tests. As cosmology is entering the era of precision science, in which

the next generation of cosmological surveys will dramatically improve constraints on GR by up to two orders of magnitude [87], N-body simulations are quintessential, as they are one of the most powerful ways to obtain theory predictions in the fully nonlinear regime, in real- and redshift-space, for any considered statistic.

N-body simulations follow the evolution of a portion of the Universe, by sampling the phase-space density via a finite number of tracer particles. The positions and velocities of these particles are obtained by solving the Newtonian equations of motion, embedded in an expanding (background) Universe. As mentioned in Sec 1.1.1, the majority of matter in the Universe is dark matter (DM). As we are only interested in extragalactic phenomena that involve the distribution and dynamics of DM, we can simplify our N-body simulations by neglecting any baryonic or radiation physics and only treat DM particles.

Thus, the central task of our simulations is to solve the gravitational forces acting on each particle, as DM interacts through gravity only. There are two common ways to do this computation: summation of forces from individual and groups of particles, or finite difference of the gravitational potential computed on a grid. Although the former approach is computationally inefficient it can be sped up using recursive tree algorithms, where nearby particles are treated collectively as a single large particle to reduce the number of summation operations. It is however not suitable for nonstandard models of gravity, as it assumes the law of superposition for the gravitational force, which generally does not hold. The latter approach calculates the potential on a mesh first to find the forces through finite difference. This allows the discrete Poisson equation to be solved through fast Fourier transform in standard cosmological simulations and through the relaxation method for nonstandard gravity models [for more details see 132].

To run a single N-body simulation, the first step is to create the ICs by positioning the tracer particles in accordance to a matter power spectrum, $P(k) \sim |\delta|^2$ that provides the information of the initial small scale matter inhomogeneities, $\delta\rho_m$, at some time t. Here, it is important that

the Fourier modes of the perturbations at the scales k and time t at which the ICs are generated are well inside the linear regime, so that linear theory approximations are valid. Each particle is then attributed with gravitationally-induced velocities following e.g. the Zel'dovich approximation (first order perturbation theory) or a second-order Lagrangian perturbation theory (`2LPTic`). This creation of ICs is identical for ΛCDM and screened modified gravity theories with the same cosmological parameters and simulation specifications, because the effect of modified gravity – and to some extent dark energy in many dark energy models – is negligible at high redshifts, $z_{\rm ini} \gtrsim 50$.

Once the ICs is set up, the remaining tasks are to evolve the particle positions and velocities following Vlasov equation which represents the EOM for the particles. For Chapter 2 and 3 we use modified versions of the publicly available simulation code `RAMSES` [205], while for Sec. 4 we use the Outer Rim simulation [113] run with `HACC` [100].

DM-only simulations are able to study the evolution of structure formation, at a much lower computational cost than more physically motivated hydrodynamical simulations. In Chapter 3 we will outline the creation of 25 DM-only N-body simulations to create five lightcones, each for a different cosmology that is based on the GP gravity theory. State of the art computing facilities and simulation codes enable far larger numbers of N-bodysimulation than used in this work, such as the QUIJOTE simulation suite [216] which comprises 43100 full N-body simulations encompassing over 7000 different cosmological models, specifically designed to provide high quality data to train machine learning algorithms.

1.4 Outline of Contents

In this thesis we study the nonlinear growth of large-scale structure in the GP theory of gravity, and the constraining power of strong lensing time-delays on H_0 using various N-body cosmological simulations. The thesis is split into two parts as described below.

The first part of the thesis focuses on the analysis of the GP model.

In Chapter 2, we present the first N-body code that can solve the field equations of a sub-class of the GP model. In Chapter 3, we conduct a comprehensive study of the phenomenology of this model by analysing a total of 13 matter, halo, weak lensing and void statistics.

The second part, Chapter 4, we assess the influence of additional structures along the line-of-sight on time-delay measurements of $D_{\Delta t}$ and in turn, on the inferred value of H_0.

Finally, in Chapter 5, we present our general conclusions and summarise our findings as well as advise on future research directions.

2

Proca-stinated Cosmology I: A N-body code for the vector Galileon

We investigate the nonlinear growth of large-scale structure in the Generalised Proca (GP) theory, in which a self-interacting massive vector field plays the role of driving the acceleration of the cosmic expansion. Focusing to the Proca Lagrangian at cubic order – the cubic vector Galileon model – we derive the simplified equations for gravity as well as the longitudinal and transverse modes of the vector field under the weak-field and quasi-static approximations, and implement them in a modified version of the ECOSMOG N-body code. Our simulations incorporate the Vainshtein screening effect, which reconciles the fifth force propagated by the longitudinal mode of the cubic vector Galileon model with local tests of gravity. The results confirm that for all scales probed by the simulation, the transverse mode has a negligible impact on structure formation in a realistic cosmological setup. It is well known that in this model the strength of the fifth force is controlled by a free model parameter, which we denote as $\tilde{\beta}_3$. By running a suite of cosmological simulations for different values of $\tilde{\beta}_3$, we show that this parameter also determines the effectiveness of the Vainshtein screening. The model behaves identically to the cubic scalar Galileon for $\tilde{\beta}_3 \to 0$, in which the fifth force is strong in unscreened regions but is efficiently screened in high-density regions. In the opposite limit, $\tilde{\beta}_3 \to \infty$, the model ap-

proaches its 'quintessence' counterpart, which has a vanishing fifth force but a modified expansion history compared to ΛCDM. This endows the model with rich phenomenology, which will be investigated in future works.

2.1 Introduction

Our present understanding about the Universe is founded upon GR, which is the only theory that is compatible with the basic requisite of a single massless spin-2 field that respects Lorentz invariance [99, 218, 66]. Even though the predictions of GR have been validated against many tests, these tests are usually limited to small scales such as the solar system, and it leaves the cosmological scales underexplored [128]. These latter scales coincide with those on which the dynamics of luminous matter within galaxies and at Mpc scales, as well as the expansion rate of the Universe, currently lack clear and convincing explanations. These enigma are commonly attributed to invisible energy contents that interact with gravity but not with baryons, called dark matter (motivated by e.g. galaxy dynamics) and dark energy (motivated by observed late time acceleration) [181]. However, it is also possible that they are simply signatures that the law of gravity is modified on large scales, as exemplified by many modified gravity (MG) models [9, 109, 87].

The last decades have seen many attempts to modify GR. According to the Lovelock theorem, GR is the only theory with second-order local equations of motion for the metric field, which is derivable from a 4-dimensional action [128], and therefore modifications to GR often involve new dynamical degrees of freedom in addition to the metric field, non-locality, higher-dimensional spacetimes and/or higher-order equations. The simplest MG models, for example, usually involve a single scalar degree of freedom with self-interactions or interactions with curvature. It has been well-established that such models can be brought under the umbrella of the Horndeski theory [118, 123, 70].

One of the well-known subclasses of the Horndeski theory is the

Galileon model [160, 69, 68], a 4-dimensional effective theory which involves a scalar field with universal coupling to matter and derivative self-interactions. The theory implements the Vainshtein screening effect [213] – a mechanism encountered in theories such as Fierz-Pauli massive gravity [12] and the Dvali-Gabadadze-Porrati (DGP) model [78] – to decouple the scalar field from matter near massive objects and therefore can be compatible with Solar system tests of gravity. The model modifies the background expansion history such that it reaches a de Sitter solution in the future without requiring a cosmological constant. Its simplicity makes it possible to study its phenomenology with the help of cosmological N-body simulations [17, 136].

In contrast to the scalar Galileon, the GP theory [108, 8, 29], involves a massive vector field, A_μ, with a broken $U(1)$ gauge symmetry and second-order equation of motion (EOM). The theory features Galileon-type derivative self-interactions and couplings to matter. At the background level, the temporal component of the vector field, A_0, gives rise to a self-accelerating de Sitter attractor, corresponding to a dark energy equation of state $w_{\rm DE} = -1$ [61]. From the gravitational wave event GW170817 [2] with accompanying gamma-ray burst GRB170817A [95] and other optical counterparts, the speed of propagation of the gravitational waves c_T has been tightly constrained to be identical to the speed of light, c. This places strong constraints on the allowed operators within the higher order GP Lagrangian. However, even with this restriction, the GP theory is still cosmologically interesting, with a theoretically consistent parameter space that is free of ghost and Laplacian instabilities [61].

By introducing non-linear functions into the field Lagrangian of the GP theory to describe its derivative self interactions and couplings with matter, it is very versatile and flexible. However, in cosmological applications one often specialises to simple choices of these non-linear functions, such as power laws, and a number of studies have been conducted, leading to a good understanding of the cosmological behaviours of the model at background and linear levels. For example, in Ref. [64], an MCMC like-

lihood analysis was performed for the particular GP theories proposed in Refs. [61, 62], by exploiting the observational data from type Ia supernovae (SNIa), Cosmic Microwave Background (CMB), Baryonic Acoustic Oscillations (BAO), the Hubble expansion rate $H(z)$, and Redshift Space Distortion (RSD). The cross correlation between galaxy field and the Integrated Sachs Wolfe (ISW) effect, which has been a powerful probe to constrain the scalar Galileon models, has also been used to constrain parameters of the GP theory [154].

The aim of this Chapter is to carry on the analyses into the non-linear regime, beyond the use of linear perturbation theory [65] or statistical field theory [110], by using cosmological N-body simulations. From a phenomenological point of view, there are several reasons for doing so. One is that we know perturbation theory to not be good at quantifying the effects of screening, which is an inherently non-linear phenomenon. N-body simulations are the only known tool to accurately quantify the evolution of the Universe on small, highly non-linear, scales, and can be used to validate or calibrate the predictions of other approaches. Being able to probe small scales will enable us to test a given model against more observational data more accurately, e.g., access scales or regimes that are inaccessible to perturbation theory. To this end, we have developed a modified version of the `ECOSMOG`code [135], which can be easily adapted to any variant of the GP theory. This is the first Chapter of two to explore the non-linear regime for this theory; here we will focus on deriving the simplified equations, code tests and initial simulations to gain some qualitative insight into its cosmological behaviour.

This Chapter is arranged as follows. In Section 2.2 we give a brief review of the key points of the GP theory, specialise to a simple variant of it, and derive the simplified Einstein and GP field equations of motion that are applicable to typical cosmological simulations which are featured by weak fields and slow motions of matter. A particularly detailed account will be given of the approximations used and their justifications. In Section 2.3 we introduce an internal unit system which is used to write the background and perturbation evolution equations into dimension-

less forms. We give expressions of various physical quantities that are key to understanding the behaviours of the theory, and compare them with the predictions from other related gravity models. In Section 2.4, we first carry out a range of tests of a new N-body code developed for simulating the GP field, and then show the first results from a suite of cosmological simulations. We show that the transverse mode of the GP vector field plays a negligible role in the non-linear evolution of the Universe, as it does in linear theory. We also demonstrate how the enhanced growth of non-linear cosmic structures and the screening of fifth force depends on the single additional parameter of the model. Finally we summarise, conclude and layout a future workplan in Section 2.5.

Throughout this Chapter, we use the $(-,+,+,+)$ notation for the signature of the metric. We set $c = 1$ except in expressions where c appears explicitly. Greek indices run over $0,1,2,3$ while Roman indices run over $1,2,3$. $M_{\rm Pl}$ is the reduced Planck mass and is related to Newton's constant, G, by $M_{\rm Pl}^{-2} = 8\pi G$.

2.2 Generalised Proca Theory

This section gives a short description of the GP theory. We start from a complete form and then specialise to a particular case with a simple functional form of the Lagrangian. The choice of the theory and the resulting field equations are given in Section 2.2.1. In Section 2.2.2 we apply these to a perturbed spacetime around a flat homogeneous and isotropic Friedmann-Lemaître-Robertson-Walker (FLRW) metric, to derive the equations which govern the dynamics of the Proca field and its effect on the total gravitational force. These will provide us with the essential equations for the N-body simulations.

2.2.1 Action and general field equations

In its standard form, the Proca action describes the dynamics of a massive vector field A_μ, and is of little use to modify GR. This is because, since we observe no deviation from GR in our solar system, any new

terms which we add to the Einstein-Hilbert action have to converge to GR in deep potentials. This requires the mass of the vector field to be so small, that it makes the field negligible on all scales. One way around this dilemma is by adding further terms to the action that make the behaviour of the vector field dependent on potential depths. This can be achieved by derivative self-interactions of the vector field. Interestingly, there exist only six derivative self-interactions that preserve the number of degrees of freedom of the vector field and do not create ghosts (such as the Ostrogradsky instability) [108, 29]. The resulting four-dimensional action has the following structure [108],

$$S = \int d^4x \sqrt{-g} \left[\mathcal{L}_m + \mathcal{L}_F + \sum_{i=2}^{6} \mathcal{L}_i \right], \tag{2.1}$$

where g denotes the determinant of the metric tensor $g_{\mu\nu}$, and $\mathcal{L}_m$ is the matter Lagrangian, which is related to the energy-momentum tensor of a perfect fluid as,

$$T^{(m)}_{\mu\nu} = -\frac{2}{\sqrt{-g}} \frac{\delta(\sqrt{-g}\mathcal{L}_m)}{\delta g^{\mu\nu}}. \tag{2.2}$$

Assuming that matter is minimally coupled to gravity, $T^{(m)}_{\mu\nu}$ satisfies the standard conservation equation

$$\nabla^\mu T^{(m)}_{\mu\nu} = 0, \tag{2.3}$$

where ∇^μ denotes the covariant derivative compatible with $g_{\mu\nu}$. Introducing the first derivative of the vector field as $B_{\mu\nu} = \nabla_\mu A_\nu$, we can build the anti-symmetric Faraday tensor as $F_{\mu\nu} \equiv B_{\mu\nu} - B_{\nu\mu}$. The dynamics of A_μ is described by the kinetic term of the Proca Lagrangian, $\mathcal{L}_F$,

$$\mathcal{L}_F = -\frac{1}{4} b_F F_{\mu\nu} F^{\mu\nu}, \tag{2.4}$$

and the self-interaction terms of the vector field,

$$\mathcal{L}_2 = G_2(X, F_{\mu\nu}, \tilde{F}_{\mu\nu}), \tag{2.5}$$

$$\mathcal{L}_3 = G_3(X)[B], \tag{2.6}$$

$$\mathcal{L}_4 = G_4(X)R + G_{4,X}(X)([B]^2 - [B^2]), \tag{2.7}$$

$$\mathcal{L}_5 = G_5(X)\mathcal{G}_{\mu\nu}B^{\mu\nu} - \frac{1}{6}G_{5,X}(X)([B]^3 - 3[B][B^2] + 2[B^3]) + \tilde{G}_5(X)\tilde{F}^{\alpha\mu}\tilde{F}^{\beta}_{\mu}B_{\alpha\beta}, \tag{2.8}$$

$$\mathcal{L}_6 = G_6(X)L^{\mu\nu\alpha\beta}B_{\mu\nu}B_{\alpha\beta} + \frac{1}{2}G_{6,X}(X)\tilde{F}^{\alpha\beta}\tilde{F}^{\mu\nu}B_{\alpha\mu}B_{\beta\nu}, \tag{2.9}$$

where $X \equiv \frac{1}{2}A_\mu A^\mu$, $G_{2,3,4,5,6}$ are general algebraic functions of X, $\tilde{F} \equiv {}^*F$ is the Hodge-dual of the Maxwell tensor given by $\tilde{F}^{\mu\nu} = \mathcal{E}^{\mu\nu\alpha\beta}F_{\alpha\beta}/2$, where $\mathcal{E}^{\mu\nu\alpha\beta}$ is the Levi-Civita tensor satisfying the normalization $\mathcal{E}^{\mu\nu\alpha\beta}\mathcal{E}_{\mu\nu\alpha\beta} = -4!$. The square brackets around an operator designate the trace of a tensor. While $\mathcal{L}_{3,4,5,6}$ contain the derivative self interactions, the non-minimal derivative couplings of the vector field to the Ricci scalar R, the Einstein tensor $\mathcal{G}_{\mu\nu}$, and the double dual Riemann tensor $L^{\mu\nu\alpha\beta}$ defined by

$$L^{\mu\nu\alpha\beta} = \frac{1}{4}\mathcal{E}^{\mu\nu\rho\sigma}\mathcal{E}^{\mu\nu\gamma\delta}R_{\rho\sigma\gamma\delta}, \tag{2.10}$$

where $R_{\rho\sigma\gamma\delta}$ is the Riemann tensor, are due to $\mathcal{L}_{4,5,6}$. Note that b_F in Eq. (2.4) is a constant coefficient which has mass dimension zero in natural unit, and thus is sometimes set to 1 in the literature; in physical unit it is not dimensionless, which is important when converting the field equations into code units, as will be seen below.

Exposing the full action given by Eq. (2.1) to constraints from the observed gravitational wave event GW170817 [2] with gamma-ray burst GRB170817A [95] and other optical counterparts, we can already make a judgement on the viability of $\mathcal{L}_{4,5}$. The GW170817/GRB170817A event measured a speed of tensor perturbations c_T very close to that of light c [1]. In this work we consider the subclass of Proca theory with $\mathcal{L}_5 = \mathcal{L}_6 = 0$ and $\mathcal{L}_4 = \frac{1}{2}M_{\rm Pl}^2 R$, which satisfies the requirement that $c_T = c$[1]:

[1] Note that this requirement does not exclude $\mathcal{L}_5$ entirely (as $\tilde{G}_5$ remains) and leaves interactions within $\mathcal{L}_6$ viable, since they are not sensitive to the background due to involved symmetries of the background and the interactions themselves [109].

$$\sum_{i=2}^{4}\mathcal{L}_i = G_2(X) + G_3(X)\nabla_\mu A^\mu + \left(\frac{M_{\rm Pl}^2}{2}\right)R, \tag{2.11}$$

where $\mathcal{L}_4$ has simplified to the standard Einstein-Hilbert term. In the literature, a common choice of the functions $G_{2,3}(X)$ is the power-law form,

$$G_2(X) = b_2 X^{p_2}, \qquad G_3(X) = b_3 X^{p_3}, \tag{2.12}$$

where $b_2 \equiv m^2$ is the mass-squared of the vector field that characterises the onset of the acceleration epoch, and b_3, p_2, p_3 of mass dimension zero in natural unit. The choice is generic enough, leaving a viable parameter space in which the theory is free of ghost and Laplacian instabilities. Importantly, due to the derivative self-interaction of the vector field in $\mathcal{L}_3$, the gravitational effect of the field can be screened in dense regions as required by solar system tests. The screening mechanism in this model is known to be analogous to the Vainshtein mechanism for scalar Galileons [61], as we will also demonstrate below, but there are also important differences between these two classes of models.

Based on the analyses of linear perturbations in this model, observational constraints on $p_{2,3}$ have been obtained in the literature, e.g., [64, 154, 65]. In this work we set $p_2 = p_3 = 1$ as a working example to study the qualitative behaviour of the Proca field and its impact on the cosmic structure formation, and leave the study of general functions $G_{2,3}(X)$ to future work. With this choice, the GP theory behaves as the standard scalar Galileon model in certain limits, as we will show later.

Having carefully chosen the components in our action, we can derive the EOM from it [63]. Variation with respect to $g^{\mu\nu}$ gives us the modified Einstein equation,

$$\mathcal{G}_{\mu\nu}^{(F)} + \mathcal{G}_{\mu\nu}^{(2)} + \mathcal{G}_{\mu\nu}^{(3)} + \mathcal{G}_{\mu\nu}^{(4)} = \frac{1}{2}T_{\mu\nu}^{(m)}, \tag{2.13}$$

with

$$\mathcal{G}^{(F)}_{\mu\nu} = \frac{1}{4} g_{\mu\nu} (\nabla_\rho A_\sigma \nabla^\rho A^\sigma - \nabla_\rho A_\sigma \nabla^\sigma A^\rho) - \frac{1}{2} \left(\nabla_\rho A_\mu \nabla^\rho A_\nu + \nabla_\mu A_\rho \nabla_\nu A^\rho - 2 \nabla_\rho A_{(\nu} \nabla_{\mu)} A^\rho \right) \tag{2.14}$$

$$\mathcal{G}^{(2)}_{\mu\nu} = -\frac{1}{2} g_{\mu\nu} G_2 - \frac{1}{2} G_{2,X} A_\mu A_\nu \tag{2.15}$$

$$\mathcal{G}^{(3)}_{\mu\nu} = -\frac{1}{2} G_{3,X} (A_\mu A_\nu \nabla_\rho A^\rho + g_{\mu\nu} A^\lambda A_\rho \nabla_\lambda A^\rho - 2 A_\rho A_{(\mu} \nabla_{\nu)} A^\rho) \tag{2.16}$$

$$\mathcal{G}^{(4)}_{\mu\nu} = \frac{M_{Pl}^2}{2} \left(R_{\mu\nu} - \frac{1}{2} g_{\mu\nu} R \right). \tag{2.17}$$

where we have used the shorthand notation $G_{i,X} \equiv \partial G_i / \partial X$ with $i = 2, 3$. Variation with respect to A_μ gives us the EOM of the vector field,

$$0 = \nabla_\mu F^{\mu\nu} - b_2 A^\nu + 2 b_3 A^{[\mu} \nabla^{\nu]} A_\mu, \tag{2.18}$$

where the square bracket around indices mean their anti-symmetrisation. We can see from Eq. (2.13), that the existence of a vector field with derivative self-coupling induces additional gravitational interactions with matter. We want to study whether such interactions are viable in non-linear regimes of cosmological structure formation.

2.2.2 Cosmological field equations

In order to derive the perturbation equations relevant for the study of large-scale structure formation, we work with the perturbed FLRW metric in the Newtonian gauge

$$g_{\mu\nu} = -(1 + 2\Psi) \mathrm{d}t^2 + a^2(t)(1 - 2\Phi) \delta_{ij} \mathrm{d}x^i \mathrm{d}x^j, \tag{2.19}$$

where $a(t)$ is the time-dependent scale factor which is normalised to $a(t_0) = 1$ at the present day, and $\delta_{ij} = \mathrm{diag}(+1, +1, +1)$ represents the spatial sector of the background metric that is taken here to be flat, $k = 0$.

We write the Proca field A_μ in its component form as $A_\mu = (A_0, A_i) = (\varphi, A_i)$, and further disentangle the spatial part of the Proca field, A_i,

through the Helmholtz's theorem into a longitudinal and a transverse component

$$A_i = B_i + \nabla_i \chi, \tag{2.20}$$

where B_i obeys the divergence-free condition, $\nabla^i B_i = 0$, and χ is the longitudinal scalar. Thus when deriving the components of the Einstein equations, we can apply the curl operator to filter out B_i and the divergence operator to obtain the contribution of χ.

Note that, rigorously speaking, the metric in Eq. (2.19) does not have enough physical degrees of freedom to fully describe the spacetime perturbations induced by a GP field. For example, the helicity-1 modes of the vector field produces vector mode perturbations of the metric. However, the interactions of the helicity-0 modes are typically stronger (in magnitude) than those of the helicity-1 modes [67]. We will verify this numerically below, so that we can neglect their effects on cosmological structure formation[2]. For this reason, our approach to treat the transverse component in this study is a 'passive' one, where we solve B_i as sourced by matter and χ, but neglect the 'backreaction' of B_i on the evolution of the latter, with *a posteriori* check that such a neglecting is justified. This greatly simplifies the field equations solved in the N-body simulation, which would have been extremely cumbersome otherwise.

[2] In the linear perturbation regime or for spherical mass distributions, it has been shown that the transverse component of the vector field vanishes identically, e.g. [63].

Solving cosmological structure formation is inherently computationally expensive, even without adding the transverse degree of freedom B_i to the action. Therefore we apply two other approximations to further simplify the field equations. The first is the quasi-static approximation (QSA), under which all time derivatives of the field *perturbations* are assumed to be small compared with their spatial derivatives (e.g., $|\dot{\delta\varphi}| \ll |\delta\varphi_{,i}|$) and can therefore be dropped. We shall in addition assume that the time derivatives of the gravitational potentials are much smaller than their corresponding spatial derivatives,

$$|\dot{\Phi}| \sim |\dot{\Psi}| \ll |\Phi_{,i}| \sim |\Psi_{,i}|, \quad \ddot{\Phi} \sim H\dot{\Phi} \ll |\Phi^{,i}_{,i}|, \tag{2.21}$$

where $_{,i}$ denotes derivative with respect to the comoving coordinate x^i and an overdot the derivative with respect to the physical time t. As galaxy-survey data are still mostly available on scales small compared to the cosmological horizon, the QSA is usually a good approximation for N-body simulations. Nevertheless, we add the caveat here that for models like scalar Galileons and GP theory, the field equations are so complicated that a full N-body simulation in which all time derivatives are included is yet to be done, which means that the validity of the QSA remains largely an assumption. Actually, there have been suspicions that the approximations used to simplify the field equations in the scalar Galileon models, including QSA, may be linked to some artificial numerical issues encountered in simulations (see, e.g., [16, 17, 136, 224] for some discussions). Due to this caveat, we shall explicitly mention it every time we apply the QSA. The second is the weak-field limit (WFL), which says that terms such as $\varphi'^i\varphi_{,i}$ are much smaller compared with $\varphi'^i{}_{,i}$. The application of both the QSA and the WFL considerably reduce the computational cost of running a simulation.

The physical units of quantities

Before proceeding to the cosmological field equations, and convert them into code-unit equations to be implemented in the N-body simulation code, it is useful to first clarify the physical unit of physical quantities in the GP theory.

Based on the action of the GP theory, we know that $G_2(X)$, $G_3(X)\nabla_\mu A^\mu$ and $G_4(X)R = c^4R/(16\pi G)$ have the same unit. Given that $[R] = L^{-2}$, $[c] = LT^{-1}$ and $[G] = M^{-1}L^3T^{-2}$, where L, T, M represent respectively the units for length, time and mass, the unit of $G_4(X)R$ and hence of $G_2(X)$ and $G_3(X)\nabla_\mu A^\mu$, must be $ML^{-1}T^{-2}$. Therefore,

$$ML^{-1}T^{-2} = [G_2(X)] = [b_2][X] = [b_2][A^\mu]^2, \tag{2.22}$$

and

$$ML^{-1}T^{-2} = [G_3(X)\nabla_\mu A^\mu] = [b_3][L]^{-1}[A^\mu]^3 \tag{2.23}$$

where we have used $G_2(X) = b_2 X$ and $G_3(X) = b_3 X$. We choose the unit of the time component of the Proca field, φ, as $[\varphi] = L^{-1}$ so that the field has mass dimension 1 in natural unit as required (it is also possible to choose $[\varphi] = T^{-1}$ by rescaling φ with c). Thus $[b_2] = MLT^{-2}$, $[b_3] = ML^3T^{-2}$ and similarly $[b_F] = ML^3T^{-2}$. Note that because φ has the same unit as $A_i = B_i + \nabla_i\chi$, it follows that χ is dimensionless and $[B_i] = L^{-1}$.

The modified Poisson equation

The (00) component of the perturbed Einstein equation, Eq. (2.13), after dropping terms according to the QSA and WFL, can be simplified as (with all c factors restored)

$$\frac{1}{2}\bar{\rho}_m c^2\left(1+\delta_m\right) = \frac{c^4}{16\pi G}\left[\frac{2}{a^2}\partial^2\Phi + 3\frac{H^2}{c^2}\right] - \frac{1}{4}b_F a^{-4}\partial_i B_j\left(\partial^i B^j - \partial^j B^i\right) - \frac{1}{4}b_2\varphi^2 + \frac{1}{2}b_3\varphi^2\left[3\frac{H}{c}\varphi - a^{-2}\partial^2 \right. \tag{2.24}$$

Note that we replaced ∇ by ∂ (which is the partial derivative with respect to the comoving coordinate) since $k = 0$, $\varphi = \bar{\varphi}(t) + \delta\varphi(t, \vec{x})$, where an overbar denotes background averaged quantities and $\delta\varphi$ the field perturbation; $\bar{\rho}_m$ and δ_m denote respectively the background density and density contrast of non-relativistic matter, where radiation has been neglected. We have, for this equation only, included the contribution from the transverse component of the Proca field (i.e., the term containing B_i), for illustration purpose, since it gives us a rough idea of what quantities to look at when comparing the contributions by the transverse versus longitudinal components to justify the neglecting of the former.

The above equation can be cleanly split into a purely background part, i.e., the modified Friedmann equation,

$$3H^2 = 8\pi G\bar{\rho}_m(a) + \frac{1}{2}\beta_2 c^2\bar{\varphi}^2 - 3\beta_3 cH\bar{\varphi}^3, \tag{2.25}$$

and a perturbation part, which corresponds to the modified Poisson equation (including the contribution from B_i again)

$$\partial^2\Phi \approx \frac{4\pi G}{c^2}\bar{\rho}_m a^2\delta + \frac{1}{2}\beta_3\bar{\varphi}^2\partial^2\chi + \frac{1}{2}\beta_F c^2 a^{-4}\partial_i B_j\left(\partial^i B^j - \partial^j B^i\right), \tag{2.26}$$

where we have redefined the parameters b_2, b_3, b_F as $\beta_i \equiv 8\pi G c^{-4} b_i$ with $i = 2, 3, F$. Note that β_2 is dimensionless while $[\beta_3] = [\beta_F] = L^2$.

Eq. (2.26) solves the metric potential Φ provided a matter density field and configuration of χ. However, it is the other potential Ψ whose gradient is the gravitational force. The EOM of the (ij) components of the perturbed Einstein equation contain further information on the relation between $\partial^2\Psi$, A_i, and matter perturbation, as well as between the sum of $\partial^2(\Phi + \Psi)$ and the anisotropic stress of the Proca field A_i. The latter can be used to solve Ψ given Φ. However, to the same approximation that the contribution from the transverse component B_i is negligible to leading order, it can be shown that the anisotropic stress of the Proca field vanishes, allowing us to approximate

$$\Phi \approx -\Psi. \tag{2.27}$$

In this case, χ behaves very similarly to the (cubic) scalar Galileon field. As a sanity check, we have confirmed that the expressions for $\mathcal{G}_{\mu\nu}^{(F,2,3)}$ we have found satisfy the Bianchi identity.

Equation of motion for the longitudinal mode

Proceeding with the EOM of the Proca field given in Eq. (2.18), we begin with the temporal component, φ, which is given by,

$$0 = b_F a^{-2}\left(\partial^2\dot{\chi} - c\partial^2\varphi\right) + b_2 c\varphi - 3b_3 H\varphi^2 + a^{-2}b_3 c\varphi\partial^2\chi. \tag{2.28}$$

The background part of this equation reads

$$b_2 c = 3b_3 H\bar{\varphi}, \tag{2.29}$$

which can be used to solve the background value of φ given H. This can be further rewritten, using β_2 and β_3, as

$$\beta_2 c = 3\beta_3 H\bar{\varphi}. \tag{2.30}$$

On the other hand, at the perturbation level we have

$$b_F\left(c\partial^2\varphi - \partial^2\dot{\chi}\right) \approx b_3 c\bar{\varphi}\partial^2\chi, \tag{2.31}$$

where we have employed the WFL to neglect terms such as $b_2\delta\varphi$ and $-6b_3H\bar{\varphi}\delta\varphi$, and we have also used $\partial^2\varphi$ instead of $\partial^2\delta\varphi$ to lighten the notation. This equality makes it possible to replace the time derivatives of $\partial_i\chi$ and $\partial_i\varphi$ in the equation of motion for χ. To see this, let us consider the EOM of the spatial component, $A_i = (\partial_i\chi, B_i)$,

$$\begin{aligned} 0 \;=\; & b_F\left(c\partial^j\dot{\varphi} - \partial^j\ddot{\chi} - \ddot{B}^j\right) + b_F H\left(c\partial^j\varphi - \partial^j\dot{\chi} - \dot{B}^j\right) \\ & + b_F a^{-2}c^2\partial^2 B^j - b_2c^2\left(\partial^j\chi + B^j\right) - b_3c^2\bar{\varphi}\left(\partial^j\varphi - \bar{\varphi}\partial^j\Psi\right) \\ & + b_3\left(c\dot{\bar{\varphi}} + 3cH\bar{\varphi} - a^{-2}c^2\partial^2\chi\right)\left(\partial^j\chi + B^j\right) \\ & - b_3c^2a^{-2}\left(\partial^j\partial^k\chi + \partial^j B^k\right)\left(\partial_k\chi + B_k\right). \end{aligned} \tag{2.32}$$

We make two simplifications to this equation. First, as we are interested in the EOM for the longitudinal component χ in this subsection, we remove all the transverse components and leave them for the next subsection. Note that this does not mean that all terms involving B_i should be dropped: for example, the term $B_k\partial^j B^k = \partial^j(B^k B_k)/2$ is a total derivative and has a nonzero divergence; on the other hand, terms such as $\ddot{B}^j$, $\dot{B}^j$ and $\partial^2 B^j$ will be considered in the next subsection. Second, terms such as $B^j\partial^2\chi$, $\partial^j B^k\partial_k\chi$ and $B_k\partial^j\partial^k\chi$ are dropped on the ground that the 'back-reaction' of B^i on the dynamics of χ is negligible (the argument for this requires a better knowledge of the equation that governs B^i, and will be deferred to the next subsection).

Taking the divergence of Eq. (2.32) to single out the longitudinal con-

tributions, and dropping the terms that contain B^i, we find

$$\begin{aligned} 0 &= b_F\left(c\partial^2\dot{\varphi}-\partial^2\ddot{\chi}\right)+b_F H\left(c\partial^2\varphi-\partial^2\dot{\chi}\right)-b_2c^2\partial^2\chi \\ &\quad -b_3c^2\bar{\varphi}\left(\partial^2\varphi-\bar{\varphi}\partial^2\Psi\right)+b_3c\left(\dot{\bar{\varphi}}+3H\bar{\varphi}\right)\partial^2\chi \\ &\quad -b_3c^2a^{-2}\left[\left(\partial^2\chi\right)^2-\partial_i\partial_j\chi\partial^i\partial^j\chi\right], \end{aligned} \tag{2.33}$$

This equation has two undesirable properties: first, it contains not just the spatial derivatives of χ but also of φ; second, it contains also spatial derivatives of $\dot{\chi}$ and $\ddot{\chi}$. On the face it seems to suggest that some sort of quasi-static approximation should be employed to drop terms such as $\partial^j\ddot{\chi}$ and $\partial^j\dot{\chi}$. It however turns out that one can use Eq. (2.31) and its time derivative

$$b_F\left(c\partial^2\dot{\varphi}-\partial^2\ddot{\chi}\right)=b_3c\dot{\bar{\varphi}}\partial^2\chi+b_3c\bar{\varphi}\partial^2\dot{\chi}, \tag{2.34}$$

to rewrite Eq. (2.33) in the following more convenient form,

$$\begin{aligned} \bar{\varphi}^2\partial^2\Psi &= \left[\frac{b_2}{b_3}-2c^{-1}\left(\dot{\bar{\varphi}}+2H\bar{\varphi}\right)+\frac{b_3}{b_F}\bar{\varphi}^2\right]\partial^2\chi \\ &\quad +a^{-2}\left[\left(\partial^2\chi\right)^2-\partial_i\partial_j\chi\partial^i\partial^j\chi\right]. \end{aligned} \tag{2.35}$$

Note that this means all time derivatives are eliminated exactly, so that we do not have to resort to the QSA. As a final step, we replace $b_{2,3,F}$ with $\beta_{2,3,F}$ as before, and use the modified Poisson equation, (2.26) (excluding the contributions from B^i) and the relation $\Phi \approx -\Psi$ in Eq. (2.27) to eliminate Ψ, and obtain

$$\begin{aligned} \frac{4\pi G}{c^2}a^2\bar{\rho}_m\delta_m=\nabla^2\Phi_N &= \left[\frac{1}{\bar{\varphi}^2}\frac{\beta_2}{\beta_3}-2c^{-1}\left(\frac{\dot{\bar{\varphi}}}{\bar{\varphi}^2}+2H\frac{1}{\bar{\varphi}}\right)+\frac{\beta_3}{\beta_F}-\frac{1}{2}\beta_3\bar{\varphi}^2\right]\partial^2\chi \\ &\quad +\frac{1}{\bar{\varphi}^2a^2}\left[\left(\partial^2\chi\right)^2-\partial_i\partial_j\chi\partial^i\partial^j\chi\right], \end{aligned} \tag{2.36}$$

where $\Phi_N = \Psi_N$ is the standard Newtonian potential. This is the main equation that we will convert to code unit and implement into the N-body simulation code in the next section.

Equation of motion for the transverse mode

Singling out the transverse part of Eq. (2.32) by applying the curl operator once would leave a numerically inconvenient equation behind. This can be bypassed by simply applying the curl once more on itself and simplifying things using the vector identity,

$$\nabla \times (\nabla \times \mathbf{B}) = \nabla (\nabla \cdot \mathbf{B}) - \nabla^2 \mathbf{B} = -\nabla^2 \mathbf{B}, \tag{2.37}$$

where in the second step we have used the fact that $\mathbf{B}$ satisfies $\nabla \cdot \mathbf{B} = 0$. Thus we obtain, for the EOM of B_i,

$$\begin{aligned} 0 \quad = \quad & b_F c^{-2} \partial^2 \ddot{\mathbf{B}} + b_F c^{-2} H \partial^2 \dot{\mathbf{B}} - a^{-2} b_F \partial^4 \mathbf{B} + b_2 \partial^2 \mathbf{B} \\ & - b_3 \left(c^{-1} \ddot{\bar{\varphi}} + 3 c^{-1} H \dot{\bar{\varphi}} - a^{-2} \partial^2 \chi \right) \partial^2 \mathbf{B} \\ & + b_3 \left[\partial^2 \Psi \vec{\partial} \varphi^2 - \partial^2 \varphi^2 \vec{\partial} \Psi + \left(\vec{\partial} \Psi \cdot \vec{\partial} \right) \vec{\partial} \varphi^2 - \left(\vec{\partial} \varphi^2 \cdot \vec{\partial} \right) \vec{\partial} \Psi \right] \\ & + b_3 \partial^2 \chi \vec{\partial} \left(c^{-1} \dot{\varphi} + 3 c^{-1} H \varphi - a^{-2} \partial^2 \chi \right) \\ & - b_3 \partial^2 \left(c^{-1} \dot{\varphi} + 3 c^{-1} H \varphi - a^{-2} \partial^2 \chi \right) \left(\vec{\partial} \chi + \mathbf{B} \right) \\ & + b_3 \left[\left(\vec{\partial} \chi + \mathbf{B} \right) \cdot \vec{\partial} \right] \vec{\partial} \left(c^{-1} \dot{\varphi} + 3 c^{-1} H \varphi - a^{-2} \partial^2 \chi \right) \\ & - b_3 \left[\vec{\partial} \left(c^{-1} \dot{\varphi} + 3 c^{-1} H \varphi - a^{-2} \partial^2 \chi \right) \cdot \vec{\partial} \right] \left(\vec{\partial} \chi + \mathbf{B} \right), \end{aligned} \tag{2.38}$$

where we have used $\vec{\partial}$ to denote the vector gradient. This expression is still too complex for a cosmological simulation, making it necessary to apply further simplifications with the following arguments.

First, the QSA is applied to drop the time derivatives of B^i, namely $|\partial^2 \ddot{\mathbf{B}}| \sim |H \partial^2 \dot{\mathbf{B}}| \ll |\partial^4 \mathbf{B}|$, from the equation. Therefore, the above equation can be considered as a constraint equation in which $\mathbf{B}$, or $\partial^2 \mathbf{B}$, is sourced by various terms. The term $a^{-2} b_F \partial^4 \mathbf{B}$ contains the Laplacian of $\partial^2 \mathbf{B}$, which should be what other terms are compared against to decide the relative importance.

For example, we start with comparing the magnitudes of $b_2 \partial^2 \mathbf{B}$ and $a^{-2} b_F \partial^4 \mathbf{B}$. Schematically we can write $|\partial^2 \mathbf{B}| \sim \eta^{-2} |\Delta \mathbf{B}|$, where η is the size (in Mpc$/h$) of the mesh cells on which we will discretise the equation and numerically solve it in the simulation, and $\Delta \mathbf{B}$ is the

typical difference between the values of $\mathbf{B}$ in neighbouring cells of the mesh. Likewise, $|\partial^4\mathbf{B}| \sim \eta^{-4}|\Delta\mathbf{B}|$[3]. Therefore, the ratio of these two quantities can be estimated as

[3] Because we are only interested in an order-of-magnitude estimate, we neglect the fact that the $\Delta\mathbf{B}$ values are different in these two cases, and assume that they are of similar magnitudes.

$$\frac{|b_2\partial^2\mathbf{B}|}{|a^{-2}b_F\partial^4\mathbf{B}|} \sim \frac{b_2}{b_F}\eta^2 = \frac{\beta_2}{\beta_F}\eta^2 = \frac{\tilde{\beta}_2}{\tilde{\beta}_F}\eta^2\left(\frac{c}{H_0}\right)^{-2} \tag{2.39}$$

where we have defined the dimensionless variables

$$\begin{aligned}\tilde{\beta}_2 &\equiv \beta_2,\\ \tilde{\beta}_{3,F} &\equiv \beta_{3,F}\left(\frac{c}{H_0}\right)^{-2},\end{aligned} \tag{2.40}$$

that will be used later to write the field equations in code unit. We have the freedom to set $\tilde{\beta}_F = 1$ by a field redefinition, $\tilde{\beta}_3$ is a free parameter of the model studied here for which we are interested in $\mathcal{O}(10^{-6}) \lesssim \tilde{\beta}_3 \lesssim \mathcal{O}(100)$, and $\tilde{\beta}_2$ is related to $\tilde{\beta}_3$ through Eq. (2.51) below as $\tilde{\beta}_2 = -54^{1/3}(1-\Omega_m)^{1/3}\tilde{\beta}_3^{2/3}$ with $\Omega_m \approx 0.3$ being the matter density parameter today. Therefore $\tilde{\beta}_2 \lesssim 70$; combining with the fact that $c/H_0 \approx 3000h^{-1}$Mpc and $\eta \lesssim 1h^{-1}$Mpc in typical simulations, this means that the ratio in Eq. (2.39) is much smaller than 1, and so the term $b_2\partial^2\mathbf{B}$ can be neglected from Eq. (2.38).

As another example, we compare $b_3c^{-1}\dot{\bar{\varphi}}\partial^2\mathbf{B}$ and $b_3c^{-1}H\bar{\varphi}\partial^2\mathbf{B}$ against $a^{-2}b_F\partial^4\mathbf{B}$. We can regard the former two quantities as the same order because $\dot{\bar{\varphi}} \sim H\bar{\varphi}$, so we focus on $b_3c^{-1}H\bar{\varphi}\partial^2\mathbf{B}$. The ratio is

$$\frac{|b_3c^{-1}H\bar{\varphi}\partial^2\mathbf{B}|}{|a^{-2}b_F\partial^4\mathbf{B}|} \sim \frac{b_3}{b_F}c^{-1}H\bar{\varphi}\eta^2 = \frac{\tilde{\beta}_3}{\tilde{\beta}_F}c^{-1}H\bar{\varphi}\eta^2 = \frac{\tilde{\beta}_2}{3\tilde{\beta}_F}\eta^2\left(\frac{c}{H_0}\right)^{-2} \ll 1, \tag{2.41}$$

where in the last equality we have used Eq. (2.30). Therefore these terms can also be dropped from Eq. (2.38).

Second, consider the term $b_3a^{-2}\partial^2\chi\partial^2\mathbf{B}$. We have for cosmological objects $|\Phi_\mathrm{N}| \lesssim \mathcal{O}(10^{-4})$, and can use Eq. (2.36) to estimate the size of χ. This can be divided into two cases. The first is when the left-hand side of Eq. (2.36) is dominated by the first term, which is linear in $\partial^2\chi$ – there are four terms in the bracket in front of $\partial^2\chi$ in Eq. (2.36), and with a lengthy

but trivial calculation it can be shown that their relative magnitudes vary depending on the parameter value of $\tilde{\beta}_3$ and the time a. For simplicity, this whole bracket can be written as $\epsilon\,(\tilde{\beta}_3/\tilde{\beta}_2) + (\tilde{\beta}_3/\tilde{\beta}_F)$, where ϵ is a time-dependent function of order $\mathcal{O}(10)$ or larger. In the second case, the non-linear term dominates the left-hand side of Eq. (2.36), and one has

$$\frac{1}{a^2\bar{\varphi}^2}\frac{1}{\eta^4}|\Delta\chi|^2 \sim \frac{1}{\eta^2}|\Delta\Phi_N| \Rightarrow \frac{\tilde{\beta}_3}{\tilde{\beta}_2}|\Delta\chi| \sim \frac{1}{3}a\sqrt{|\Phi_N|}\eta\left(\frac{c}{H_0}\right)^{-1}\frac{H_0}{H}, \tag{2.42}$$

where we have used

$$\bar{\varphi}^{-1} = \frac{3\tilde{\beta}_3}{\tilde{\beta}_2}\frac{c}{H_0}\frac{H}{H_0}, \tag{2.43}$$

which itself is derived from Eq. (2.30). Following the previous logic, the ratio to $b_F a^{-2}\partial^4\mathbf{B}$ is given by

$$\frac{|b_3 a^{-2}\partial^2\chi\partial^2\mathbf{B}|}{|b_F a^{-2}\partial^4\mathbf{B}|} \sim \frac{b_3}{b_F}\frac{\eta^{-2}|\Delta\chi|\cdot\eta^{-2}|\Delta\mathbf{B}|}{\eta^{-4}|\Delta\mathbf{B}|} \sim \frac{\tilde{\beta}_3}{\tilde{\beta}_F}|\Delta\chi|. \tag{2.44}$$

It can then be straightforwardly checked that the ratio in Eq. (2.44) is always much smaller than 1 for both cases, and when either $\tilde{\beta}_3/\tilde{\beta}_2$ or $\tilde{\beta}_3/\tilde{\beta}_F$ dominates in the first case. Therefore this term can also be dropped from Eq. (2.38).

Third, consider the terms such as $\partial^2\Psi\vec{\partial}\varphi^2 \sim \bar{\varphi}\partial^2\Psi\vec{\partial}\varphi$ that can also source $\partial^2\mathbf{B}$, in the second line of Eq. (2.38). Integrating Eq. (2.31) once, one finds

$$b_F\,(c\partial_i\varphi - \partial_i\dot{\chi}) \approx b_3 c\bar{\varphi}\partial_i\chi \Rightarrow \partial_i\varphi \approx c^{-1}\partial_i\dot{\chi} + \frac{b_3}{b_F}\bar{\varphi}\partial_i\chi, \tag{2.45}$$

so that $|\partial_i\varphi|$ is approximately of the same order as $b_3/b_F\bar{\varphi}|\partial_i\chi|$ or $c^{-1}|\partial\dot{\chi}| \sim c^{-1}H|\partial_i\chi|$, whichever dominates. In practice, the two terms on the right-hand side of Eq. (2.45) can differ by a factor of up to $\mathcal{O}(10)$. To demonstrate that terms such as $b_3\bar{\varphi}\partial^2\Psi\vec{\partial}\varphi$, instead of showing that its amplitude is much smaller than $|b_F a^{-2}\partial^4\mathbf{B}|$, we will seek to show that it is much smaller than the amplitude of certain other

terms in Eq. (2.38), in particular $b_3\partial^2\chi\vec{\partial}^i\partial^2\chi$ – consider the ratio

$$\begin{aligned}\frac{|b_3\bar{\varphi}\partial^2\Psi\vec{\partial}\varphi|}{|b_3\partial^2\chi\vec{\partial}\partial^2\chi|} &\sim c^{-1}H\bar{\varphi}\frac{|\partial^2\Phi_N|\cdot|\vec{\partial}\chi|}{|\partial^2\chi\vec{\partial}\partial^2\chi|}\\ &\sim c^{-1}H\bar{\varphi}\frac{\eta^{-3}|\Delta\chi|^2}{\eta^{-5}|\Delta\chi|^2}\left[\epsilon\frac{\tilde{\beta}_3}{\tilde{\beta}_2}+\frac{\tilde{\beta}_3}{\tilde{\beta}_F}\right]\\ &\sim \frac{\tilde{\beta}_2}{3\tilde{\beta}_3}\left[\epsilon\frac{\tilde{\beta}_3}{\tilde{\beta}_2}+\frac{\tilde{\beta}_3}{\tilde{\beta}_F}\right]\eta^2\left(\frac{c}{H_0}\right)^{-2}\\ &\ll 1,\end{aligned} \tag{2.46}$$

where in the first '$\sim$' we have assumed that $|\vec{\partial}\varphi| \sim c^{-1}H|\vec{\partial}\chi| \gg (b_3/b_F)\bar{\varphi}|\vec{\partial}\chi|, |\Phi_N| \sim |\Phi|$, and in the second '$\sim$' we have assumed that the term proportional to $\nabla^2\chi$ dominates the left-hand side of Eq. (2.36). It can be similarly shown that the ratio is also much smaller than 1 in the other limits, e.g., when $|\vec{\partial}\varphi| \sim (b_3/b_F)\bar{\varphi}|\vec{\partial}\chi| \gg c^{-1}H|\vec{\partial}\chi|$ and/or the non-linear term dominates the left-hand side of Eq. (2.36), though the details are omitted here for brevity. This indicates that these source terms can also be safely dropped off from Eq. (2.38).

Fourth, in Eq. (2.38) a number of terms can be neglected by realising that $c^{-1}|\vec{\partial}\dot{\varphi}| \sim c^{-1}H|\vec{\partial}\varphi| \ll a^{-2}|\vec{\partial}\partial^2\chi|$. The proof of these relations is straightforward and we shall not repeat them here.

Finally, therefore, we see that terms like $\partial^2\chi\partial_i\partial^2\chi$ are the remaining sources for $\partial^4 B^i$. For the former, we have $|\partial^2\chi\partial_i\partial^2\chi| \sim \eta^{-5}|\chi|\cdot|\Delta\chi|$, and for the latter we have $|\partial^4 B^i| \sim \eta^{-4}|\Delta B^i|$. This suggests that $|\Delta B^i| \sim |\chi|\cdot\eta^{-1}\Delta\chi \ll \eta^{-1}|\Delta\chi|$ and confirms that $|\partial B^i| \ll |\partial^2\chi|$ is self-consistent.

With the above approximations, the equation can be simplified to

$$\beta_F\partial^4 B^i = \beta_3\partial^j\left[\partial_i\chi\partial_j\partial^2\chi - \partial_j\chi\partial_i\partial^2\chi\right]. \tag{2.47}$$

Eqs. (2.26, 2.36, 2.47) are the key equations of this Chapter – the last one is used to calculate B^i and verify that the transverse component makes negligible contribution ('feedback') to the dynamics of Φ and χ, the second one is used to solve χ given a matter distribution, and finally the first one is used to find the total gravitational potential (and therefore the total gravity force) for the given matter distribution and the resulting

spatial configuration of χ.

As $\tilde{\beta}_3 \equiv b_3(8\pi G H_0^2)/(c^6)$ is the only 'free' parameter that enters in all three key equations it is practical to use it as the model parameter. Previous works denote the model parameters that behave similarly to $\tilde{\beta}_3$ as λ [64, 154] and q_v [62, 110], which are both inversely proportional to $\tilde{\beta}_3$. We do not present the exact relations between those parameters and $\tilde{\beta}_3$ here.

2.3 N-body Equations

In this section we describe the numerical implementation of the above-derived equations into the N-body code ECOSMOG[135]. For this purpose, we will need to recast the equations in ECOSMOG's code units, in which all quantities are rescaled so that only dimensionless quantities appear. In order to acquire a better understand about the cvG model behaviour we juxtapose it with the well studied cosmologies of ΛCDM, self-accelerating branch of the Dvali-Gabadadze-Porrati model (sDGP, [78]), and the tracker solution of the cubic scalar Galileon (csG, [16, 19])[4] where appropriate. For the csG model, we assume that for the entire time period of interest here the model follows the *tracker solution* [60], which is an attractor of the evolution; in practice, the time at which the model merges onto this common late-time evolution trajectory depends on the initial conditions (ICs) of the background csG field, but it was demonstrated in Ref. [20] that the merging onto the tracker solution should happen before the onset of the acceleration era, $a \sim 0.5$, in order to satisfy CMB constraints. In all visualisations of the models we adopt the following two cosmological parameters: $\Omega_m = 0.3089$ and $H_0 = 67.74$ kms/s/Mpc. For the sDGP specific parameters we use $\Omega_{rc} = 0.25$, while the csG specific parameters are the following: $\Omega_\varphi = 1 - \Omega_m$, $\xi = \sqrt{6\Omega_\varphi}$, $c_2 = -1$, and $c_3 = 1/(6\xi)$ (see Ref. [19] for more details). To better understand the effects of the fifth force we compare the csG and cvG model to their quintessence counterpart, Quintessence Cold Dark Matter (QCDM), which is a variant that only considers the modified background expansion his-

[4] Note that although the csG is a generalisation of the sDGP that arises from its decoupling limit, their phenomenology is very different.

tory, but uses standard Newtonian gravity, in the simulation.

2.3.1 Code units

The main challenge in N-body simulations of models such as cvG gravity is to solve the scalaron Eq. (2.60), which is in general highly nonlinear. One way to achieve this is to use a mesh (or a set of meshes) on which cvG could be solved. This implies that mesh-based N-body codes are most convenient. On the other hand, tree-based codes are more difficult to apply here, as we do not have an analytical formula for the modified force law (such as r^{-2} in the Newtonian case) due to the complexities stemmed from the breakdown of the superposition principal, or the invalidity of Birkhoff theorem in modified gravity.

In order to implement the equations into `ECOSMOG`, we introduce a set of dimensionless quantities that are based on H_0^{-1} for measuring time, the simulation box size L in units of Mpc$/h$, the particle velocity v, the critical density today $\rho_{c0} = 8\pi G/(3H_0^2)$ and the matter density $\Omega_m = \Omega_b + \Omega_c$ at the present day:

$$\begin{aligned} \tilde{x} &= \frac{x}{L} & \tilde{\rho} &= \frac{\rho a^3}{\rho_{\rm c0}\Omega_{\rm m}} & \tilde{v} &= \left(\frac{a}{LH_0}\right) v \\ \tilde{c} &= \frac{c}{H_0 L} & d\tilde{t} &= H_0 a^{-2} dt & \tilde{\Phi} &= \left(\frac{ac}{LH_0}\right)^2 \Phi. \end{aligned} \tag{2.48}$$

The N-body solver is implemented in conformal time, $\tilde{t}$, which allows a straightforward implementation of comoving coordinates. The details of these so-called "super-comoving coordinates" can be found in [144] and references therein. In this coordinate system the background matter density is unity, $\tilde{\bar{\rho}} = 1$.

To transform the quantities introduced by the Proca theory to code units, we need to know their physical units. As mentioned above, the Proca field A_μ has mass dimension 1 in natural unit, and we have $[A_i] = L^{-1}$ in physical unit, so that the longitudinal mode χ is dimensionless. However, since χ plays an equivalent role as Φ in determining the force, we transform it into code unit in the same way as for Φ; on the other hand, the transverse component B_i has unit $[B_i] = L^{-1}$, we multiply it

by the box size L to get $\tilde{B}_i$; to get the code-unit expression for $\bar{\varphi}$, which has unit $[\bar{\varphi}] = L^{-1}$, instead of multiplying it by L, we multiply it by c/H_0 because this variable is only used to calculate background quantities. The results are:

$$\tilde{\varphi} = \frac{c}{H_0}\bar{\varphi} \qquad \tilde{B}_i = a^4\tilde{c}^4 L B_i \qquad \tilde{\chi} = \left(\frac{ac}{LH_0}\right)^2 \chi, \tag{2.49}$$

where we have also included a factor $a^4\tilde{c}^4$ in $\tilde{B}_i$ to further simply the code-unit equation of Eq. (2.47).

2.3.2 Background and perturbation equations

The modified Friedmann equation, Eq. (2.25), can be simplified as

$$3H^2 = 8\pi G\bar{\rho}_m(a) - \frac{1}{18}\frac{\tilde{\beta}_2^3}{\tilde{\beta}_3^2}\frac{H_0^4}{H^2}, \tag{2.50}$$

where we have used Eq. (2.30) and the definitions of $\tilde{\beta}_2$ and $\tilde{\beta}_3$.

As the Friedmann equation is commonly expressed as a relation between density parameters today, we can follow this practice for the Proca field by defining Ω_P (similar to Ω_φ in the csG model) as the links between the two coupling constants $\tilde{\beta}_2$ and $\tilde{\beta}_3$ through

$$\Omega_P \equiv -\frac{1}{54}\frac{\tilde{\beta}_2^3}{\tilde{\beta}_3^2} = 1 - \Omega_m, \tag{2.51}$$

where note that $\tilde{\beta}_2 < 0$. This leads to the following result of $E(a) \equiv H(a)/H_0$ for the cvG model, which we show together with the expressions for the other cosmologies for clarity,

$$E^2 = \begin{cases} \Omega_m a^{-3} + \Omega_\Lambda, & \Lambda\text{CDM}, \\ \Omega_m a^{-3} + 2\Omega_{rc} + 2\sqrt{\Omega_m a^{-3} + 2\Omega_{rc}}, & \text{sDGP}, \\ \frac{1}{2}\left[\Omega_m a^{-3} + \sqrt{\Omega_m^2 a^{-6} + 4\left(1-\Omega_m\right)}\right], & \text{cvG, csG, QCDM}. \end{cases} \tag{2.52}$$

where we have assumed the Universe to be spatially flat ($k = 0$) and considered only non-relativistic matter; the inclusion of radiation and massive neutrinos is straightforward. Therefore, the background expansion history in this model is completely determined by H_0 and Ω_m, and mimics precisely the tracker solution of the csG model, e.g., [16, 19]. This can be seen clearly in the top-left panel of Fig. 2.1, which shows a comparison of the background expansion history in the cvG model with those of the DGP and csG models.

We also give the effective equation of state, $w_{\rm eff} = -1 - 2\dot{H}/(3H^2)$, in the top-right panel of the same figure

$$w_{\rm eff} = \begin{cases} \frac{\Omega_m - 1}{1 - \Omega_m + \Omega_m a^{-3}}, & \Lambda\text{CDM}, \\ \frac{2}{3\beta_{\rm sDGP}}, & \text{sDGP}, \\ -1 + \frac{\Omega_m a^{-3} + \frac{\Omega_m^2 a^{-6}}{\sqrt{\Omega_m^2 a^{-6} + 4(1-\Omega_m)}}}{\Omega_m a^{-3} + \sqrt{\Omega_m^2 a^{-6} + 4(1-\Omega_m)}}, & \text{cvG, csG, QCDM}. \end{cases} \tag{2.53}$$

The modified Poisson equation, Eq. (2.26), takes the following form in code unit,

$$\tilde{\partial}^2 \tilde{\Phi} = \frac{3}{2}\Omega_m a\,(\tilde{\rho} - 1) + \alpha \tilde{\partial}^2 \tilde{\chi}, \tag{2.54}$$

where

$$\alpha(a) \equiv \frac{1}{2}\tilde{\beta}_3 \tilde{\varphi}^2 = \frac{1}{2\sqrt[3]{2}} \tilde{\beta}_3^{1/3} \Omega_P^{-1/3} \left[\sqrt{\Omega_m^2 a^{-6} + 4\Omega_P} - \Omega_m a^{-3} \right], \tag{2.55}$$

is a time-dependent function that is fully fixed by specifying Ω_m and $\tilde{\beta}_3$. The left-bottom panel of Fig. 2.1 shows how $\alpha(a)$ evolves in time for different values of $\tilde{\beta}_3$.

Recasting Eq. (2.47) in code units gives

$$\tilde{\partial}^4 \tilde{B}^i = \frac{\tilde{\beta}_3}{\tilde{\beta}_F} \tilde{\partial}^j \left[\tilde{\partial}_i \tilde{\chi} \tilde{\partial}_j \tilde{\partial}^2 \tilde{\chi} - \tilde{\partial}_j \tilde{\chi} \tilde{\partial}_i \tilde{\partial}^2 \tilde{\chi} \right]. \tag{2.56}$$

As mentioned above, we can set $\tilde{\beta}_F = 1$, which is achievable by a field redefinition, without loss of generality. Therefore $\tilde{\beta}_F$ is not a free parameter of the Proca model here.

Finally, the EOM for the longitudinal mode of the Proca field, χ, Eq. (2.36), can be rewritten in code unit as,

$$\begin{aligned} \frac{3}{2}\Omega_m a \left(\tilde{\rho} - 1\right) &= \left[\frac{\tilde{\beta}_2}{\tilde{\beta}_3 \tilde{\varphi}^2} - 6\frac{\tilde{\beta}_3}{\tilde{\beta}_2}\left(2 - \frac{H'}{H}\right) E^2 + \frac{\tilde{\beta}_3}{\tilde{\beta}_F} - \frac{1}{2}\tilde{\beta}_3 \tilde{\varphi}^2 \right] \tilde{\partial}^2 \tilde{\chi} \\ &\quad + \frac{1}{\tilde{\varphi}^2 a^4} \left[\left(\tilde{\partial}^2 \tilde{\chi}\right)^2 - \tilde{\partial}_i \tilde{\partial}_j \tilde{\chi} \tilde{\partial}^i \tilde{\partial}^j \tilde{\chi} \right], \end{aligned} \tag{2.57}$$

where we have used Eq. (2.29), so that $H\dot{\varphi} = \dot{H}\varphi$, to eliminate $\dot{\varphi}$, and $'$ denotes the dimensionless derivative with respect to $\ln(a)$. If we define the following two dimensionless and time-dependent functions

$$\beta(a) \equiv \frac{\tilde{\beta}_2}{\tilde{\beta}_3 \tilde{\varphi}^2} - 6\frac{\tilde{\beta}_3}{\tilde{\beta}_2}\left(2 - \frac{E'}{E}\right) E^2 + \frac{\tilde{\beta}_3}{\tilde{\beta}_F} - \frac{1}{2}\tilde{\beta}_3 \tilde{\varphi}^2, \tag{2.58}$$

and

$$R_c(a) \equiv \frac{1}{\tilde{\varphi}}, \tag{2.59}$$

the equation can be further simplified to

$$\tilde{\partial}^2 \tilde{\chi} + \frac{R_c^2}{\beta a^4} \left[\left(\tilde{\partial}^2 \tilde{\chi}\right)^2 - \tilde{\partial}_i \tilde{\partial}_j \tilde{\chi} \tilde{\partial}^i \tilde{\partial}^j \tilde{\chi} \right] = \frac{3}{2\beta}\Omega_m a \left(\tilde{\rho} - 1\right). \tag{2.60}$$

This has a very similar form to the corresponding equations in the DGP or the csG model. Note that $|R_c|$ plays a similar role as the crossover radius in the DGP braneworld model.

One can again use Eq. (2.29) to further simplify $\beta(a)$ by eliminating $\tilde{\varphi}$ as

$$\beta(a) = -3\frac{\tilde{\beta}_3}{\tilde{\beta}_2}\left(1 - 2\frac{H'}{H}\right) E^2 + \tilde{\beta}_3 + 3\Omega_P \frac{\tilde{\beta}_3}{\tilde{\beta}_2} E^{-2}, \tag{2.61}$$

where we have used $\tilde{\beta}_F = 1$ and Eq. (2.51). Using the following relations

$$E^{-2} = \frac{1}{2\Omega_P}\left[\sqrt{\Omega_m^2 a^{-6} + 4\Omega_P} - \Omega_m a^{-3}\right], \tag{2.62}$$

$$E^2 - 2EE' = 2\Omega_m a^{-3} + 2\frac{\Omega_m^2 a^{-6} + \Omega_P}{\sqrt{\Omega_m^2 a^{-6} + 4\Omega_P}}, \tag{2.63}$$

and using again Eq. (2.51) this further becomes

$$\beta(a) = \frac{1}{2}\left(\frac{\tilde{\beta}_3}{2\Omega_P}\right)^{1/3}\left[5\Omega_m a^{-3} + \frac{3\Omega_m^2 a^{-6}}{\sqrt{\Omega_m^2 a^{-6} + 4\Omega_P}}\right] + \tilde{\beta}_3. \tag{2.64}$$

Similarly

$$R_c^2(a) = \frac{1}{2}\tilde{\beta}_3^{2/3}\left(2\Omega_P\right)^{-2/3}\left[\Omega_m a^{-3} + \sqrt{\Omega_m^2 a^{-6} + 4\Omega_P}\right]. \tag{2.65}$$

The top-right panel of Fig. 2.1 shows how $R_c^2(a)$ depends on the model parameter $\tilde{\beta}_3$. Note that both functions, $\beta(a)$ and $R_c(a)$, are fully fixed by specifying Ω_m and $\tilde{\beta}_3$. Therefore there is one free parameter in this model, given by $\tilde{\beta}_3 > 0$.

2.3.3 Vainshtein screening

One of the key quantities in models employing the Vainshtein screening mechanism is the distance to the source, called the Vainshtein radius, r_V, where the linear perturbation analysis breaks down and the theory enters the non-linear regime. For scalar field models with derivative self-interactions it is the cubic- and higher-order terms that produce Vainshtein screening. It has been demonstrated that to explain the late-time cosmic acceleration, the Proca field has to be very light, $b_2 = m^2 \to 0$, and a non-zero coupling coefficient b_3 activates the screening mechanism to ensure the theory is consistent with solar-system tests of gravity [63].

We have seen in Eq. (2.60) that the non-linear term, which is what produces Vainshtein screening, is determined by $\beta(a)$ and $R_c^2(a)$, both of which depend on the free model parameter b_3, or its code-unit counterpart $\tilde{\beta}_3$. To make an educated choice of $\tilde{\beta}_3$, we compare the cvG model

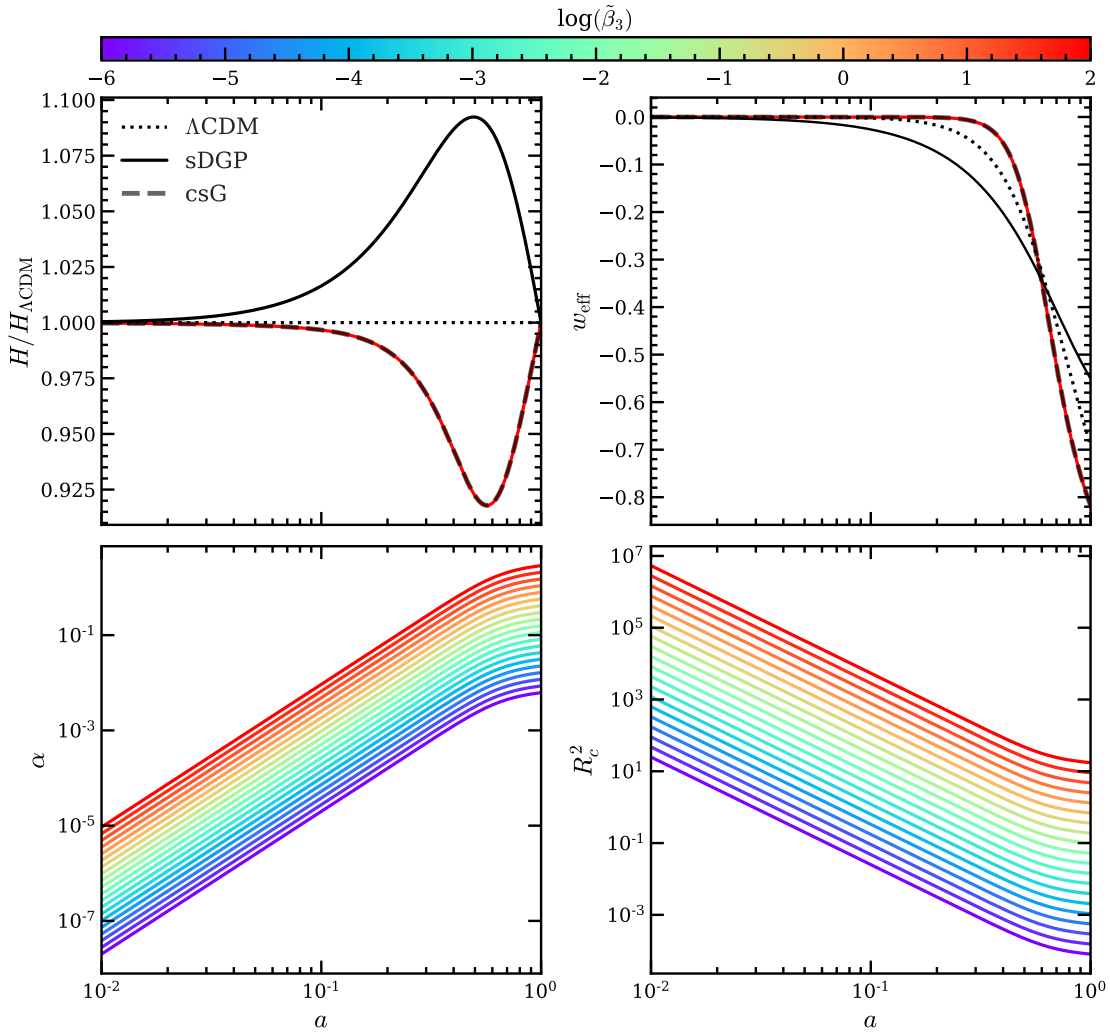

Figure 2.1: The time evolution of various background quantities in the cvG (coloured lines with different $\tilde{\beta}_3$ values as indicated by the colour bar on the top), csG (grey dashed line), sDGP (black solid line) and ΛCDM (black dotted line) models. *Top left:* The ratios of Hubble expansion rate in other cosmologies with respect to ΛCDM; note that the cvG results do not depend on $\tilde{\beta}_3$ and are identical to the csG prediction. *Top right:* The effective equation of state parameter, w_{eff}, given in Eqs. (2.53). *Bottom left:* The cvG model function α given in Eq. (2.55). *Bottom right:* The cvG model function R_c^2 given in Eq. (2.65).

with the sDGP and csG models, whose behaviour has been well understood. To do this fairly, we follow [17] (for the case of csG) to re-scale $\tilde{\chi}$ such that the source term of Eq. (2.60) becomes exactly identical to that of the EOM of the sDGP brane-bending mode as given by Eq. (18) in [137]; then we can simply compare the coefficients of the non-linear terms in these equations to decide for which values of $\tilde{\beta}_3$ does csG have a stronger Vainshtein screening than sDGP. This is achieved by introducing the redefined scalar mode, $\tilde{\chi}'$, as

$$\tilde{\chi} = \frac{3\beta_{\mathrm{sDGP}}}{2\beta}\tilde{\chi}', \tag{2.66}$$

where we have used the $\beta_{\rm sDGP}$ function, which describes the coupling strength to matter of the brane-bending mode in the sDGP model given by

$$\beta_{\rm sDGP} = -\frac{\frac{1}{2}\Omega_m a^{-3} + \Omega_{rc}}{\sqrt{\Omega_{rc}\left(\Omega_m a^{-3} + \Omega_{rc}\right)}}, \tag{2.67}$$

with a typical value $\Omega_{rc} = \frac{1}{4H_0^2 R_c^2} = 0.25$. In this case, Eq. (2.60) can be rewritten as the following equation for $\tilde{\chi}'$:

$$\tilde{\partial}^2\tilde{\chi}' + \frac{1}{3\gamma a^4}\left[\left(\tilde{\partial}^2\tilde{\chi}'\right)^2 - \left(\tilde{\partial}_i\tilde{\partial}_j\tilde{\chi}'\right)\left(\tilde{\partial}^i\tilde{\partial}^j\tilde{\chi}'\right)\right] = \frac{1}{\beta_{\rm sDGP}}\Omega_m a\left(\tilde{\rho}-1\right), \tag{2.68}$$

where the source term on the right-hand side is now identical to that in the sDGP equation [137], and we have defined a new time-dependent function

$$\gamma(a) \equiv \frac{2\beta^2}{9\beta_{\rm sDGP}R_c^2}. \tag{2.69}$$

Similarly, the Poisson equation, Eq. (2.54), should be changed to

$$\tilde{\partial}^2\tilde{\Phi} = \frac{3}{2}\Omega_m a\left(\tilde{\rho}-1\right) + \frac{3\beta_{\rm sDGP}}{2\beta}\alpha\tilde{\partial}^2\tilde{\chi}'. \tag{2.70}$$

From here on, without otherwise specified, we will drop the prime in $\tilde{\chi}'$ to lighten our notations.

To have a sense of the effect of Vainshtein mechanism analytically, we consider a static spherically symmetric top-hat density distribution of radius $\tilde{R}$ with the enclosed mass $\tilde{M}$ being

$$\tilde{M}(\tilde{r}) \equiv 4\pi\int_0^{\tilde{r}}\left(\tilde{\rho}(\xi)-1\right)\xi^2 d\xi, \tag{2.71}$$

where we are using code units, such that $\tilde{\rho}$ is defined as in Eq. (2.48); $\tilde{r}$ is also in code unit such that $\tilde{r} = r/L$ and similarly $\tilde{R} = R/L$ with R being the radius of the top-hat in physical unit. Note that $\tilde{\rho} = 1$ outside the top-hat, so that the mass $\tilde{M}$ stops growing and becomes a constant at $\tilde{r} \geq \tilde{R}$.

We relate the mass distribution to $\tilde{\chi}$ using Eq. (2.68). Realising that $\tilde{\chi}$

depends only the radial coordinate, $\tilde{r}$, we obtain

$$\frac{1}{\tilde{r}^2}\frac{d}{d\tilde{r}}\left(\tilde{r}^2\tilde{\chi}_{,\tilde{r}}\right)+\frac{2}{3\gamma a^4}\frac{1}{\tilde{r}^2}\frac{d}{d\tilde{r}}\left(\tilde{r}\tilde{\chi}_{,\tilde{r}}^2\right)=\frac{\Omega_m a}{\beta_{\rm sDGP}}\left(\tilde{\rho}-1\right), \tag{2.72}$$

where $_{,\tilde{r}}\equiv d/d\tilde{r}$. We integrate over the top-hat density distribution to yield

$$\tilde{\chi}_{,\tilde{r}}+\frac{2}{3\gamma a^4}\frac{1}{\tilde{r}}\tilde{\chi}_{,\tilde{r}}^2=\frac{\Omega_m a}{4\pi\beta_{\rm sDGP}}\frac{\tilde{M}(\tilde{r})}{\tilde{r}^2}. \tag{2.73}$$

Solving this second-order algebraic equation for $\tilde{\chi}_{,\tilde{r}}$ we get

$$\tilde{\chi}_{,\tilde{r}}=\frac{4\tilde{R}^3}{3\beta_{\rm sDGP}\tilde{R}_V^3}\left[\sqrt{\left(\frac{\tilde{R}_V}{\tilde{R}}\right)^3+1}-1\right]\tilde{F}_{\rm N}(\tilde{r}), \tag{2.74}$$

for $\tilde{r}\leq\tilde{R}$, where we substituted the Newtonian acceleration in code unit (which can be solved using Eq. (2.70) without taking into account the Proca field contributions),

$$\tilde{F}_{\rm N}(\tilde{r})=\frac{d\tilde{\Phi}}{d\tilde{r}}=\frac{3\Omega_m a}{8\pi}\frac{\tilde{M}(\tilde{r})}{\tilde{r}^2}, \tag{2.75}$$

and

$$\tilde{\chi}_{,\tilde{r}}=\frac{4\tilde{r}^3}{3\beta_{\rm sDGP}\tilde{R}_V^3}\left[\sqrt{\left(\frac{\tilde{R}_V}{\tilde{r}}\right)^3+1}-1\right]\tilde{F}_{\rm N}(\tilde{r}), \tag{2.76}$$

for $\tilde{r}>\tilde{R}$, where the Newtonian acceleration in code unit becomes

$$\tilde{F}_{\rm N}(\tilde{r})=\frac{3\Omega_m a}{8\pi}\frac{\tilde{M}(\tilde{R})}{\tilde{r}^2}. \tag{2.77}$$

Here we identified the Vainshtein radius (in code unit) to be

$$\tilde{R}_V^3=\frac{8\tilde{c}^2\tilde{R}_S}{9\beta_{\rm sDGP}\gamma a^3}=\frac{4\tilde{c}^2R_c^2\tilde{R}_S}{\beta^2a^3}, \tag{2.78}$$

where $\tilde{R}_S\equiv 3\Omega_m\tilde{M}(\tilde{R})/(4\pi\tilde{c}^2)$ is the Schwarzschild radius of the source in code unit. We note that the screening mechanism in the cubic-order Proca theory has been previously studied in Ref. [63]. However, due to different coordinate systems, our redefinition of the scalar mode ($\tilde{\chi}'$), and defining the vector field as covariant instead contravariant, a direct

comparison of the solutions of $\tilde{\chi}_{,\tilde{r}}$ between this Chapter and Ref. [63] is difficult and not pursued here. We have, however, checked that our spherical equation for φ agrees with that given in Ref. [112] in the weak-field limit. The physical meaning of the Vainshtein mechanism can be seen by considering the two limits, $\tilde{r}, \tilde{R} \ll \tilde{R}_V$ and $\tilde{r} \gg \tilde{R}_V$. In the former case the solution Eq. (2.74) applies and we obtain, according to Eq. (2.70), the following result for the fifth-force (in code unit),

$$\frac{3\beta_{\rm sDGP}}{2\beta}\alpha\frac{d\tilde{\chi}}{d\tilde{r}} \to 2\frac{\alpha}{\beta}\left(\frac{\tilde{R}}{\tilde{R}_V}\right)^{\frac{3}{2}}\tilde{F}_{\rm N}(\tilde{r}) \ll \tilde{F}_{\rm N}(\tilde{r}), \tag{2.79}$$

which represents the regime in which the fifth-force is strongly suppressed. In the latter case, we find

$$\frac{3\beta_{\rm sDGP}}{2\beta}\alpha\frac{d\tilde{\chi}}{d\tilde{r}} \to \frac{\alpha}{\beta}\tilde{F}_{\rm N}(\tilde{r}), \tag{2.80}$$

which shows that the fifth-force takes a constant ratio α/β to the Newtonian acceleration.

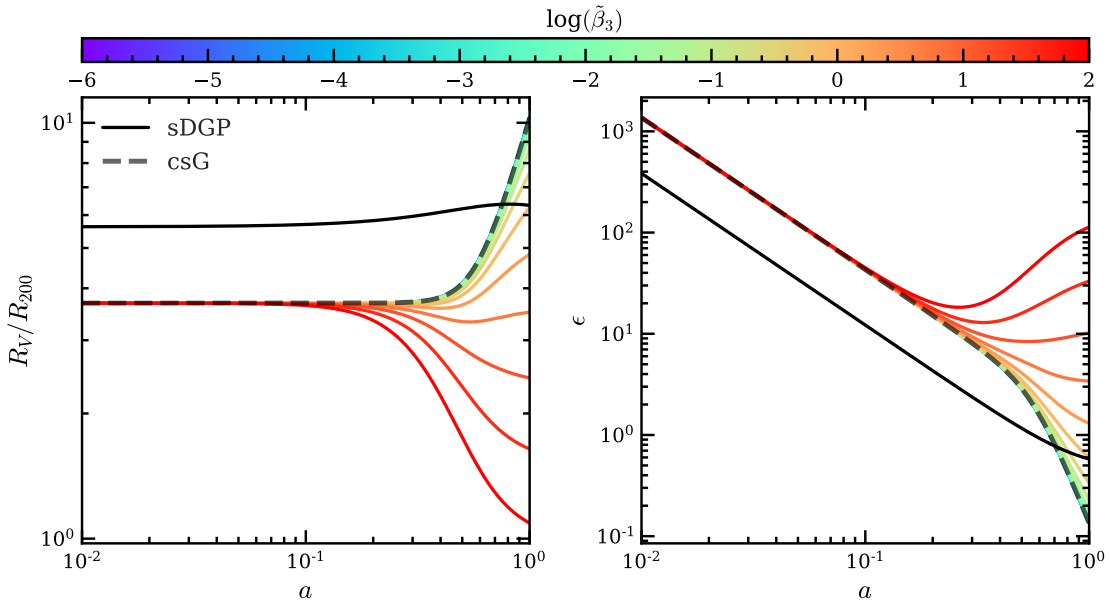

Figure 2.2: *left:* The time evolution of the relation between Vainshtein radius and top-hat radius for a given body. *right:* Coefficient of the non-linear derivative terms of the re-scaled scalar field equations. The figure compares the cvG model for different $\tilde{\beta}_3$ model parameters (colored solid lines) to sDGP (black solid lines), csG (grey dashed line).

In the left panel of Fig. 2.2 we show the ratio between the Vainshtein radius $\tilde{R}_V$ and the top-hat radius $\tilde{R}_{200}$, for different values of

$\tilde{\beta}_3$ (coloured solid lines), and compare to sDGP (black solid line) and csG (dashed line). Note, that due to the different background expansions this is not a fair comparison of sDGP to csG and cvG. In order to calculate the ratio, we have assumed that the spherical top-hat has a constant density within $\tilde{r} \leq \tilde{R}$ which is equal to 200 times the critical density $\rho_c(a) = 3H(a)^2/8\pi G$ and equals

$$R_{200}^3 = \frac{3M_{200}}{4\pi 200\rho_c(a)}, \tag{2.81}$$

making the ratio between R_V and R_{200} (note that here we ignore the tildes as this is equal to the ratio between the code-unit versions $\tilde{R}_V$ and $\tilde{R}_{200}$)

$$\left(\frac{R_V}{R_{200}}\right)^3 = \frac{800R_c^2}{\beta^2}\left(\frac{H}{H_0}\right)^2 = \frac{800R_c^2}{\beta^2}E^2. \tag{2.82}$$

For clarity we write down the corresponding equations for each of the considered cosmologies,

$$\frac{R_V}{R_{200}} = \begin{cases} \sqrt[3]{\frac{1600R_c^2E^2}{9\beta_{\rm sDGP}^2}}, & \text{sDGP}, \\ \sqrt[3]{\frac{1600E^2}{9\beta_{1,\rm csG}\beta_{2,\rm csG}}}, & \text{csG}, \\ \sqrt[3]{\frac{800R_c^2E^2}{\beta^2}}, & \text{cvG}, \end{cases} \tag{2.83}$$

where $\beta_{1,\rm csG}$ and $\beta_{2,\rm csG}$ are β functions defined for the csG model in Ref. [17] (to avoid confusion with the β function for the cvG model in this Chapter we have added a csG label to the subscript of its β's, separated by a comma).

It can be seen from the left panel that the Vainshtein radius in the cvG model is insensitive to $\tilde{\beta}_3$ at early times, but becomes very strongly dependent on $\tilde{\beta}_3$ at $a \gtrsim 0.1$. For example, choosing a $\tilde{\beta}_3 \sim \mathcal{O}(100)$ results in a screening radius that is nearly an order-of-magnitude smaller than its csG counterpart (the dashed line, which corresponds to $\tilde{\beta}_3 \to 0$)

at $a \simeq 1$, setting it approximately equal to the size R_{200} of the over-density itself (note that at $a \simeq 1$ we have $E \simeq 1$).

In the right panel of the same figure we show the time evolution of the coefficient of the non-linear derivative terms of the re-scaled scalar field equations, as given in Eq. (2.68) for the cvG model. This coefficient can be thought of as the controlling strength of the Vainshtein screening – the larger it is, the more efficient the screening becomes. Because it is also present in the sDGP and csG cosmology, we show a comparison to the sDGP and the re-scaled csG model. Instead of showing the coefficients themselves, we have defined a new quantity ϵ as follows,

$$\epsilon = \begin{cases} -R_c^2 / \beta_{\rm sDGP}, & {\rm sDGP}\,, \\ -\beta_{1,{\rm csG}}\beta_{2,{\rm csG}} / \beta_{\rm sDGP}, & {\rm csG}\,, \\ -\gamma, & {\rm cvG}\,. \end{cases} \tag{2.84}$$

Again we note that values of $\tilde{\beta}_3 < \mathcal{O}(0.01)$ seem to closely mimic the csG model behaviour. While for $\tilde{\beta}_3 \sim \mathcal{O}(100)$ there is less efficient screening, we can now see that the fifth-force starts to become weaker compared to the csG model starting from $z \approx 4$, ending with a ϵ that is $\sim \mathcal{O}(3)$ larger today.

The fact that R_V / R_{200} and ϵ of the cvG model approach their corresponding values in the csG model for $\tilde{\beta}_3 \to 0$ deserves a couple of comments here. First, as mentioned earlier, the dynamics of the csG model depends on the initial condition (ICs) of the scalar field, and different ICs can lead to different late-time behaviour. However, as we consider the tracker solution of the csG model, the late-time model behaviour show in Fig. 2.2 is a unique limiting case.

Second, it may seem that, because $\tilde{\beta}_3 \propto b_3$, as $\tilde{\beta}_3 \to 0$ we have $b_3 \to 0$, and we would expect the G_3 term in the Proca Lagrangian vanishes and the theory goes back to the GR limit with a massive vector field,

rather than the csG limit. Here we distinguish between two scenarios. The first is to keep $\tilde{\beta}_2$ (or equivalently b_2) fixed while reducing $\tilde{\beta}_3$ (or b_3): here we do get back to the GR limit but the expansion history will also be dependent on $\tilde{\beta}_3$ – this is *not* the scenario followed in this Chapter. The second scenario is to keep the background expansion history fixed and decrease $\tilde{\beta}_3$: then according to Eq. (2.51) $\tilde{\beta}_2$ decreases accordingly; this is the scenario of this Chapter. In this case, there is a special scaling degeneracy which exists for Galileon-type models (see, e.g., Section IIIB of [18] for a more detailed discussion), which we briefly review here. For simplicity, let us assume that the Proca vector field has only a longitudinal mode, and so the Lagrangians $\mathcal{L}_{2,3}$ can be schematically written as

$$\begin{aligned} \mathcal{L}_2 &\propto b_2 \nabla^\mu \chi \nabla_\mu \chi, \\ \mathcal{L}_3 &\propto b_3 \nabla^\mu \chi \nabla_\mu \chi \Box \chi. \end{aligned} \tag{2.85}$$

If we multiply b_2 by T^2, multiply b_3 by T^3 and divide χ by T, with T being an arbitrary constant, then the physics is unaffected. Therefore, reducing $\tilde{\beta}_2$ and $\tilde{\beta}_3$ simultaneously with $\tilde{\beta}_2^3 / \tilde{\beta}_3^2$ fixed would keep the physics unchanged by increasing $\tilde{\chi}$ accordingly. This is what happens in the csG model. In the cvG model, the presence of the $\mathcal{L}_F$ Lagrangian slightly complicates things, and breaks this scaling degeneracy, but the scaling degeneracy can be approximately restored with $\tilde{\beta}_3 \to 0$ (or $b_3 \to 0$). To see this, let us look at Eqs. (2.58) - (2.60) and consider the limit where $\tilde{\beta}_{2,3} \to 0$ simultaneously with $\tilde{\beta}_2^3 / \tilde{\beta}_3^2$ fixed. To be concrete, we introduce the following scalings (with $T \ll 1$):

$$\tilde{\beta}_2 \to T^2 \tilde{\beta}_2, \tag{2.86}$$

$$\tilde{\beta}_3 \to T^3 \tilde{\beta}_3, \tag{2.87}$$

$$\tilde{\chi} \to T^{-1} \tilde{\chi}, \tag{2.88}$$

$$\tilde{\varphi} \to T^{-1} \tilde{\varphi}, \tag{2.89}$$

$$R_c \to T R_c, \tag{2.90}$$

in which Eq. (2.89) is needed for the rescaled quantities to still satisfy Eq. (2.43), and Eq. (2.90) is because of Eq. (2.59). Then, of the 4 terms on the right-hand side of Eq. (2.58), all scale as T apart from $\tilde{\beta}_3/\tilde{\beta}_F$ – however, because $\tilde{\beta}_F = 1$, we can see that with $T \to 0$ the term $\tilde{\beta}_3/\tilde{\beta}_F$ goes to zero more quickly than the other three terms and can therefore be neglected in this limit, and the function β scales as T approximately. Then all terms in Eq. (2.60) scale as T^{-1}, which means that the physics encoded in this equation is unaffected by the scaling, which is exactly the case for the csG discussed in [18]. The observation that in this limit the cvG model behaves similarly to csG can be explained by the fact that the only term contributed by $\mathcal{L}_F$ and involving $\tilde{\beta}_F$ (i.e., the $\tilde{\beta}_3/\tilde{\beta}_F$ term in Eq. (2.58)) – which has no counterpart in the csG model – has been neglected (as well as the similarity between $\mathcal{L}_{2,3}$ in the two models).

2.3.4 Linear growth of the density field

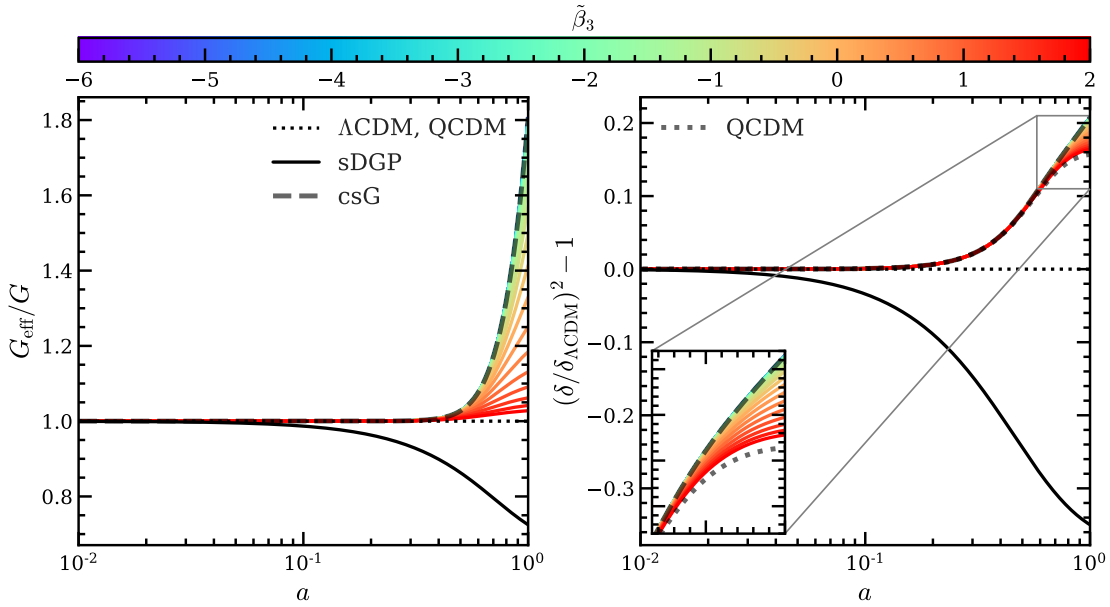

Figure 2.3: *Left:* Time evolution of the effective gravitational constant $G_{\rm eff}/G$. *Right:* Time evolution of the relative difference of the square of the density contrast. The figure compares the cvG model for different $\tilde{\beta}_3$ model parameters (colored solid lines) to sDGP (black solid lines), csG (grey dashed line), and ΛCDM(black dotted line).

Before we continue to explore late-time perturbations on sub-horizon scales, it is instructive to study the evolution of density fluctuations in linear perturbation theory. Of particular relevance is the linear rate of

growth of cosmic structures, $\delta_{\rm M}(a) = D(a)\delta_0$, where D is the normalized linear growth factor with $D(a=1) = 1$. The growth is governed by

$$D'' + (2+F)\,D' - \frac{3}{2}\frac{G_{\rm eff}}{G}\Omega_m(N)D = 0, \tag{2.91}$$

where a prime denotes the derivative with respect to $N = \ln(a)$ as before, $F = E'/E$ is the friction term, and $G_{\rm eff}/G$ is a time-dependent function that carries the modifications of the Newtonian potential, either due to a modified gravitational force or the clustering of dark energy. In the linear regime, each mode of the perturbed density field evolves independently. Their evolution is fully determined by $\Omega_m(N)$, F and $G_{\rm eff}$. Note that in this Chapter we use $\Omega_m(N)$ to denote the matter density parameter at time a, to be distinguished from Ω_m, which is the present-day value of the matter density parameter. To disentangle the relative importances of the modified gravitational strength $G_{\rm eff}$ and modified expansion history E (or F) on the growth factor, we introduce the QCDM version of the cvG. The QCDM considers only modifications to the expansion history but not to the Newtonian potential, and is therefore identical for the cvG and csG models. For the set of considered models, the matter density parameter evolves as

$$\Omega_m(N) = \frac{\Omega_m e^{-3N}}{E^2}, \tag{2.92}$$

with E^2 given by Eq. (2.52). The friction coefficient for the different models can be written as,

$$F = \begin{cases} -\frac{3}{2}\Omega_m(N), & \Lambda\text{CDM}, \\ -\frac{3}{2}\Omega_m \frac{e^{-3N}}{\sqrt{\Omega_{rc}}\sqrt{\Omega_m e^{-3N}+\Omega_{rc}}+\Omega_m e^{-3N}+\Omega_{rc}}, & \text{sDGP}, \\ \frac{1}{2} - \frac{1}{E^2}\left(\Omega_m e^{-3N} + \frac{\Omega_m^2 e^{-6N}+(1-\Omega_m)}{\sqrt{\Omega_m^2 e^{-6N}+4(1-\Omega_m)}}\right), & \text{cvG, csG, QCDM}. \end{cases} \tag{2.93}$$

The modification of the Newtonian potential, which is proportional to the ratio between the fifth force, F_5, and the Newtonian gravity force, $F_{\rm N}$, is characterised by $G_{\rm eff}/G$ which in linear theory is given by the following time-dependent but scale-independent functions for the various models:

$$\frac{G_{\rm eff}}{G} = 1 + \frac{F_5}{F_{\rm N}} = \begin{cases} 1, & \Lambda\text{CDM, QCDM,} \\ 1 + \frac{1}{3\beta_{\rm sDGP}}, & \text{sDGP,} \\ 1 - \frac{4c_3\beta_{1,\rm csG}}{3\beta_{2,\rm csG}^2}, & \text{csG,} \\ 1 + \frac{\alpha}{\beta}, & \text{cvG.} \end{cases} \tag{2.94}$$

The deviation of $G_{\rm eff}$ from ΛCDM for the various models can be seen in the left-hand panel of Fig. 2.3. To solve Eq. (2.91) we use the ICs at $a_i = 0.01$: $D(a = a_i) = a_i$ and $D'(a = a_i) = 1$, which correspond to the matter-dominated-era solution, $\delta \propto a$. The results can be seen on the right-hand panel of Fig. 2.3.

At early times, $a \lesssim 0.1$, $G_{\rm eff}/G \approx 1$ in all models, and therefore the differences from ΛCDM are mainly driven by the modified expansion history, H, and different matter densities $\Omega_m(a)$. In all modified gravity models except sDGP, both H and Ω_m are larger than in ΛCDM, so that their effects cancel out. The same happens in the sDGP cosmology though in this case H and Ω_m are smaller than in ΛCDM, and the growth of linear density perturbations is slightly slower. As a result, the relative difference $(\delta/\delta_{\Lambda\rm CDM})^2 - 1$ is almost zero in such early times.

At $a \gtrsim 0.1$, the evolution of δ is determined by the interplay of the modifications in H, Ω_m, and $G_{\rm eff}/G$. We see how the modifications to effective gravitational constant enhance structure formation at late times for the cvG and csG models, while suppressing it in the sDGP

model. As shown in the left panel of Fig. 2.3, for values of $\tilde{\beta}_3 \lesssim 0.01$, the evolution of $G_{\rm eff}$ in cvG is indistinguishable from that in csG. This, together with the fact that $H(z)$ and Ω_m are identical in the csG and cvG models, explains why in the right-hand panel of Fig. 2.3 the evolutions of $(\delta/\delta_{\Lambda\rm CDM})^2$ are also indistinguishable between csG and cvG with $\tilde{\beta}_3 \lesssim 0.01$. On the other hand, for large values of $\tilde{\beta}_3$, the behaviour of the cvG model approaches that of QCDM due to $G_{\rm eff}/G \to 1$[5]. This indicates that the cvG model, with a proper QCDM limit, could have a healthy behaviour regarding the ISW effect, which has proven to be an issue for the viability of the csG model. Cosmological constraints on the Proca theory have been studied in several works, e.g., Refs. [64, 154, 65] – some of which actually have made use of the ISW data – and these have placed strong constraints on the functional forms $G_2(X)$ and $G_3(X)$, disfavouring the simple model studied here with $G_2 = G_3 = X$. We will briefly comment on this and on the viability of the model in the end of Section 2.4.2.

[5] Note that it is possible to achieve a weaker gravity, $G_{\rm eff}/G < 1$, if one uses the full Lagrangian described in Eq. (2.1). With our restriction to the cubic order of the Lagrangian, we neglect the contributions of $\mathcal{L}_{4,5,6}$ which enter in very specific ways into $G_{\rm eff}$ as explained in the Ref. [62].

2.4 Code tests and N-body Simulations

In this section we present the results of full N-body simulations based on the equations derived in the previous section. We begin in Section 2.4.1 with showing the outcomes of multiple tests which are essential for us to be confident about the reliability of the code. Afterwards in Section 2.4.2, we present the results of the first set of the cosmological simulations of the simplified GP theory given in Section 2.2. For details on the code algorithm we refer the reader to [135] and [17].

2.4.1 Code Tests

All tests of the N-body code use a box-size of $L = 64\,\mathrm{Mpc}/h$, and a domain grid of 256^3 cells with no grid refinement.

One dimensional density fields

The first set of tests is concerned with verifying the correct implementation of the linear terms in the cvG equation. By limiting ourselves to a one-dimensional matter distribution, the non-linear terms in the cvG equations simply vanish, and Eq. (2.68) reduces to,

$$\frac{d^2}{dx^2}\tilde{\chi}(x) = \frac{\Omega_m a}{\beta_{\text{sDGP}}}\delta(x). \tag{2.95}$$

This means that an analytical expression can be easily obtained and comparable with the code results. Following [135], we first distribute the dark matter according to a one-dimensional sine field specified by,

$$\delta(x) = -4\pi^2 \frac{\beta_{\text{sDGP}}}{\Omega_m a} A\cos(2\pi x), \tag{2.96}$$

such that the scalar field becomes

$$\tilde{\chi}(x) = A\cos(2\pi x). \tag{2.97}$$

We have performed the test with various values of A and $\tilde{\beta}_3$. The result for $A = 10^{-8}$ and $\tilde{\beta}_3 = 10^{-6}$ can be seen in the left column of Fig. 2.4, where the numerical solution (red dots), taken along a line which is parallel to the x-axis, are compared to the analytical solution (blue line) of $\tilde{\chi}$. In the top panel we show the chosen dark matter distribution, followed by the confirmation that the longitudinal mode, $\tilde{\chi}$, matches the analytical result. In the bottom panel we show just the x-component of the second partial derivative of the transverse mode, $\tilde{\partial}^2\tilde{B}_x$, as the y- and z-component share the same result. As the matter distribution is one dimensional, the source term in Eq. (2.47) vanishes and therefore the transverse mode is expected to be zero. The fact that the numerical result for the transverse modes is zero, furthermore indicates not only that the linear terms are correctly implemented, but also that the non-linear source term of Eq. (2.47) does not cause unwanted behaviour.

The second test uses a one dimensional Gaussian dark matter distri-

bution, given by

$$\delta(x) = 1 + \frac{\beta_{\rm sDGP}}{\Omega_m a}\frac{2\alpha}{\sigma^2} A \left(1 - 2\frac{(x-0.5)^2}{\sigma^2}\right) \exp\left[-\frac{(x-0.5)^2}{\sigma^2}\right], \tag{2.98}$$

and leads to a scalar field distribution of

$$\chi(x) = A\left(1 - \alpha \exp\left[-\frac{(x-0.5)^2}{\sigma^2}\right]\right). \tag{2.99}$$

Again we have conducted multiple test for various values of A, σ, α, and $\tilde{\beta}_3$. The result for $A = 10^{-6}$, $\sigma = 0.09$, $\alpha = 0.01$ and $\tilde{\beta}_3 = 10^{-6}$ can be seen in the central column of Fig. 2.4, where the numerical (red dots) and analytical (blue line) are compared. Again, $\tilde{\chi}$ follows accurately the analytical result and the transverse mode vanishes with high precision.

Three dimensional density fields

After having performed tests for one dimensional matter distributions, we now move on to conduct more advanced tests using three dimensional distributions. This will reveal if there are any implementation errors of the non-linear terms, when they are needed. The simplest test in three-dimensions is the spherical symmetric top-hat distribution of matter. The analytical solution for $\tilde{r} \leq \tilde{R}$ is given by Eq. (2.74), which can be re-written as

$$\frac{d\tilde{\chi}}{d\tilde{r}} = \frac{\beta^2 a^4}{6\beta_{\rm sDGP} R_c^2}\left[\sqrt{\frac{4\Omega_m \delta_{\rm in} R_c^2}{\beta^2 a^3} + 1} - 1\right]\tilde{r}, \tag{2.100}$$

and Eq. (2.76) for $\tilde{r} > \tilde{R}$ which can be re-written as

$$\frac{d\tilde{\chi}}{d\tilde{r}} = \frac{\beta^2 a^4}{6\beta_{\rm sDGP} R_c^2}\left[\sqrt{\frac{4\Omega_m \delta_{\rm out} R_c^2}{\beta^2 a^3}\left(\frac{\tilde{R}}{\tilde{r}}\right)^3 + 1} - 1\right]\tilde{r}, \tag{2.101}$$

where $\tilde{r}$ is the comoving coordinate scaled by the boxsize L, while $\tilde{R}$ is the radius of the spherical over-density scaled by L. The density inside the top-hat is given by $\delta_{\rm in}$ while it is $\delta_{\rm out}$ outside, which are both constants by definition.

Given the value $\tilde{\chi}(\tilde{r} = 0)$, these equations can be integrated to find

$\tilde{\chi}(\tilde{r} > 0)$ from its analytical expression. We call the $\tilde{\chi}(\tilde{r})$ obtained in this way the 'analytical solution', even though in practice a numerical integration is required to get it. We tested various values of $\tilde{R}$, $\delta_{\rm in}$, and $\delta_{\rm out}$, where these values are always tuned in such a way as to make the average matter density $\tilde{\rho} = 1$ (and equivalently the average $\delta = 0$) in the entire simulation box. In the numerical implementation, the spherical top-hat is placed at the centre of the box, as illustrated in the upper right panel of Fig. 2.4.

The middle and bottom panels of the right column of Fig. 2.4 shows the test result for a spherical top-hat of radius $\tilde{R} = 0.1$ with $\delta_{\rm in} = 23.77$ and $\delta_{\rm out} = -0.1$. We can see that the numerical result for $\tilde{\chi}$ (red points in the middle row), taken along a line which is parallel to the x-axis in a y-z plane at the centre of the box, is in excellent agreement with the analytical solution (blue line), especially on small $\tilde{r}$. Far away from the centre, the agreement becomes less perfect since the analytical solution does not assume periodicity of the spherical density, while the numerical code uses periodic boundary condition so that the spherical density sees its own images.

With regards to $\tilde{\partial}^2 \tilde{B}_x$, we can verify its accuracy by considering the analytical solution of $\tilde{B}_i$ in the spherical coordinate system centered on the top-hat. In this setting, the θ- and ϕ-components of $\tilde{B}_i$ vanish as $\tilde{\chi}$ only varies along the radial coordinate, r. Furthermore, as the transverse mode must obey the traceless condition $\nabla^i \tilde{B}_i = 0$ and boundary condition $\tilde{B}_r(\tilde{r} = 0) = 0$, the radial component of $\tilde{B}_i$ has to vanish too. The numerical test solutions of $\partial^2 B_i$, for $i = x$ and along the same axis as above, are shown as the red dots in the lower right panel of Fig. 2.4, where we can see that it is indeed very close to zero, with a small nonzero amplitude of order $\mathcal{O}(10^{-8})$ due to numerical error and due to the fact that exact spherical symmetry is broken on a mesh of cubic cells.

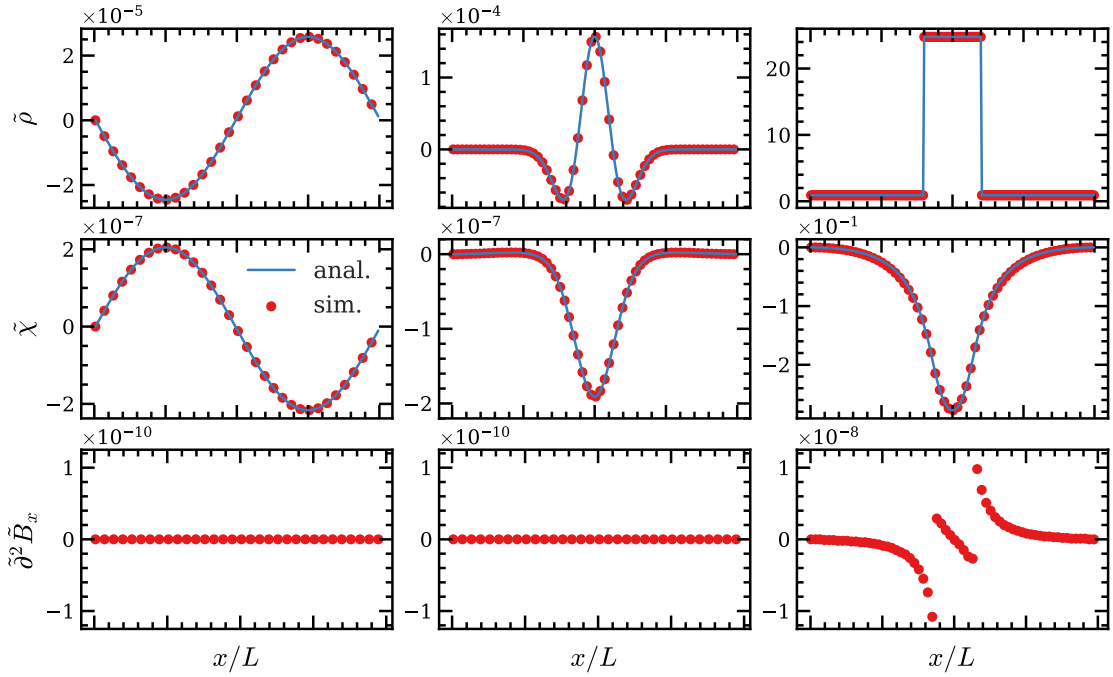

Figure 2.4: The various code tests conducted by assuming that the matter distribution is given by the following three ideal cases. *Left column:* A 1D sine-type matter density field as described by Eq. (2.96) with $A = 10^{-8}$. *Middle column:* A 1D Gaussian-shaped matter density field described by Eq. (2.98), with $A = 10^{-6}$, $\sigma = 0.09$, and $\alpha = 0.01$. *Right column:* A 3D spherical top-hat over-density with $\delta_{\rm in} = 23.77$, $\delta_{\rm out} = -0.1$, and $R_0 = 0.1$, as described in Section 2.4.1. For all three tests we have used $\tilde{\beta}_3 = 10^{-6}$, a simulation box of $L = 64\,\mathrm{Mpc}/h$, and 256 grid cells in each dimension. For each test and field quantity we compare the numerical result of the test simulations (red points), taken along a line which is parallel to the x-axis in a y-z plane near the centre of the box, to its analytical solution (blue line).

2.4.2 Cosmological simulations

Having verified the code implementation, we move on to run the code in a cosmological context with two objectives in mind. Firstly, we want to justify our assumptions, described in Section 2.2.2, in which we neglect any 'backreaction' of B_i on the evolution of χ. Secondly, we want to study what influence the model parameter $\tilde{\beta}_3$ has on large-scale structure formation.

To this end, all simulations used in this section employ the same ICs, which were generated using `2LPTic` [54]. The power spectrum of the initial density field, at a scale factor of $a_{\rm ini} = 0.02$, assumes a flat ΛCDM cosmology obtained with `CAMB` [131]. One possible concern may be that, at this scale factor, differences of matter clustering are already present. However, judging from Fig. 2.3, at this time the difference between the growth factors of the cvG model with ΛCDM is well below sub-percent level. The fact that we use the same initial condition for simulations of different cosmologies ensures that the initial density fields have the same phases, and any differences at later times can solely be attributed the different dynamics and force laws. For comparisons, for every cvG simulation, we also run one for its QCDM counterpart, which has the expansion history of cvG but without modifications to the law of gravity.

The standard cosmological parameters used in the creation of the initial condition and simulations are

$$h = 0.6774, \quad \Omega_\Lambda = 0.6911, \quad \Omega_m = 0.3089, \quad \Omega_B = 0.0223, \quad \sigma_8 = 0.8159 \tag{2.102}$$

(taken from the *Planck Collaboration* [5]). All cosmic simulations use a box-size of $L = 200\,\text{Mpc}/h$, and a total number of dark matter particles of $N_p = 256^3$. The convergence criterion for the Gauss-Seidel algorithm is set to $|d^h| < \epsilon = 10^{-9}$. As it is not our objective to explore in great detail the predictions of various observables in the cvG model here, we use these small simulations in this Chapter to get a sense of the qualitative behaviours, and will report results from larger, higher-

resolution simulations in follow-up works.

In N-body simulations for cubic and quartic scalar Galileon models, there is a well-documented problem that the numerical computation fails [17, 136] because the equation does not admit a physical solution under certain conditions [16]. In the case of csG, this happens during a simulation when the scale factor $a \gtrsim 0.8$ (the exact time at which this happens depends on the resolution, initial condition and cosmological parameters), in regions where matter density is very low, i.e., $\tilde{\rho} \to 0$. This problem can be traced to Eq. (2.73), which does not posses real solutions of $\tilde{\chi}_{,\tilde{r}}$ if

$$\Delta \equiv 1 + \frac{12\Omega_m}{H_0^2 a^3 \tilde{r}^3} \int_0^{\tilde{r}} \left[\tilde{\rho}(\xi) - 1\right] \xi^2 d\xi < 0. \tag{2.103}$$

There has been suggestion [224] that this is a real problem of the model itself, rather than a consequence of the approximations employed to simplify the field equations. Given that csG is a limiting case of the cvG model, we have found the same problem in our simulations for the latter, and followed the *ad hoc* fix employed in [17] by setting $\Delta = 0$ whenever the corresponding quantity becomes negative in a simulation mesh cell.

The role of B_i in cosmological simulations

In order to confirm that the negligence of B_i proposed in Section 2.2.2 is justified, we ran a cosmological simulation with $\tilde{\beta}_3 = 10^{-6}$, and a domain grid of 256^3 cells with no grid refinement.

A visualisation of the resulting fields including the gravitational potential and the extra degrees of freedom is shown in Fig. 2.5. The maps have the same side length as the box, a depth of 0.86 Mpc$/h$, and are cut out around the centre of the box. In the top row we show the gravitational potential $\Phi_{\rm cvG}$ (left) and the difference of Φ between cvG and its QCDM counterpart (right). As outlined earlier, the QCDM version only contains the background expansion and misses the fifth-force term which results in a weaker clustering of matter as compared to cvG. This is clearly visible in the right panel, where the blue (red) indicates a higher matter density

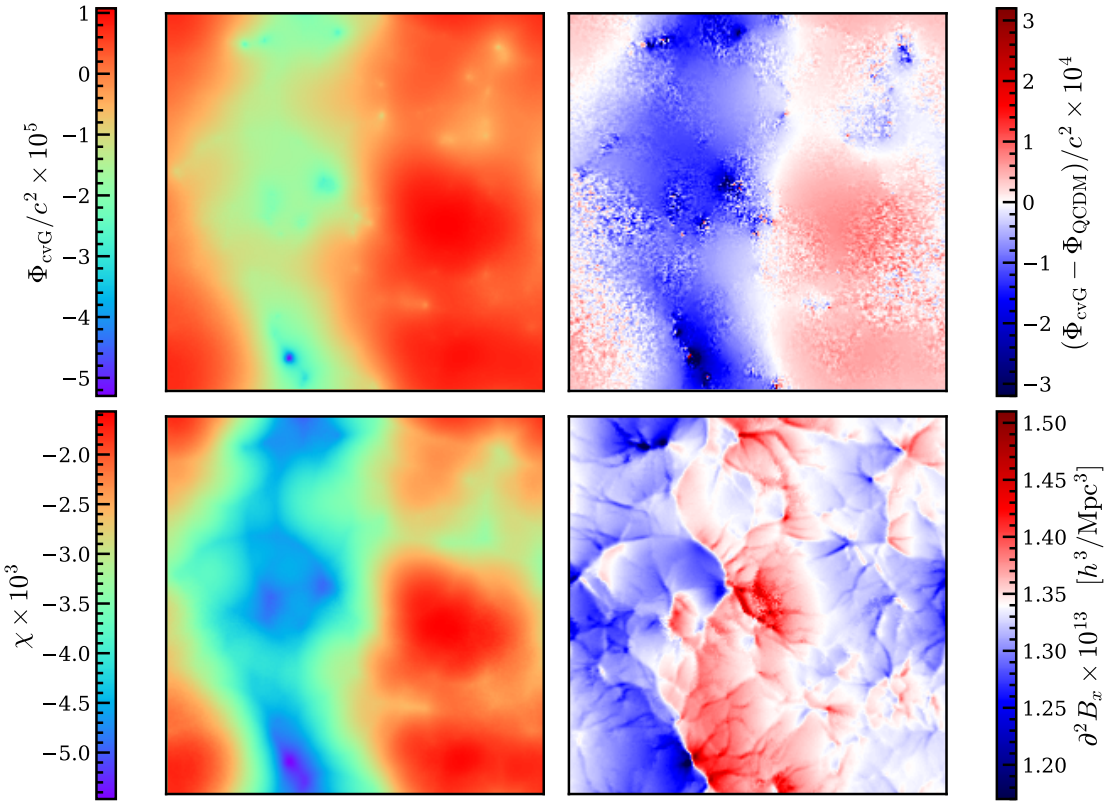

Figure 2.5: A visualisation of the spatial configurations of various fields taken from a slice of one cell size (with a thickness of $0.86{\rm Mpc}/h$) in the simulations. *Top left:* Distribution of the total potential, Φ, in the full cvG simulation. *Top right:* Difference between Φ in cvG and QCDM simulations, from which a stronger clustering in the former can be seen. *Bottom left:* The longitudinal vector mode, χ. *Bottom right:* The second derivative of the transverse vector mode, B_x.

around haloes in the cvG model (voids in the QCDM model).

In the bottom panels we present visualisations of the χ field (left) and the $\partial^2 B_x$ component of the transverse mode (right) for the same slice of the simulation box. The χ field, like the potential Φ, is very smooth with a similar dependence on the underlying dark matter density and reaches local minima within halos and local maxima in voids. This is as expected as, apart from strongly screened regions, the fifth-force due to $\vec{\nabla}\chi$ generally has the same direction as and is proportional in magnitude to standard gravity. The distribution of $\partial^2 B_i$ on the other hand is very rich in texture. This is because $\partial^2 B_i$ is sourced by higher-order derivatives of χ, cf. Eq. (2.47). While the complexity of Eq. (2.47) makes it difficult to interpret this map intuitively, we observe that it follows the patterns of the other maps in general.

While Fig. 2.5 intuitively shows the spatial configurations of various physical quantities in their own physical units, the comparison between the amplitudes of χ and $\partial^2 B_i$ should not be used as a direct indicator to assess the relative importance of the longitudinal and transverse modes in affecting structure formation. Actually, from the field decomposition, Eq. (2.20) in Section 2.2, we can see that a fairer comparison can be done by comparing the magnitudes of $\partial_i \chi$ and B_i. For simpler computation, we show the power spectra of $\partial_x \partial^2 \chi$ and $\partial^2 B_x$ at various times in Fig. 2.6. Note that, because $\partial_i \partial^2 \chi$ and $\partial^2 B_i$ both have unit of $(h/\mathrm{Mpc})^3$, their power spectra have the unit of $(h/\mathrm{Mpc})^3$.

As the magnitude of the cvG longitudinal mode χ increases with matter density perturbations, the $P(k)$ of $\partial^2 \partial_i \chi$, which we visualise for $a \in [0.3, 1.0]$ in Fig. 2.6, also increases continuously as expected. It is interesting to note that while the matter power spectrum peaks $k \sim \mathcal{O}\left(10^{-2}\right) h/\mathrm{Mpc}$, the power spectrum for $\partial^2 \partial_i \chi$ has a significantly more flattened shape until $k \sim \mathcal{O}(1) h/\mathrm{Mpc}$, which is because of the additional spatial derivative in $\partial_x \partial^2 \chi$ (on large scales the power spectra of $\partial^2 \chi$, $\partial^2 \Phi$ and matter density are expected to have similar shapes because of the weak screening).

The right panel of Fig. 2.6 shows the time evolution of the power spectrum of $\partial^2 B_x$. While this quantity also increases over time, we note that its amplitude is $\sim$ 15-20 orders of magnitude smaller than the $\partial_x \partial^2 \chi$ power spectrum on all scales probed by the simulation. This serves as a confirmation that the transverse mode plays a very minor role compared with the longitudinal mode, on linear scales (as it was previously shown by [62]) as well as on non-linear scales. In particular, it verifies that it is a good approximation to neglect the terms involving B_i in the vector field equation of motion (2.32). This is the approximation that we shall take in what follows, and in future simulations of the cvG model.

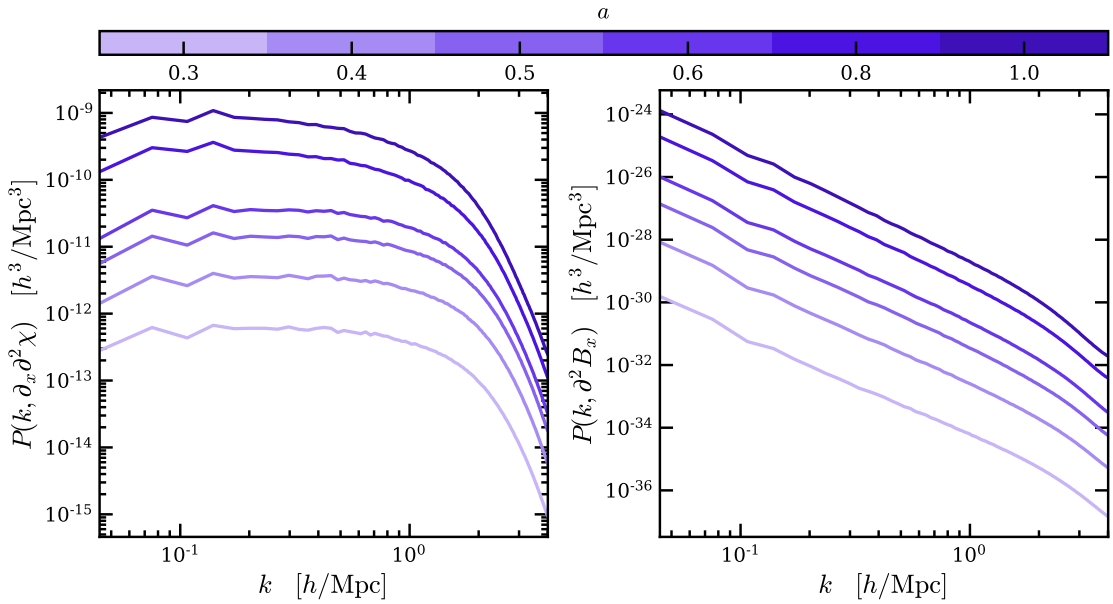

Figure 2.6: The power spectrum of (spatial derivatives of) the longitudinal (left) and transverse (right) mode of the Proca field, for $\tilde{\beta}_3 = 10^{-6}$. The different lines are results at different values of the scale factor a, as indicated by the colour bar on the top. Note the large amplitude differences between the two panels.

The dependence on $\tilde{\beta}_3$

We have seen above that, unlike the csG model, the cvG model has a free parameter which we choose to be represented by $\tilde{\beta}_3$. This parameter does not affect the background expansion history of the model, but controls the strength of the fifth-force of $G_{\rm eff}/G$, cf. Eq. (2.94) and Fig. 2.3. Also, in Fig. 2.2 we have seen that the degree of non-linear Vainshtein screening depends on $\tilde{\beta}_3$. As the screening effect on large-scale structure formation is most accurately captured by N-body simulations, here we give a first idea about this effect, while leaving a more detailed study of various non-linear observables in the cvG model to future works.

For this, we have run three cosmological simulations employing the full set of equations derived in Section 2.3 using $\tilde{\beta}_3 = (10^{-6}, 1, 100)$, using a domain grid of 256^3 cells. The cells are refined when the effective number of particles $N_p > 9.0$ up until a finest resolution of 2^{16} cells per dimension (if they were to cover the whole simulation box) is reached. The simulations each ran in only about 1500 core-hours, underlining the viability of much larger and better resolution simulations simulations with our code.

To get an understanding of the impact of $\tilde{\beta}_3$ on the cvG cosmology through a enhanced effective gravitational constant, $G_{\rm eff}/G$, and the Vainshtein screening, R_V, we have run four additional simulations using the same settings as outline above. One of these is the above-mentioned QCDM variant, which differs from a ΛCDM simulation only by a modified (cvG) background expansion history[6], and is used to isolate the effect of the latter. For the other three sets of simulations, we neglect the non-linear terms in the EOM of χ, which is equivalent to removing the screening mechanism by simply re-writing Eq. (2.70) as,

[6] Note that that the background expansion history is independent of $\tilde{\beta}_3$, so that only one QCDM simulation is needed.

$$\tilde{\partial}^2\tilde{\Phi} = \frac{3}{2}\Omega_m a\left(1+\frac{\alpha}{\beta}\right)(\tilde{\rho}-1)\,, \tag{2.104}$$

using Eq. (2.94). These are what we call *linearised* simulations, and the comparison of them with the full simulations can illustrate the quantitative impact of the Vainshtein screening.

Fig. 2.7 compares the linear matter power spectrum (black dotted lines) with the predictions by the linearised (black dashed) and fully non-linear (coloured) simulations, at $a = 0.6$ (left), $a = 0.8$ (centre) and $a = 1.0$ (right). The linear power spectrum $P(k;z)$ is obtained by multiplying the initial power spectrum $P(k;z_{\rm ini})$ with $[D(z)/D(z_{\rm ini})]^2$, where D is the linear growth factor discussed in Section 2.3.4. The non-linear matter power spectra are measured from the simulations using `POWMES` [52]. The relative difference of the matter power spectra of the cvG and QCDM models, $\Delta P(k)/P_{\rm QCDM}(k)$, has been smoothed using a Savitzky–Golay filter of third order with a kernel width of 51 data-points. The shaded region in each panel indicates the regime of k beyond the Nyquist frequency[7]. The lower row of Fig. 2.7 shows the relative differences of the matter power spectra given by linear theory (dotted lines), linearised simulations (dashed) and full simulations (solid) with respect to their QCDM counterparts (i.e., QCDM linear theory and simulation predictions).

[7] Note that the Nyquist frequency, $k_{\rm Ny}$, marks the absolute maximum up to which we can the power spectrum can be trusted. First alterations can already appear at $k_{\rm Ny}/8$.

Fig. 2.7 allows for a number of conclusions. Firstly, we have seen in

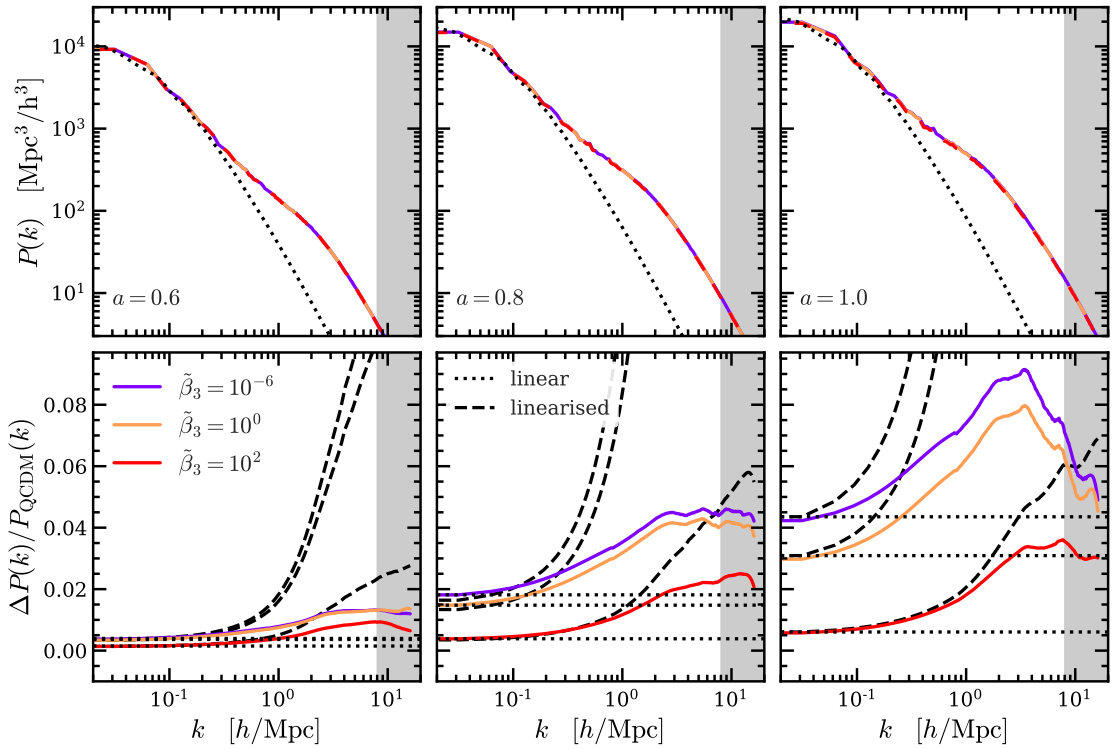

Figure 2.7: The matter power spectrum in the cvG model. Each column shows the results for a different scale factor: *left:* $a = 0.6$, *centre:* $a = 0.8$, *right:* $a = 1.0$. *Top:* The matter power spectrum of linear perturbation theory (dotted) and the cvG model for three values of $\tilde{\beta}_3 = (10^{-6}, 1, 100)$, indicated by a purple, orange, and red line respectively. *Bottom:* Relative difference of the matter power spectra of the cvG and QCDM models, $\Delta P(k)/P_{\rm QCDM}(k) \equiv (P_{\rm cvG}(k) - P_{\rm QCDM}(k))/P_{\rm QCDM}(k)$. A Savitzky–Golay filter has been used to smooth $\Delta P(k)/P_{\rm QCDM}(k)$. Each panel compares linear perturbation theory (black dotted), to results obtained from full (coloured solid) and linearised (black dashed) simulations. The vertical grey shaded region in each panel indicates where $k > k_{\rm Ny}$ where $k_{\rm Ny}$ is the Nyquist frequency.

Section 2.3 that the csG model is a limiting case of the cvG model with $\tilde{\beta}_3 \to 0$, and the result in Fig. 2.7 confirms that the power spectrum in the case of $\tilde{\beta}_3 = 10^{-6}$ behaves similarly to what was found in Ref. [17] for the csG model – this serves as an independent check of the new numerical implementation in `ECOSMOG`.

Secondly, as expected from Fig. 2.3, a larger value of $\tilde{\beta}_3$ leads to a smaller enhancement of matter clustering with respect to QCDM. We can also assess how effective the Vainshtein screening is for the different values of $\tilde{\beta}_3$ by comparing the results of the full (coloured solid lines) and linarised (black dashed) simulations in the bottom row. It becomes strikingly clear how the neglect of the non-linear terms in the EOM of χ leaves over-densities unscreened, leading to a much higher clustering power at small scales. The effect of the neglected screening mechanism propa-

gates to larger scales the smaller $\tilde{\beta}_3$ is: at $a = 1$, scales of $k \gtrsim 4\,h\,/\,\mathrm{Mpc}$ are screened for $\tilde{\beta}_3 = 10^{-6}$ and 1, while for $\tilde{\beta}_3 = 100$ the clustering is only weakly damped. This is as expected from the left panel of Fig. 2.2, which shows that the screening radius decreases when $\tilde{\beta}_3$ increases, meaning that for large values of $\tilde{\beta}_3$ the non-linear screening effect will be restricted to smaller scales and will be weaker. The observable peaks in the coloured lines in the lower panels, that becomes more pronounced with time, are a clear signature of the Vainshtein mechanism at work to bring gravity back to Newtonian on small scales. Interestingly, a qualitatively similar result has been obtained in Ref. [110] based on the kinetic field theory.

Thirdly, we note that on large scales ($k < k_*$) the predictions by linear theory, the full and the linearised simulations all agree. The exact value of k_* depends on redshift and the model parameter $\tilde{\beta}_3$. As an example, at $a = 0.6$ we have $k_* \simeq 0.3h\,/\,\mathrm{Mpc}$ for $\tilde{\beta}_3 = 100$ while $k_* \simeq 0.15h\,/\,\mathrm{Mpc}$ for $\tilde{\beta}_3 \leq 1$; by the time $a = 1$, however, k_* has become much smaller for all $\tilde{\beta}_3$ values. The dependence on $\tilde{\beta}_3$ is due to the same reason as mentioned above, namely a larger $\tilde{\beta}_3$ means a smaller Vainshtein radius. The dependence on redshift is a combined consequence of the time evolution of the Vainshtein radius (cf. the left panel of Fig. 2.2) and the progressively non-linear matter clustering. Overall, the full simulation result actually agrees better with linear perturbation theory than the linearised simulation, due to the stronger fifth-force effect of the latter, and we can conclude that the screening mechanism does not affect the large scales typically associated with linear perturbation theory ($k \lesssim 0.1h/\mathrm{Mpc}$), which is therefore still a valid approximation on those scales.

Finally, we stress again that in this plot the linear matter power spectrum is calculated by simply extrapolating the initial power spectrum using the linear growth factor in the cvG model, rather than based on a full perturbation analysis. Therefore the good agreement between the linear theory and full simulation predictions can not be used as an evidence of the validity of the quasi-static approximation employed in this

Chapter. However, it was shown, by using a modified version of CAMB, in [17] that the QSA does not have appreciable impact on $P(k)$ at large scales for the csG model which is very similar to the cvG model with $\tilde{\beta}_3 = 10^{-6}$. Comparing the behaviour of the relative difference between the full theory cvG and QCDM power spectra to the results of [17] adds confidence on the applicability of the QSA on large scales for the cvG model.

Before finishing this subsection, let us briefly comment on the implication of the $\tilde{\beta}_3$-dependence of the fifth-force effect in the cvG model on its viability. The cvG model has an identical background expansion history to the csG model with the same cosmological parameters, and both do not have a ΛCDM limit, which suggests that the simple model studied in this Chapter could struggle in matching observations such as the CMB shift parameter and BAO [64, 154, 65]. In Ref. [19], including massive neutrinos was proposed as an alternative way to generalising G_2 and G_3 into non-linear functions of X to bring compatibility of the csG model with those observations. But the simplest csG model with linear G_2 and G_3 still faces other challenges including void lensing (e.g., [22, 14]) and a wrong sign of the ISW effect (e.g., Refs. [19, 20, 176, 168]), due to a very fast increase of $G_{\rm eff}/G$ at late times (cf. Fig. 2.3, $\tilde{\beta}_3 = 10^{-6}$). The cvG model with $\tilde{\beta}_3 \gg 1$ offers a potential way around this problem while maintaining other properties of the csG model, because $G_{\rm eff}/G$ can be strongly suppressed towards unity. We hope to revisit the cosmological constraints on the cvG model in a future publication.

2.5 Discussion and conclusions

To summarise, in this Chapter we have performed the first self-consistent non-linear cosmological simulations of the GP theory, or the vector Galileon model, up to cubic order (cvG). This was achieved by adapting the ECOSMOG simulation code, to implement the relevant equations under the weak-field and quasi-static approximations. We find that the cvG equation for the longitudinal mode of the vector field has the same

structure in terms of spatial derivatives as, while differing in the time evolution of the coefficients from, the cubic scalar Galileon (csG) and sDGP models (see Section 2.2 for equations in natural units and Section 2.3 for equations in code units). In particular, cvG has the same background expansion history as csG for the same cosmological parameters. However, unlike the csG model, the cvG model has a free parameter $\tilde{\beta}_3$ which controls the strength of the fifth-force and the effectiveness of the Vainshtein screening.

We investigated the time evolution of various quantities including the screening radius, R_V, the magnitude of non-linear screening terms, ϵ, the effective gravitational constant, $G_{\rm eff}$, and the relative difference of the density contrast $\delta / \delta_{\Lambda\rm CDM}$ (cf. Fig. 2.2, 2.3). For all quantities we found their evolution in the cvG and csG models to be indistinguishable at early times, $a \lesssim 0.1$. This trend is continued at late times, $a \gtrsim 0.1$, for a cvG model parameter $\tilde{\beta}_3 \to 0$. If however $\tilde{\beta}_3 \to \infty$, than $R_V \to 0$, $\epsilon \to \infty$, $G_{\rm eff} / G \to 1$, and $\delta / \delta_{\Lambda\rm CDM}$ converges to the QCDM variant of the cvG model. This makes the cvG model more versatile and endows it with richer phenomenology.

In deriving the equations for N-body implementation, we have made a couple of simplifications. The first is that we have used the perturbed constraint equation satisfied by the temporal component of the Proca field, φ, to eliminate the time derivatives within the equation of motion for the longitudinal mode χ, cf. Eq. (2.35). This is done exactly, *without* resorting to the usual quasi-static approximation. The second is that we have manipulated the equation of motion for the transverse model, Eq. (2.38), to obtain a much simplified approximate version, Eq. (2.47). This allows the B^i field to be calculated easily in simulations, and allows the validity of the approximations used to be tested *a posteriori*.

We ran a set of moderate cvG cosmological simulations to investigate three questions. Firstly, proof that the transverse mode, B_i, is negligible compared with the longitudinal mode, χ. By measuring their power spectra, we show that $P(k; \partial_i \partial^2 \chi)$ is about 15-20 orders of magnitude larger than $P(k; \partial^2 B_i)$ on all scales probed by the simulation. Conse-

quently, we expect the 'back-reaction' of B_i on the evolution of χ to be very small, justifying the neglect of the B^i field in future simulations and confirming the findings of [62].

Secondly, verification of the suppression of the fifth-force by the Vainshtein mechanism for the cvG model. To this end we have run cosmological simulations of the full cvG model and its *linearised* counterpart with $\beta_3 = (10^{-6}, 10^0, 10^2)$. By comparing their relative power spectrum enhancement with respect to QCDM, $\Delta P(k) / P_{\rm QCDM}(k)$, the suppression of the fifth-force is quantified, c.f. Fig. 2.7. The comparison has made it clear how the neglect of the non-linear terms in the EOM of χ leaves over-densities unscreened, leading to a much higher clustering power at small scales.

Finally, we show how the cvG model parameter $\tilde{\beta}_3$ affects the screening behaviour. The results in Fig. 2.7 confirm that the matter power spectrum in the case of $\tilde{\beta}_3 = 10^{-6}$ behaves similarly to what was found in Ref. [17] for the csG model. However, the larger $\tilde{\beta}_3$ is, the smaller the enhancement of matter clustering with respect to QCDM becomes. The effect of the weakened screening mechanism also propagates to larger scales the smaller $\tilde{\beta}_3$ is: at $a = 1$, scales of $k \gtrsim 4\,h\,/\,\text{Mpc}$ are screened for $\tilde{\beta}_3 = (10^{-6}, 1)$, while for $\tilde{\beta}_3 = 100$ the clustering is only weakly damped. This agrees qualitatively with what we find in Fig. 2.2, but the full non-linear simulations allow the effects to be more accurately quantified.

A more comprehensive investigation of the predictions of various physical quantities by the cvG model is needed to better understand the cosmological behaviours and observational implications of the model. This, however, requires more independent realisations of higher-resolution simulations covering more values of $\tilde{\beta}_3$, which are beyond

the scope of this work and will be left for future work. We also note that, while this publication has focused on the simplest Proca theory at cubic order, with $G_2 = G_3 = X$, it should be very straightforward to extend our code to simulate models with generic non-linear functions for $G_{2,3}$ in the future. Such functions add further flexibilities to the GP theory – indeed, ongoing research conducted by one of the authors has found that the GP theory up to cubic order can offer a better fit to available observational data than the standard ΛCDM model; see also Ref. [65] for some recent progress in developing linear Boltzmann codes for the GP theory.

Even for the simplest case with $G_2 = G_3 = X$, the cvG model's dependency on $\tilde{\beta}_3$ makes it an extension of the csG model from a phenomenological point of view, and this opens up possibilities to overcome the challenges the csG model faces in terms of void lensing and the ISW effect. These challenges originate from the fact that, if the csG field is the driving force of the accelerated cosmic expansion at late times, a byproduct is the quickly-deepening gravitational potential during this period. For the ISW effect, this is in contrast to ΛCDM, where the potential becomes shallower due to the accelerated expansion, and therefore leads to a wrong sign of the ISW-galaxy correlation. As the deepening of the gravitational potential at late times can be weakened using an increased $\tilde{\beta}_3$, the cvG model offers a potential way around these issues, while maintaining the other properties of csG. We will investigate these possibilities in the future.

Finally, even though we have justified the neglect of the transverse mode of the vector field B^i in cosmological simulations, it is possible that in other situations this is no longer a good approximation. For example, the Proca field does not have to be the driving force behind the accelerated cosmological background expansion, but might have effects on galactic scales and the transverse modes could give rise to a change of structure formation on such scales. With some appropriate adaption and extension, our code will be able to be used as a tool for investigations in such circumstances.

3

Proca-stinated Cosmology II: Matter, Halo, and Lensing Statistics in the vector Galileon

THE GP theory is a modified gravity model in which the acceleration of the cosmic expansion rate can be explained by self interactions of a cosmological vector field. In this Chapter we study a particular sub-class of the GP theory, with up to cubic order Lagrangian, known as the cubic vector Galileon (cvG) model. This model is similar to the cubic scalar Galileon (csG) in many aspects, including a fifth force and the Vainshtein screening mechanism, but with the additional flexibility that the strength of the fifth force depends on an extra parameter – interpolating between zero and the full strength of the csG model – while the background expansion history is independent of this parameter. It offers an interesting alternative to ΛCDM in explaining the cosmic acceleration, as well as a solution to the tension between early- and late-time measurements of the Hubble-Lemaître constant H_0 [64, 111]. To identify the best ways to test this model, in this Chapter we conduct a comprehensive study of the phenomenology of this model in the nonlinear regime of large-scale structure formation, using a suite of N-body simulations run with the modified gravity code ECOSMOG. By inspecting thirteen statistics of the dark matter field, dark matter haloes and weak lensing maps, we find that the fifth force in this model can have particularly significant effects on the large-scale velocity field and lensing potential at late times, which

suggest that redshift-space distortions and weak lensing can place strong constraints on it.

3.1 Introduction

Understanding the laws of physics that govern cosmic structure formation is indispensable for probing into the true nature of gravity, because gravity is the dominant one of the four fundamental forces on cosmological scales. Ever since its establishment, General Relativity (GR) has been a cornerstone of modern cosmology. Even though the predictions of GR have been validated against many tests, these tests are usually limited to small scales such as the solar system [223], leaving the cosmological scales underexplored. The current observational results of these latter scales, which trace the dynamics of luminous and dark matter such as stars, galaxies, galaxy clusters, and extended filaments surrounding enormous voids, are generally in good agreement with the current concordance model of cosmology, ΛCDM, despite the fact that in recent years a number of tensions between the cosmological parameter estimates from different observational probes have emerged [e.g., 215, 212, 116, 11, 117]. However, there is currently no compelling explanation of the smallness of the cosmological constant in this model, which is why alternative models to explain the cosmic acceleration, such as dynamical dark energy and modified gravity (MG), have been widely considered. In particular, in most alternative theories of gravity, the time evolution of large-scale structures can be significantly influenced, so that the observational data in cosmology may allow accurate tests of such models on large scales [for a recent review see 128].

The last decades have seen many attempts to modify GR. According to the Lovelock theorem, GR is the only theory with second-order local equations of motion for the metric field, which is derivable from a 4-dimensional action [128], and therefore modifications to GR often involve new dynamical degrees of freedom in addition to the metric field, nonlocality, higher-dimensional spacetimes and/or higher-order equations.

The simplest MG models, for example, usually involve a single scalar degree of freedom with self-interactions or interactions with curvature. It has been well-established that such models can be brought under the umbrella of the Horndeski theory [118, 123, 70].

One of the most well-known subclasses of the Horndeski theory is the Galileon model [160, 69, 68], a 4-dimensional effective theory which involves a scalar field with universal coupling to matter and derivative self-interactions. The theory implements Vainshtein screening [213] – a nonlinear mechanism also encountered in theories such as Fierz-Pauli massive gravity [12] and the Dvali-Gabadadze-Porrati (DGP) model [78] – to decouple the scalar field from matter near massive objects and therefore can be compatible with Solar system tests of gravity. The model modifies the background expansion history such that it reaches a de Sitter solution in the future without requiring a cosmological constant. Its simplicity makes it possible to study its phenomenology with the help of cosmological N-body simulations [136, 17]. We refer to this model as the scalar Galileon below.

In contrast to the scalar Galileon, the GP theory [108, 8, 29], involves a massive vector field, A_μ, with a broken $U(1)$ gauge symmetry and second-order equation of motion (EOM). The theory features Galileon-type derivative self-interactions and couplings to matter. At the background level, the temporal component of the vector field, A_0, gives rise to a self-accelerating de Sitter attractor, corresponding to a dark energy equation of state $w_{\rm DE} = -1$ [61]. From the gravitational wave event GW170817 [2] with accompanying gamma-ray burst GRB170817A [95] and other optical counterparts, the speed of propagation of the gravitational waves c_T has been tightly constrained to be identical to the speed of light, c. This places strong constraints on the allowed operators within the higher order GP Lagrangian. However, even with this restriction, the GP theory is still cosmologicaly interesting, with a theoretically consistent parameter subspace that is free of ghost and Laplacian instabilities [61], and in which $c_T = c$.

By introducing non-linear functions into the field Lagrangian of the

GP theory to describe its derivative self interactions and couplings with matter, it can be very versatile and flexible. However, in cosmological applications one often specialises to simple choices of these non-linear functions, such as power-law functions, and a number of studies have been conducted along this direction, leading to a good understanding of the cosmological behaviours of the model at background and linear levels. For example, in Refs. [64, 111], Markov Chain Monte Carlo likelihood analyses were performed for the particular GP theories proposed in Refs. [61, 62], by exploiting the observational data from type Ia supernovae (SNIa), the cosmic microwave background (CMB), Baryonic Acoustic Oscillations (BAO), the Hubble expansion rate $H(z)$, and redshift-space distortions (RSD). The cross correlation between galaxy field and the Integrated Sachs Wolfe (ISW) effect, which has been a powerful probe to constrain the scalar Galileon models, has also been used to constrain parameters of the GP theory [154].

In this work, we conduct a broad phenomenological study of a set of five cosmologies based on the toy GP model studied in [26]. Using the N-body code developed in [26] and augmenting it with an independent set of ray-tracing modules taken from `Ray-RAMSES`[24], we can supplement previous results with the measurements of non-linear scales and unexplored statistics of the matter field, haloes, weak lensing, and voids. There are several motivations for doing so. One is that we know perturbation theory is not good at quantifying the effects of screening, which is an inherently non-linear phenomenon. N-body simulations are the only known tool to accurately study the evolution of the Universe on small, highly non-linear, scales, and can be used to validate or calibrate the predictions of other approaches. Being able to probe small scales ($k \gtrsim 1h^{-1}\mathrm{Mpc}$) will enable us to test a given model against more observational data more accurately, e.g., access scales or regimes that are inaccessible to perturbation theory. For this reason, we will analyse a total of 13 matter, halo, weak lensing and void statistics, in the effort to identify the ones which are most sensitive to the effect of the fifth force in the GP theory.

In Section 3.2 we describe the set up of the N-body and ray-tracing simulations on which all following results are based. This is followed by presentations of the main results of the dark matter field (Section 3.3), haloes (Section 3.4), and weak lensing (Section 3.4.6). Finally, we summarise and discuss in Section 3.5.

Throughout this Chapter, we will use the $(-,+,+,+)$ signature of the metric and abbreviations $\partial A = \partial_\mu A^\mu$, $(\partial A)^2 = \partial_\mu A^\mu \partial_\nu A^\nu$. We set $c = 1$ except in expressions where c appears explicitly. Greek indices run over $0, 1, 2, 3$ while Roman indices run over $1, 2, 3$.

3.2 Cosmological simulations

In this section we present the set of dark-matter-only simulations for five different cosmologies which we use to investigate the phenomenology of the cvG model. Four of these take different values of the model parameter of the cvG model, $\tilde{\beta}_3 = [10^{-6}, 10^0, 10^1, 10^2]$, and one is their QCDM counterpart[1], in the simulation. It is equivalent to the limit $\tilde{\beta}_3 \to \infty$ [26]. To study the cvG effects on the weak lensing (Weak Lensing (WL)) signal, we extended the N-body code developed in the previous work [26] by adding an independent set of ray-tracing modules taken from `Ray-RAMSES`[24]. This allows us to calculate the WL signal 'on-the-fly' as proposed by [221, 134], while taking full advantage of the time and spatial resolution available in the N-body simulation.

[1] This is a variant that only considers the modified background expansion history, but uses standard Newtonian gravity to evolve particles

We construct a light-cone for each cosmology by tiling a set of five simulation boxes, all having an edge-length of $L_{\rm box} = 500\,h/{\rm Mpc}$, as shown in Fig. 3.1. The simulations treats dark matter as collisionless particles described by a phase-space distribution function $f(\mathbf{x}, \mathbf{p}, t)$ that satisfies the Vlasov equation

$$\frac{df}{dt} = \frac{\partial f}{\partial t} + \frac{\mathbf{p}}{m_0 a^2} \cdot \nabla f - m_0 \left(\nabla \Psi\right) \cdot \frac{\partial f}{\partial \mathbf{p}} = 0, \tag{3.1}$$

where $\mathbf{p} = a^2 m_0 \partial \mathbf{x}/\partial t$, m_0 is the particle mass, and Ψ is the modified Newtonian potential given by Eq. (2.70). Note that, as we do not include matter species such as photons and massive neutrinos the two Bardeen

potentials are equivalent, $\Psi = \Phi$. The exclusion of photons should not have a noticeable impact on our simulations, which are only run at low redshifts. The impact of neglecting massive neutrinos depends on the neutrino mass, and for the currently allowed mass range, we do not expect qualitative changes. We plan to run simulations including massive neutrinos in the future. Hence to solve Ψ, and prior to it the longitudinal Proca mode, via Eq. (2.68), they are discretised and evaluated on meshes using the nonlinear Gauss-Seidel relaxation method [137]. The domain grid – which is the coarsest uniform grid that covers the entire simulation box – consists of $N_{\rm grid} = 512^3$ cells, which is equal to the number of tracer particles, N_p. `ECOSMOG` is based on the adaptive-mesh-refinement (AMR) code `RAMSES` [205], which allows mesh cells in the domain grid to be hierarchically refined – split into 8 child cells – when some refinement criterion is satisfied. In our simulations, a cell is refined whenever the effective number of particles inside it exceeds 8. This gives a higher force resolution in dense non-linear regions, where the Vainshtein screening becomes important. The Gauss-Seidel algorithm is run until the difference of the two sides of the PDE, d^h, is smaller than a predefined threshold ϵ. We verified that for a value of $\epsilon = 10^{-9} > |d^h|$, the solution of the PDE no longer changes significantly when ϵ is further reduced.

We use the same set of five different initial conditions (ICs), for each of the five simulations that make up a light-cone for a given cosmology are different, for the different cosmologies. The ICs were generated using `2LPTic` [54], with cosmological parameters taken from the Planck Collaboration [5],

$$h = 0.6774, \quad \Omega_\Lambda = 0.6911, \quad \Omega_m = 0.3089, \quad \Omega_B = 0.0223, \quad \sigma_8 = 0.8159. \tag{3.2}$$

The linear matter power spectrum used to generate the ICs is obtained with `CAMB` [131]. The simulation starts at a relatively low initial redshift[2] $z_{\rm ini} = 49$, or $a_{\rm ini} = 0.02$, justifying the use of second-order Lagrangian perturbation theory codes such as `2LPTic`. One possible concern may

[2] Note, that differences of matter clustering between the different cosmologies are already present at this redshift but negligible as shown in [26].

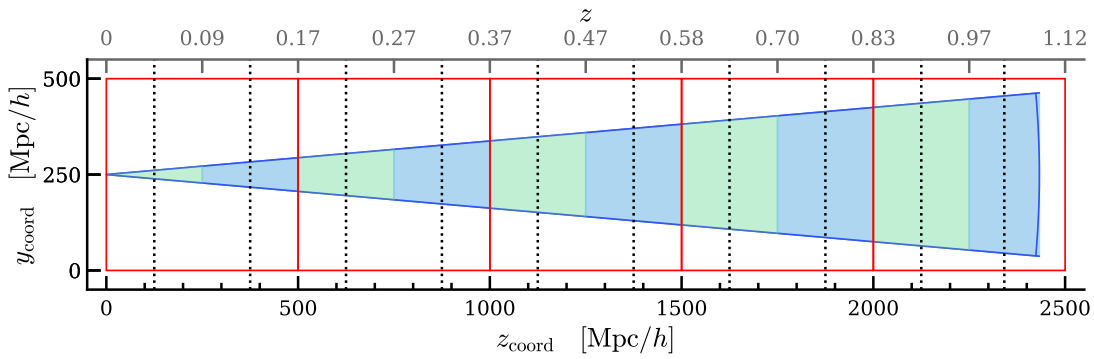

Figure 3.1: Light-cone layout. The light cone (solid blue line) is made up of five simulation boxes (red squares). All simulated boxes have a side length of $500\,h/\mathrm{Mpc}$ and the light cone has an opening angle of $10 \times 10\,\mathrm{deg}^2$. The comoving distance to the observer and redshift are respectively labelled in the lower and upper axes. The vertical dotted lines, which are at distances equal to $1/4$ and $3/4$ times the box size from the nearer side of each box, correspond to the redshifts at which particle snapshots are outputted.

be that, at this scale factor, differences of matter clustering are already present. However, judging from our experience [26], at this time the difference between the growth factors of the cvG model with ΛCDM is well below sub-percent level, so that modified effects on the initial matter clustering can be neglected. Additionally, it has been shown that ICs generated with 2LPTic at $z_{\rm ini} = 49$ can produce accurate matter field statistics for our simulation size and resolution at $z = 0$ [54].

Table 3.1: Summary of technical details that are identical for all simulations performed for this work. Here $k_{\rm Ny}$ denotes the Nyquist frequency. ϵ is the residual for the Gauss-Seidel relaxation used in the code [135], and the two values of the convergence criterion are for the coarsest level and refinements respectively.

$L_{\rm box}$	Nr. of particles	$k_{\rm Ny}$	force resolution	convergence
$500\ h/\mathrm{Mpc}$	512^3	$3.21\,h^{-1}\mathrm{Mpc}$	$30.52\,h/\mathrm{kpc}$	$\lvert\epsilon\rvert < 10^{-12}/10^{-9}$

The light-cone, outlined by solid blue lines in Fig. 3.1, is constructed by positioning the five simulation boxes, outlined by solid red lines in Fig. 3.1, relative w.r.t. the observer. The geometrical set-up was constructed to place the sources at $z_s = 1$, which is the starting point when the growth rate of matter density perturbations becomes higher than in ΛCDM [26]. The Field-Of-View (Field-of-View (FOV)) is set to $10 \times 10\,\mathrm{deg}^2$ (so that the wide end of the light-cone is still narrow enough to fit in the simulation box), within which 2048×2048 rays are followed by Ray-RAMSES to compute quantities of interest. Ray-RAMSES is an on-the-fly

ray-tracing code. The rays are initialised when a given simulated box reaches a defined redshift (for the closest and furthest box to the observer the initialisation redshift is respectively $z_i = 0.17$ and $z_i = 1.0$), and end after they have traveled the covered length of the box, meaning $500\,h/\mathrm{Mpc}$. As here we are interested in the lensing convergence, κ, the quantity that is computed along the rays is the two-dimensional Laplacian of the lensing potential,

$$\tilde{\nabla}^2\tilde{\Phi}_{\mathrm{lens,2D}} = \tilde{\nabla}_1\tilde{\nabla}^1\tilde{\Phi}_{\mathrm{lens,2D}} + \tilde{\nabla}_2\tilde{\nabla}^2\tilde{\Phi}_{\mathrm{lens,2D}}, \tag{3.3}$$

where 1, 2 denote the two directions on the sky perpendicular to the line of sight (LOS). The values of these two-dimensional derivatives of $\Phi_{\mathrm{lens,2D}}$ can be obtained from its values at the centre of the adaptive mesh refinement (AMR) cells via finite differencing and some geometrical considerations (see Refs. [134, 24]). Integrating this quantity as

$$\kappa = \frac{1}{c^2}\int_0^{\chi_s} \frac{\chi\,(\chi_s - \chi)}{\chi_s}\,\tilde{\nabla}^2\tilde{\Phi}_{\mathrm{lens,2D}}(\chi, \vec{\beta}(\chi))\mathrm{d}\chi, \tag{3.4}$$

where c is the speed of light, χ is the comoving distance, χ_s the comoving distance to the lensing source, and $\vec{\beta}(\chi)$ indicates that the integral is performed along the perturbed path of the photon (χ is not to be confused with the longitudinal mode of the Proca field). The integral is split into the contribution from each AMR cell that is crossed by a ray, which ensures that the ray integration takes full advantage of the (time and spatial) resolutions attained by the N-body run. For the WL signal we wish to study in this Chapter, we employ the Born approximation, in which the lensing signal is accumulated along unperturbed ray trajectories. We will make further notes on the calculations in Sec. 3.4.7.

3.3 Matter field statistics

In this section we present the results of various dark matter statistics of the different cvG models and compare them with the predictions by QCDM, to study the impact of the Proca field on these key observables.

We start with an analysis of the power spectra in Sect. 3.3.1. In Section 3.3.2, we consider the leading non-Gaussian statistic in large-scale structure clustering, the bispectrum, which is thus sensitive to deviations from linear evolved perturbations from single field inflation.

To support the analysis and interpretation of the results, we will compare the results of the N-body simulations to Eulerian standard perturbation theory (SPT), and limit the comparison only to the tree-level statistics. In SPT, the energy and momentum conservation equations can be solved order by order to obtain higher-order corrections to the quantities of interest. The expansion in powers of the linear density field is a simple time dependent scaling of the initial density field (in the Einstein de Sitter approximation),

$$\delta(\mathbf{k},\tau) = \sum_{i=1}^{\infty} D^n(\tau)\delta^{(i)}(\mathbf{k}), \tag{3.5}$$

for which the n-th order solution is

$$\delta^{(n)}(\mathbf{k}) \sim \int d^3\mathbf{k}_1 ... d^3\mathbf{k}_n \delta^{(\mathrm{D})}(\mathbf{k}-\mathbf{k}_{1...n})\mathcal{F}_n(\mathbf{k}_1,...,\mathbf{k}_n)\delta^{(1)}(\mathbf{k}_1,\tau_{\mathrm{ini}})...\delta^{(1)}(\mathbf{k}_n,\tau_{\mathrm{ini}}), \tag{3.6}$$

with the conformal time $\tau = \int dt/a$, $\mathbf{k}_{1...n} \equiv \mathbf{k}_1 + ... + \mathbf{k}_n$, the density contrast $\delta = \rho/\bar{\rho}$, $\delta^{(\mathrm{D})}$ the 3D Dirac delta function, and $\mathcal{F}_n$ the SPT fundamental mode coupling kernel [96, 188].

When comparing a cvG model to the QCDM counterpart, we do so through their relative difference which we write in short hand as

$$\frac{\Delta A}{A_{\mathrm{QCDM}}} \equiv \frac{A_X - A_{\mathrm{QCDM}}}{A_{\mathrm{QCDM}}}, \tag{3.7}$$

with A a placeholder of the summary statistics, and X will be one of the four cvG models. We calculate $\Delta A / A_{\mathrm{QCDM}}$ for each of the five pairs of cvG and QCDM simulations that share the same initial conditions to find its average and 1σ uncertainty. Taking this ratio removes contributions from cosmic variance, and so its uncertainty is not a direct indicator of how sensitive the various summary statistics are to differences between

the cvG models. To provide an estimate of this sensitivity given a survey volume as large as our simulation box, we calculate the signal-to-noise ratio (Signal-to-Noise Ratio (SNR)) of the difference between cvG models and their QCDM counterpart for some summary statistics using the expression

$$\mathrm{SNR} \equiv \frac{\Delta A}{\sigma} = \frac{A_X - A_{\mathrm{QCDM}}}{\sqrt{\sigma_X^2 + \sigma_{\mathrm{QCDM}}^2}}, \tag{3.8}$$

where ΔA is the average and σ is the standard deviation of the five simulations per cosmological model. We note that the SNR values obtained in this way could be subject to sample variance, owing to the small number of realisations. This is not a problem for the qualitative study presented in this Chapter, but more simulation volume is needed before we can place reliable quantitative constraints on this model. This will be left for future work.

3.3.1 Matter and velocity power spectra

To gain insights into the differences of matter clustering and peculiar velocities on linear and nonlinear scales among the various models in this work, we begin our study of dark matter phenomenology by considering the auto power spectra of the matter over-density, δ, given by

$$\langle \delta(\mathbf{k}_1, t)\delta(\mathbf{k}_2, t)\rangle = (2\pi)^3 \delta^{(\mathrm{D})}(\mathbf{k}_1 + \mathbf{k}_2) P_{\delta\delta}(\mathbf{k}_1, t). \tag{3.9}$$

Cosmic structure formation is driven by the spatially fluctuating part of the gravitational potential, $\Phi(\mathbf{x}, t)$, in Eq. (2.19), induced by the density fluctuation δ. In cvG cosmologies we expect an additional boost to the standard gravitational potential with respect to its QCDM counterpart, induced by χ described by Eq. (2.70), in regions where the fifth force is not screened by the Vainshtein mechanism. Thus, clustering will be enhanced in the cvG models on some scales, which can be captured by $P_{\delta\delta}$.

The top row of Fig. 3.2 compares the linear matter power spectra

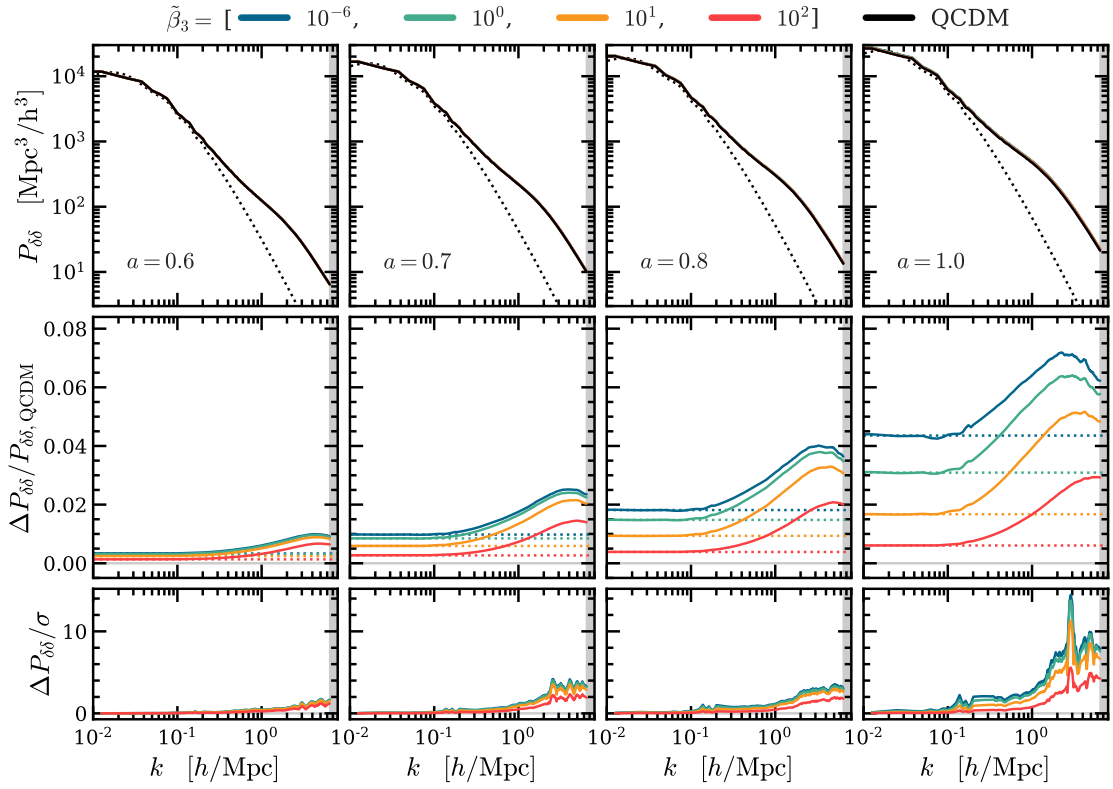

Figure 3.2: The matter power spectrum in the cvG model. Each column shows the results for a different scale factor: *outer left:* $a = 0.6$, *inner left:* $a = 0.7$, *inner right:* $a = 0.8$, *outer right:* $a = 1.0$. *Top:* The matter power spectrum of linear perturbation theory (dotted) and the cvG model for four values of $\tilde{\beta}_3 = (10^{-6}, 1, 10, 100)$, indicated by a blue, green, orange and red line respectively. *Centre:* Relative differences between the matter power spectra of the cvG and QCDM models. A Savitzky–Golay filter has been used to smooth $\Delta P_{\delta\delta}(k)/P_{\delta\delta,\mathrm{QCDM}}(k)$ for $k > 0.2\,h^{-1}\mathrm{Mpc}$. Each panel compares linear perturbation theory (black dotted), to results obtained from full simulation (coloured solid). The vertical grey shaded region in each panel indicates where $k > k_{\mathrm{Ny}}$ where k_{Ny} is the Nyquist frequency. *Bottom:* The signal-to-noise ratio of the difference between the cvG models and their QCDM counterpart.

(black dotted lines) with the simulation results of each cosmology (coloured lines with shaded regions), at $a = 0.6$ (outer left), $a = 0.7$ (inner left), $a = 0.8$ (inner right), and $a = 1.0$ (outer right). The linear power spectrum, $P^{(11)}_{\delta\delta}(k;z)$, is obtained by multiplying the initial matter power spectrum at $z_{\mathrm{ini}} = 49$, $P_{\delta\delta}(k;z_{\mathrm{ini}})$, with $[D(z)/D(z_{\mathrm{ini}})]^2$. The nonlinear matter power spectra are measured from particle snapshots using the POWMES[3] code [52]. The mean $P_{\delta\delta}$ of the five realisations per cosmology is shown as a coloured line while the standard deviation is indicated as shaded region. The standard deviation is largest at large scales ($k \lesssim 0.1h^{-1}\mathrm{Mpc}$) due to cosmic variance and the limited simulation size. The vertical shaded region near the right edge of each panel indicates the regime of k beyond the Nyquist frequency[4].

[3] The code is in the public domain, www.vlasix.org/index.php?n=Main.Powmes

[4] Note that the Nyquist frequency, k_{Ny}, marks the absolute maximum up to which we can trust the power spectrum.

The centre row of Fig. 3.2 shows the relative differences, Eq. (3.7), of the matter power spectra. The relative difference has been smoothed to remove noise at scales $k > 0.2\,h^{-1}\mathrm{Mpc}$, using a Savitzky–Golay filter of second order with a kernel width of 13 data points [182]. The power spectrum results agree with the results found in Ref. [26] and extend them by including larger scales and measurement uncertainties.

The bottom panel of Fig. 3.2 shows the SNR of the difference between cvG cosmologies and their QCDM counterpart. From it we can see that the SNR is larger at large k as σ is smaller, reflecting the fact that more Fourier modes can be sampled in that k regime. This implies that the effects of the cvG model are stronger on smaller, more non-linear scales, and for smaller $\tilde{\beta}_3$ values. However, note that the matter power spectrum is not directly observable, and later in this Chapter we will look at the behaviours of quantities more directly related to observables, such as the lensing power spectrum and halo correlation function.

The real-space positions of tracers of the matter distribution are not directly measurable, preventing us from comparing $P_{\delta\delta}$ to observations, which rely on the redshift measurement to infer distances. The reason is that peculiar velocities (i.e., additional velocities to the Hubble flow) of the tracers distort the redshift signal along the line of sight. Thus, $P_{\delta\delta}$ is different from its counterpart in redshift space, $P^{\mathrm{s}}_{\delta\delta}$, which becomes anisotropic despite the statistical isotropy of the Universe; on large scales the two are related by the linear Kaiser formula

$$P^{\mathrm{s}}_{\delta\delta}(k,\mu) = \left(1 + f\mu^2\right)^2 P_{\delta\delta}(k), \tag{3.10}$$

where μ is the angle between the wavevector and the LOS, and f is the linear growth rate defined as $f = \mathrm{d}(\ln\delta)/\mathrm{d}(\ln a)$ [121].

The Kaiser formula can be improved down to quasi linear scales with additional information about the auto power spectrum of the velocity divergence[5], $\theta = \nabla \cdot \mathbf{v}$, denoted as $P_{\theta\theta}$, as well as their cross spectrum

[5] Strictly speaking, one should consider the complete velocity field, which would also involve its vorticity $\nabla_i \times v_i$. However, just as the transverse mode of the Proca field, $\nabla_i \times B_i$, it has a much smaller magnitude than its divergence and is thus neglected in SPT.

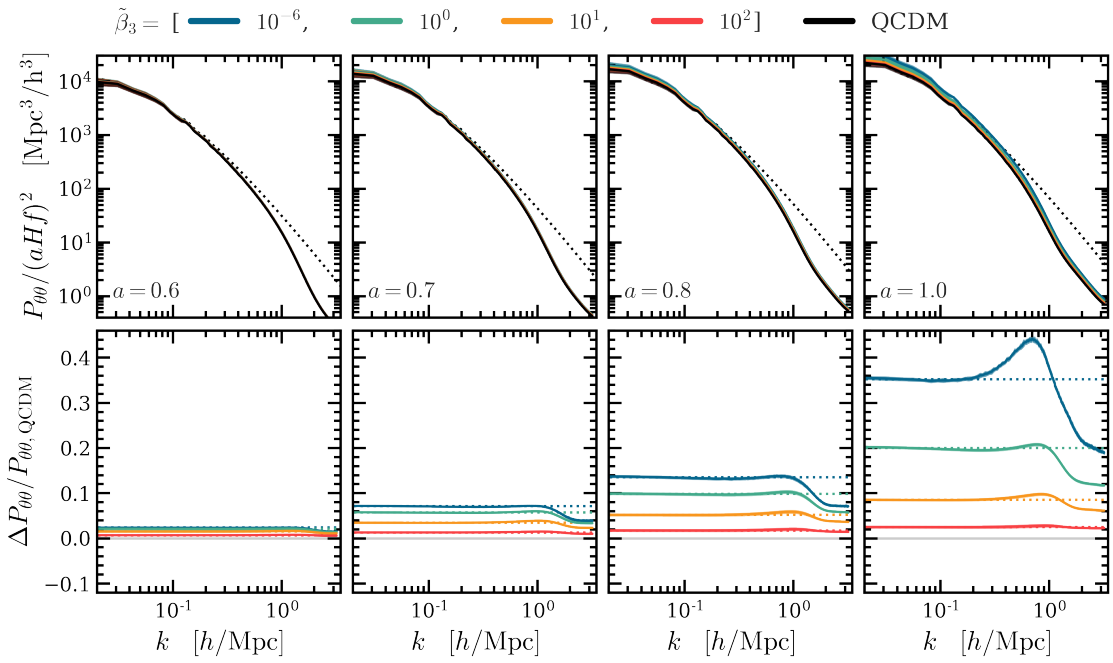

Figure 3.3: The velocity divergence power spectrum in the cvG model. Each column shows the results for a different scale factor: *outer left:* $a = 0.6$, *inner left:* $a = 0.7$, *inner right:* $a = 0.8$, *outer right:* $a = 1.0$. *Top:* The velocity divergence power spectrum of linear perturbation theory (dotted) and the cvG model for four values of $\tilde{\beta}_3 = (10^{-6}, 1, 10, 100)$, indicated by a blue, green, orange and red line respectively. *Bottom:* Relative differences between the velocity divergence power spectra of the cvG and QCDM models.

$P_{\delta\theta}$, since the velocity field is more sensitive to tidal gravitational fields compared to the density field on large scales [186, 204, 120].

The first row of Fig. 3.3 compares the linear velocity divergence power spectrum (black dotted lines) and measured nonlinear (coloured) simulations, at $a = 0.6$ (outer left), $a = 0.7$ (inner left), $a = 0.8$ (inner right), and $a = 1.0$ (outer right). The linear power spectrum $P^{(11)}_{\theta\theta}(k;z)$ can be related to $P^{(11)}_{\delta\delta}(k;z)$ through the zeroth-moment of Eq. (3.1), yielding the continuity equation,

$$\dot{\delta} + \frac{1}{a}\nabla \cdot [\mathbf{v}\,(1+\delta)] = 0. \tag{3.11}$$

On linear scales we can assume that the quadratic terms in Eq. (3.11) vanish leaving us with

$$\theta = -a\dot{\delta} = -aHf\delta. \tag{3.12}$$

Thus, the linear power spectrum of the velocity divergence is given by

$$P^{(11)}_{\theta\theta}(k;z) = (aHf)^2\, P^{(11)}_{\delta\delta}(k;z). \tag{3.13}$$

This relation is expected to fail on non- and quasi-linear scales, as velocities grow more slowly than the linear perturbation theory predicts. Therefore, any differences in $P^{(11)}_{\theta\theta}$ between the different cvG models will appear on these scales.

In order to measure the non-linear $P_{\theta\theta}$ from the numerical simulations, we first use a Delaunay tessellation field estimator (DTFE[6], [44]) to obtain the volume weighted velocity divergence field on a regular grid. This procedure constructs the Delaunay tessellation from the dark matter particle locations and interpolates the field values onto a regular grid, defined by the user, by randomly sampling the field values at a given number of sample points within the Delaunay cells and then taking the average of those values. For our $500\,h/\mathrm{Mpc}$ simulation boxes, we generate a grid with 512^3 cells. From that we then measure $P_{\theta\theta}$ using the public available code `nbodykit`[7][106].

[6] The code is in the public domain, www.astro.rug.nl/ voronoi/DTFE/dtfe.html.

[7] The code is in the public domain, nbodykit.readthedocs.io.

We can see from the top row of Fig. 3.3 that the results of the simulations for all models have approached the linear theory prediction on scales $k \lesssim 0.1\,h^{-1}\mathrm{Mpc}$ for all times. On these scales, the time evolution of the power spectrum of all models is scale independent and, the relative difference encapsulates the modifications to the time evolution of $P^{(11)}_{\theta\theta}$ via H and f in Eq. (3.13). On smaller scales, the formation of non-linear structures tends to slow down the coherent (curl-free) bulk flows that exist on larger scales. This leads to an overall suppression of the divergence of the velocity field compared to the linear theory results for scales $k \gtrsim 0.1\,h^{-1}\mathrm{Mpc}$.

A careful look into the relative difference $\Delta P_{\theta\theta}(k)\,/\,P_{\theta\theta,\mathrm{QCDM}}(k)$ in the bottom row of Fig. 3.3 also reveals a number of other interesting features on all scales. Firstly, we see that the wavenumber at which linear theory and simulation results for $\Delta P_{\theta\theta}(k)\,/\,P_{\theta\theta,\mathrm{QCDM}}(k)$ agree, k_*, depends both on $\tilde{\beta}_3$ and the scale factor. The value of k_* is pushed

to ever larger scales as $a \to 1$ and $\tilde{\beta}_3 \to 0$. A similar observation has been made by [137] for the DGP model. This is important for the growth rate measurement from redshift distortions, because it gives useful information about on which scales we can extract the growth rate based on the predictions of linear perturbation theory. Secondly, on small scales, $k \gtrsim 1h^{-1}\mathrm{Mpc}$, we can see how deviations from QCDM are suppressed by the screening mechanism, reflecting the fact that inside dark matter haloes the screening is very efficient. As also shown by $\Delta P_{\delta\delta}(k)/P_{\delta\delta,\mathrm{QCDM}}(k)$, the screening mechanism becomes more effective as $\tilde{\beta}_3 \to 0$. Thirdly, for $a \to 1$ and $\tilde{\beta}_3 \to 0$ we see a growing peak that for the case of $\tilde{\beta}_3 = 10^{-6}$ protrudes above the linear theory prediction at $k \sim 0.7h^{-1}\mathrm{Mpc}$. A similar feature was also observed by [137] for the DGP model.

The difference of $P_{\theta\theta}$ between the cosmological models compared to its magnitude is very small at early times, e.g., at percent level for all models when $a \lesssim 0.6$, but increases rapidly over time, reaching 35% for $\tilde{\beta}_3 = 10^{-6}$ at $a = 1.0$. This is unlike the behaviour of $\Delta P_{\delta\delta}(k)/P_{\delta\delta,\mathrm{QCDM}}(k)$ which increases much more slowly and only reaches $\sim 5\%$ for $\tilde{\beta}_3 = 10^{-6}$ at $a = 1.0$. This difference is because the velocity field, being the first integration of the forces, responds more quickly to a rapid growth of the fifth-force magnitude than does the matter field, which is the second integration of the forces. It shows the rapid increase of the linear growth rate of the cvG model at late times ($a \gtrsim 0.8$), and suggests that redshift-space distortions (RSD) in this time window can be a strong discriminator of this model.

3.3.2 Matter Bispectrum

As we have mentioned, even if cosmological fields are initially Gaussian, they inevitably develop non-Gaussian features as the dynamics of gravitational instability is nonlinear. Consequently, the structures found in the density field can no longer be fully described by two-point statistics alone, and higher-order correlation functions are needed in order

to unlock additional information, in particular regarding the nature of gravitational interactions. To obtain first impressions of this information we use the Fourier space counterpart of the three-point correlation function, the bispectrum, which is receiving increased attention in the recent literature, not only for making more accurate predictions (see, e.g., [107, 80, 72, 161]), but also as a probe of effects beyond ΛCDM (e.g. [94, 28, 152, 40, 41, 101, 150]).

We restrict ourselves to the study of the matter field in real space at $z = 0$, for which the bispectrum is given by

$$\langle \delta(\mathbf{k}_1)\delta(\mathbf{k}_2)\delta(\mathbf{k}_3)\rangle = (2\pi)^3\delta^{(\mathrm{D})}(\mathbf{k}_1+\mathbf{k}_2+\mathbf{k}_3)B(\mathbf{k}_1,\mathbf{k}_2,\mathbf{k}_3), \tag{3.14}$$

with the three wave vectors forming a closed triangle. If we were measure the bispectrum in redshift space we expect the small-scales to be heavily damped by the Finger-of-God effect [166], which leads to an increased impact of shot noise and thus less significant deviations from ΛCDM. As the study of the effects on bispectrum due to modifications to GR are still in its infancy, we shall be as comprehensive as possible by considering all possible triangle configurations between the two extreme scales k_{min} and k_{max}, given a specific bin width $\Delta k_1 = |\Delta\mathbf{k}_1|$ for each side. A detection of strong configuration dependence can be regarded as a compelling motivation to further investigate higher-order statistics. It would allow us to disentangle the modified gravity signal from other potential cosmological effects, which might be degenerate in two-point statistics and other alternative measures.

The top panel of Fig. 3.4 compares the bispectrum of equilateral triangles at the tree-level (dotted line), to the measurements (solid line). It furthermore contains the measured bispectrum of squeezed triangles (long dashed), folded triangles (short dashed), and all other triangle configurations (scattered dots). Vertical lines are spaced $\Delta k = |\Delta\mathbf{k}|$ apart. As we assume a primordial Gaussian random field, we can apply the Wick theorem to write the bispectrum as products of power spectra summed over all possible pairings. Thus, the lowest-order bispectrum

that is able to capture non-Gaussian features at late times has to expand one of the fields in the correlator of three Fourier modes to second order, yielding

$$B^{(211)}(\mathbf{k}_1,\mathbf{k}_2,\mathbf{k}_3) = \langle\delta^{(2)}(\mathbf{k}_1)\delta^{(1)}(\mathbf{k}_2)\delta^{(1)}(\mathbf{k}_3)\rangle' + \text{cyc.} = 2\mathcal{F}_2(\mathbf{k}_1,\mathbf{k}_2)P^{(11)}(k_1)P^{(11)}(k_2) + \text{cyc.}, \tag{3.15}$$

where $\delta^{(n)}$ is given in Eq. (3.6), the primed ensemble average indicates that we have dropped the factor of $(2\pi)^3$ as well as the momentum conserving Delta function, and "cyc." stands for the two remaining permutations over $\mathbf{k}_1$, $\mathbf{k}_2$ and $\mathbf{k}_3$. Note here, that we have assumed that SPT gives an appropriate description of perturbations in the cvG model and does not fail to include further mode couplings that might be introduced through the additional Proca vector field. We will see below that this is indeed an excellent approximation. The resulting bispectrum scales as square of the linear power spectrum, $P^{(11)}$, and exhibits a strong configuration dependence as it is directly proportional to the second-order perturbation theory kernel, $\mathcal{F}_2$, which is given by [30],

$$\mathcal{F}_2 = \frac{17}{21} + \frac{1}{2}\frac{\mathbf{k}_1\cdot\mathbf{k}_2}{k_1k_2}\left[\frac{k_2}{k_1}+\frac{k_1}{k_2}\right] + \frac{2}{7}\left[\frac{(\mathbf{k}_1\cdot\mathbf{k}_2)^2}{k_1^2k_2^2} - \frac{1}{3}\right]. \tag{3.16}$$

To measure the bispectrum from the simulations, we first use fourth-order density interpolation on two interlaced cubic grids [189] of $N = 256$ cells per side. Next, we measure $B(\mathbf{k}_1,\mathbf{k}_2,\mathbf{k}_3)$ using an implementation of the bispectrum estimator presented in Ref. [187]. Starting from $k_{\min} = 2k_f = 0.025h^{-1}\text{Mpc}$, where k_f denotes the fundamental mode, we loop through all configurations satisfying $k_1 > k_2 > k_3$ and $k_1 \leq k_2 + k_3$ (the triangle closure condition). We stop after the values of $\mathbf{k}$, which are evenly spaced by $\Delta k = 2k_f$, reach the $k_{\max} = 1.0h^{-1}\text{Mpc}$, up until which point the shot noise is sub-dominant. With these settings – which are chosen to keep memory consumption at bay, as it would increase rapidly otherwise – we obtain a total of 5910 distinct triangle configurations.

The top panel of Fig. 3.4 shows that the tree-level prediction $B^{(211)}$

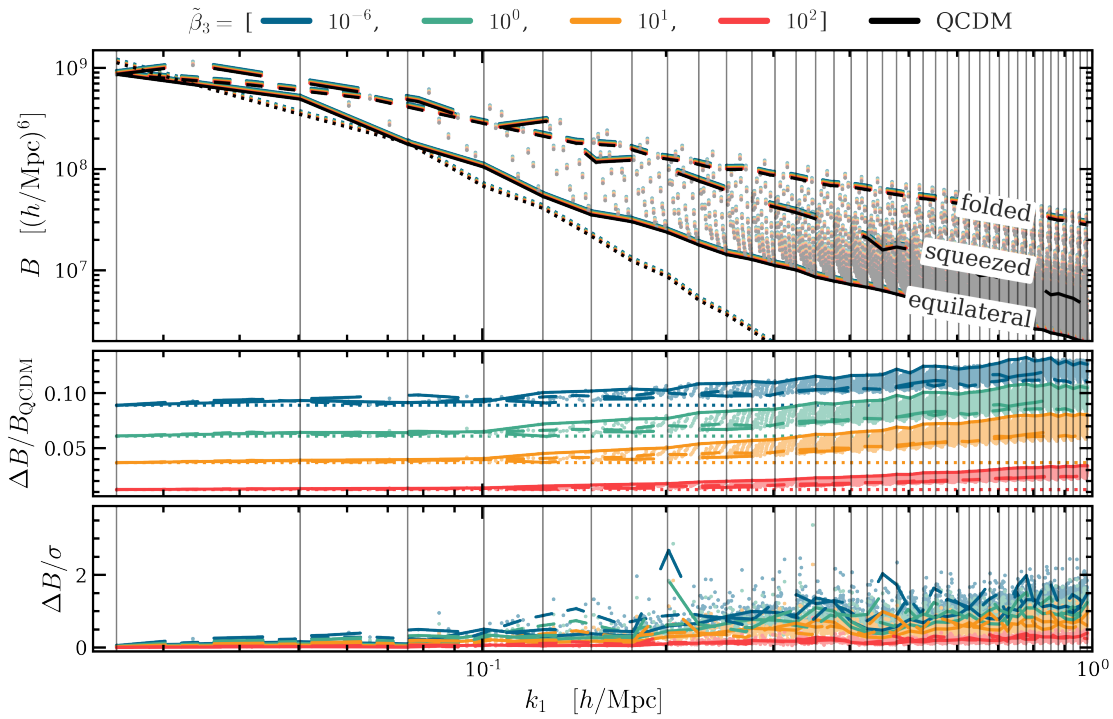

Figure 3.4: *Top*: real-space bispectrum measurements for cvG cosmologies (coloured points) and their QCDM counterpart (black points). Each data point corresponds to one of 5910 triangle configurations (see the text for more details). The vertical lines are spaced by the bin width $\Delta k \approx 0.025h^{-1}\mathrm{Mpc}$ and indicate the value of $|\mathbf{k}_1|$, i.e., the largest triangle side. The bispectrum for equilateral configurations are shown at the tree-level (dotted), B_{211}, and simulation measurement (solid). The measured bispectra for the squeezed and folded configurations are shown as long and short dashed lines respectively. *Middle*: The relative difference between the cvG models and their QCDM counterpart. Again we show the tree-level (dotted lines) and simulation (using the same line styles as in the top panel) results. *Bottom*: The signal-to-noise ratio of the difference between the cvG models and their QCDM counterpart.

(dotted line) for the equilateral configuration converges to the simulation measurements of B (solid line) on $k \approx 0.07h^{-1}\mathrm{Mpc}$, which is agreement with $P_{\delta\delta}(k)$ and [15]. In this panel we have also indicated the folded, squeezed and equilateral configurations by lines (see the legends). It does not come as a surprise that the measured bispectrum for equilateral triangles is consistently lower than all other configurations as in our considered range of k, the power spectrum decreases with increasing k (as can be seen in Fig. 3.2). The folded triangles, on the other hand, tend to have the largest amplitude, while the squeezed triangles are in between.

The middle panel of Fig. 3.4 shows the relative difference, Eq. (3.7), of the bispectrum of equilateral triangles at the tree-level (dotted line),

and measurements (solid line); for the latter the bispectra for all triangle configurations are indicated by scattered dots. Again, the results which correspond to equilateral, squeezed and folded triangle configurations are shown by lines (the same line styles as in the top panel). We can draw the following conclusions. Firstly, as it is the case for matter and velocity divergence power spectra, the tree-level bispectrum is a good estimator on large scales ($k < k_*$) while the exact value of k_* depends on redshift and the model parameter $\tilde{\beta}_3$. However, we can see that in general linear theory gives accurate predictions of $\Delta B / B_{\rm QCDM}$ at $k < k_* \sim 0.1 h^{-1}{\rm Mpc}$ for all models. Compared to the matter power spectra, the relative difference of the bispectra is roughly twice as large as $\Delta P_{\delta\delta} / P_{\delta\delta,{\rm QCDM}}$, monotonically increasing from 1% for $\tilde{\beta}_3 = 100$ to $\sim 9\%$ for $\tilde{\beta}_3 = 10^{-6}$. Secondly, the order of triangle configurations yielding the largest signal is reversed to the top row, with the equilateral triangles yielding the largest relative difference between cosmologies with fifth force and those without, while squeezed and folded triangles seem to converge to the same relative difference for larger values of $\tilde{\beta}_3$. This is in agreement with [40], who arrived at a similar conclusion for $f(R)$ and DGP cosmologies.

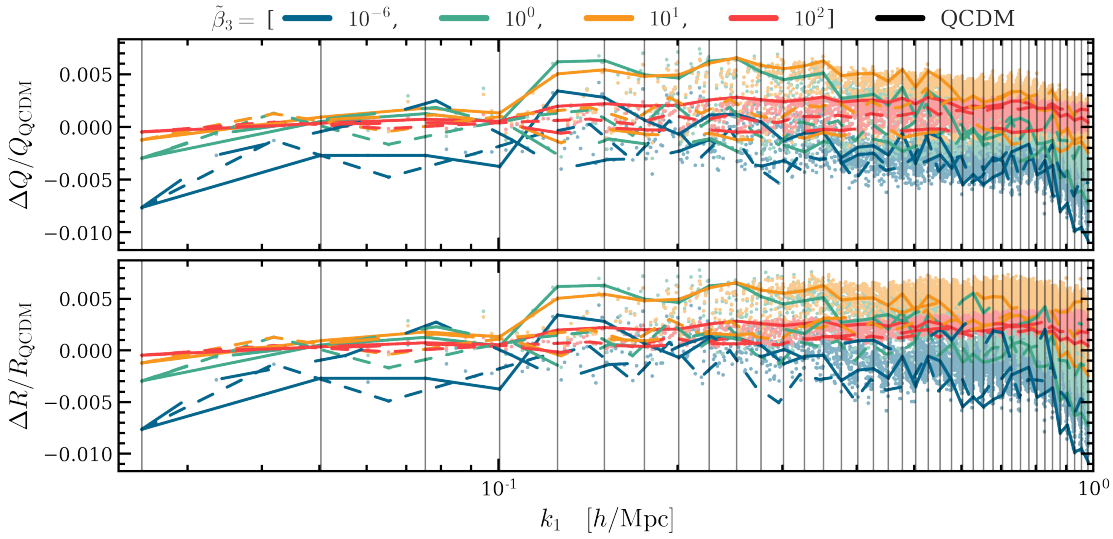

Figure 3.5: *Top*: relative difference between cvG models and their QCDM counterpart of the reduced bispectrum measurements, Q. *Bottom*: relative difference between cvG models and their QCDM counterpart of the ratio between the measured reduced bispectrum and its tree-level approximation, $Q^{(0)}$. Each data point corresponds to one of 5910 triangle configurations (see the text for more details). The lines represent equilateral (solid), squeezed (long dashed), and folded (short dashed) triangle configurations as in Fig. 3.4.

The bottom panel of Fig. 3.4 shows the SNR of the difference between cvG cosmologies and their QCDM counterpart. Three general trends are revealed: Firstly, an enhancement in the bispectrum signal with increasing $\tilde{\beta}_3$ relative to QCDM, as we have seen in the middle panel above. Secondly, the SNR significantly increases towards smaller, nonlinear, scales. Thirdly, there is no clear trend which triangular configuration results in the highest SNR. The median taken over the range $0.1 < k\,[h^{-1}\mathrm{Mpc}] < 1$ for each cvG cosmology is: 0.88 ($\tilde{\beta}_3 = 10^{-6}$), 0.77 ($\tilde{\beta}_3 = 1$), 0.54 ($\tilde{\beta}_3 = 10$) and 0.22 ($\tilde{\beta}_3 = 100$), respectively.

A very useful statistical quantity, that isolates the configuration dependence of the triangles by removing the propagator corrections from the modified Poisson equation (contained in the nonlinear power spectrum), is the reduced bispectrum,

$$Q(\mathbf{k}_1, \mathbf{k}_2, \mathbf{k}_3) \equiv \frac{B(\mathbf{k}_1, \mathbf{k}_2, \mathbf{k}_3)}{P(k_1)P(k_2) + \text{cyc.}}. \tag{3.17}$$

The relative difference between the reduced bispectra for the cvG models and their QCDM counterpart is displayed in the top row of Fig. 3.5. We indeed see how the strong scale dependencies of $\Delta B / B_{\mathrm{QCDM}}$ are removed, leaving only sub-percent deviations. The SNR of the difference of Q between the cvG models and their QCDM counterpart (not shown) revealed a very weak signal on all scales for all models, with a median of $\Delta Q/\sigma \lesssim 0.05$. Therefore we shall not try to interpret the trends revealed by the individual cvG models, and instead conclude that Q is very weakly dependent on $\tilde{\beta}_3$.

To quantify how much extra mode coupling the cvG models have experienced compared to their QCDM counterpart beyond the leading term, $\mathcal{F}_2$ (defined in Eq. (3.16)), we can divide the reduced bispectrum by its tree level term to define a new quantity,

$$R(\mathbf{k}_1, \mathbf{k}_2, \mathbf{k}_3) \equiv \frac{Q}{Q^{(0)}} = \frac{B(\mathbf{k}_1, \mathbf{k}_2, \mathbf{k}_3)}{2\mathcal{F}_2(\mathbf{k}_1, \mathbf{k}_2)P(k_1)P(k_2) + \text{cyc.}}. \tag{3.18}$$

The relative difference between the R of the cvG models and their QCDM counterpart is displayed in the bottom row of Fig. 3.5. Again, the results

are in the sub-percent level and the SNR of the difference of R between the cvG models and their QCDM counterpart (not shown) reveals a very weak signal on all scales for all models, with a median of $\Delta Q/\sigma \lesssim 0.06$.

The fact that for Q and R the relative difference between the cvG models and QCDM is fairly small, suggests that the fifth force in the cvG model does not produce substantial extra mode coupling corrections. This is a useful result because it means that the cvG effect mainly enters through the modified growth factors, which simplifies the modelling of the bispectrum. We stress that this does not imply that the bispectrum is incapable of placing additional constraints on the cvG models. That is because the bispectrum has a different dependence on the growth factors than the power spectrum and its configuration dependence is useful in breaking degeneracies with other parameters, e.g. parameters that describe the background model or galaxy bias, such that the combination of the two statistics can still be expected to yield significant improvements.

Modifications of gravity will not only impact the clustering of galaxies, but also their infall and virial velocities, and consequently alter the RSD of clustering statistics. In Sec. 3.4.4 below, we discuss the monopole and quadrupole of the two-point correlation function in redshift space. While we have not studied the effect of RSD on the bispecctrum, based on results in [7] for the nDGP model, we expect that the same qualitative changes would affect the bispectrum in cvG gravity.

Finally, let us note again that here we have only looked at the bispectrum of the matter density field, rather than the halo or galaxy fields. We have tried haloes, but due to the box size and resolution in our simulations, the results are noisy and the model differences unclear. Therefore we have decided not to show them here.

3.4 Halo statistics

This section is devoted to a detailed study of halo properties. Haloes are identified using two different algorithms, as they give complementary

information about the haloes and can serve in some cases as verification. Firstly, we use the algorithm developed by [198] to find friends-of-friends groups to represent the 'main' haloes, and then run SUBFIND to identify substructures in the 'main' haloes (from now on we shall refer to the halo and subhaloes identified in this way as SUBFIND halos). Secondly, we use ROCKSTAR[8] [27] to identify FOF haloes in the 6D phase space where substructure is more easily identifiable (from now on we will refer to these as ROCKSTAR haloes). In most of this section we show results of SUBFIND haloes, although we have checked that the ROCKSTAR haloes give similar results. We use ROCKSTAR haloes to study the halo concentration mass relation, because this is directly measured by ROCKSTAR.

[8] The code is in the public domain, https://bitbucket.org/gfcstanford/rockstar/src/main/

Note that, in principle, the unbinding procedure employed by the halo finding algorithms would need to be modified due to the presence of the fifth force induced by the Proca field. However, [133] found the effect of this modification to be quite small for chameleon models. Also, we will see below, the fifth force in the cvG models is strongly suppressed by Vainshtein screening, and so we expect its effect will be even smaller here. Thus, we use identical versions of SUBFIND and ROCKSTAR for the different cosmologies.

We compare the cvG models to their QCDM counterpart in the same way as we have done in Sec. 3.3 via Eq. (3.7) and Eq. (3.8).

3.4.1 Halo mass function

We start the analysis of the halo populations with the one-point distribution of halo masses – the halo mass function (HMF). The halo mass is defined as the mass enclosed in the spherical region of radius R_{200} around the centre of the over-density, within which the mean density is 200 times the critical density ρ_c at the halo redshift,

$$M_{200c} = \frac{4\pi}{3} R_{200}^3 200\rho_c, \text{ with } \rho_c = \frac{3H^2}{8\pi G}. \tag{3.19}$$

In the top row of Fig. 3.6 we show the cumulative HMF, $n(> M_{200c})$, which is the number density of dark matter haloes more massive than

the given M_{200c}, at $a = 0.6$ (outer left), 0.7 (inner left), 0.8 (inner right) and 1.0 (outer right). The *bottom-up* picture of structure formation, i.e., small-scale objects collapse first and merge to form increasingly massive objects as time proceeds, is clearly visible, which follows from the fact that in our model dark matter is cold.

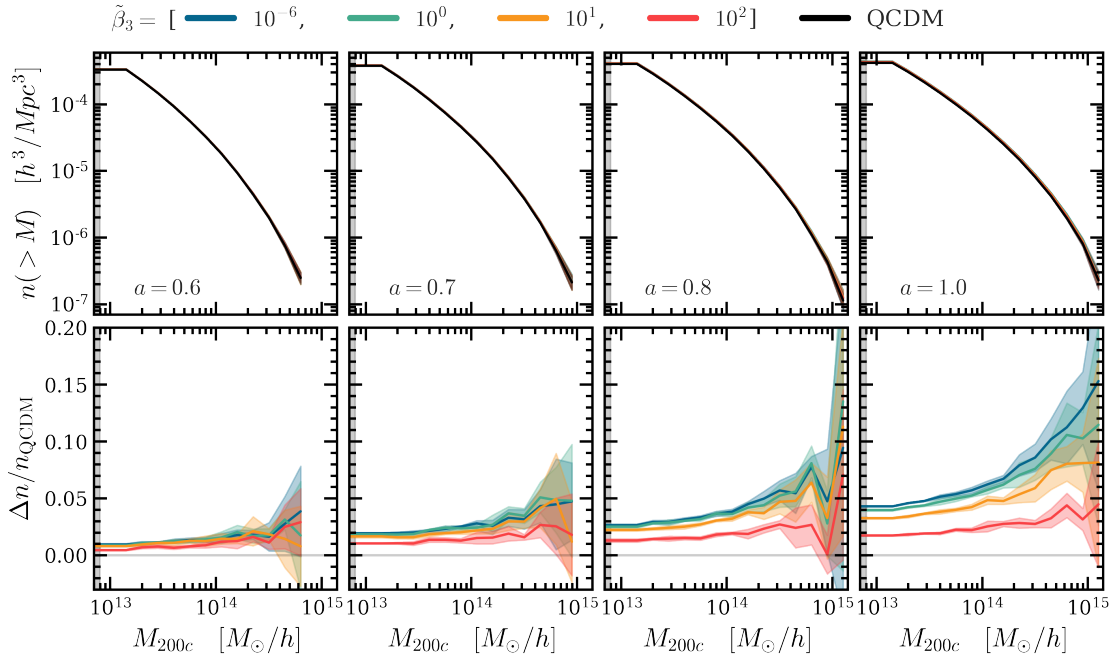

Figure 3.6: *Top*: panels show the cumulative halo mass function, $n\,(> M_{200c})$, for the cvG model (coloured) and their QCDM (black) counterpart. Each column shows the results for a different scale factor: *outer left*: $a = 0.6$, *inner left*: $a = 0.7$, *inner right*: $a = 0.8$, *outer right*: $a = 1.0$. *Bottom*: the relative differences to QCDM. The results shown are obtained by averaging over the simulations of the 5 different initial condition realizations and the shaded region show the standard deviation over these realizations. The vertical shaded region corresponds to haloes with fewer than 100 simulation particles, for which the number is incomplete due to the lack of resolution.

The bottom row of Fig. 3.6 shows the relative difference between the cvG models and their QCDM counterpart. The median of SNR of the differences between the models over the range shown in the figure is: 7.1 ($\tilde{\beta}_3 = 10^{-6}$), 6.4 ($\tilde{\beta}_3 = 1$), 5.5 ($\tilde{\beta}_3 = 10$), 2.9 ($\tilde{\beta}_3 = 100$). We find good agreement with [17], and have verified that the result is consistent between `SUBFIND` and `ROCKSTAR`. The fifth force enhances the abundance of dark matter haloes in the entire mass range probed by the simulations, with the enhancement stronger at late times and for high-mass haloes, which mimics the effect of the csG model [21]. This is to be expected because the strength of the fifth force increases over time

[26]. Note that for massive haloes the increase in abundance is mainly due to an increase in individual halo masses, as can be seen from the top panels: we remark that more massive haloes are not necessarily more strongly screened in Vainshtein models (see, e.g., Fig. 8 of [114]), and the enhanced gravity around these massive haloes helps to bring more matter from their (matter-rich) surroundings to their vicinity, allowing them to grow larger. On the other hand, models with more efficient screening, such as $\tilde{\beta}_3 > 1$, show a more restrained enhancement of the HMF.

To be able to use cluster number counts to constrain the cvG model, a few more steps have to be undertaken. The observational estimate of the halo mass function will require, in addition to the detailed specifications of individual cluster surveys (completeness, redshift distribution, observing technology, etc.), a more accurate quantification of the cvG effect on the high-mass end of the HMF (for which our simulation volume is not enough) and better knowledge of the cluster scaling relations (which are needed to connect halo mass to cluster observable such as X-ray temperature, Y_X, Y_{SZ}, because the cluster's mass is not a direct observable). A detailed study of cluster constraints on this class of models will be left as future work.

3.4.2 Two-point correlation functions

The configuration-space counterpart of the matter power spectrum, $P_{\delta\delta}$, presented in Sec. 3.3.1, is the two-point correlation function (2PCF), $\xi(r)$. In principle these two measures would carry the same information, but in practice this is not guaranteed since our analyses are restricted to a finite range of scales, and moreover, configuration and Fourier space statistics are impacted differently by systematic effects, which require slightly different analysis strategies (e.g. the treatment of shot noise).

For this analysis we use `SUBFIND` haloes, since these catalogues contain the subhaloes which can be proxies of satellite galaxies, and without which $\xi(r)$ would decay at $r \lesssim 1\text{-}2\,h/\mathrm{Mpc}$ due to the halo

exclusion effect. We show their respective 2PCFs in the top row of Fig. 3.7 for $a = 0.6$ (outer left), $a = 0.7$ (inner left), $a = 0.8$ (inner right) and $a = 1.0$ (outer right). As expected, the 2PCFs drop off with halo separation, and can be well described by a power law across the entire range of scales probed here.

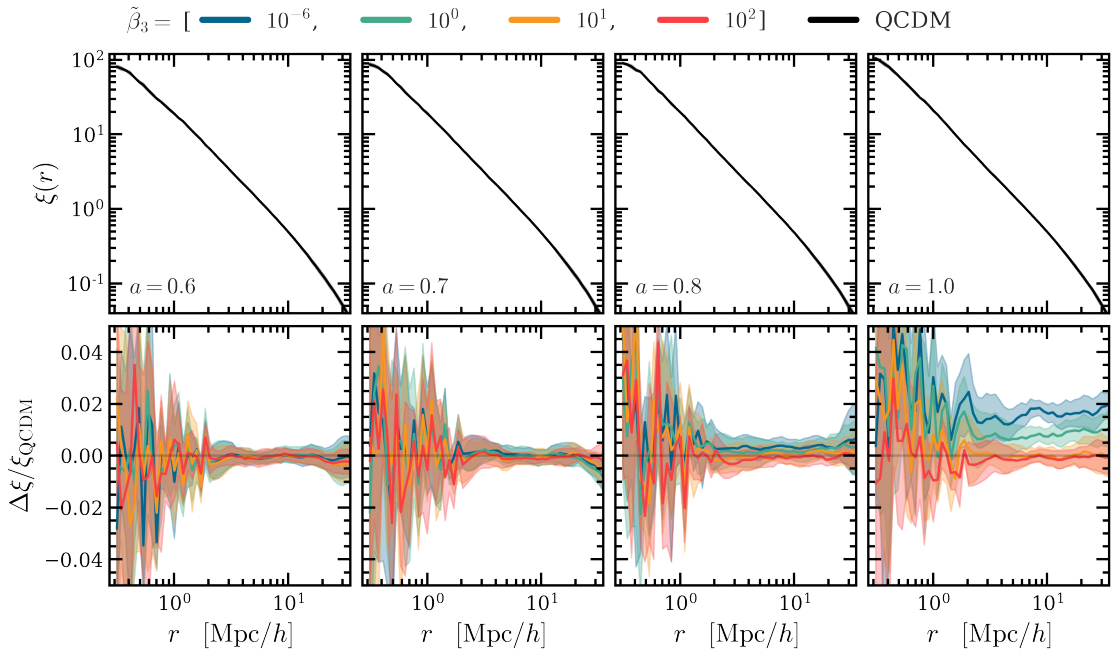

Figure 3.7: *Top*: The halo 2PCFs in the QCDM model. Each column shows the results for a different scale factor: *outer left*: $a = 0.6$, *inner left*: $a = 0.7$, *inner right*: $a = 0.8$, *outer right*: $a = 1.0$. Note that to prevent the plot from appearing cluttered we have not shown the results for the cvG models. Furthermore, we included the standard deviation as a shaded region, but it is too small to see. *Bottom*: The relative differences between models. The cvG model for four values of $\tilde{\beta}_3 = (10^{-6}, 1, 10, 100)$ are shown, indicated by a blue, green, orange and red line respectively. The shaded regions are the standard deviations among the five simulation realizations.

The relative difference between the 2PCFs of the cvG models and their QCDM counterpart for SUBFIND haloes is shown in the bottom row of Fig. 3.7. As for the power spectrum of the matter field, Fig. 3.2, we see more enhanced clustering for smaller values of $\tilde{\beta}_3$ as $a \to 1$. The rapid increase of the relative differences, $\Delta\xi/\xi_{\rm QCDM}$, starting at $a \approx 0.8$ is a consequence of the fast increase of the effective Newton constant at late times (see [26]). However, the cvG enhancement for halo clustering is smaller than for matter clustering, implying slightly smaller halo biases in stronger cvG models. This is because haloes are biased tracers of the dark matter field, and their bias generally decreases over time, as

structure formation progresses: the enhanced gravity in cvG models simply speeds this up. Note that the enhancement of the halo 2PCF is nearly constant down to $\sim 3\,h/\mathrm{Mpc}$, consistent with the behaviour of the matter power spectrum (cf. Fig. 3.2), and reflecting the fact that in the cvG model the growth factor is enhanced in a scale-independent way in the linear regime.

3.4.3 Mean halo pairwise velocity

As outlined earlier, it is quintessential to develop a theoretical model of the pairwise velocity statistics as well as the real-space correlation function for cosmological analyses with redshift surveys, such as Euclid and DESI. Although we do not strive to actually test the cosmological models investigated here, we measure the relevant quantities to gain an intuition of how they are affected by the cvG model and to aid future work.

For this analysis we use `SUBFIND` haloes, as they contain the smallest haloes and subhaloes and thus can enable measurements to smaller scales, including the virial motions of subhaloes inside main haloes. We show the measured mean pairwise velocities for the different models in the top row of Fig. 3.8, comparing linear estimates (dotted lines) to the simulation results (solid lines) at $a = 0.6$ (outer left), $a = 0.7$ (inner left), $a = 0.8$ (inner right) and $a = 1.0$ (outer right). The linear mean pairwise velocity, $v_{\langle ij\rangle}$, is intimately related to the 2PCF of the matter field, $\xi(r)$, through the pair conservation equation, Eq. (3.20), just as $P_{\theta\theta}$ is to $P_{\delta\delta}$ (see Sec. 3.3.1) through the continuity equation, Eq. (3.11) [167],

$$\dot{\xi}_{ij} + \frac{1}{a}\nabla_{ij}\cdot\left[v_{\langle ij\rangle}\left(1+\xi_{ij}\right)\right] = 0. \tag{3.20}$$

We can replace the 2PCF in Eq. (3.20) with its Fourier space counterpart in first order, $P_{\delta\delta}^{(11)}$, using the first-order Bessel function j_1, and obtain the linear theory prediction of $v_{\langle ij\rangle}$ expressed as

$$v_{\langle ij\rangle}(r) = -r\frac{fb}{\pi^2}\int dk P_{\delta\delta}^{(11)}(k) j_1(kr) k, \tag{3.21}$$

where b is the linear bias of halos, f is the linear growth rate and j_1 is the spherical Bessel function of order 1 [175]. To get the bias values used in the linear theory prediction for Fig. 3.8, cf. Eq. (3.21), we compute the halo power spectrum, P_{hh}, divide it by the matter power spectrum, $b^2 \approx P_{hh}/P_{\delta\delta}$. Due to the sparseness of haloes, the shot-noise becomes sub-Poisson on larger scales than it does for dark matter particles. Therefore we restrict the calculation of b to scales where the relation stays approximately constant, $0.025 < k\ h/\mathrm{Mpc} < 0.1$. We find that at each scale factor, the different cosmological models have the same fitted value of b (averaged over all 5 simulation realisations) up to the second decimal. Beyond the second decimal b indeed increases with $\tilde{\beta}_3$ as expected from the relation of $\xi(r)$ and $P_{\delta\delta}(k)$.

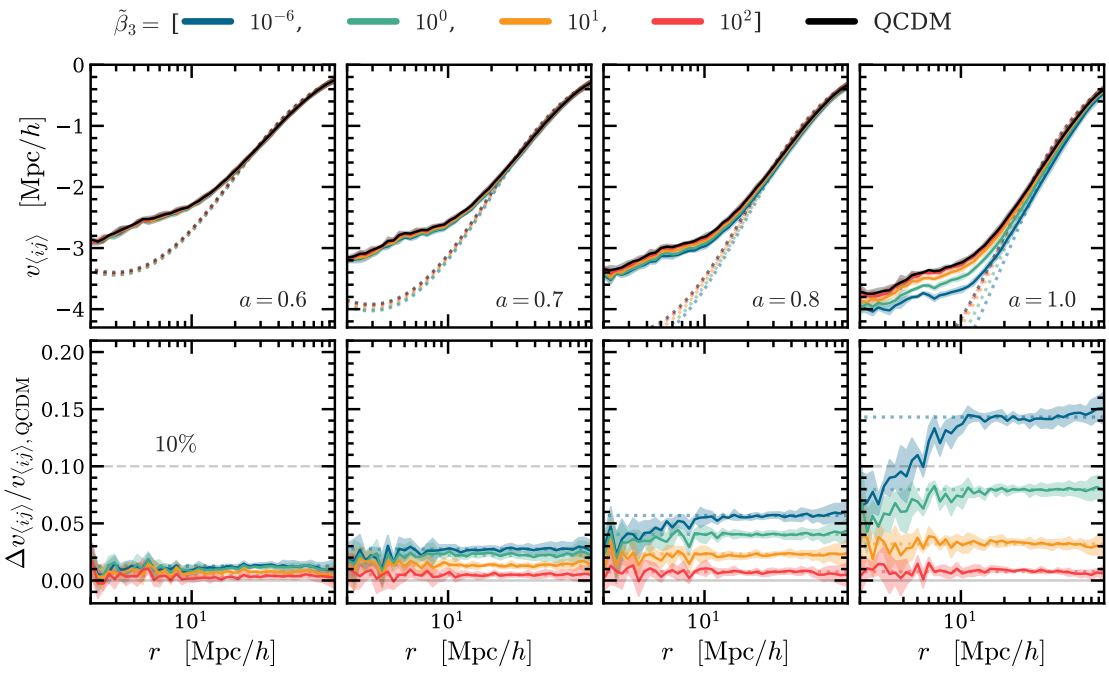

Figure 3.8: *Top*: the mean pairwise radial velocity of dark matter haloes. In each panel we show the mean measurements from the simulations (solid lines) with their one standard deviation (shaded regions), together with the linear theory predictions (dotted lines). Each column shows the results for a different scale factor: *outer left*: $a = 0.6$, *inner left*: $a = 0.7$, *inner right*: $a = 0.8$, *outer right*: $a = 1.0$. *Bottom*: the relative differences between the cvG models and QCDM. Note that the velocities are rescaled by H so that they have the unit of length.

The relative difference between $v_{\langle ij\rangle}$ of the cvG models and their QCDM counterpart is shown in the bottom row of Fig. 3.8, which converges to the linear-theory prediction for all cvG models at scales $r >$

$10\ h/\mathrm{Mpc}$. Note that in linear theory the fifth force leads to a scale-independent enhancement of the velocity [26]. From the top row of Fig. 3.8 we can see that non-linearity starts affecting the velocity statistics at $\lesssim\ 20-30\,h/\mathrm{Mpc}$. However, the bottom row shows that modified gravity effect, i.e., the enhancement with respect to QCDM can be well described by linear theory down to $\simeq\ 10\,h/\mathrm{Mpc}$. As an example, for $\tilde{\beta}_3 = 10^{-6}$ the relative difference settles on ~ 0.15 for large scales, which is approximately half of $\Delta P_{\theta\theta}(k)\,/\,P_{\theta\theta,\mathrm{QCDM}}(k)$ shown in Fig. 3.3, partially due to the fact that $P_{\theta\theta} \propto f^2$. If ROCKSTAR-halos are considered the same qualitative trend is found on the larger scales.

3.4.4 Redshift space clustering

Motivated by the results of the real space clustering and mean pairwise velocity, we carry on to study the halo 2PCF in redshift space. In real observations, instead of their radial distances, we measure the redshifts of galaxies. The conversion from redshift space to real-space galaxy coordinates is not only determined by the Hubble expansion, but also affected by the peculiar velocities of galaxies. This induces anisotropies on what would be an isotropic galaxy correlation function, known as redshift-space distortions (RSD). RSD is a useful probe of the peculiar velocity field, and consequently the growth rate of matter. In particular, the quadrupole of the redshift-space galaxy correlation function is sensitive to the galaxy (or halo) pairwise infall velocity, which we have seen above can be strongly enhanced by the fifth force in the cvG model. We use haloes (subhaloes) as proxies of galaxies in this study.

The mapping of the halo coordinates from real space to redshift space is given by,

$$\mathbf{s} = \mathbf{r} + \frac{\mathbf{v}(\mathbf{r}) \cdot \hat{z}}{a\mathcal{H}}\hat{z}, \tag{3.22}$$

where $\hat{z}$ is the unit vector in the line of sight direction which we have chosen to be along the z-axis of the simulation box, assuming that the

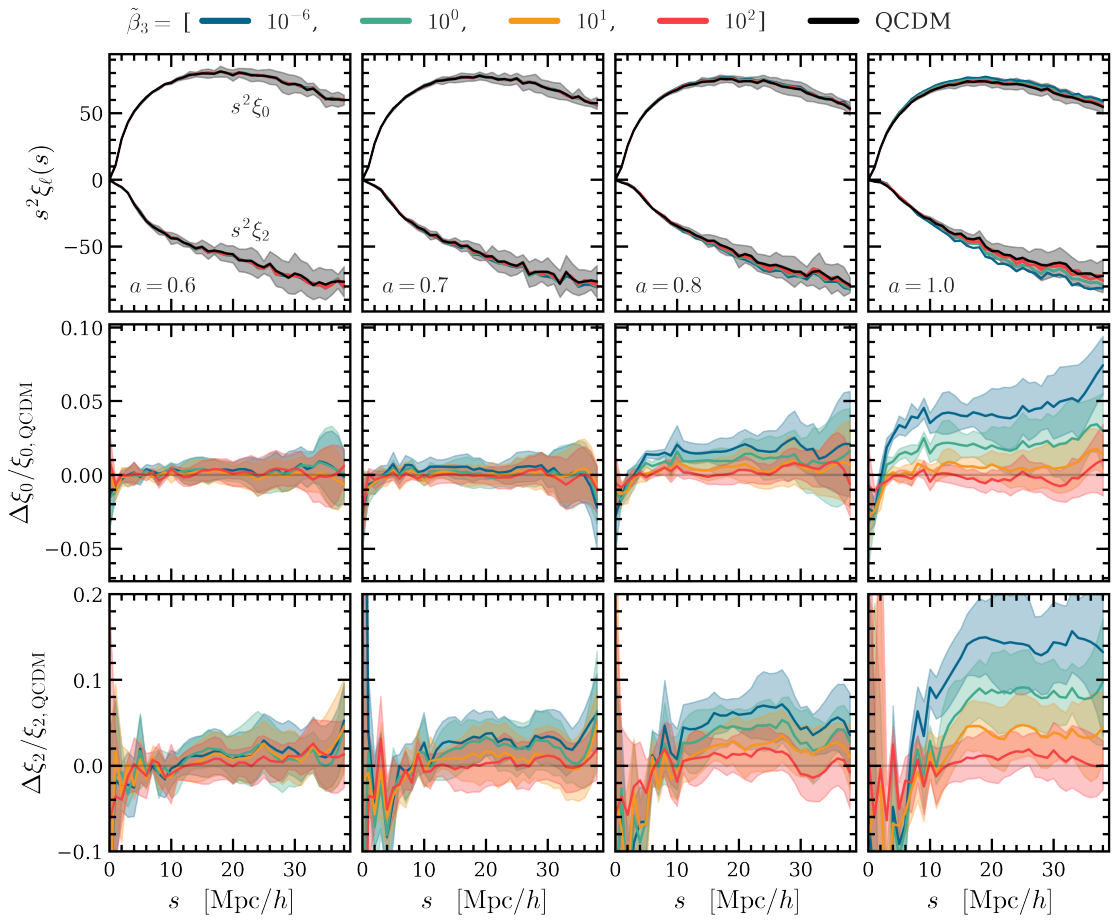

Figure 3.9: *Top*: the monopole, ξ^{s}_0, and quadrupole, ξ^{s}_2, moments of the 2PCF in redshift space. The results are obtained by averaging over the five simulations for each cosmology (solid lines) and shaded region show the standard deviation over these realization, which we show only for QCDM to maintain clearness. We have not shown the cvG results to prevent the plot from appearing cluttered. *Central and bottom*: the relative differences of ξ^{s}_0 and ξ^{s}_2 respectively. Each column shows the results for a different scale factor: *outer left*: $a = 0.6$, *inner left*: $a = 0.7$, *inner right*: $a = 0.8$, *outer right*: $a = 1.0$.

galaxies are far away from the observer (*plane-parallel* approximation). Thus, the anisotropic correlation function is given by

$$\xi^{\mathrm{s}}(s,\mu) = \langle \delta(\mathbf{x})\delta(\mathbf{x}+\mathbf{s})\rangle, \tag{3.23}$$

where $\mathbf{s}$ is the halo separation vector, s its magnitude, $s_\parallel$ the halo separation along the line of sight direction, and $\mu = \cos(s_\parallel/s)$ is the cosine of the angle between $\mathbf{s}$ and the LOS. We measure $\xi^{\mathrm{s}}(s,\mu)$, using `SUBFIND`-halos for the same reason stated in the previous section, over 40 bins of $\mu = [0,1]$ and 40 bins of $s = [0,40]$ h/Mpc. In order to increase the SNR ratio, it is helpful to project $\xi^{\mathrm{s}}(s,\mu)$ onto a one-dimensional object which depends on s only. Therefore, we decompose the measured $\xi^{\mathrm{s}}(s,\mu)$ into

multipole moments using its Legendre expansion,

$$\xi^{\rm s}(s,\mu) = \sum_\ell \xi^{\rm s}_\ell(\mu) L_\ell(\mu), \tag{3.24}$$

where ℓ is the order of the multipole and $L_\ell(\mu)$ is the Legendre polynomial at the ℓ-th order. Inverting Eq. (3.24) and integrating over μ, we find

$$\xi^{\rm s}_\ell(s) = \frac{2\ell+1}{2}\int_{-1}^{1} {\rm d}\mu \xi^{\rm s}(s,\mu) L_\ell(\mu). \tag{3.25}$$

As the redshift space correlation function is symmetric in μ, only even values of ℓ give a non-zero contributions. Of these, we study the two lowest multipoles: the monopole ($\ell = 0$), and the quadrupole ($\ell = 2$). We omit higher order multipoles ($l \geq 4$), as they do not have a big impact on the estimation of the correlation function and are noisier than the monopole and quadrupole [105].

In the top row of Fig. 3.9, we show the monopole, $\xi^{\rm s}_0$, and quadrupole, $\xi^{\rm s}_2$, moments of the QCDM model, at $a = 0.6$ (outer left), 0.7 (inner left), 0.8 (inner right) and 1.0 (outer right). We limit the study to scales $< 40\,h/{\rm Mpc}$ which is roughly $1/10$ of the simulation box size. We know, however, that the peak position of the baryon acoustic oscillations (BAO) will be affected by the cvG model, as $\tilde{\beta}_3 \to \infty$ converges to QCDM and $\tilde{\beta}_3 \to 0$ converges to the cosmology of the csG, both being different from ΛCDM. The csG model is known to be unable to reproduce the BAO position [64, 154, 65] (see however [19]).

The central and bottom rows of Fig. 3.9 show the relative differences between the cvG models and their QCDM counterpart, for the monopole and quadrupole, respectively. Both show the suppression of the fifth force due to the Vainshtein screening on small scales, $r \lesssim 10 h^{-1}{\rm Mpc}$, resulting in their respective reduction of the enhancement with respect to QCDM. As it has been the case for ξ and $v_{\langle ij\rangle}$, the relative difference of the cvG model to its QCDM counterpart increases with a decreasing value of $\tilde{\beta}_3$ especially on scales $> 20\,h/{\rm Mpc}$, due to the higher growth rate and stronger matter fluctuations, both of which are con-

sequences of the enhanced gravitational force. This implies that with decreasing $\tilde{\beta}_3$ the contours of the two-dimensional 2PCF in redshift space, $\xi^{\rm s}(s_\parallel, s_\perp)$, are more squashed, as could already be anticipated from the results shown in Fig. 3.2. The scales below $20\,h/\mathrm{Mpc}$ are in principle observable using galaxy clustering measurements from galaxy surveys. However, to accurately model galaxy clustering from the halo clustering shown here, and hence to constrain the cvG model using real observations, requires a dedicated study which will be left for the future. In this work, we only show the qualitative behaviours of the few models simulated. The values of $\Delta\xi_2/\xi_{2,\rm QCDM}$ converge on large scales for each cvG model to approximately the same values as for $\Delta v_{\langle ij\rangle}/v_{\langle ij\rangle,\rm QCDM}$. The median SNR at $a = 1$ (outer right panel), taken over the range $20 < s/(\,h/\mathrm{Mpc}) < 40$, is approximately equal up to 7.2 for the monopole and 3.5 for the quadrupole for the strongest cvG model $\tilde{\beta}_3 = 10^{-6}$. Although the relative difference is larger in the quadrupole, the SNR values are larger for the monopole, which is because the quadrupole is sensitive to the pairwise infall velocity $v_{\langle ij\rangle}$, which has a larger scatter than the real-space correlation function (see Figs. 3.8 and 3.7) that dominates the monopole signal. The RSD quadrupole can be a more promising probe to constrain the cvG model if the statistical uncertainties can be reduced by large amount of data.

3.4.5 Concentration-mass relation

For dark matter haloes, the strongest effect of Vainshtein screening is perhaps in the density profiles. This is because the interiors of haloes are expected to be strongly screened, see e.g., [84, 85, 114]. The Vainshtein screening radius can be even larger in the csG model and cvG models with $\tilde{\beta}_3 \to 0$, than in the DGP model at late times [26], so we expect the screening to be strong and the internal properties of haloes protected by it from the influence of the fifth force.

The density distribution inside dark matter halos is well described by

the universal Navarro-Frenk-White (NFW; [156, 157]) profile,

$$\rho_{\rm NFW}(r) = \frac{\rho_s}{r/R_s\,(1+r/R_s)^2}, \tag{3.26}$$

where ρ_s and R_s are the characteristic density and scale radius respectively, which can vary from halo to halo. Thus the halo mass, M_{200c}, can be obtained by integrating the NFW density profile

$$M_{200c} = \int_0^{R_{200c}} 4\pi r^2 \rho(r) {\rm d}r = 4\pi\rho_s R_{200c}^3 f\left(c_{200}\right), \tag{3.27}$$

where we have defined the function

$$f(x) = \ln(1+x) - \frac{x}{1+x}, \tag{3.28}$$

and the concentration parameter,

$$c_{200} \equiv \frac{R_{200c}}{R_s}, \tag{3.29}$$

which describes the steepness of the density profile. Using Eq. (3.26), we can relate ρ_s to c_{200}, and therefore the NFW profile can be fully parametrised using M_{200} and c_{200}. Here we use the publicly available phase-space friends-and-friends code ROCKSTAR [27] to calculate the halo concentrations. ROCKSTAR solves the concentration using the following equation:

$$\frac{GM_{200c}}{R_{200c}} \frac{c_{200}}{f\left(c_{200}\right)} = v_{\rm max}^2 \frac{2.163}{f(2.163)}, \tag{3.30}$$

where $v_{\rm max} = \sqrt{GM(<R_{\rm max})/R_{\rm max}}$ is the maximum circular velocity inside a halo, which occurs at $r = R_{\rm max} \simeq 2.163 R_s$ for an NFW density profile. Note that we do not attempt to do a full fitting of the NFW profile Eq. (3.26) for individual haloes in this work.

The top row of Fig. 3.10 shows the halo concentration-mass relations at $a = 0.6$ (outer left), $a = 0.7$ (inner left), $a = 0.8$ (inner right), and $a = 1.0$ (outer right). To ensure accurate measurements, we have excluded all

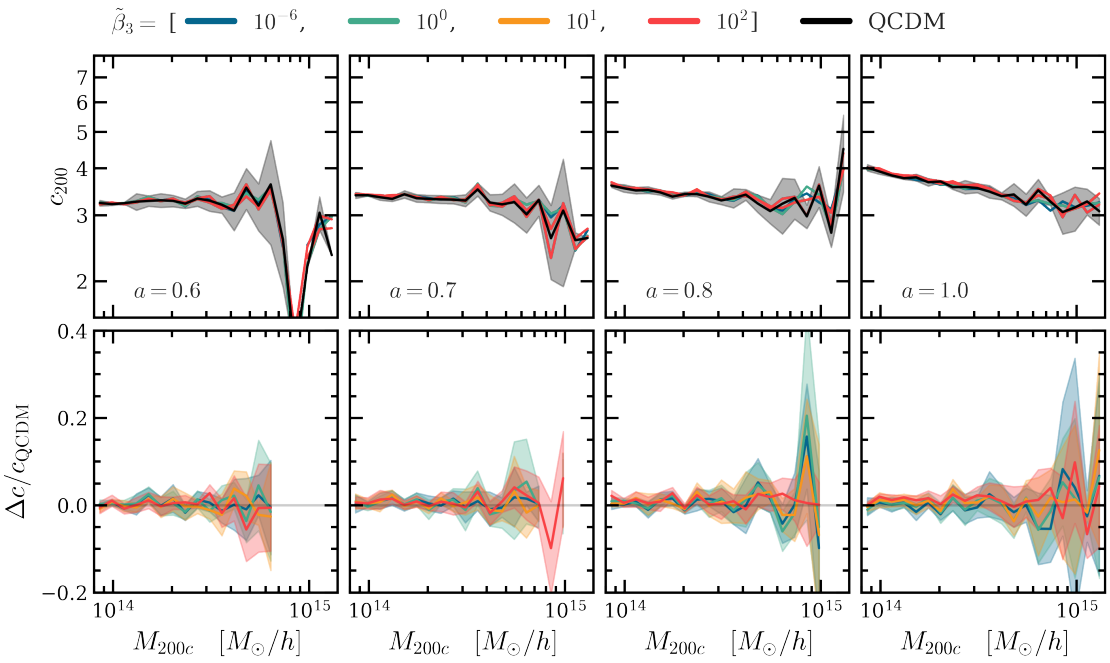

Figure 3.10: The top panels show the relationship between halo mass, M_{200c}, and the NFW definition of halo concentration, c_{200} for the QCDM model (the results for the cvG variants are not shown here because they are very close to the QCDM one). The bottom panels show the relative differences of the cvG models to QCDM, $\Delta c / c_{\rm QCDM} = (c_{\rm cvG} - c_{\rm QCDM}) / c_{\rm QCDM}$. Each column shows the results for a different scale factor: *outer left*: $a = 0.6$, *inner left*: $a = 0.7$, *inner right*: $a = 0.8$, *outer right*: $a = 1.0$. The results shown are obtained by averaging over the 5 independent realisations of simulations, and the shaded region show the standard deviation over these realisations. We do not show the results for $M_{200} \gtrsim 1.5 \times 10^{15} M_\odot/h$, since in this mass ranges there are only a few haloes.

haloes with fewer than 1000 simulation particles from this figure which, combined with the small box size of our simulations, allows us to analyse the c_{200}-M_{200c} relationship for halo masses that span only one order of magnitude. Nevertheless, we can clearly see that the relationship follows a power law [143, 158, 77]. Note that the statistics is poor at large mass and early times, due to a lack of haloes.

Without the screening mechanism we would expect haloes in a Proca universe to be more concentrated than their counterparts in a QCDM cosmology, since the strength of gravity increases quickly at late times [26], which causes a faster steepening of the gravitational potential inside haloes, attracting more matter to the central region and leading to a steeper density profile [148]. However, in the cvG model, just as for the csG model [21], the Vainshtein screening is by design effective in suppressing any effect of the fifth force, as can be seen from the bottom panels of Fig. 3.10.

3.4.6 Weak Lensing statistics

In the final section we focus on the study of weak-lensing statistics. We start by analysing the lensing convergence field (κ) which can be used together with the matter power spectrum and bispectrum to circumvent the dependence on tracer bias (e.g., [231]), and end with an analysis of the abundances and tangential shear profiles of voids identified from WL maps [56, 59].

3.4.7 Weak lensing convergence and peak statistics

Weak lensing (WL) is governed by the lensing potential, $\Phi_{\rm lens}$, which is given by

$$\Phi_{\rm lens} = \frac{\Phi + \Psi}{2}, \tag{3.31}$$

with Φ and Ψ being the two Bardeen potentials in the metric Eq. (2.19). Φ and Ψ are related to each other through the anistropic stress. At late times, since we neglect matter species such as photons and neutrinos, in the cvG and qcdm models, the anisotropic stress is negligible so that we have $\Phi = \Psi$. Therefore, in the cvG model not only massive particles can feel deviations from GR, but also can massless particles, as the dynamical and lensing potentials are equal and can both be modified substantially in the case of $\tilde{\beta}_3 \to 0$. This is in contrast to some other models of gravity, such as $f(R)$ gravity and the DGP modely, which do not modify the lensing potential directly through a modified Poisson equation.

The relation between κ and $\Phi_{\rm lens}$ and how those quantities are solved 'on-the-fly' during the simulation run time was summarised in Sec. 3.2. Here we would like to be more explicit how Eq. (4.1) is affected by the cvG compared to the QCDM. For the qcdm cosmology we have, in ECOSMOG's code units,

$$\tilde{\nabla}^2\tilde{\Phi}^{\rm QCDM}_{\rm lens} = \tilde{\nabla}^2\tilde{\Phi}^{\Lambda{\rm CDM}}_{\rm lens} = 4\pi G a^2 \delta\tilde{\rho}, \tag{3.32}$$

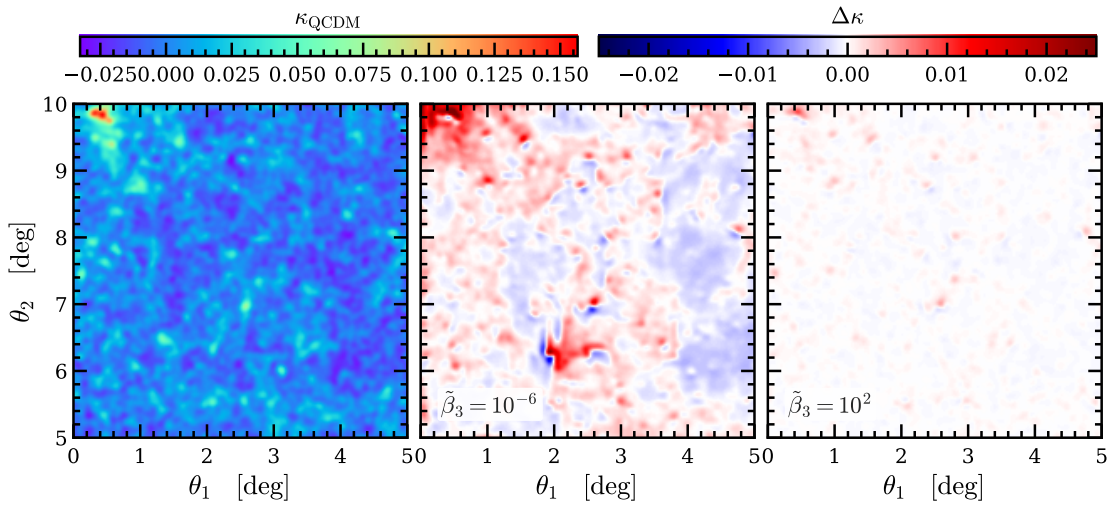

Figure 3.11: We visualise a portion of the κ maps, smoothed by a Gaussian kernel with a width $\theta = 2.5\,\mathrm{arcmin}$, of in qcdm (left), and the difference between the cvG model and their qcdm counterpart with $\Delta\kappa = \kappa(\tilde{\beta}_3) - \kappa_{\rm QCDM}$, for $\tilde{\beta}_3 = [10^{-6}, 10^{2}]$ (centre and right respectively). The maps show the ray tracing results for the redshift range $z = [0.08, 1.0]$. Notice the enhanced clustering in the centre compared to the right panel, indicating that more matter is moved towards (away from) overdense (underdense) regions in cvG cosmologies with smaller $\tilde{\beta}_3$.

where G is the gravitational constant and $\delta\tilde{\rho}$ the density contrast. However, as the expansion history is altered in qcdm compared to ΛCDM their κ field will not be the same. For the cvG model, where the fifth force and screening mechanism are included, the lensing potential is

$$\tilde{\nabla}^2\tilde{\Phi}^{\rm cvG}_{\rm lens} = \tilde{\nabla}^2\tilde{\Phi}^{\Lambda{\rm CDM}}_{\rm lens} + \frac{3\beta_{\rm sDGP}}{2\beta}\alpha\tilde{\partial}^2\tilde{\chi}, \tag{3.33}$$

where $\beta_{\rm sDGP}$ is the coupling strength between matter and the brane-bending mode in the sDGP model, and β and α are given by Eq. (2.64) and Eq. (2.55) respectively. This modification of the lensing potential will modify Eq. (4.1) in the linear regime as

$$\kappa = \frac{1}{c^2}\int_0^{\chi_s}\frac{\chi\,(\chi_s - \chi)}{\chi_s}\left(1 + \frac{\alpha}{\beta}\right)\tilde{\nabla}^2\tilde{\Phi}_{\rm lens,2D}(\chi, \vec{\beta}(\chi))\mathrm{d}\chi, \tag{3.34}$$

in addition to the modified expansion history. Here χ, which is the co-moving distance, should not be confused with the longitudinal Proca mode, $\tilde{\chi}$. This simple rescaling does not account for the effects of the screening mechanism and can only be accurately predicted through simulations as used in this work.

It is important to note here, that we solve the integral of Eq. (3.34) between $z = [0.08, 1.0]$, as we found that artefacts appear for the $\tilde{\beta}_3 = 10^{-6}$ cvG model. The reason behind this might be explained through the failure of numerical computation of the $\tilde{\chi}$ field in under-dense regions. This is a problem which has been reported multiple times [17, 136, 16, 224] and discussed in terms of the cvG model in [26].

The resulting κ map is shown in Fig. 3.11 for qcdm (left), together with the residual between qcdm and the cvG model, $\Delta\kappa = \kappa(\tilde{\beta}_3) - \kappa_{\rm QCDM}$, for $\tilde{\beta}_3 = [10^{-6}, 10^{2}]$ (centre and right respectively). All maps have been

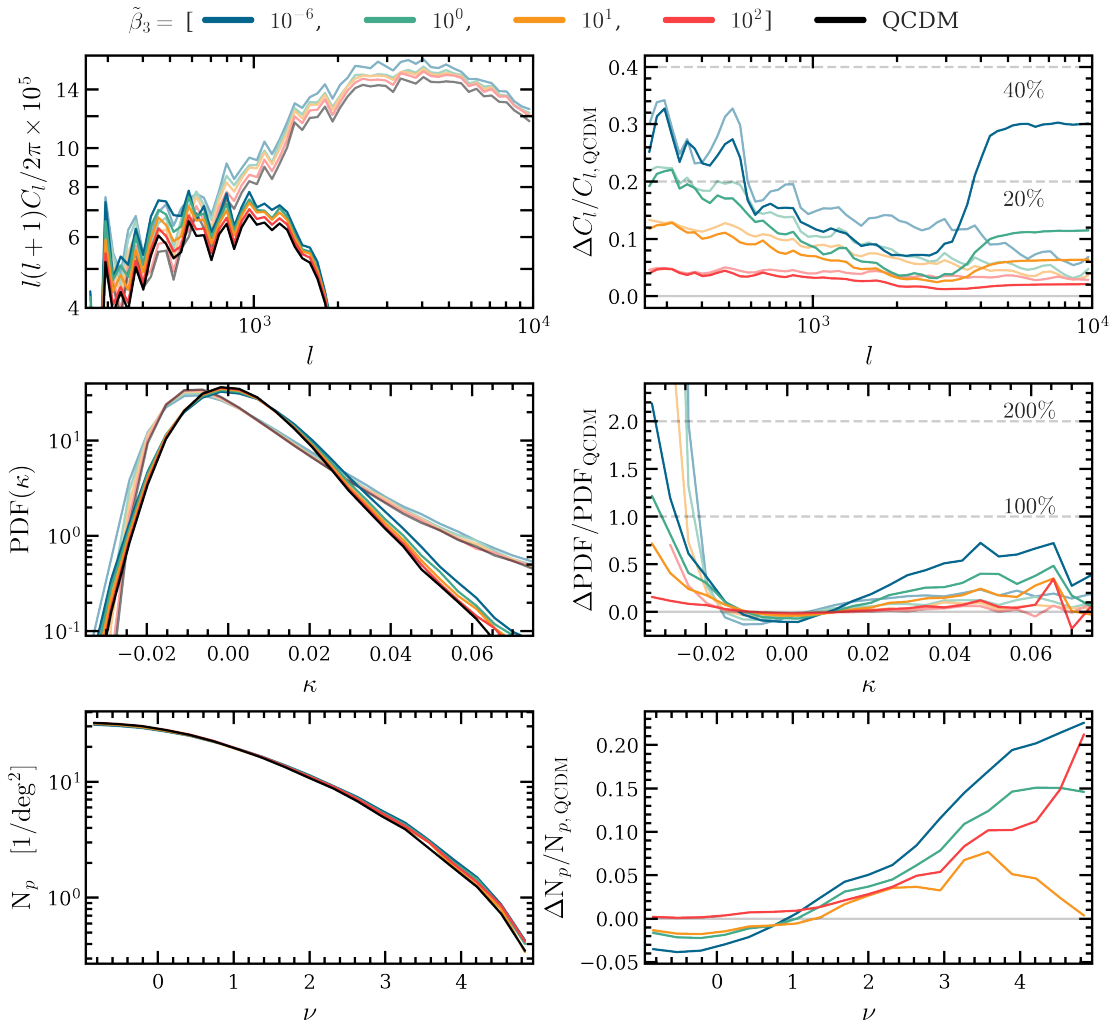

Figure 3.12: Weak lensing statistics: lensing convergence angular power spectra (*top*), probability distribution function of the weak lensing convergence field (*middle*), weak lensing peak abundance plotted as a function of peak height (*bottom*). The results shown here are obtained using a 10×10 deg^2 partial sky-map for a redshift range $z = [0.08, 1.0]$. We show results of the κ maps (faint) and the κ maps including the galaxy shape noise map, $N_{\rm GSN}$, and smoothed with a Gaussian kernel of width $\theta = 2.5\,$arcmin (bright) for the cvG model variants (colour) and their qcdm (black) counterpart.

smoothed with a Gaussian kernel of width $\theta = 2.5\,\mathrm{arcmin}$ which we will abbreviate as S_{G}. It is clearly visible how underdense and overdense regions are more pronounced for $\tilde{\beta}_3 \to 0$ while for $\tilde{\beta}_3 \to \infty$ the model approaches the behaviour of the qcdm cosmology.

In the middle panel of Fig. 3.11 we can see a number of 'dipole' features, where a positive-residual 'hot spot' ($\Delta\kappa > 0$) is aligned with a 'cold spot' ($\Delta\kappa < 0$). This is produced by the transverse (i.e., perpendicular to the line of sight) motion of the halo which contributes most for a given line of sight: for this case the κ peak in the left panel would have moved slightly, causing this dipole feature in the residual map. Such dipoles are harder to find in the right panel, again because for $\tilde{\beta}_3 \to 0$ the model behaves very similarly to QCDM, so that haloes move little compared with the latter case.

Another feature worth mentioning in the middle panel of Fig. 3.11 is that we can see that near the massive structures the convergence field is enhanced by over 10%. This is partly due to the increased halo masses, but most likely the dominant effect here is the fact that the Proca field can also modify the lensing potential, as mentioned above. While we shall not investigate it here, let us note that this means that weak lensing by galaxy clusters can be a potential probe to constrain this model. However, as in the case of csG [23], we expect that the constraining power of cluster lensing may be limited by Vainshtein screening in the vicinity of clusters. We shall see shortly that this strong enhancement of convergence can be detected in the convergence power spectrum (or the shear correlation function) which can probe large-scale variations of the lensing potential.

In observations, the WL signal is obtained by averaging the shearing of source galaxy shapes over a large number of source galaxies whose intrinsic ellipticity dominates over the physical tangential shear signal. This effect is known as galaxy shape noise (Galaxy Shape Noise (GSN)) and is a main source of uncertainty on small angular scales. We include the GSN by modelling it as a Gaussian random field which we will denote as N_{GSN}. Therefore we assume that N_{GSN} is independent of the underly-

ing κ. Furthermore, we assume that the correlation function of $N_{\rm GSN}$ is a δ function, thus pixel values show no correlation. The standard deviation of the Gaussian distribution is given by

$$\sigma^2_{\rm pix} = \frac{\sigma^2_{\rm int}}{2\theta_{\rm pix} n_{\rm gal}}, \tag{3.35}$$

where $\sigma_{\rm int}$ is the intrinsic ellipticity dispersion of the source galaxies, $\theta_{\rm pix}$ is the width of each pixel, and $n_{\rm gal}$ is the measured source galaxy number density. We use $\sigma_{\rm int} = 0.4$ and $n_{\rm gal} = 40\,{\rm arcmin}^{-2}$, which match LSST specifications [3].

The GSN can strongly impact the small-scale features of the lensing map, which is why for noisy maps one usually needs to apply a smoothing, $S_{\rm G}$. The size of the smoothing filter (i.e., the smoothing scale, θ), needs to be carefully chosen so that it is large enough to suppress the noise effects, and small enough to not smooth away too much physical signature. In practice, the smoothing scale needs to be checked for different statistics from the lensing map, and for different noise levels (e.g., different surveys have different source galaxy number densities, which can lead to different levels of noise impact). In this Chapter, because the statistics we analyse and the survey specifications are the same as those of [59], we have applied the same filter as there. Note that in this plot we are showing statistics measured from an ideal lensing map without smoothing and a noisy map after smoothing, the former is just for theoretical interest.

In the top row of Fig. 3.12 we show the results for the power spectrum of the κ maps (faint) and the κ-$N_{\rm GSN}$-$S_{\rm G}$ maps (bright). We do not include the linear theory prediction, as it holds up to $\ell \lesssim 10^2$ and is thus outside of the range of multipoles we are able to extract from the maps. The left panel shows the absolute power spectra measurements for which we have not included the results for $\ell > 10^4$ as such small angular scales are not well-resolved given our simulation resolution. In terms of the relative difference between the cvG models to their qcdm counterpart in the right panel, the curves show the expected behaviour

that, on large angular scales ($\ell < 10^4$), the amplitude is higher in the cvG models with smaller $\tilde{\beta}_3$. However, since we use a partial-sky map of $10 \times 10\,\mathrm{deg}^2$, the power spectra in the left panel could suffer from a large sample variance. This, however, should not strongly affect the result of the relative difference, as it roughly cancels out. As we go to smaller angular scales, $l \to 10^4$, all cvG models converge toward their qcdm counterpart, which reflects the operation of the screening mechanism on small scales, e.g., inside haloes. Note that the smoothed maps behave similarly, though not identically, to the unsmoothed ones at $\ell \lesssim 10^3$, while on smaller angular scales the smoothing significantly changes the model difference. This indicates a potential limitation on using the convergence power spectrum or shear two-point correlation function to test the cvG model, but we note that the large angular scales are where the model difference is most prominent anyway.

The middle row of Fig. 3.12 shows the one-point distribution of the κ maps (faint) and the κ-N_{GSN}-S_{G} maps (bright). It contains information on non-Gaussian aspects of the convergence field that are not included in the convergence power spectra. We can see that cvG models with smaller $\tilde{\beta}_3$ have larger numbers of pixels with both high and low κ values. This behaviour is expected because the fifth force in the cvG models helps to move more matter towards (from) dense (underdense) regions, as can be seen in Fig. 3.11. It is good to see that increasing the $\tilde{\beta}_3$ parameter indeed leads a smooth transition to QCDM, which is what is needed to cure the problem of having too strong a lensing effect in the csG model. The same happens to the void γ_t profiles too, as will be shown in the next subsection.

The bottom row of Fig. 3.12 shows the WL peak abundance for the κ-N_{GSN}-S_{G} maps. This result is useful on its own because WL peak statistics can be a useful cosmological probe (e.g., [119, 74, 192, 139, 141, 58, 88, 53]) but will also be useful for the study of void identified through WL peaks in the next subsection. We identify peaks as pixels whose κ values are larger than those of their eight neighbours. For consistent definitions between the different cosmological models, we define the amplitude of ν

of a map pixel as

$$\nu = \frac{\kappa}{\sigma_{\rm GSN}}, \tag{3.36}$$

where $\sigma_{\rm GSN} = 0.007$ is the standard deviation of the $N_{\rm GSN}$-$S_{\rm G}$ map generated using the LSST specifications given above. From the bottom panels of Fig. 3.12, we can see that for $\tilde{\beta}_3 \to 0$, there is a significant increase in the numbers of the high-amplitude peaks, which indicates that the fifth force strongly enhances the lensing signal of these pixels (note that the fifth force also increases the halo masses as found in Fig. 3.6, which also contributes to this). On the other hand, the abundance of small peaks ($\nu < 1$) is reduced as $\tilde{\beta}_3 \to 0$, because some of the haloes that produce peaks with $\nu < 1$ in qcdm have been able to produce peaks with $\nu > 1$ in the cvG models. This trend agrees qualitatively with results found for the nDGP cosmology [57].

Thus, in this work we only consider voids for their weak lensing and not for other properties that can be used to test gravity. One void statisic that we have not pursued in this work, but which could provide potentially stringent cosmological constraints, is the measurement of RSD around 3D voids (e.g., [102]). This is not studied here mainly due to the small box sizes our simulations, and will be left for future work.

3.4.8 Cosmic voids

Cosmic voids are regions in the Universe where the densities of dark matter or tracers are low. In recent years it has been shown that voids (e.g., [214, 47, 98]) can be a useful probe for a variety of models (e.g., [39, 42, 22, 172, 25, 103, 115, 86, 43, 164, 57, 14, 171, 13, 104]), including the test of modified gravity models that are featured by Vainshtein screening [22, 25, 86, 14]. There are a large number of methods to find voids. Typically, they are identified from the full 3D distribution of matter (traced by tracers such as galaxies), for which void statistics such as their abundance, radial galaxy/matter density profiles and shapes contain useful cosmological information (see, e.g., [222, 92, 36, 39, 129]). Recently, it

has been argued that void identification based on WL convergence maps can lead to the better constraints of certain modified gravity theories [57].

This has motivated us to use voids from the two dimensional convergence field through the tunnel and watershed algorithms as the resulting void catalogues have been shown to be amongst the most promising [59].

Whilst the convergence profiles of voids allow for a simpler physical interpretation of the mass content, where positive and negative κ correspond to projected over-dense and under-dense regions, it is the tangential shear which can be measured directly in observations. Therefore, to offer a more straightforward comparison with observations, we study the void tangential shear profile $\gamma_t(r)$, which is related to the convergence profile through

$$\gamma_t(r) = \bar{\kappa}(< r) - \kappa(r), \tag{3.37}$$

where

$$\bar{\kappa}(< r) = \frac{1}{\pi r^2} \int_0^r 2\pi r' \kappa(r') dr', \tag{3.38}$$

is the mean enclosed convergence within radius r.

Tunnels

The tunnel algorithm of [43, 56, 57] identifies voids based on a WL peaks catalogue. We will from now on refer to these voids as tunnels. We find peaks using the κ map smoothed by a compensated Gaussian kernel wither an inner kernel width of $\theta_{\rm inner} = 2.5\,\rm arcmin$ and a outer kernel width of $\theta_{\rm outer} = 15\,\rm arcmin$, which we will abbreviate as $S_{\rm cG}$. The use of $S_{\rm cG}$ instead of $S_{\rm G}$ is motivated by the larger number of identified peaks, which again will results in more identified tunnels and thus better statistics. Each identified peak is placed into three categories based on Eq. (3.36): $\nu > [1, 2, 3]$. For each category, a Delaunay tessellation

with the peaks at the vertices is constructed. This produces a tessellation of Delaunay triangles, with a peak at the corner of each triangle, and no peaks within the triangles. Each Delaunay triangle is then used to construct its corresponding circumcircle, with the three vertices of the triangle falling on the circumcircle's circumference. This unique tessellation, by definition, produces circles which do not enclose any peaks. In order to increase the number of tunnels, which is necessary because of the small area of our convergence maps, we use all possible tunnels, including neighbouring ones which have a large degree of overlap in our study.

The top row of Fig. 3.13 shows the tunnel size distribution identified from peak catalogues of different significance: $\nu > 1$ (left), $\nu > 2$ (centre), and $\nu > 3$ (right). The smallest tunnels are generated by the $\nu > 1$ peak catalogue, which also produces the most tunnels, because the large number of peaks in this catalogue tends to partition the map into smaller Delaunay triangles. As the ν threshold increases, the typical tunnel size increases, however there are also fewer tunnels overall. This

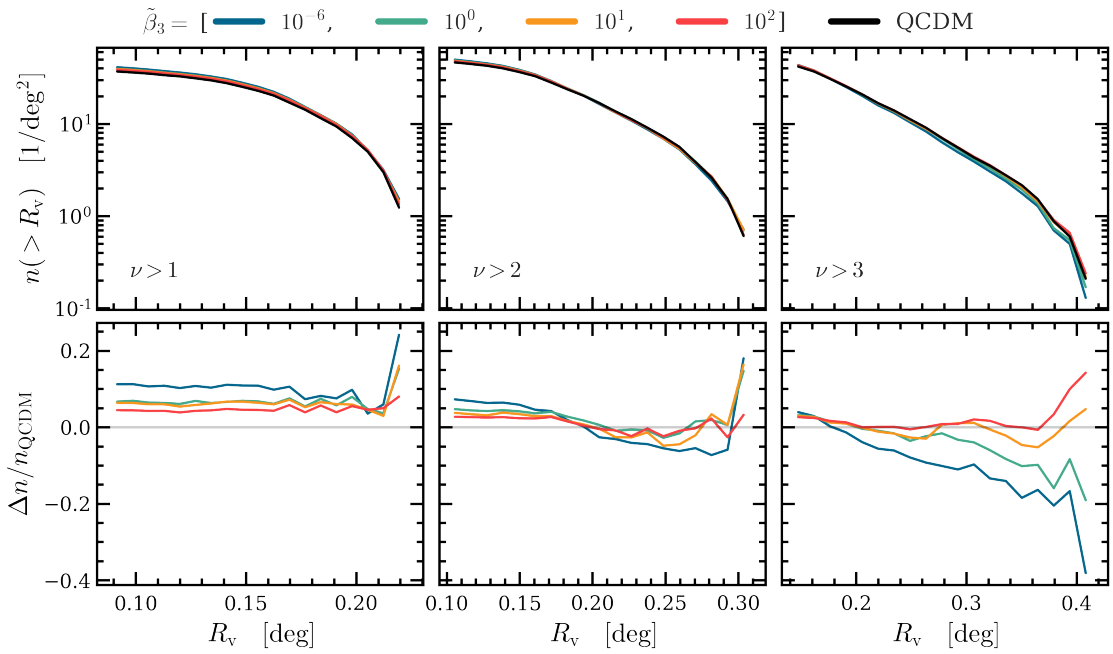

Figure 3.13: *Top*: the tunnel abundance as a function of their radii for the three WL peak categories: *left*: $\nu > 1$, *centre*: $\nu > 2$, *right*: $\nu > 3$. *Bottom*: relative difference between the cvG cosmologies and their qcdm counterpart.

implies that each of the three categories should respond differently to the large scales modes of the κ map, and thus creating the tightest constraints through combined analyses. Due to our small sample size, this remains to be tested.

The bottom row of Fig. 3.13 shows the relative difference between the cvG models and their qcdm counterpart. It is interesting to observe, that while smaller tunnels ($R_{\rm v} \lesssim 0.2$ deg) are more abundant in cvG with $\tilde{\beta}_3 \to 0$ than in qcdm it is vice versa for larger voids ($R_{\rm v} \gtrsim 0.2$ deg). This is a consequence of a higher abundance in WL peaks for the cvG cosmologies compared to their QCDM counterpart for all of our peak categories, see Fig. 3.12. The high abundance leads to the brake up of large voids into smaller ones, resulting in more small voids and fewer large voids in the cvG models.

Fig. 3.14 shows the tangential shear profiles, Eq. (3.37), of the three tunnel catalogues shown in Fig. 3.13. The profile are based on the κ-$N_{\rm GSN}$ maps, as smoothing would dampen the void profiles and the dif-

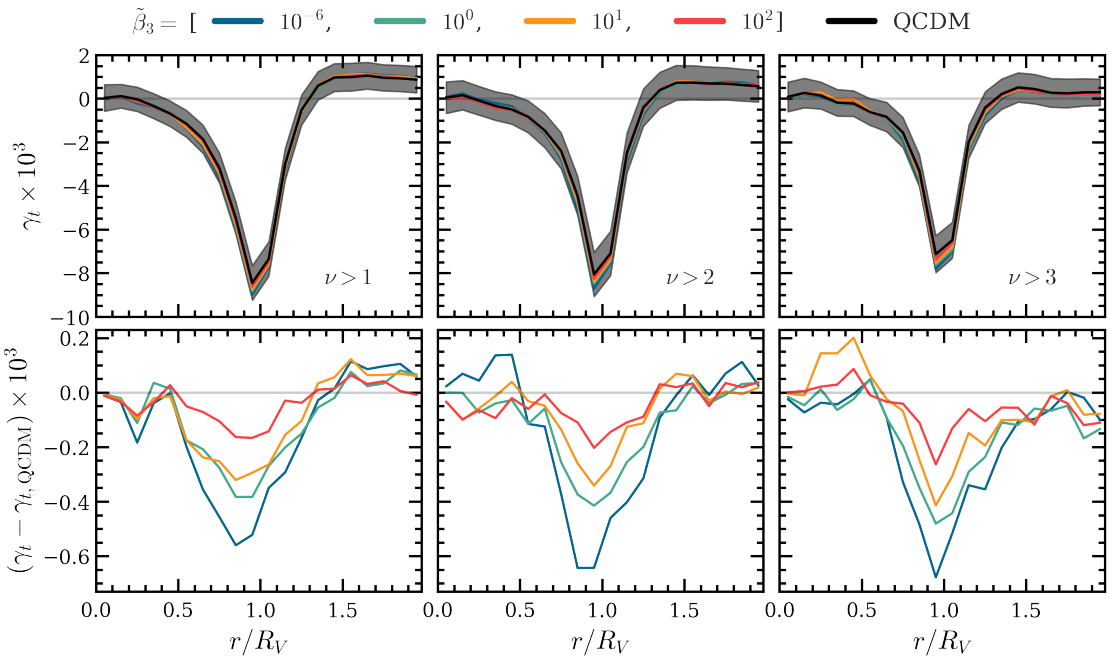

Figure 3.14: *Top*: Tunnel tangential shear profiles as a function of the scaled distance from the centre, $r/R_{\rm v}$, for qcdm (black) and cvG models with $\tilde{\beta}_3 = 10^{-6}$ (blue), 10^0 (green), 10^1 (orange) and 10^2 (red). The shaded region indicates the standard deviation of all tunnels in the qcdm map (for clarity we do not show this for the other models). The shaded region indicates the standard deviation. *Bottom*: The relative difference between the cvG models and their qcdm counterpart. From left to right the panels are respectively for tunnels identified from peak catalogues with peak height $\nu > 1, 2$ and 3. We do not show the standard deviation as they very large due to our small sample size.

ferences between the cosmological models. We compute the γ_t profiles statistics by stacking all voids in a given catalogue, weighting them depending on their size (the smaller the void, the less its statistical weight). This is done, since larger voids are better resolved, as they cover more pixels of the weak lensing map and more source galaxies. To obtain the 1-σ error, indicated by the shaded region in the top row, we loop through 100 bootstrap resamples. We recover the typical tangential shear profile, which indicates that voids act as concave lenses. The extrema of the profile is located at $r \approx R_\mathrm{v}$ for all void categories and is increasing as the void sizes increase.

In the bottom row of Fig. 3.14 we can clearly see that the potential well get deeper as $\tilde{\beta}_3 \to 0$, reflecting the effects of enhanced structure formation and modified photon geodesics. We do not show the bootstrapped 1-σ error for the relative differences, as our sample size is too small.

Watershed

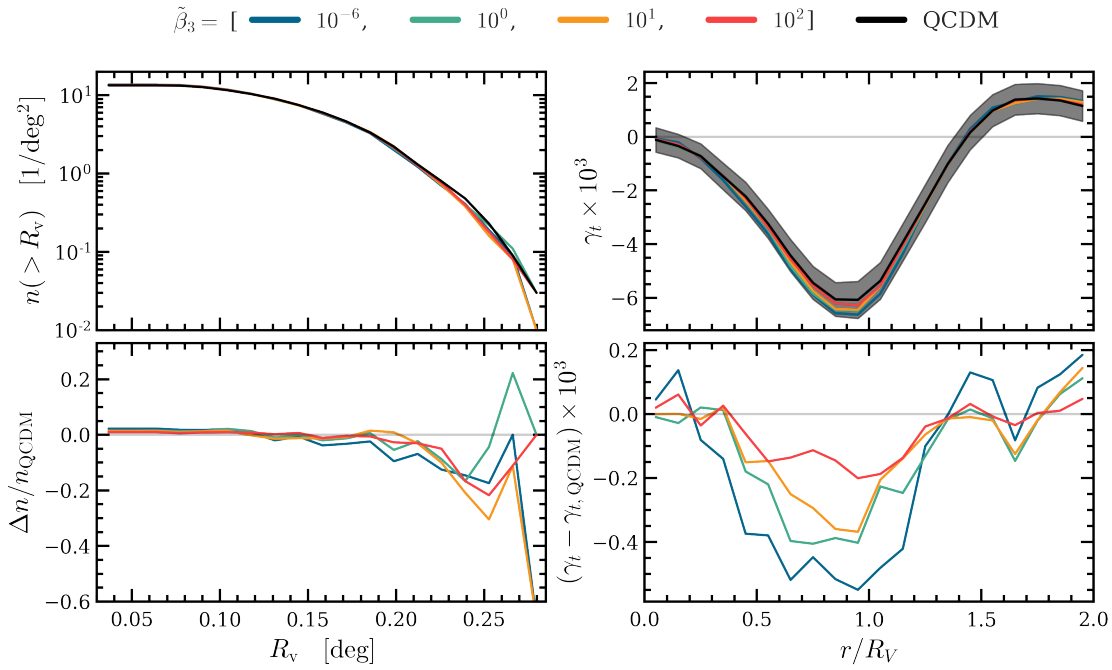

Figure 3.15: Statistics for the watershed voids. *Left*: the cumulative void abundance as a function of the effective radius of the watershed voids, R_v. *Right*: the tangential shear signal of these voids, as a function of the scaled radius from void centre, r/R_v. The upper panels show the results for qcdm (black) and cvG models with $\tilde{\beta}_3 = 10^{-6}$ (blue), 10^0 (green), 10^1 (orange) and 10^2 (red), while the lower panels show the relative (for the void abundance) and absolute (for the tangential shear profile) differences between the cvG models and their qcdm counterpart. The shaded region in the top row indicates the standard deviation of all profiles in the qcdm model.

The watershed algorithm of [174] identifies voids based on the basins in the topographic map which is constructed from the κ map. To find the watershed basins, each pixel of the κ map is connected to its neighbour with the lowest κ value – a process that is repeated for successive neighbours until a local minimum emerges. All pixels connected to the same minimum in this way form one watershed basin, with ridges of local high κ values along the basin boundary. We could have used the WL peak catalogues to identify watershed voids, as is done for tunnels, but the results are generally very noisy [59]. To mitigate the impact of GSN, [59] found that the height of the basin boundary should have a minimum κ value of $h_{\rm boundary} = \sigma_{\rm GSN}/2$. This means, that in our analysis we define the merge criteria as follows: we compare the average amplitude of each basin boundary with the amplitude of their corresponding minima. If the absolute difference in amplitude between the two is less than $h_{\rm boundary}$, we merge that basin with its neighbour, which creates a single larger basin. This choice of $h_{\rm boundary}$ allows watershed basins, that have been artificially split by spurious structures introduced by GSN, to be re-merged. The impact of varying $h_{\rm boundary}$ on our results was tested in [59] and found to have little impact on the obtained void profile statistics. Unlike tunnels, the watershed voids are formed by a collection of Delaunay cells, and therefore have irregular shapes. We define the void centre to be the barycentre of all selected cells for a given watershed void, and the void radius $R_{\rm v}$ as the radius of a sphere whose volume is equal to that of the void. The watershed algorithm has the advantage of simplicity from fewer free parameters in the void identification process, since no tracers are used, multiple WL peak catalogues do not need to be defined. However, Ref. [59] also find that tangential shear profile from the watershed algorithm is more susceptible to GSN than the tunnel algorithm.

The left column of Fig. 3.15 shows the watershed void abundance as a function of the void radius, $R_{\rm v}$, and the relative difference between the cvG models and QCDM. In contrast to tunnels, there are overall fewer watershed voids, and they never reach the large void size as tunnels do.

This is because watershed voids by definition cannot overlap. Among the different models, little difference is found, apart from the large-$R_{\rm v}$ end, where the cvG models produce up to $\sim 20\%$ fewer voids than QCDM. The main reason for this is a change of void sizes, rather than a decrease in their number. This is likely due to the enhanced κ field magnitude in local overdensities residing in larger underdense regions, which means that these structures would more easily have $\kappa > \sigma_{\rm GSN}/2$ and therefore become basin boundaries in the cvG models, leading to a split of a large waterbasin into smaller ones.

The right column of Fig. 3.15 shows the tangential shear profiles, $\gamma_t(r)$, of watershed voids and their relative difference between the cvG models and their qcdm counterpart. They are smoother, wider, and shallower compared to all tunnel categories. However, both tunnels and watershed voids reach their tangential shear profile minimum at $0.9 - 1.1\,R_{\rm v}$. The error bars on the qcdm tangential shear profiles from the two algorithms are also similar in size, which suggests that both algorithms may offer similar constraining power, consistent with Ref. [59] which finds roughly similar tangential shear signal-to-noise ratios between the two algorithms. The relative differences between the cvG models and their qcdm counterpart peak at the minimum of the profile, with a 10% difference for cvG with $\tilde{\beta}_3 = 10^{-6}$, roughly the same as the relative difference found for tunnels in the same size range (which is the tunnel category for $\nu > 1$).

3.5 Discussion and conclusions

In this Chapter, we have performed a thorough phenomenological study of a simplified version of the GP theory, the vector Galileon model (cvG). To study the impact of the cvG model's free parameter, $\tilde{\beta}_3$, we have run a set of five realizations of simulations for $\tilde{\beta}_3 = [10^{-6}, 10^0, 10^1, 10^2]$ and their qcdm counterpart, resulting in a total of 25 simulations. The study relied on an adapted version of the ECOSMOG N-body code augmented with the ray-tracing modules of the Ray-RAMSES algorithm. We used the

five independent realisations for each model to create a light cone that covers a field of view of $10 \times 10\,\mathrm{deg}^2$ from $z = 0.08$ to a source redshift of $z = 1$ (cf. Sec. 3.2 and Fig. 3.1). This allows us to study the matter, halo, weak lensing and voids statistics. In the following we shall summarise the results of each those three topics.

The study of dark matter field statistics finds good agreement with [26] about the *matter power spectrum* ($P_{\delta\delta}$, cf. Sec. 3.3.1 and Fig. 3.2), but extends the results of that Chapter by including larger scales and showing statistical uncertainties. In addition:

- the simulation measurements of the *velocity divergence power spectrum* ($P_{\theta\theta}$, cf. Sec. 3.3.1 and Fig. 3.3) converge to the linear-theory prediction on scales $k \lesssim 0.1h^{-1}\mathrm{Mpc}$ for all times, while for $k \gtrsim 0.1h^{-1}\mathrm{Mpc}$ we reproduce the well-known result that $P_{\theta\theta}$ is suppressed compared to the linear theory results. The relative difference, $\Delta P_{\theta\theta}(k) / P_{\theta\theta,\mathrm{QCDM}}(k)$, shows that the wavenumber at which linear theory and simulation results agree reasonably, k_*, is pushed to ever larger scales as $a \to 1$ and $\tilde{\beta}_3 \to 0$. Finally, for $a \to 1$ and $\tilde{\beta}_3 \to 0$ we see a growing peak that for the case of $\tilde{\beta}_3 = 10^{-6}$ protrudes above the linear theory prediction at $k \sim 0.7\,h^{-1}\mathrm{Mpc}$. A similar feature was also observed by [137] for the DGP model.

- for the *matter bispectrum* (B, cf. Sec. 3.3.2 and Figs. 3.4, 3.5), we find that the magnitudes depend on the triangle configurations, and increase in the order of equilateral, squeezed, and folded triangle configurations. However, this order is reversed when considering the relative difference. The relative difference confirms that, as it is the case for $P_{\delta\delta}$ and $P_{\theta\theta}$, the tree-level bispectrum is a good estimator on large scales $k < k_* \sim 0.1\,h^{-1}\mathrm{Mpc}$, while the exact value of k_* decreases with $a \to 1$ and $\tilde{\beta}_3 \to 0$. We show that the enhancement of the bispectrum due to the fifth force is marginally stronger than in the case of power spectrum, but the reduced bispectrum shows that B / B_{QCDM} is to a very good approximation equal to $\left(P / P_{\mathrm{QCDM}}\right)^2$. The scales at which we are able to measure the bispectrum do not show a strong signature of the Vainshtein screening.

The study of halo statistics is mostly based on SUBFIND cagalogues, as they contain the smallest haloes and subhaloes and thus can enable measurements to smaller scales, although where possible we have also cross-validated the results with FOF haloes. The main observations are the following:

• the *halo mass function* ($n(> M)$, cf. Sec. 3.4.1 and Fig. 3.6) shows that the fifth force enhances the abundance of dark matter haloes in the entire mass range probed by the simulations, with the enhancement stronger at late times and for high-mass haloes. Models with a weaker fifth force, e.g., with $\tilde{\beta}_3 \to \infty$, show a more restrained enhancement of the HMF.

• the *two-point correlation function* ($\xi(r)$, cf. Sec. 3.4.2 and Fig. 3.7) shows more strongly enhanced clustering for smaller values of $\tilde{\beta}_3$, for which the fifth force is stronger. The enhancement of the halo $\xi(r)$ is nearly constant down to $\sim 3\ h/\mathrm{Mpc}$, consistent with $P_{\delta\delta}$, and reflecting the fact that in the cvG model the growth factor is enhanced in a scale-independent way in the linear regime. However, the enhancement in halo clustering is weaker than in matter clustering, for all models at all times.

• the relative difference of the *mean halo pairwise velocity* ($v_{\langle ij \rangle}$, cf. Sec. 3.4.3 and Fig. 3.8) remains constant for all cvG models at scales $r > 10\ h/\mathrm{Mpc}$, in very good agreement with linear-theory prediction. For the latter, we have measured the halos bias, b, for four different scale factors through the relation between the halo and matter correlation functions. The resulting measurements of b for the different models are similar, but show a slight decrease as $\tilde{\beta}_3 \to 0$, as the fifth force enhances matter clustering more than halo clustering, as mentioned above.

• the *redshift space halo clustering* ($\xi_\ell(s)$, cf. Sec. 3.4.4 and Fig. 3.9) is sensitive to the halo pairwise velocity and hence the fifth force. The relative difference between cvG and qcdm can be up to ~ 3 times larger for the quadrupole, $\xi_2(s)$, than for the monopole, $\xi_0(s)$, although its SNR is ~ 0.5 times smaller on the range $20 < s\,h^{-1}\mathrm{Mpc} < 40$ due to larger statistical uncertainly in the halo velocity field. Future data of redshift

space distortions should provide strong constraints on $\tilde{\beta}_3$.

• the result of the *halo concentration-mass relation* (c_{200}, cf. Sec. 3.4.5 and Fig. 3.10) shows that in the cvG model, just as for the csG model, the Vainshtein screening is strong enough inside haloes that there is little effect of the fifth force.

Our final section concerns the properties of the weak lensing convergence, peak and void statistics, where voids are identified using the tunnel and watershed algorithms. The main results are the following:

• the difference of the *convergence map* (κ, cf. Sec. 3.4.7 and Fig. 3.11) between qcdm and cvG for $\tilde{\beta}_3 = 10^{-6}$ shows that around massive structures the convergence field is enhanced by over 10%. However, we caution about taking this as an indication that weak lensing by galaxy clusters can be a potential probe to constrain this model, as we have not performed an analysis of stacked weak lensing convergence profiles.

• the relative difference of the *angular power spectrum* (C_ℓ, cf. Sec. 3.4.7 and Fig. 3.11) is largest on linear scales $\ell \lesssim 3 \times 10^2$, reaching $\sim 30\%$ for $\tilde{\beta}_3 \to 0$. These scales are also where the smoothing of the map has little impact on the relative difference. For higher multipoles the model differences reduce.

• the relative difference of the *probability distribution function of* κ ($\mathrm{PDF}(\kappa)$, cf. Sec. 3.4.7 and Fig. 3.11) shows that cvG models with $\tilde{\beta}_3 \to 0$ have more pronounced under- and overdense regions.

• the relative difference of the *weak lensing peak abundance* (N_p, cf. Sec. 3.4.7 and Fig. 3.11) shows larger (smaller) numbers of high- (low-)amplitude peaks for $\nu > 1$ ($\nu < 1$) in the cvG models with $\tilde{\beta}_3 \to 0$, because the fifth force enhances the convergence values of the peak pixels.

• the relative difference of the tunnel and watershed *void abundances* ($N(> R_\mathrm{v})$, cf. Sec. 3.4.8 and Fig. 3.13, 3.15) shows fewer large-sized voids in the cvG cosmologies compared to their qcdm counterpart, since they produce more weak lensing peaks which splits large voids into smaller ones (for the tunnel case), or increase the convergence values so that the regions satisfying the chosen void definition criterion shrink in size (for

the watershed case).

• the relative difference of the *tangential shear profile* for tunnels and watershed voids (cf. Sec. 3.4.8 and Fig. 3.14, 3.15) peak at approximately the void radius, with up to 10% difference for the cvG model with $\tilde{\beta}_3 = 10^{-6}$ (similar to what has been observed in the convergence maps), and the model difference decreases as $\tilde{\beta}_3 \to \infty$.

Overall, we find that for the cvG model studied here, the fifth force effect is strongest on velocity and lensing statistics. The former is because velocity is the first integration of acceleration, and thus reacts quickly to the enhancement of gravity due to the fifth force, which happens only at late times; the matter density field, in contrast, reacts more slowly as the second integration of acceleration. The latter is because in the cvG model, unlike for some other MG models, photon geodesics are affected in two different ways: (1) indirectly, by the modified growth of matter fluctuations, and (2) directly, by the fifth force. This suggests that redshift space distortions and weak lensing shear correlation functions can both be promising cosmological probes to constrain the $\tilde{\beta}_3$ parameter in this model. On small scales, the models are generally more difficult to constrain because the screening mechanism suppresses the fifth force effect; for example, internal properties of haloes, such as the concentration-mass relation, are insensitive to the fifth force. Another potentially useful way to constrain this model is by cross-correlating galaxies with the integrated Sachs-Wolfe effect [154], because as $\tilde{\beta}_3 \to 0$ the fifth force becomes stronger, causing the lensing potential to getting deeper rather than shallower [26] as suggested by observations. This possibility will be investigated in future. What is a bit surprising is that weak lensing by voids do not seem to be as promising a probe, even though the lensing potential is significantly modified in low-density regions: perhaps this is because weak lensing is a cumulative effect along the line of sight, and this strong effect in low-density regions is somehow cancelled out by the weaker effects in high-density regions. However, this conclusion only applies to voids found from the lensing maps. It will be of interest to look at the properties of the 3D voids found from halo or mock galaxy

catalogues, especially the redshift-space distortion around them, using larger-volume simulations in a future work.

Recently, various studies to constrain the GP theory using cosmological observations have been conducted, see, e.g., [64, 65, 111]. These studies focused on general nonlinear functional forms for $G_{2,3}$, because linear forms of these functions, such as the models studied here, have been found as a poor fit to observational data. However, as suggested by [26], adding massive neutrinos with significantly nonzero mass (see, e.g., [19]) may be a way to make the GP model with linear $G_{2,3}$ agree better with data. This possibility will be studied in a follow-up work, and correspondingly we hope to include massive neutrinos in future simulations.

4

The impact of line-of-sight structures on measuring H_0 with strong lensing time-delays

Measurements of The Hubble-Lemaître constant from early- and local-universe observations show a significant discrepancy. In an attempt to understand the origin of this mismatch, independent techniques to measure H_0 are required. One such technique, strong lensing time delays, is set to become a leading contender amongst the myriad methods due to forthcoming large strong lens samples. It is therefore critical to understand the systematic effects inherent in this method. In this Chapter, we quantify the influence of additional structures along the line-of-sight by adopting realistic light cones derived from the *CosmoDC2* semi-analytical extra-galactic catalogue. Using multiple lens plane ray-tracing to create a set of simulated strong lensing systems, we have investigated the impact of line-of-sight structures on time-delay measurements and in turn, on the inferred value of H_0. We have also tested the reliability of existing procedures for correcting for line-of-sight effects. We find that if the integrated contribution of the line-of-sight structures is close to a uniform mass sheet, the bias in H_0 can be adequately corrected by including a constant external convergence $\kappa_{\rm ext}$ in the lens model. However, for realistic line-of-sight structures comprising many galaxies at different redshifts, this simple correction over-estimates the bias by an amount that depends linearly on the median external convergence. We therefore

conclude that lens modelling must incorporate multiple lens planes to account for line-of-sight structures for accurate and precise inference of H_0.

4.1 Introduction

The Hubble-Lemaître constant, H_0, is a cornerstone of the standard cosmological model, setting the distance scale, age and critical density of the Universe. Accurate estimation of the value of H_0 is therefore critical for constraining cosmological models in the era of precision cosmology. However, presently, there is a significant mismatch between H_0 determined from early- and late-universe probes [177, 177], for instance, measurements of the Cosmic Microwave Background [CMB; see 177, 177] and Baryon Acoustic Oscillations [BAO; see 4, 48] and those made in the more local Universe using supernovae [SNe;see 73, 142], the tip of the red giant branch [TRGB; see 90, 230] and Cepheid variables [177, 169]. Independent from any of the aforementioned methods, strong lensing time delays provide valuable measurements of H_0 [e.g., 228, 191] which may assist in the understanding of these discrepancies once systematic uncertainties in the technique are fully calibrated. With such systematics in mind, in this Chapter we focus on the effects of line-of-sight structure, one of the most dominant sources of error in the lens time delay method.

Strong lensing time delays are observed when a variation in flux of a strongly-lensed background source such as a quasar, supernova or a gravitational wave event is detected at different times between its multiple images. The deflection of the light path from the source due to the gravitational potential of a lens, as well as the structures along the line-of-sight, leads to both a geometrical and a gravitational delay of the arrival time of the light from the source. The geometrical delays are sensitive to H_0 [see 185]. Therefore, measuring the time delays and reconstructing the mass distribution of the lens accurately allows H_0 to be estimated. The existing relative paucity of strong-lens systems suitable for this method and the necessary long monitoring campaigns

has somewhat limited the use of this technique but good progress has already been made with only a handful of systems [e.g., 199, 200, 34, 227, 38, 228, 46, 55]. However, this is set to dramatically change [162, 49] with the advent of the Rubin Observatory Legacy Survey of Space and Time[1] (LSST), which will give rise to about 400 well-measured time delay systems to constrain H_0 to within only a few percent [140, 75].

[1] https://www.lsst.org/

Even with precise time delay measurements, the reliability of estimates of H_0 depends on how faithfully the lens mass model follows the true lensing mass. Degeneracies and inadequacies in the parameterisation of the lens mass model can directly propagate into the inferred value of H_0 [e.g., see 184, 190, 229, 153, 209, 203, 220, 217] as can selection effects within the lens sample [see 50]. In addition, perturbative effects from sub-structure within the main lens and from structure along the line-of-sight can significantly modify time delays which can bias measurements of H_0 if not properly taken into account. One approach to account for these effects is to directly characterise perturbing structures identified in observations [e.g., 226, 149, 179, 195, 225]. Another common technique is to use external shear, $\gamma_{\rm ext}$, and external convergence, $\kappa_{\rm ext}$, in the lens model. By connecting cosmological simulations and real observations, an estimate of the distribution function of the amplitude of these external lensing effects can be obtained [e.g., 199, 200, 97, 51, 179, 35, 210]. However, the corrections provided by $\gamma_{\rm ext}$ and $\kappa_{\rm ext}$ are isotropic and cannot properly capture the complexity of real perturbing structures. Motivated by this, more sophisticated approaches have been developed using multiple lens planes or approximations thereof [e.g., 146, 35, 147].

In this work, we investigate the influence of halos along the line-of-sight on measurements of H_0 by using multiple lens plane ray-tracing simulations. To obtain simulated time delays we construct the light cone of each lens from a state-of-the-art semi-analytic model [CosmoDC2[2]; 127] based upon the large Outer Rim cosmological N-body simulation [113]. By modelling these time delays with the same methods used for real data, we directly assess the biases introduced by line-of-sight effects

[2] https://portal.nersc.gov/project/lsst/cosmoDC2

and the efficacy with which these can be accounted for using external corrections such as $\gamma_{\rm ext}$ and $\kappa_{\rm ext}$.

The Chapter is structured as follows. We outline the methodology used for determining strong lensing time delays in the cases of the single-lens plane and multiple-lens planes in Section 4.2. Details of the simulations and the process of estimating H_0 from the simulated data are given in Sections 4.3 and 4.4 respectively. We present our findings in Section 4.5, then conclude with a summary and discussion in Section 4.6. The cosmological model adopted in this Chapter is that used by CosmoDC2: ΛCDM with $\Omega_\Lambda = 0.735$, $\Omega_{\rm M} = 0.265$, and $H_0 = 71\,{\rm km\,s^{-1}\,Mpc^{-1}}$.

4.2 Strong Lensing Time Delays

In this section, we present a basic description of the theory of time-delays in strong lensing systems with multiply-lensed point sources we have used in this work, for the cases of single and multiple lens planes. Throughout the Chapter, we have applied the thin lens approximation. For more details, we refer the reader to [183] and [155].

4.2.1 Time Delays in Single Lens Planes

For the case of a lensing system with a single deflector, adhering to the thin lens approximation, one can project the three-dimensional mass distribution to a two-dimensional mass sheet normal to the line-of-sight from the observer to the source. The dimensionless surface mass density of a thin lens plane can be written as a function of the lens plane angular position vector, $\boldsymbol{\theta}$, as

$$\kappa(\boldsymbol{\theta}) = \Sigma(\boldsymbol{\theta} D_{\rm d}) / \Sigma_{\rm crit}\ , \tag{4.1}$$

with the critical surface mass density

$$\Sigma_{\rm crit} = \frac{c^2}{4\pi G}\frac{D_{\rm s}}{D_{\rm d} D_{\rm ds}}\ , \tag{4.2}$$

where D_s and D_d are the angular diameter distances from the source and lens to the observer respectively, D_ds is the angular diameter distance from the lens to the source, and $\Sigma(\boldsymbol{\theta} D_\mathrm{d})$ is the surface mass density of the lens. The lensing potential is given by

$$\psi(\boldsymbol{\theta}) = \frac{1}{\pi} \int \mathrm{d}^2\boldsymbol{\theta}' \kappa(\boldsymbol{\theta}') \ln|\boldsymbol{\theta} - \boldsymbol{\theta}'| \ , \tag{4.3}$$

and the deflection angle vector is given by

$$\boldsymbol{\alpha}(\boldsymbol{\theta}) = \frac{1}{\pi} \int \mathrm{d}^2\boldsymbol{\theta}' \kappa(\boldsymbol{\theta}') \frac{\boldsymbol{\theta} - \boldsymbol{\theta}'}{|\boldsymbol{\theta} - \boldsymbol{\theta}'|^2} \ . \tag{4.4}$$

Once the deflection field at the lens plane is known, we can construct the lensing equation for a given set of source planes. For example, in the case of a single lens plane and a single source plane, the lensing equation is simply

$$\boldsymbol{\beta} = \boldsymbol{\theta} - \boldsymbol{\alpha}(\boldsymbol{\theta}) \ , \tag{4.5}$$

where $\boldsymbol{\beta}$ is the angular source plane position vector that maps to $\boldsymbol{\theta}$ in the image plane (or, equivalently, "lens plane" for the case of single lens-plane). Based on Eq. 4.5, ray-tracing simulations can be performed from the observer, crossing the lens plane to the source plane to produce lensed images. For extended source-like galaxies, to create distorted lensed images, interpolation can be used in the source plane to map spatially varying surface brightness back to the image plane. However, for the point sources used in this work, one has to adopt triangle mapping and a barycentric coordinate system to solve the lensing equations numerically. Details of the approach are discussed in Sec. 4.3.3.

In the case of a single lens plane, the delay of the arrival time of a light ray from the source to the observer is

$$\tau(\boldsymbol{\theta}, \boldsymbol{\beta}) = \frac{(1 + z_\mathrm{d})}{c} \frac{D_\mathrm{d} D_\mathrm{s}}{D_\mathrm{ds}} \left[\frac{(\boldsymbol{\theta} - \boldsymbol{\beta})^2}{2} - \psi(\boldsymbol{\theta}) \right] \ , \tag{4.6}$$

where z_d is the redshift of the lens. The last term in Eq. 4.6 is also known

as the Fermat potential,

$$\Phi(\boldsymbol{\theta}, \boldsymbol{\beta}) \equiv \left[\frac{(\boldsymbol{\theta} - \boldsymbol{\beta})^2}{2} - \psi(\boldsymbol{\theta}) \right] . \tag{4.7}$$

This delay is undetectable, the true observable being the difference between the arrival time of two separate lensed images (say, image A and image B), $t_{\mathrm{AB}} \equiv \tau_{\mathrm{A}} - \tau_{\mathrm{B}}$. From Eq. 4.6, the time difference can be written

$$t_{\mathrm{AB}} = \frac{D_{\Delta\tau}}{c} \Delta\Phi_{\mathrm{AB}} \ , \tag{4.8}$$

where,

$$D_{\Delta\tau} \equiv (1 + z_{\mathrm{d}}) \frac{D_{\mathrm{d}} D_{\mathrm{s}}}{D_{\mathrm{ds}}} \tag{4.9}$$

and

$$\Delta\Phi \equiv \Phi(\boldsymbol{\theta}_{\mathrm{A}}, \boldsymbol{\beta}) - \Phi(\boldsymbol{\theta}_{\mathrm{B}}, \boldsymbol{\beta}) \ . \tag{4.10}$$

Note that

$$D_a(z) = \frac{c}{H_0(1+z)} \int_0^z \frac{dz'}{E(z')} \tag{4.11}$$

where

$$E(z) = \sqrt{\Omega_r (1+z)^4 + \Omega_m (1+z)^3 + \Omega_k (1+z)^2 + \Omega_\Lambda} \ . \tag{4.12}$$

These equations show that

$$t_{\mathrm{AB}} \propto D_{\Delta\tau} \propto \frac{1}{H_0} \tag{4.13}$$

and thus H_0 can be measured from t_{AB} if the mass distribution of the lens is reconstructed accurately.

4.2.2 Time Delays in Multiple Lens Planes

In the case of multiple lens planes, the lens equation must be modified to account for multiple deflections;

$$\boldsymbol{\beta} = \boldsymbol{\theta} - \sum_{i=1}^{N} \boldsymbol{\alpha}_i(\boldsymbol{\theta}_i) \ , \tag{4.14}$$

where the quantities retain their definition from the single lens plane case but now take on a subscript referring to a specific lens plane. We consider N mass distributions, each characterised by a surface mass density Σ_i, at redshift z_i, ordered such that $z_i < z_j$ for $i < j$ and such that the source has a redshift $z_s > z_N$. The physical distance, $\boldsymbol{\xi}_j$, of the intersections on the lens planes from the optic axis (i.e., the impact parameters) are then

$$\boldsymbol{\xi}_j = \frac{D_j}{D_1}\boldsymbol{\xi}_1 - \sum_{i=1}^{j-1} D_{ij}\hat{\boldsymbol{\alpha}}_i(\boldsymbol{\xi}_i) \ , \tag{4.15}$$

where D_i is the angular diameter distance from the observer to each lens plane, D_{ij} (such that $i < j$) is the angular diameter distance from the ith lens plane to the jth lens plane and $\hat{\boldsymbol{\alpha}}_i$ is the deflection angle at the ith lens plane (see Fig. 4.1). For simplicity, we convert the physical distance to angular positions on the sky $\boldsymbol{\theta}_i = \boldsymbol{\xi}_i / D_i$ and the deflection angles to effective movements on the sky

$$\boldsymbol{\alpha}_i = \frac{D_{is}}{D_s}\hat{\boldsymbol{\alpha}}_i \ , \tag{4.16}$$

where D_{is} is the angular diameter distance from the ith lens plane to the source plane. By defining a factor B_{ij}

$$B_{ij} = \frac{D_{ij}D_s}{D_j D_{is}} \ , \tag{4.17}$$

eq. 4.15 becomes

$$\boldsymbol{\theta}_j = \boldsymbol{\theta}_1 - \sum_{i=1}^{j-1} B_{ij}\boldsymbol{\alpha}_i(\boldsymbol{\theta}_i) \ . \tag{4.18}$$

In particular, for $j = N + 1 = s$, $B_{is} = 1$, thus,

$$\boldsymbol{\beta} \equiv \boldsymbol{\theta}_{N+1} = \boldsymbol{\theta}_1 - \sum_{i=1}^{N} \boldsymbol{\alpha}_i(\boldsymbol{\theta}_i) \,. \tag{4.19}$$

The delay of the arrival time of a deflected light path compared to a straight light path is the integral of the time difference along the line-of-sight though all lens planes. For instance, the time delay created by lens plane i and j is

$$\tau_{ij}(\boldsymbol{\theta}_i, \boldsymbol{\theta}_j) = \frac{1 + z_i}{c} \frac{D_i D_j}{D_{ij}} \left[\frac{1}{2} (\boldsymbol{\theta}_i - \boldsymbol{\theta}_j)^2 - B_{ij} \psi(\boldsymbol{\theta}_i) \right] \,, \tag{4.20}$$

where the first term is the geometric delay and the second is the gravitational delay. Replacing j with $i + 1$ and summing over all time delays gives the total time delay through the whole line-of-sight,

$$\tau(\boldsymbol{\theta}_1, ..., \boldsymbol{\theta}_N, \boldsymbol{\beta}) = \sum_{i=1}^{N} \tau_{i,i+1}(\boldsymbol{\theta}_i, \boldsymbol{\theta}_{i+1}) \,. \tag{4.21}$$

Therefore, similar to the case of a single lens plane, the time delay between two separate lensed images A and B can be given by

$$\begin{aligned} t_{\mathrm{AB}} &\equiv \tau_{\mathrm{A}} - \tau_{\mathrm{B}} \\ &= \sum_{i=1}^{N} \tau_{i,i+1}(\boldsymbol{\theta}_{\mathrm{A},i}, \boldsymbol{\theta}_{\mathrm{A},i+1}) - \sum_{i=1}^{N} \tau_{i,i+1}(\boldsymbol{\theta}_{\mathrm{B},i}, \boldsymbol{\theta}_{\mathrm{B},i+1}) \,, \end{aligned} \tag{4.22}$$

which means that deflection fields, lensing potentials and the angular positions of the intersections on the lens planes are all required for the calculation of time delays in multiple lens plane systems. In section 3, we discuss how we construct a light cone and model the lenses to obtain the information required to implement time-delay simulations with multiple lens planes.

4.3 Simulations

To quantify the influence of galaxies along the line-of-sight on measuring H_0 with strong lensing time-delays, we generated simulated images fol-

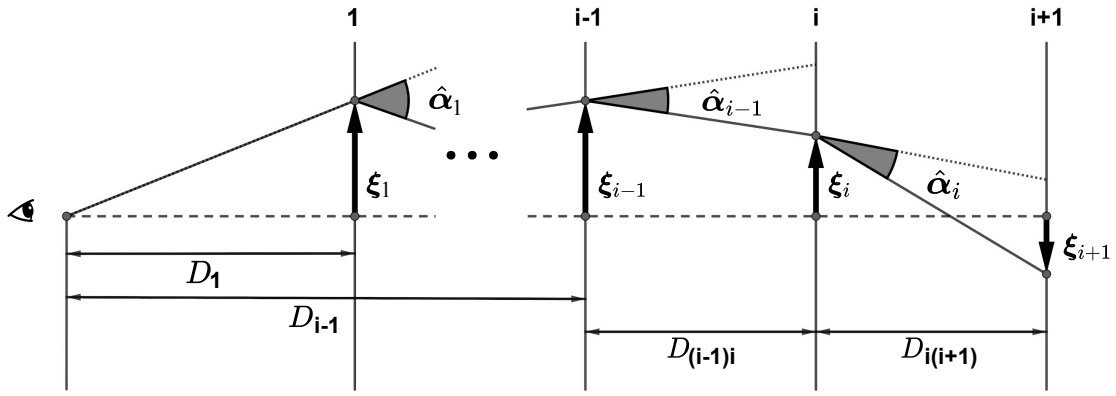

Figure 4.1: A schematic view of the multi-plane formalism, as described in Section 4.2.2. A light ray (solid black line) experiences a deflection only when it passes through a lens plane (vertical solid grey lines). The deflection angle $\hat{\boldsymbol{\alpha}}_i$ is the actual deflection of a ray passing through the ith lens plane, calculated from the surface density Σ_i on the ith lens plane. Using the deflection angle $\hat{\boldsymbol{\alpha}}_i$ and the position of the intersection of the light ray at the $(i-1)$th lens plane, $\boldsymbol{\xi}_{i-1}$, and that at the ith lens plane, $\boldsymbol{\xi}_i$, the physical position of the intersection at the $(i+1)$th plane, $\boldsymbol{\xi}_{i+1}$, can be obtained.

lowing the formalism in Sec. 4.2 for both single and multiple lens planes with a strong lensing simulation pipeline named PICS [138]. In this section, we describe the simulations used and how the lens equations are solved using a triangle-mapping algorithm.

4.3.1 Semi-Analytic Lightcones

For creating light cones with realistic spatial and redshift distributions of the galaxies, we extract light cones from the CosmoDC2 synthetic source catalogue [127]. Designed for an LSST data challenge project, it is established upon a large cosmological simulation called The Outer Rim Simulation run by the Argonne Cosmology Group using the Hybrid/Hardware Accelerated Cosmology Code [HACC, 100]. CosmoDC2 covers 500 square degrees in the redshift range $0.0 \leq z \leq 3.0$ and is complete to a magnitude depth of 28 in the r-band. Each galaxy is characterised by a multitude of properties including stellar mass, morphology, spectral energy distributions, broadband filter magnitudes, host halo information and weak lensing shear.

The light cones for each of our strong lensing simulations are cut out from the full light cone of CosmoDC2. Each extracted light cone is centred on a bright central galaxy (BCG) identified in the cosmoDC2 catalogue since these massive central elliptical galaxies are likely strong lens-

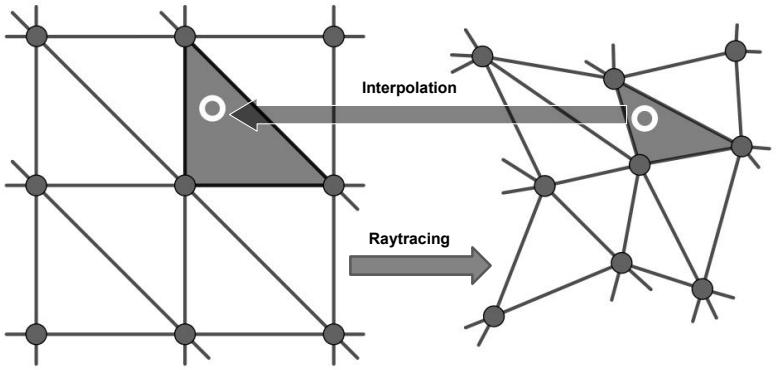

Figure 4.2: The Interpolation scheme used for determining image positions of point sources. The regular grid of rays in the image plane (left filled circles) is used to partition the image plane into triangles (grey lines in the left panel). The image positions (the open white circle in the left panel) of a source inside a triangle (the grey triangle in the right panel) formed by the backtraced rays on the source plane (grey filled circles in the right panel) is then determined by using linear interpolation in the barycentric coordinates.

ing candidates. Each BCG forms the primary lens mass in its corresponding light cone (see Section 4.3.2). The field of view of the light cones is $20'' \times 20''$, and the corresponding simulated images are 512×512 pixels in size. To focus on the impact of line-of-sight galaxies, we select light cones with the primary lens located in the redshift range $z_d = 0.5 \pm 0.01$ and we assume a fixed source redshift of $z_s = 2.0$. We calculate the Einstein radius of the primary lens of each light cone and then discard light cones that yield Einstein radii outside the range of $[1.3'', 2.4'']$. The lower limit avoids resolution issues encountered by ground-based telescopes/surveys (such as CFHT, DES, and LSST) and the upper limit discards systems which give year-like time delays. In total, we selected 500 light cones adhering to these criteria (although this is ultimately reduced further by additional selection criteria - see the following section and Section 4.5). Furthermore, within each light cone, we remove any deflectors with Einstein radii larger than $0.3''$ to concentrate our study on the effects of secondary perturbations to the lensing potential. The substructures of the primary lens are also not included so that our analysis solely concentrates on the influence of line-of-sight structures.

4.3.2 Ray-tracing Simulations

For each light cone, we run two sets of simulations for generating the lens time delays. The first set includes only a single lens plane containing the primary lens galaxy. In this set, the omitted line-of-sight halos are approximated with a constant external convergence, $\kappa_{\rm ext}$, and a constant external shear, $\gamma_{\rm ext}$, in the lens model when computing deflection angles. For each light cone, we estimate the value of $\kappa_{\rm ext}$ and $\gamma_{\rm ext}$ by tracing multiple rays throughout it as described in more detail below. In the second set of simulations, we include all halos in the light cone and use a separate lens plane for each halo including the primary lens.

In both sets of simulations, we assume a Singular Isothermal Ellipsoid (SIE) density profile for all halos (although in our lens modelling, we use a more general elliptical power-law profile; see Section 4.4). The SIE profile, which provides a realistic model for the total mass profile of real elliptical galaxies [125, 37, 193], has deflection angles given by [126, 122],

$$\alpha_x \equiv \psi_x = \frac{bq}{\sqrt{(1-q^2)}} \tan^{-1}\left[\frac{\sqrt{1-q^2}\theta_x}{\phi}\right] , \tag{4.23}$$

$$\alpha_y \equiv \psi_y = \frac{bq}{\sqrt{(1-q^2)}} \tanh^{-1}\left[\frac{\sqrt{1-q^2}\theta_y}{\phi}\right] , \tag{4.24}$$

where $\phi^2 = q^2x^2 + y^2$, q is the minor to major axis ratio and b is an effective factor to represent Einstein radius,

$$b = \frac{4\pi}{\sqrt{q}}\left(\frac{\sigma}{c}\right)^2 \frac{D_{ls}}{D_s} . \tag{4.25}$$

In the case of circular lenses, b can be calculated from the velocity dispersion. The lensing potential can be computed according to the relationship between the lensing potential and the deflection field of SIE model [122],

$$\psi(\theta_x, \theta_y) = \theta_x\psi_x + \theta_y\psi_y . \tag{4.26}$$

The complete parameter set required by equations (4.23 – 4.26) is $\{x_1, x_2, \sigma_v, q, \Theta, z_d\}$, where (x_1, x_2) is the angular position of the SIE profile centre with respect to the centre of the field of view, σ_v is the velocity dispersion of the lens, q is the ellipse axis ratio, Θ is the position angle of the ellipsoid and z_d is the redshift of the deflector. The parameters x_1, x_2, q, Θ, z_d are taken directly from the cosmoDC2 catalogue. σ_v is derived from the $L - \sigma$ scaling relation from the bright sample of [165] given by

$$\sigma_v = 142 \left(\frac{L}{L_\star} \right)^{(1/3)} \text{km s}^{-1} , \tag{4.27}$$

where, $\log_{10}(L/L_\star) = -0.4(mag_r - mag_{r\star})$, and mag_r is the apparent r-band magnitude of the galaxy given by the cosmoDC2 catalogue. We adopt the assumption in [151] that $mag_{r\star}$ evolves with redshift as $mag_{r\star} = +1.5(z - 0.1) - 20.44$ [83].

Sources are described by the parameter set $\{y_1, y_2, m_s, z_s\}$, where (y_1, y_2) is the angular position of the source with respect to the optic axis, m_s is the apparent r-band magnitude of the source and z_s is the redshift, fixed to $z_s = 2$. The angular positions are randomly sampled in the source plane in the vicinity of the caustic structures. We only retain simulated data in which quadruply-lensed images are produced in both versions of a given light cone, i.e. both the single and the multiple lens-plane version. This reduces our initial selection of 500 light cones (see Section 4.3.1) to 400.

With a fully parametrically-defined light cone, the simulated lensed images can be produced by ray-tracing and image-finding. For our single lens-plane simulations, we determine κ_{ext} and γ_{ext} in the following manner. First, we trace rays through a given light cone from the image plane, computing the deflections caused by all halos (including the primary lens), each in their own lens plane. To obtain γ_{ext}, along each ray, we compute the cumulative external shear from all halos. We take γ_{ext} to be the median of the distribution of values of the cumulative external shear along different rays in the light cone. For the external

convergence, along each ray, we compute an 'external halo convergence' by summing κ as given by Eq. 4.1 for all secondary halos excluding the primary lens halo. This external halo convergence ignores the divergence caused by voids and so we must apply a correction to obtain $\kappa_{\rm ext}$. The correction uses the results of [51] who showed that $\kappa_{\rm ext}$ can be obtained by subtracting the median convergence along random sight lines from the external halo convergence. The resulting $\kappa_{\rm ext}$ has an uncertainty associated with it due to the scatter in the relationship between the two quantities, but negligible bias. Firing rays along random lines-of-sight in our light cones and computing the convergence, again using Eq. 4.1, yields a value of $\kappa_{\rm corr} = 0.048$. When correcting the external halo convergence, we distribute $\kappa_{\rm corr}$ across all lens planes according to the lensing weights ($D_{ds}D_d\,/\,D_s$) for each plane and subtract them separately.

Figure 4.3 shows the probability distribution functions (PDFs) of the mean and median values of $\kappa_{\rm ext}$ across all light cones obtained in the manner described. We note that our peak of $\kappa_{\rm ext} \simeq 0.1$ is higher than that of previous studies, for example, peaks of 0.075 and 0.05 in [200] and [147] respectively. We speculate that this is mainly due to our selection of BCGs from cosmoDC2 and their location within more over-dense galaxy groups. Secondary effects also likely include a difference in mass models and simulated light cones. Nevertheless, many of our light cones yield external convergences that are consistent with these studies and so in our analysis, we explore how inferred values of H_0 vary with varying $\kappa_{\rm ext}$.

With $\kappa_{\rm ext}$ determined, we include it in the primary lens model for the single-plane simulations and calculate maps of the deflection angle and the lensing potential. The lensing equation in Eq. 4.5 is used to map the image plane back to the source plane. Since the sources in this Chapter are point sources, we have to adopt a triangle-mapping algorithm to solve the lensing equation. This is described further in Section 4.3.3.

For the case of multiple lens-planes, we ray-trace through the whole light cone in the same manner as outlined above when computing the

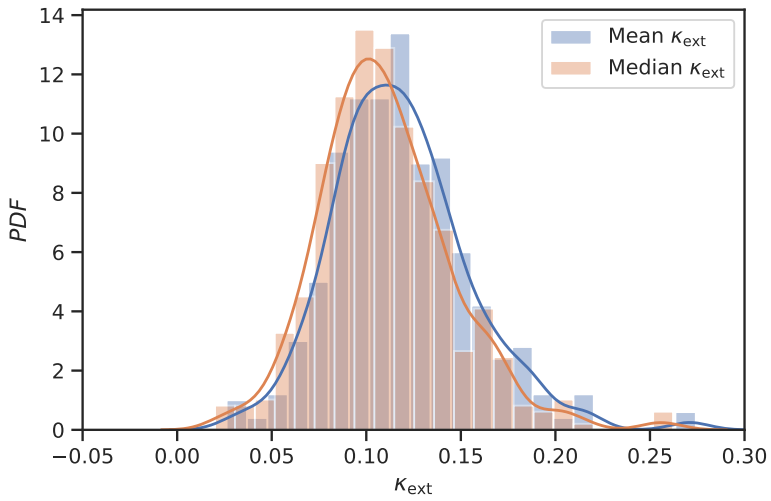

Figure 4.3: The distribution of the mean (blue) and median (orange) convergence of all fully ray-traced light cones used in this work. The blue and orange curves show a smoothed version of the distributions calculated using kernel density estimates.

external halo convergence, placing each halo on its own lens plane. As Eq. 4.20 shows, to calculate the total time delay, the deflection map and lensing potential for every lens plane must be computed. The intersections of the light rays traced from the image plane (given by Eq. 4.18) are required for the calculation of the time delay between two lens planes. These are summed over all neighbouring pairs of lens planes to obtain the total time delay according to Eq. 4.21. Again, for our adopted point source, we have to apply triangle mapping and barycentric interpolation to obtain the position of lensed images for a given source position on the source plane (see Section 4.3.3). The same image-finding process is applied to locate the intersections of the light rays between neighbouring lens planes (see Eq. 4.20).

Since we are concerned purely with the effects of line-of-sight structure in this study, we have not included the effects of measurement error in our simulated data, i.e. we do not scatter any of the time delays, image positions or flux ratios. However, we do use priors in the modelling to allow exploration of parameter degeneracies. More details are given in Section 4.4.

4.3.3 Image Finding

Since we are concerned with multiply-imaged point-like sources, e.g. AGNs or SNe, in this work, solving the lensing equation for point sources is a critical issue in the simulation. To determine the apparent positions of our point-sources, we make use of a triangle mapping technique described in [185]. First, a set of Delaunay triangles is constructed from a regular grid of image plane positions which define the intersections of light rays from the source (see Fig. 4.2). These image plane vertices are then mapped to the source plane. Any image plane triangles which map to a triangle in the source plane containing the source position are identified. For each of these identified image-plane triangles, we compute the barycentric coordinate of the source position inside the corresponding source-plane-mapped triangle using the relation

$$\begin{pmatrix} x_1 & x_2 & x_3 \\ y_1 & y_2 & y_3 \\ 1 & 1 & 1 \end{pmatrix} \begin{pmatrix} \lambda_1 \\ \lambda_2 \\ \lambda_3 \end{pmatrix} = \begin{pmatrix} x_P \\ y_P \\ 1 \end{pmatrix} \tag{4.28}$$

where, (x_P, y_P) are the Cartesian coordinates of the point source inside its triangle of vertices (x_1, y_1), (x_2, y_2), and (x_3, y_3); the corresponding barycentric coordinates are $(\lambda_1, \lambda_2, \lambda_3)$. We then assume that the barycentric co-ordinates are conserved between the image and source planes and use them, with the vertices of the image-plane triangle to determine the position of each image of the source.

For the case of multiple lens planes, the intersections between the light rays from the source and the lens planes are required for the calculation of total time-delays. Hence, we need to ascertain all the intersections. If there are N lens planes plus one source plane in the lensing system, there are N parent triangles for the triangle on the source plane. Also, we assume the barycentric coordinates of the source are conserved in the source triangle and all parent triangles. Then the intersections can be obtained. The intersections on the first lens plane (0th plane in Fig. 4.1) are the positions of the lensed images.

4.4 Strong Lens Modelling

We use the multi-purpose open-source lensing package LENSTRONOMY[3] [33, 32] to measure H_0 from our simulated data. For our lens modelling, instead of the SIE profile used to create our simulated data, we use the more general Singular Elliptical Power Law (SEPL) profile. The parameters of the SEPL are the Einstein radius, $\theta_{\rm E}$, the two components of complex ellipticity, e_1 and e_2, the SEPL power-law index, γ and the co-ordinates of the SEPL centre, (θ_1, θ_2). Also included as free parameters in the modelling are the co-ordinates of the source, (β_1, β_2), in the source plane. Finally, we apply the SEPL model both with and without external shear (see below). We use the complex shear parameterised by $\gamma_{\rm ext,1}$ and $\gamma_{\rm ext,2}$. We apply generous uniform priors to all model parameters in LENSTRONOMY as detailed in Table 4.1.

[3] https://github.com/sibirrer/lenstronomy

We model all four different combinations arising from the two lens model configurations (i.e., the SEPL with and without external shear) and the two sets of simulated data (i.e., the single and multiple lens plane light cones). We designate the simulations with a single lens plane as 'SGK' (SIE + $\gamma_{\rm ext}$ + $\kappa_{\rm ext}$) and those with the multiple lens plane as 'SL' (SIE + Lens planes). Similarly, we designate the lensing model that includes external shear as 'SG' (SEPL + $\gamma_{\rm ext}$) and that without as 'S'. The four combinations, labelling the simulation type first, are therefore referred to hereafter as 'SGK|S', 'SGK|SG', 'SL|S' and 'SL|SG'. Note that in all cases we fix $\kappa_{\rm ext} = 0$ and retrospectively apply the correction to H_0 for external convergence determined from the simulated light cones following the procedure used by existing studies (see Section 4.5). In cases where external shear is not included as a free parameter in the lens model (SGK|S and SL|S), we fix $\gamma_{\rm ext} = 0$.

The simulated data that we fit with LENSTRONOMY are the four image positions, the three flux ratios, and the three time delays. For optimisation of the lens model parameters and H_0, we use LENSTRONOMY's particle swarm optimiser (PSO) [79] since this technique performs well in lower dimensional parameter spaces such as ours [see 33]. We apply

Model component	Parameter	Prior
Lens, Einstein radius	θ_E (arcsec)	$\mathcal{U}(0.01, 10)$
Lens, power index	γ	$\mathcal{U}(1.7, 2.3)$
Lens, ellipticity	$e_{1,2}$	$\mathcal{U}(-0.5, 0.5)$
Lens, position	$\theta_{1,2}$ (arcsec)	$\mathcal{U}(-10, 10)$
External shear	$\gamma_{\rm ext,1}$	$\mathcal{U}(0.0, 0.5)$
External shear angle	$\theta_{\gamma,\rm ext}$ (rad)	$\mathcal{U}(-\pi, \pi)$
Source, position	$\beta_{1,2}$ (arcsec)	$\mathcal{U}(-10, 10)$
Hubble-Lemaître constant	H_0 (km/s/Mpc)	$\mathcal{U}(20, 120)$

Table 4.1: Uniform priors applied to parameters in the lens modelling.

the PSO with 200 particles, a particle scatter of 1, and a maximum number of iterations of 500. These choices yield an acceptable computation time whilst still allowing a thorough exploration of the model parameter space.

4.5 Results

In carrying out the modelling, we find that not all measurements of H_0 obtained are valid. This is due to the limited precision of the simulations; when a source is almost coincident with the caustic in the source plane, the magnifications of the simulated lensed images become unreliable because of the finite image grid size, despite our interpolation. These problematic cases can be effectively removed by imposing a likelihood threshold of $\log(L) > -1000$. This further reduces our sample of 400 lens systems to 364, 372, 366, and 394 lenses in the cases of SGK|S, SGK|SG, SL|S, and SL|SG respectively. By applying this threshold in likelihood, we also remove poor fits arising from large perturbations from substructures not caught by the $0.3''$ cut in Einstein radius.

First we consider our analysis of the simulations created with LOS structure approximated by a constant external convergence and shear. Fig 4.4 shows the PDFs of the fractional difference between the input and inferred H_0 obtained for the two different lens models applied, i.e. the SEPL-only model (SGK|S) and the SEPL+$\gamma_{\rm ext}$ model (SGK|SG). Taking the median of each of these distributions, we find that without including any external convergence in the modelling, the inferred value of H_0 is biased

high by $\sim$ 11 per cent in both cases. The inclusion of external shear in the lens model reduces the spread of the distribution but does nothing to remove the bias.

Following the procedure commonly used in the literature to correct for external convergence effects [see, for example 202], we apply a correction of $1 - \kappa_{\rm ext}$ (with $\kappa_{\rm ext}$ determined from the simulations as explained in Section 4.3.2) to the biased measurements of H_0 from the $SGK|SG$ configuration. The green histogram shown in Fig 4.4 shows the results of this correction. Clearly, the correction in this simplified case works well, recovering a median value of H_0 that differs from the input value by only -0.7 per cent.

In Fig 4.5, we show the two-dimensional probability distributions of all parameter pair combinations for the $SGK|SG$ configuration. Note that in addition to the bias in H_0, there is also a similar bias in the inferred Einstein radius, $\theta_{\rm E}$. This is a result of the strong degeneracy between $\theta_{\rm E}$ and H_0 caused by the fact that the external convergence impacts both quantities by the same factor of $1 - \kappa_{\rm ext}$. As Fig 4.5 shows, correcting $\theta_{\rm E}$ by the factor $1 - \kappa_{\rm ext}$ (to give the quantity $\theta_{\rm E}^{\rm c}$ in the figure), the input value of the Einstein radius is reliably recovered.

Second, we consider our modelling of the simulations created with the full light cones containing halos (i.e., the cases of $SL|S$ and $SL|SG$). Fig. 4.6 shows the distribution of inferred values of H_0 for both cases. This time, we find that the biases in inferred H_0 are significantly smaller than the biases observed with the single lens plane light cones. Now, we find a median value that is 3 and 4 percent higher than the input value of H_0 for the $SL|S$ and $SL|SG$ cases respectively. Once again, the inclusion of external shear in the lens model does little to improve the bias. Furthermore, the inclusion of external shear does not reduce the scatter in inferred values of H_0, unlike the single lens plane modelling. Fig. 4.6 also shows the histogram of inferred H_0 from the modelling that includes external shear (SL|SG) corrected by $1 - \kappa_{\rm ext}$, where again, $\kappa_{\rm ext}$ is determined from ray tracing through the light cone. This time, the correction is too severe and leads to an underestimation of H_0 such

that the corrected distribution has a median that is offset by -7 per cent from the input value. We therefore conclude that statistically, the $1 - \kappa_{\rm ext}$ correction can not be reliably used to account for clumpy external convergence.

Similar to Fig 4.5, Fig 4.7 shows the two-dimensional probability distributions of all parameter pair combinations for the SL|SG configuration. Again, the figure includes both $H_0^{\rm c}$ and $\theta_{\rm E}^{\rm c}$, the inferred values of H_0 and Einstein radius corrected by $1 - \kappa_{\rm ext}$. This time, however, the degeneracy between H_0 and $\theta_{\rm E}$ has been removed by the more complex lens geometry caused by the line-of-sight structure; clumpy external convergence affects the time delays in a different way to the way in which it affects the inferred Einstein radius, unlike when a uniform external convergence is assumed. In the same way that the inferred H_0 is not biased as high with the full light cones, neither is the inferred Einstein radius and so the correction provided by the factor of $1 - \kappa_{\rm ext}$ is also too severe and also results in a bias of -7 per cent from the input value on average.

Since our simulations span a range of lens systems each with a different median external convergence, $\kappa_{\rm ext}$, we can investigate whether there is any correlation between the bias we see in inferred H_0 and $\kappa_{\rm ext}$. Identifying such a correlation might instruct future studies on how best to minimise the bias. Fig. 4.8 shows the scatter plot of the bias in inferred H_0 versus $\kappa_{\rm ext}$ for each lens system with the SL|SG configuration. As the figure shows, there is a positive correlation such that the fractional bias in H_0 due to the over-correction correlates with the median external convergence. The scatter plot can be fitted using a linear function $\Delta H_0 / H_0 = 0.626 \kappa_{\rm ext} - 0.005$. Unsurprisingly, selecting a lens system in an environment with a stronger level of external convergence is more likely to bias the value of H_0 inferred from that system.

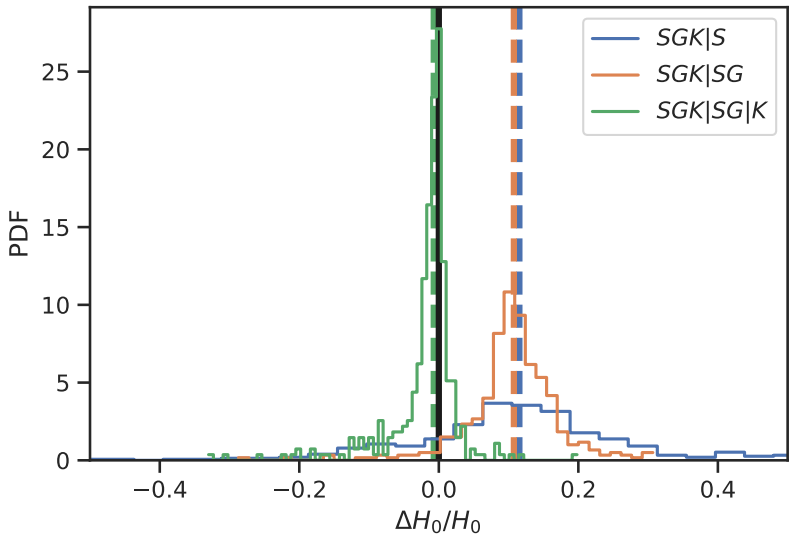

Figure 4.4: PDFs of the fractional differences between measured H_0 and the true value in the case of the simulations with constant $\kappa_{\rm ext}$ and $\gamma_{\rm ext}$. The blue histogram shows the PDF of fractional differences in H_0 with the single $SEPL$ mass model only. The orange histogram shows the PDF of fractional differences with the mass model of $SEPL$+$\gamma_{\rm ext}$, i.e. including external shear as a free parameter. The green histogram shows the corrected fractional differences of the orange histogram with constant $\kappa_{\rm ext}$ correction. The vertical dashed lines show the median of each PDF whilst the black vertical solid line is placed at zero bias.

4.6 Discussion and Conclusions

To quantify the influence of secondary deflectors on the measurement of H_0 with strong lensing time delays, we have simulated approximately 800 galaxy-scale strong lensing systems with quadruply-lensed variable point sources; half of these were created with a primary lens and line-of-sight halos and half with the same primary lens plus a constant external convergence and shear. The light cones were extracted from a semi-analytic model based on the Outer Rim large-scale cosmological simulation and are centred on the location of central galaxies of groups of galaxies. In the simulations constructed with external convergence and shear, we used a single lens-plane located at the redshift of the primary lens galaxy whereas in the simulations containing halos, each halo has its own lens plane. Using an SIE mass profile for the primary lens galaxy and the halos, and an interpolative mapping method to refine the location of the lensed point source images, we generated time de-

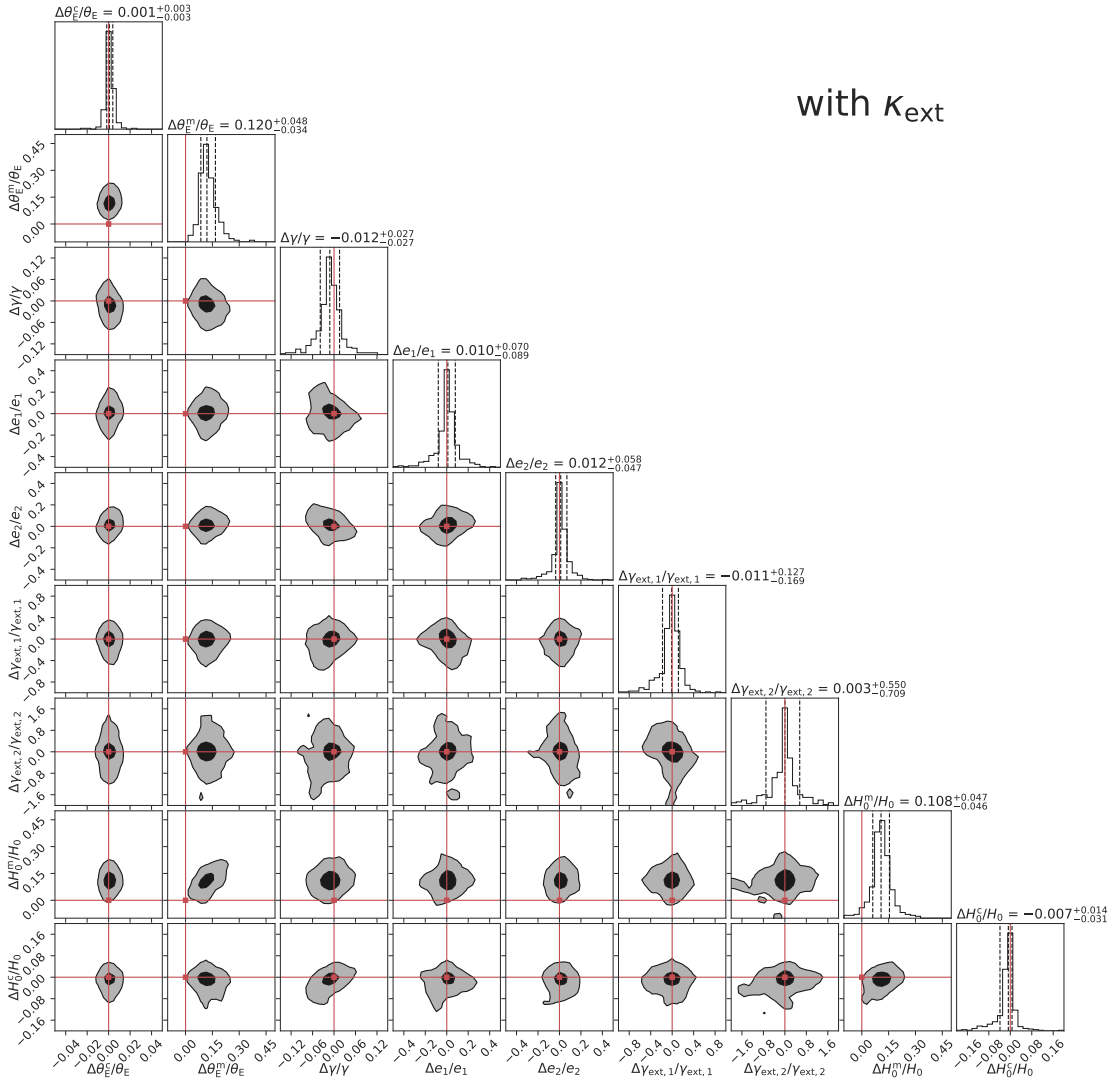

Figure 4.5: Corner plot showing the distribution of best-fit parameters of all 372 systems simulated with a single lens plane and uniform external convergence and shear. The plot includes the Einstein radius and H_0 corrected by the simplistic factor of $1 - \kappa_{\rm ext}$. These are denoted $\theta_{\rm E}^{\rm c}$ and $H_0^{\rm c}$ respectively. γ is the power index of the $SEPL$ mass model, e_1 and e_2 are the two components of the complex ellipticity of lenses, $\gamma_{\rm ext,1}$ and $\gamma_{\rm ext,2}$ are the two components of the complex external shear, $H_0^{\rm m}$ is the best-fit uncorrected Hubble constant and H_0 is the input Hubble constant. The contours show the 1- and 2-sigma confidence intervals. The plot is created with *Corner.py* [89].

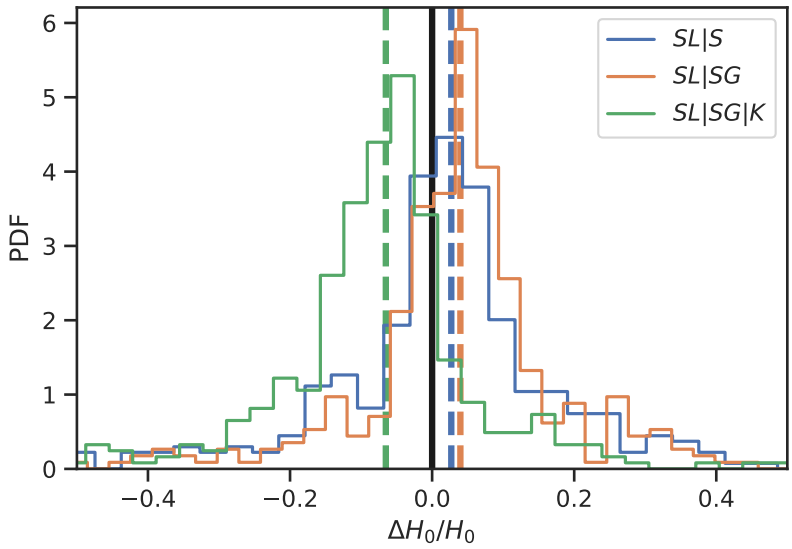

Figure 4.6: The same as Fig 4.4, except using the fully ray-traced simulations containing line-of-sight halos.

lay data. This time-delay data was then modelled using LENSTRONOMY to estimate H_0 with a singular ellipsoidal power law lens profile and external shear and compared to the known input value of H_0.

Our main conclusion is that incorporating constant external convergence in the modelling only works reliably if the lensed time delays are subjected to a uniform external convergence. If time-delays are subjected to perturbations due to halos lying close to the line-of-sight as expected in the real Universe, and no correction for external convergence is made in the modelling, the inferred value of H_0 is over-estimated by approximately 4 per cent on average. However, if a constant external convergence is incorporated in the lens model with a normalisation set by the median or mean convergence of the line-of-sight halos, then an over-correction of H_0 occurs such that it is biased low by $\sim$ 7 per cent on average. These results were obtained from our simulations where we measure a relatively high median external convergence of $\kappa_{\rm ext} \simeq 0.11$ but we find that the size of the fractional bias in H_0 scales almost proportionally with $\kappa_{\rm ext} = 0.11$ on average (see below for details). Nevertheless, even with low levels of external convergence, this effect can not be ignored, since the uncertainties of current measurements of H_0 from strong lensing time delays are typically quoted as being lower than this [38, 46, 228, 31, 180]. With the forthcoming large sample of strong

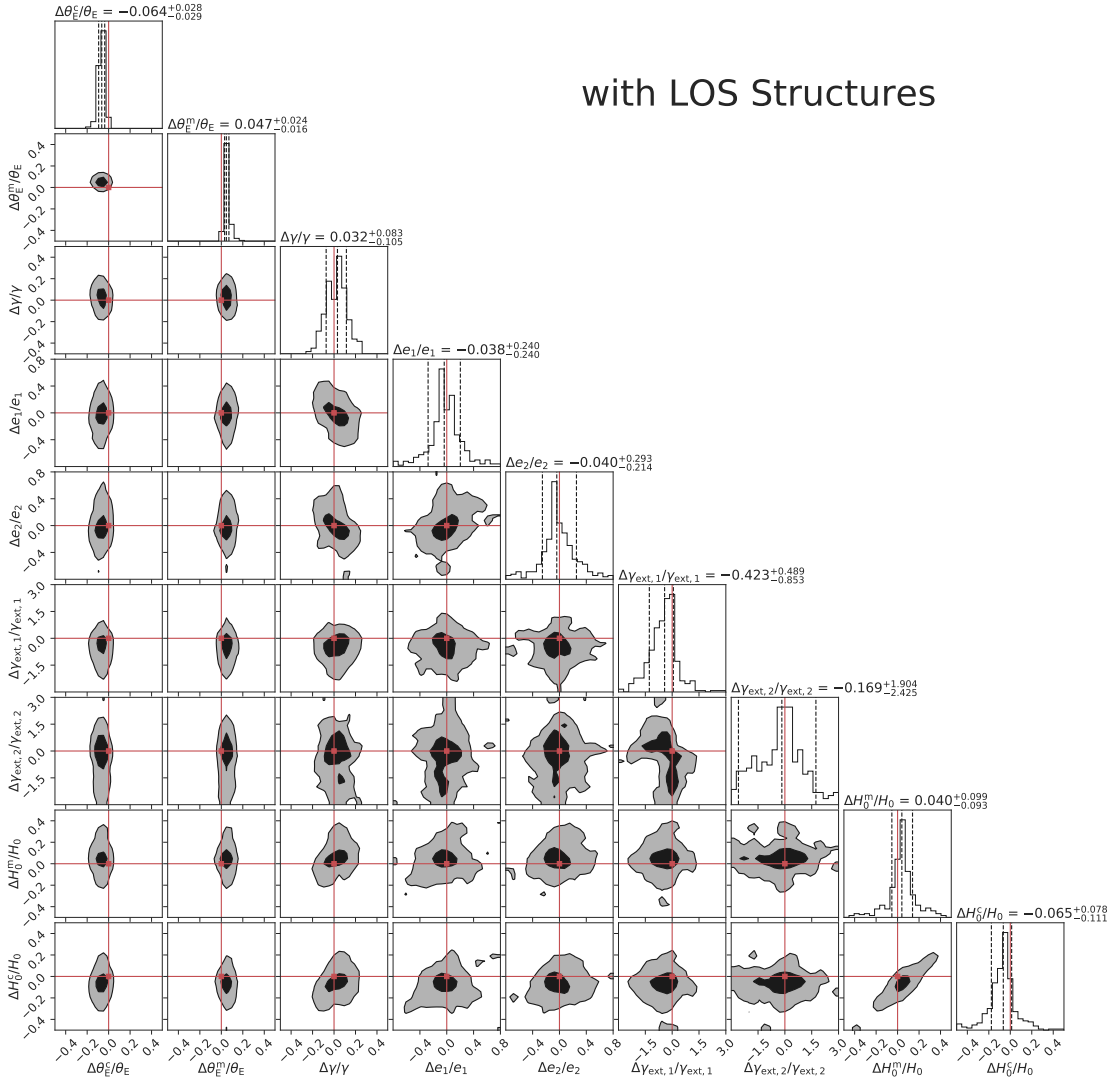

Figure 4.7: Corner plot showing the distribution of best-fit parameters of all 394 systems simulated by ray tracing through light cones containing line of sight halos. All parameters are the same as those in Fig 4.5 and the contours again show the 1- and 2-sigma confidence intervals.

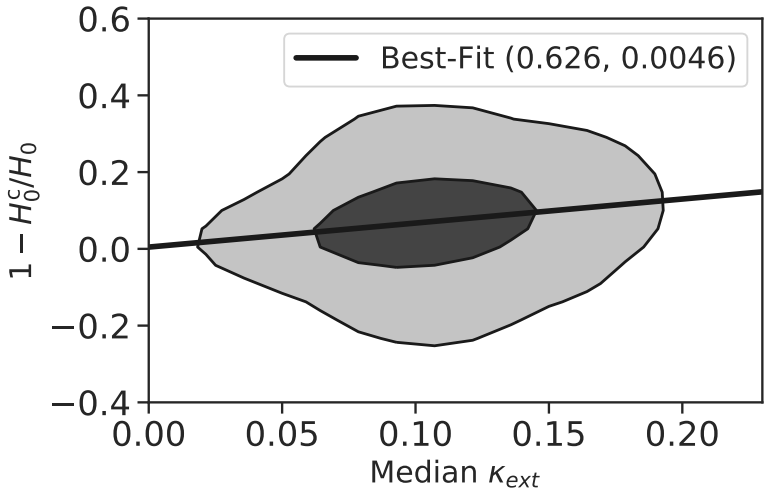

Figure 4.8: The relationship between the fractional bias seen in the corrected value of H_0, H_0^c, and the median external convergence measured across all 394 fully ray-traced light cones containing line of sight halos. The contours show the 1- and 2-sigma confidence intervals and the black line shows the best-fit linear relationship which exhibits almost exact proportionality: $1 - H_0^c / H_0 = 0.626\kappa_{\rm ext} - 0.005$.

lensing time delay systems observed by the future time domain large scale surveys, e.g., Mephisto[4] and LSST, the effect becomes even more problematic.

[4] http://www.swifar.ynu.edu.cn/info/1015/1073.htm

Qualitatively, our conclusions are consistent with those of [147] in the sense that line-of-sight structures significantly affect the accuracy of the measurement of H_0. We find a larger median external convergence of $\kappa_{\rm ext} \simeq 0.11$ compared to the value of 0.05 from [147]. We attribute this to the fact that we have selected central galaxies of galaxy groups as the primary lenses in our light cones and because we have included more line-of-sight structures; we include galaxies from cosmoDC2 down to an r-band apparent magnitude of 28, compared to the i-band limit of 21.5 adopted by [147]. Nevertheless, our findings indicate that even small values of $\kappa_{\rm ext}$ bias H_0 on average. We have shown that the fractional bias in inferred H_0 correlates with median external convergence according to the linear relationship $\Delta H_0 / H_0 = 0.626\kappa_{\rm ext} - 0.005$.

We have also investigated the effects of incorporating external shear in the lens model. In the simulations using line-of-sight halos, adding an external shear term to the $SEPL$ lens model makes a negligible impact on the distribution of recovered values of H_0. Not unexpectedly, we also find that correcting this $SEPL$+$\gamma_{\rm ext}$ model with the average constant

external convergence also leads to a $\sim$ 7 per cent underestimation, which implies that the influence of external shear is negligible in the case of our study. This conclusion differs from that of McCully et al., most likely because we cleaned our lens sample by removing secondary halos that give rise to an Einstein radius of greater than 0.3 arcsec.

The Outer Rim simulations used to populate our lensing light cones with halos include only dark matter. As such, we have used SIE profiles in place of identified halos to better represent the total mass (baryons + dark matter) profiles of real lens galaxies. One effect this may have is that the lensing strength of any lower mass halos, which in the real Universe may not have accrued baryons, could be artificially enhanced by the more efficient isothermal profile. In addition, our simulated datasets do not include any large scale structure such as filaments although this is expected to be a small effect. We have explored the use of truncated SIE profiles in place of the non-truncated profiles used in this work but find that our results do not change significantly. Finally, we have ignored the effects of environmental structure in the simulations in the sense that our assumed smooth SIE profiles for the primary lens do not include substructure. We will leave consideration of these additional effects for future work.

To summarise, simple corrections for line-of-sight structure such as external shear or external convergence in estimations of H_0 using lensed time delays can not be relied upon in general. Time delay studies opt for lens systems that are apparently free of strong perturbers in an attempt to exclude line-of-sight effects, or they select systems where the perturbers are low in number and can be easily incorporated in the lens model. Our simulations have mimicked the former selection to a degree by removing halos from all of our light cones that produce a deflection resulting in an Einstein radius larger than 0.3 arcsec. Since this may still allow a significant flexion shift, an improved technique is to include perturbers in the lens model with a flexion shift above a certain threshold [e.g., 180]. However, our work reveals that the culmination of many small line of sight perturbers continues to result in a significant portion

of the measured bias in H_0 and more sophisticated modelling methods, for example, including more lens planes by lowering flexion shift thresholds are key to reliable measurements of H_0 from the hundreds of well-measured time-delay systems anticipated in forthcoming large strong lens samples.

5

Summary, Conclusions, and Future Work

5.1 Summary and Conclusions

THE CONCORDANCE MODEL OF COSMOLOGY, ΛCDM, has undoubtedly withstood the tests of time. In many ways, it is remarkable that this relatively simple model is able to successfully fit and predict a vast range of phenomena in the Universe, such as the temperature fluctuations observed in the CMB, and the large-scale distribution of galaxies. The continuous development of sophisticated numerical and semi-analytic techniques have facilitated tests of this model on non-linear scales where, recently, hydrodynamical simulations within a ΛCDM context have managed to successfully reproduce a large set of observed galaxy properties at low redshift.

Cubic Vector Galileon

The analysis of Chapters 2 and 3 was devoted to the investigation of nonlinear growth of large-scale structure in a sub-class of the GP theory of gravity, the Cubic Vector Galileon (cvG). We derived the simplified equations for gravity as well as the longitudinal and transverse modes of the vector field under the weak-field and quasi-static approximation, and implemented them in a modified version of the `ECOSMOG` code.

The study of various cvG quantities (Sec. 2.3), that define the Vain-

shtein mechanism and the strength of the fifth-force, revealed that their evolution at early times ($a \lesssim 0.1$) is indistinguishable from equivalent quantities in the Cubic Scalar Galileon (csG) model. At late tames ($a \gtrsim 0.1$), the evolution of the cvG quantities is determined by the free model parameter $\tilde{\beta}_3$. For $\tilde{\beta}_3 \to 0$ the evolution is identical to csG while for $\tilde{\beta}_3 \to \infty$ the quantities evolve according to the QCDM variant of the cvG model. Furthermore have we found, that the EOM of longitudinal mode of the cvG field posseses the same structure in terms of spatial derivatives as the csG and the Dvali-Gabadadze-Porrati (sDGP) models.

The first set of cosmological simulations of the cvG model (presented in Sec. 2.4) have shown the following. Firstly, the transverse vector mode is negligible compared with the longitudinal vector mode on all scales probed by the simulations (Fig. 2.6). Consequently, we expect the 'back-reaction' of transverse mode on the evolution of longitudinal mode to be very small, justifying the neglect of the transverse vector field in future simulations and confirming the findings of [62]. Secondly, the Vainshtein mechanism efficiently suppresses the cvG fifth force (Fig. 2.7). This was shown through the comparison of the relative power spectrum enhancement with respect to QCDM of the full cvG model simulations and its *linearised* counterpart. The comparison has made it clear how the neglect of the non-linear terms in the EOM of the longitudinal vector mode leaves over-densities unscreened, leading to a much higher clustering power at small scales. Finally, we have investigated what effect the cvG model parameter $\tilde{\beta}_3$ has on the Vainshtein screening behaviour. As we have seen from the time evolution of various cvG quantities, for small(large) $\tilde{\beta}_3$ values, $\tilde{\beta}_3 = 10^{-6}$ (10^2), the cvG model behaves similar to the csG(QCDM) model.

Chapter 3 was devoted to a thorough phenomenological study of the cvG model and its matter, halo, weak lensing and void statistics. In that pursuit we have created a set of five simulated lightcones for the free model parameter $\tilde{\beta}_3 = [10^{-6}, 10^0, 10^1, 10^2]$ and their QCDM counterpart. The N-body code of Chapter 2 was hereto augmented with the ray-tracing modules of the `Ray-RAMSES` algorithm. We have

compared the simulation results to linear perturbation theory when possible and found that their agreement is pushed to ever larger scales as $a \to 1$ and $\tilde{\beta}_3 \to 0$. In the following we summarise the results of each of those four topics.

We extend the study of dark matter field statistics by including the simulation measurements of the *velocity divergence power spectrum* ($P_{\theta\theta}$, cf. Sec. 3.3.1 and Fig. 3.3) and the *matter bispectrum* (B, cf. Sec. 3.3.2 and Figs. 3.4, 3.5). On small scales ($k \gtrsim 0.1\, h/\mathrm{Mpc}$) we reproduce the well-known result that $P_{\theta\theta}$ is suppressed compared to the linear theory results. For $a \to 1$ and $\tilde{\beta}_3 \to 0$ we see a growing peak that for the case of $\tilde{\beta}_3 = 10^{-6}$ protrudes above the linear theory prediction at $k \sim 0.7\ h/\mathrm{Mpc}$. For B we find that the magnitudes depend on the triangle configurations, and increase in the order of equilateral, squeezed, and folded triangle configurations. We show that the enhancement of B due to the fifth force is marginally stronger than in the case of $P_{\delta\delta}$, but the reduced bispectrum shows that $B\,/\,B_{\mathrm{QCDM}}$ is to a very good approximation equal to $\left(P\,/\,P_{\mathrm{QCDM}}\right)^2$.

The study of halo statistics includes five different summary statistics which are mostly based on `SUBFIND` cagalogues. Firstly, the *halo mass function* ($n(>M)$, cf. Sec. 3.4.1 and Fig. 3.6) shows that the fifth force enhances the abundance of dark matter haloes in the entire mass range probed by the simulations, with the enhancement stronger at late times, small $\tilde{\beta}_3$, and high-mass haloes. Secondly, the *two-point correlation function* ($\xi(r)$) shows the smaller $\tilde{\beta}_3$ is the more enhanced the clustering, which is nearly constant down to $\sim 3\ h/\mathrm{Mpc}$. However, the enhancement in halo clustering is weaker than in matter clustering, for all models at all times. Thirdly, the relative difference of the *mean halo pairwise velocity* ($v_{\langle ij\rangle}$, cf. Sec. 3.4.3 and Fig. 3.8) remains constant for all cvG models at scales $r > 10\ h/\mathrm{Mpc}$, in very good agreement with linear-theory prediction. For the latter, we have measured the haloes bias, b, through the relation between the halo and matter correlation functions, which showed a slight decrease as $\tilde{\beta}_3 \to 0$, as the fifth force enhances matter clustering more than halo clustering, as mentioned

above. Fourthly, the results of the *redshift space halo clustering* ($\xi_\ell(s)$, cf. Sec. 3.4.4 and Fig. 3.9) reveal that the relative difference between cvG and QCDM can be up to ~ 3 times larger for the quadrupole, $\xi_2(s)$, than for the monopole, $\xi_0(s)$, although its SNR is ~ 0.5 times smaller on the range $20 < s\,h^{-1}\mathrm{Mpc} < 40$ due to larger statistical uncertainty in the halo velocity field. Lastly, the result of the *halo concentration-mass relation* (c_{200}, cf. Sec. 3.4.5 and Fig. 3.10) shows that in the cvG model, just as for the csG model, the Vainshtein screening is strong enough inside haloes that there is little effect of the fifth force.

The study of the weak lensing convergence and peak statistics are based on $10 \times 10\,\mathrm{deg}^2$ partial-sky maps. Firstly, the analysis of the *convergence map* (κ, cf. Sec. 3.4.7 and Fig. 3.11) shows that for smaller $\tilde{\beta}_3$ the convergence field is enhanced around massive structures for cvG with respect to its QCDM counterpart. This is reflected in the relative difference of the *probability distribution function of* κ ($\mathrm{PDF}(\kappa)$, cf. Sec. 3.4.7 and Fig. 3.11), which shows that cvG models with $\tilde{\beta}_3 \to 0$ have more pronounced under- and overdense regions. Secondly, the relative difference of the *angular power spectrum* (C_ℓ, cf. Sec. 3.4.7 and Fig. 3.11) is largest on linear scales $\ell \lesssim 3 \times 10^2$, while for higher multipoles the model differences reduce. Lastly, the relative difference of the *weak lensing peak abundance* (N_p, cf. Sec. 3.4.7 and Fig. 3.11) shows larger (smaller) numbers of high- (low-)amplitude peaks for $\nu > 1$ ($\nu < 1$) in the cvG models with $\tilde{\beta}_3 \to 0$, because the fifth force enhances the convergence values of the peak pixels.

The last topic we studied was 2D void statistics based on the same partial-sky maps that we used for weak lensing statistics. Firstly, the relative difference of the tunnel and watershed *void abundances* ($N(> R_\mathrm{v})$, cf. Sec. 3.4.8 and Fig. 3.13, 3.15) show fewer large-sized voids in the cvG cosmologies compared to their QCDM counterpart, since they produce more weak lensing peaks which split large voids into smaller ones in case of tunnel voids, or increase the convergence values so that the regions satisfying the chosen void definition criterion shrink in size in case of watershed voids. Secondly, the relative difference of the *tangential*

shear profile for tunnels and watershed voids (cf. Sec. 3.4.8 and Fig. 3.14, 3.15) peak at approximately the void radius, with larger enhancements as $\tilde{\beta}_3 \to 0$.

In conclusion, we find that for the studied cvG model, the strongest imprint of the modifications to Einstein's theory of gravity is on velocity and lensing statistics. This suggests that redshift space distortions and weak lensing shear correlation functions can both be promising cosmological probes to constrain the $\tilde{\beta}_3$ parameter in this model. On small scales, the cvG model is generally more difficult to constrain because the screening mechanism suppresses the fifth force effect; for example, internal properties of haloes, such as the concentration-mass relation, are insensitive to the fifth force.

Strong Lensing

The last part of the thesis, Chapter 4, is devoted to quantify the influence of secondary deflectors along the line-of-sight on time-delay measurements of H_0. We base our analysis on 800 galaxy-scale lensing systems with quadruply-lensed variable point sources. Half of the lensing systems were created with multiple lens plane ray-tracing, one plane for the primary lens and each line-of-sight halo, while the other half use one lens plane that includes the same primary lenses plus a constant external convergence and shear. The light cones were derived from the *CosmoDC2* semi-analytical extra-galactic catalogue. As it is based on a DM-only simulation, we have used SIE profiles in place of identified haloes to better represent the total mass (baryons + dark matter) profiles of real lens galaxies. A side effect of this can be that the lensing strength of any lower mass haloes, which in the real Universe may not have accrued baryons, could be artificially enhanced by the more efficient isothermal profile. In addition, our simulated datasets do not include any large scale structure such as filaments although this is expected to be a small effect. As time delay studies select lens systems that are apparently free of strong perturbers in an attempt to exclude line-of-sight effects, we mimicked

this choice to a degree by removing haloes from all of our light cones that produce a deflection resulting in an Einstein radius larger than 0.3 arcsec.

Our main conclusion is that simple corrections for line-of-sight structure, such as through constant external shear or external convergence, in estimations of H_0 using lensed time delays can not be relied upon in general. If time-delays are subjected to perturbations due to haloes lying close to the line-of-sight the inferred value of H_0 is over-estimated by approximately 4% on average with no correction or the incorporation of a constant external shear and under-estimated by $\sim 7\%$ per cent on average if a constant external convergence is incorporated.

These results were obtained from simulations with a relatively high median external convergence ($\kappa_{\rm ext} \simeq 0.11$). Our findings indicate however, that even small values of $\kappa_{\rm ext}$ bias H_0 on average. We have shown that the fractional bias in inferred H_0 correlates with median external convergence according to the linear relationship $\Delta H_0 / H_0 = 0.626\kappa_{\rm ext} - 0.005$.

With the forthcoming large sample of strong lensing time delay systems observed by the future time domain large scale surveys, e.g., Mephisto[1] and LSST, the effect becomes even more problematic.

[1] http://www.swifar.ynu.edu.cn/info/1015/1073.htm

5.2 Future Work

Naturally, the work developed for this thesis could only cover a finite number of investigations of the phenomenology of the cvG model and time-delay cosmography. Next, and before we finish, we briefly outline what we believe are amongst the most interesting ways to extend the analysis.

Cubic Vector Galileon

To better understand the cosmological behaviours and observational implications of the cvG model studied in this thesis, a more comprehensive investigation of the predictions of various physical quantities is

needed, which requires more independent realisations of larger volume and higher resolution simulations. This will allow us to, e.g., understand better why weak lensing by 2D voids do not seem to be as promising a probe, even though the lensing potential is significantly modified in low-density regions. Extending the analysis to properties of 3D voids found from halo or mock galaxy catalogues is also of interest, especially the redshift-space distortion around them. We have also seen indications for weak lensing by galaxy clusters being a powerful probe to constrain the cvG model. To follow up on this finding, we will need to perform an analysis of stacked weak lensing convergence profiles, which will be doable once we have produced lightcones that cover a larger patch of sky.

Furthermore in Chapter 3 we set out to find key statistics that can be used to put tight constrains the cvG model parameter. However, in order to make a connection between the N-body simulations and galaxy surveys, it is necessary to include galaxies. This can be done through semi-analytical models of galaxy formation, such as GALFORM. The coupling of semi-analytical models to the cvG simulations is not straightforward as care needs to be taken to ensure that the equations of the semi-analytical models are appropriately modified to take the effects of the screening mechanisms into account. This would open up the possibility to investigate more accurately how the cvG model can be constrained using cross-correlation between galaxies and the integrated Sachs-Wolfe (ISW) effect, a test that has already been shown to be promising by [154], using our ray-tracing code presented in Sec. 3.2.

Another approach would be to include baryonic matter and run hydrodynamic simulations. Although they are far slower than DM-only simulations, they have increased in computational efficiency and are now able to model in detail the evolution galaxy population in cosmological volumes over cosmic time, achieving encouraging matches to observations [e.g., 145, 170, 130]. Recently, [114] have extended the SHYBONE (Simulating HYdrodynamics BeyONd Einstein) simulations [10] to explore galaxy formation in the nDGP model. These simulations use the Arepo code [197] and employed its AMR modified gravity solver together

with the IllustrisTNG galaxy formation model [219, 170]. Modifying the SHYBONE extensions, one can implement the cvG model in a similar manner.

Besides improving the cosmological simulations, we can also improve the cosmological model that was studied. Various studies that use observations to constrain the GP model [e.g., 64, 65, 111] have shown that the model studied here, with linear functional form for $G_{2,3}$, has a poor fit to the observational data. Therefore it is of interest to extend the simulations to the more general case in the $G_{2,3}$ are not linear. However, our work suggests, that adding massive neutrinos with significantly nonzero mass [see, e.g., 19] may be a way to make the GP model with linear $G_{2,3}$ agree better with data. A promising path to add massive neutrinos into the cosmological simulations would be to make use of the "δf" method as implemented by [82] in `SWIFT` [208].

Finally, even though we have justified the neglect of the transverse mode of the vector field B^i in cosmological simulations, it is possible that in other situations this is no longer a good approximation. For example, the GP field does not have to be the driving force behind the accelerated cosmological background expansion, but might have effects on galactic scales and the transverse modes could give rise to a change of structure formation on such scales. With some appropriate adaption and extension, our code will be able to be used as a tool for investigations in such circumstances.

Strong Lensing

To decrease the measurement uncertainties of H_0 based on strong lensing time-delays, we can improve our methodology along multiple paths.

Firstly, the results based on the Outer Rim cosmological N-body simulation can be made more accurate by including sub-structure of the primary lens in to the ray-tracing routine through which lensing observables are obtained. These are currently neglected as we assume a single smooth SIE profile for each primary lens. Their inclusion will improve

bias and uncertainty estimates, as it is known that even microlensing can significantly magnify and demagnify the lensed object [e.g., 45, 76]. Since our simulations span a range of lens systems each with a different median external convergence, $\kappa_{\rm ext}$, it will also be interesting to investigate whether there is any correlation between the bias we see in inferred H_0 and $\kappa_{\rm ext}$. Identifying such a correlation might instruct future studies on how best to minimise the bias. Another open question that should be answered in the future, is how our results are affected by changing the lens system selection criterion, which currently depends solemnly on the size of the Einstein radius, to consider the flexion shift as done by [180]. Their approach would result in a different catalogue of lens systems and thus might alter the estimation of H_0. A removal of the H_0 bias through a different lens system catalogue alone is however not expected as long as the lens modelling does not incorporate multiple lens planes to account for line-of-sight structures that will be present in some systems.

Secondly, as for the cvG simulations our current results are based on DM-only simulations which can be improved by using hydrodynamic simulation. Besides leading to more realistic lens mass profiles, it would allow for a more realistic lens-galaxy selection based on currently confirmed strong lenses from, e.g., the Sloan Lens ACS Survey (SLACS, [e.g., 159, 194]) and the Strong Lensing Legacy Survey (SL2S, [e.g., 93, 196]). Using hydrodynamic simulations lets us include more observables based on the stellar population of galaxies to select and model lens-galaxies, such as stellar mass and stellar velocity dispersion. Especially including measurements of the latter in the modelling process can reduce the error on $D_{\Delta t}$ by a factor of 10 [201]. With next generation lensing surveys (for example with EUCLID [206]), the number of lenses for which such additional observables will be available will increase by orders of magnitude and it is thus important to study different methodologies through simulations.

5.3 Concluding remarks

It is an exciting time to be cosmologist. The deluge of data, both on the scales of the faintest galaxies in the local Universe, as well as on the largest, cosmological scales means that we currently have more information in our hands about our Universe than at any time previously. It brings with it potential challenges to our current understanding of the physical foundations of cosmology. One of the most statistically significant challenges is the disagreement between predictions of the Hubble-Lemaître constant made by a number of independent early- and late-time probes from measurements of distances and redshifts. This thesis has presented the study of a novel theoretical model that could alleviate and systematic errors within strong lensing time delay measurements that could explain the Hubble tension. The results presented here will help to design new observational tests and avoid catastrophic systematic errors in the interpretation of upcoming high-precision data delivered by, e.g., DESI, LSST, EUCLID.

Bibliography

[1] B. P. Abbott and others. Gravitational Waves and Gamma-rays from a Binary Neutron Star Merger: GW170817 and GRB 170817A. *Astrophys. J.*, 848(2):L13, 2017. doi: 10.3847/2041-8213/aa920c. _eprint: 1710.05834.

[2] B. P. Abbott and others. GW170817: Observation of Gravitational Waves from a Binary Neutron Star Inspiral. *Phys. Rev. Lett.*, 119(16):161101, 2017. doi: 10.1103/PhysRevLett.119.161101. _eprint: 1710.05832.

[3] Paul A. Abell and others. LSST Science Book, Version 2.0. 2009. _eprint: 0912.0201.

[4] G. E. Addison, D. J. Watts, C. L. Bennett, M. Halpern, G. Hinshaw, and J. L. Weiland. Elucidating \ensuremath\LambdaCDM: Impact of Baryon Acoustic Oscillation Measurements on the Hubble Constant Discrepancy. *apj*, 853(2):119, February 2018. doi: 10.3847/1538-4357/aaa1ed. _eprint: 1707.06547.

[5] P.A.R. Ade and others. Planck 2015 results. XIII. Cosmological parameters. *Astron. Astrophys.*, 594: A13, 2016. doi: 10.1051/0004-6361/201525830. _eprint: 1502.01589.

[6] Rachel Akeson, Lee Armus, Etienne Bachelet, Vanessa Bailey, Lisa Bartusek, Andrea Bellini, Dominic Benford, David Bennett, Aparna Bhattacharya, Ralph Bohlin, Martha Boyer, Valerio Bozza, Geoffrey Bryden, Sebastiano Calchi Novati, Kenneth Carpenter, Stefano Casertano, Ami Choi, David Content, Pratika Dayal, Alan Dressler, Olivier Doré, S. Michael Fall, Xiaohui Fan, Xiao Fang, Alexei Filippenko, Steven Finkelstein, Ryan Foley, Steven Furlanetto, Jason Kalirai, B. Scott Gaudi, Karoline Gilbert, Julien Girard, Kevin Grady, Jenny Greene, Puragra Guhathakurta, Chen Heinrich, Shoubaneh Hemmati, David Hendel, Calen Henderson, Thomas Henning, Christopher Hirata, Shirley Ho, Eric Huff, Anne Hutter, Rolf Jansen, Saurabh Jha, Samson Johnson, David Jones, Jeremy Kasdin, Patrick Kelly, Robert Kirshner, Anton Koekemoer, Jeffrey Kruk, Nikole Lewis, Bruce Macintosh, Piero Madau, Sangeeta Malhotra, Kaisey Mandel, Elena Massara, Daniel Masters, Julie McEnery, Kristen McQuinn,

Peter Melchior, Mark Melton, Bertrand Mennesson, Molly Peeples, Matthew Penny, Saul Perlmutter, Alice Pisani, Andrés Plazas, Radek Poleski, Marc Postman, Clément Ranc, Bernard Rauscher, Armin Rest, Aki Roberge, Brant Robertson, Steven Rodney, James Rhoads, Jason Rhodes, Russell Ryan Jr., Kailash Sahu, David Sand, Dan Scolnic, Anil Seth, Yossi Shvartzvald, Karelle Siellez, Arfon Smith, David Spergel, Keivan Stassun, Rachel Street, Louis-Gregory Strolger, Alexander Szalay, John Trauger, M. A. Troxel, Margaret Turnbull, Roeland van der Marel, Anja von der Linden, Yun Wang, David Weinberg, Benjamin Williams, Rogier Windhorst, Edward Wollack, Hao-Yi Wu, Jennifer Yee, and Neil Zimmerman. The Wide Field Infrared Survey Telescope: 100 Hubbles for the 2020s. *arXiv:1902.05569 [astro-ph]*, February 2019. URL http://arxiv.org/abs/1902.05569. arXiv: 1902.05569.

[7] Shadab Alam, Alejandro Aviles, Rachel Bean, Yan-Chuan Cai, Marius Cautun, Jorge L. Cervantes-Cota, Carolina Cuesta-Lazaro, N. Chandrachani Devi, Alexander Eggemeier, Sebastien Fromenteau, Alma X. Gonzalez-Morales, Vitali Halenka, Jian-hua He, Wojciech A. Hellwing, Cesar Hernandez-Aguayo, Mustapha Ishak, Kazuya Koyama, Baojiu Li, Axel de la Macorra, Jennifer Menesses Rizo, Christopher Miller, Eva-Maria Mueller, Gustavo Niz, Pierros Ntelis, Matias Rodriguez Otero, Cristiano G. Sabiu, Zachary Slepian, Alejo Stark, Octavio Valenzuela, Georgios Valogiannis, Mariana Vargas-Magana, Hans A. Winther, Pauline Zarrouk, Gong-Bo Zhao, and Yi Zheng. Testing the theory of gravity with DESI: estimators, predictions and simulation requirements. *arXiv:2011.05771 [astro-ph]*, November 2020. URL http://arxiv.org/abs/2011.05771. arXiv: 2011.05771.

[8] Erwan Allys, Patrick Peter, and Yeinzon Rodriguez. Generalized Proca action for an Abelian vector field. *JCAP*, 02:004, 2016. doi: 10.1088/1475-7516/2016/02/004. _eprint: 1511.03101.

[9] Luca Amendola and Shinji Tsujikawa. *Dark Energy: Theory and Observations*. Cambridge University Press, 2015. ISBN 978-1-107-45398-2.

[10] Christian Arnold, Matteo Leo, and Baojiu Li. Realistic simulations of galaxy formation in f(R) modified gravity. *Nature Astronomy*, 3(10):945–954, October 2019. ISSN 2397-3366. doi: 10.1038/s41550-019-0823-y. URL http://www.nature.com/articles/s41550-019-0823-y.

[11] Marika Asgari and others. KiDS-1000 Cosmology: Cosmic shear constraints and comparison between two point statistics. *arXiv*, page arXiv:2007.15633, 2020. _eprint: 2007.15633.

[12] E. Babichev, C. Deffayet, and R. Ziour. The Recovery of General Relativity in massive gravity via the Vainshtein mechanism. *Phys. Rev. D*, 82:104008, 2010. doi: 10.1103/PhysRevD.82.104008. _eprint: 1007.4506.

[13] Tessa Baker and others. The Novel Probes Project – Tests of Gravity on Astrophysical Scales. 2019. _eprint: 1908.03430.

[14] Tessa Baker, Joseph Clampitt, Bhuvnesh Jain, and Mark Trodden. Void Lensing as a Test of Gravity. *Phys. Rev. D*, 98(2):023511, 2018. doi: 10.1103/PhysRevD.98.023511. _eprint: 1803.07533.

[15] Tobias Baldauf. Effective Field Theory of Large-Scale Structure. *Les Houches Lect. Notes*, 108, 2020. doi: 10.1093/oso/9780198855743.003.0007.

[16] Alexandre Barreira, Baojiu Li, Carlton M. Baugh, and Silvia Pascoli. Spherical collapse in Galileon gravity: fifth force solutions, halo mass function and halo bias. *JCAP*, 1311:056, 2013. doi: 10.1088/1475-7516/2013/11/056. _eprint: 1308.3699.

[17] Alexandre Barreira, Baojiu Li, Wojciech A. Hellwing, Carlton M. Baugh, and Silvia Pascoli. Nonlinear structure formation in the Cubic Galileon gravity model. *J. Cosmo. Astropart. Phys.*, 1310:027, 2013. doi: 10.1088/1475-7516/2013/10/027. _eprint: 1306.3219.

[18] Alexandre Barreira, Baojiu Li, Ariel Sanchez, Carlton M. Baugh, and Silvia Pascoli. Parameter space in Galileon gravity models. *Phys. Rev. D*, 87:103511, 2013. doi: 10.1103/PhysRevD.87.103511. _eprint: 1302.6241.

[19] Alexandre Barreira, Baojiu Li, Carlton Baugh, and Silvia Pascoli. Modified gravity with massive neutrinos as a testable alternative cosmological model. *Phys. Rev. D*, 90(2):023528, 2014. doi: 10.1103/PhysRevD.90.023528. _eprint: 1404.1365.

[20] Alexandre Barreira, Baojiu Li, Carlton Baugh, and Silvia Pascoli. The observational status of Galileon gravity after Planck. *JCAP*, 08:059, 2014. doi: 10.1088/1475-7516/2014/08/059. _eprint: 1406.0485.

[21] Alexandre Barreira, Baojiu Li, Wojciech A. Hellwing, Lucas Lombriser, Carlton M. Baugh, and Silvia Pascoli. Halo model and halo properties in Galileon gravity cosmologies. *JCAP*, 04:029, 2014. doi: 10.1088/1475-7516/2014/04/029. _eprint: 1401.1497.

[22] Alexandre Barreira, Marius Cautun, Baojiu Li, Carlton Baugh, and Silvia Pascoli. Weak lensing by voids in modified lensing potentials. *JCAP*, 08:028, 2015. doi: 10.1088/1475-7516/2015/08/028. _eprint: 1505.05809.

[23] Alexandre Barreira, Baojiu Li, Elise Jennings, Julian Merten, Lindsay King, Carlton Baugh, and Silvia Pascoli. Galaxy cluster lensing masses in modified lensing potentials. *Mon. Not. Roy. Astron. Soc.*, 454(4):4085–4102, 2015. doi: 10.1093/mnras/stv2211. _eprint: 1505.03468.

[24] Alexandre Barreira, Claudio Llinares, Sownak Bose, and Baojiu Li. RAY-RAMSES: a code for ray tracing on the fly in N-body simulations. *J. Cosmo. Astropart. Phys.*, 05:001, 2016. doi: 10.1088/1475-7516/2016/05/001. _eprint: 1601.02012.

[25] Alexandre Barreira, Sownak Bose, Baojiu Li, and Claudio Llinares. Weak lensing by galaxy troughs with modified gravity. *J. Cosmo. Astropart. Phys.*, 02:031, 2017. doi: 10.1088/1475-7516/2017/02/031. _eprint: 1605.08436.

[26] Christoph Becker, Christian Arnold, Baojiu Li, and Lavinia Heisenberg. Proca-stinated Cosmology I: A N-body code for the vector Galileon. *J. Cosmo. Astropart. Phys.*, page ıt in press, 2020. _eprint: 2007.03042.

[27] Peter S. Behroozi, Risa H. Wechsler, and Hao-Yi Wu. The Rockstar Phase-Space Temporal Halo Finder and the Velocity Offsets of Cluster Cores. *Astrophys. J.*, 762:109, 2013. doi: 10.1088/0004-637X/762/2/109. _eprint: 1110.4372.

[28] Emilio Bellini, Raul Jimenez, and Licia Verde. Signatures of Horndeski gravity on the Dark Matter Bispectrum. *JCAP*, 05:057, 2015. doi: 10.1088/1475-7516/2015/05/057. _eprint: 1504.04341.

[29] Jose Beltran Jimenez and Lavinia Heisenberg. Derivative self-interactions for a massive vector field. *Phys. Lett.*, B757:405–411, 2016. doi: 10.1016/j.physletb.2016.04.017. _eprint: 1602.03410.

[30] F. Bernardeau, S. Colombi, E. Gaztañaga, and R. Scoccimarro. Large-scale structure of the Universe and cosmological perturbation theory. *Physics Reports*, 367(1-3):1–248, September 2002. ISSN 03701573. doi: 10.1016/S0370-1573(02)00135-7. URL https://linkinghub.elsevier.com/retrieve/pii/S0370157302001357.

[31] S. Birrer and others. H0LiCOW - IX. Cosmographic analysis of the doubly imaged quasar SDSS 1206+4332 and a new measurement of the Hubble constant. *Mon. Not. Roy. Astron. Soc.*, 484:4726, 2019. doi: 10.1093/mnras/stz200. _eprint: 1809.01274.

[32] Simon Birrer and Adam Amara. Lenstronomy: multi-purpose gravitational lens modelling software package. *ArXiv e-prints*, 2018. doi: 10.1016/j.dark.2018.11.002. _eprint: 1803.09746.

[33] Simon Birrer, Adam Amara, and Alexandre Refregier. Gravitational lens modeling with basis sets. *Astrophys. J.*, 813(2):102, 2015. doi: 10.1088/0004-637X/813/2/102. _eprint: 1504.07629.

[34] Simon Birrer, Adam Amara, and Alexandre Refregier. The mass-sheet degeneracy and time-delay cosmography: Analysis of the strong lens RXJ1131-1231. *JCAP*, 1608(08):020, 2016. doi: 10.1088/1475-7516/2016/08/020. _eprint: 1511.03662.

[35] Simon Birrer, Adam Amara, and Alexandre Refregier. Lensing substructure quantification in RXJ1131-1231: a 2 keV lower bound on dark matter thermal relic mass. *jcap*, 2017(5):037, May 2017. doi: 10.1088/1475-7516/2017/05/037. _eprint: 1702.00009.

[36] Rahul Biswas, Esfandiar Alizadeh, and Benjamin D. Wandelt. Voids as a precision probe of dark energy. *Physical Review D*, 82(2):023002, July 2010. ISSN 1550-7998, 1550-2368. doi: 10.1103/PhysRevD.82.023002. URL https://link.aps.org/doi/10.1103/PhysRevD.82.023002.

[37] Adam S. Bolton, Joel R. Brownstein, Christopher S. Kochanek, Yiping Shu, David J. Schlegel, Daniel J. Eisenstein, David A. Wake, Natalia Connolly, Claudia Maraston, Ryan A. Arneson, and Benjamin A. Weaver. The BOSS Emission-Line Lens Survey. II. Investigating Mass-density Profile Evolution in the SLACS+BELLS Strong Gravitational Lens Sample. *apj*, 757:82, September 2012. doi: 10.1088/0004-637X/757/1/82.

[38] V. Bonvin, F. Courbin, S. H. Suyu, P. J. Marshall, C. E. Rusu, D. Sluse, M. Tewes, K. C. Wong, T. Collett, C. D. Fassnacht, T. Treu, M. W. Auger, S. Hilbert, L. V. E. Koopmans, G. Meylan, N. Rumbaugh, A. Sonnenfeld, and C. Spiniello. H0LiCOW - V. New COSMOGRAIL time delays of HE 0435-1223: H_0 to 3.8 per cent precision from strong lensing in a flat \ensuremath\LambdaCDM model. *mnras*, 465(4): 4914–4930, March 2017. doi: 10.1093/mnras/stw3006. _eprint: 1607.01790.

[39] E. G. Patrick Bos, Rien van de Weygaert, Klaus Dolag, and Valeria Pettorino. The darkness that shaped the void: dark energy and cosmic voids: The darkness that shaped the void. *Monthly Notices of the Royal Astronomical Society*, 426(1):440–461, October 2012. ISSN 00358711. doi: 10.1111/j.1365-2966.2012.21478.x. URL https://academic.oup.com/mnras/article-lookup/doi/10.1111/j.1365-2966.2012.21478.x.

[40] Benjamin Bose and Atsushi Taruya. The one-loop matter bispectrum as a probe of gravity and dark energy. *J. Cosmo. Astropart. Phys.*, 10:019, 2018. doi: 10.1088/1475-7516/2018/10/019. _eprint: 1808.01120.

[41] Benjamin Bose, Joyce Byun, Fabien Lacasa, Azadeh Moradinezhad Dizgah, and Lucas Lombriser. Modelling the matter bispectrum at small scales in modified gravity. *J. Cosmo. Astropart. Phys.*, 02: 025, 2020. doi: 10.1088/1475-7516/2020/02/025. _eprint: 1909.02504.

[42] Yan-Chuan Cai, Nelson Padilla, and Baojiu Li. Testing Gravity using Cosmic Voids. *Mon. Not. Roy. Astron. Soc.*, 451(1):1036–1055, 2015. doi: 10.1093/mnras/stv777. _eprint: 1410.1510.

[43] Marius Cautun, Enrique Paillas, Yan-Chuan Cai, Sownak Bose, Joaquin Armijo, Baojiu Li, and Nelson Padilla. The Santiago–Harvard–Edinburgh–Durham void comparison – I. SHEDding light on chameleon gravity tests. *Mon. Not. Roy. Astron. Soc.*, 476(3):3195–3217, 2018. doi: 10.1093/mnras/sty463. _eprint: 1710.01730.

[44] Marius C. Cautun and Rien van de Weygaert. The DTFE public software: The Delaunay Tessellation Field Estimator code. May 2011. _eprint: 1105.0370.

[45] K. Chang and S. Refsdal. Flux variations of QSO 0957 + 561 A, B and image splitting by stars near the light path. *Nature*, 282(5739):561–564, December 1979. ISSN 0028-0836, 1476-4687. doi: 10.1038/282561a0. URL http://www.nature.com/articles/282561a0.

[46] Geoff C. F. Chen, Christopher D. Fassnacht, Sherry H. Suyu, Cristian E. Rusu, James H. H. Chan, Kenneth C. Wong, Matthew W. Auger, Stefan Hilbert, Vivien Bonvin, Simon Birrer, Martin Millon, Léon V. E. Koopmans, David J. Lagattuta, John P. McKean, Simona Vegetti, Frederic Courbin, Xuheng Ding, Aleksi Halkola, Inh Jee, Anowar J. Shajib, Dominique Sluse, Alessand ro Sonnenfeld, and Tommaso Treu. A SHARP view of H0LiCOW: H_0 from three time-delay gravitational lens systems with adaptive optics imaging. *mnras*, 490(2):1743–1773, December 2019. doi: 10.1093/mnras/stz2547. _eprint: 1907.02533.

[47] Joseph Clampitt and Bhuvnesh Jain. Lensing Measurements of the Mass Distribution in SDSS Voids. *Mon. Not. Roy. Astron. Soc.*, 454(4):3357–3365, 2015. doi: 10.1093/mnras/stv2215. _eprint: 1404.1834.

[48] DES Collaboration. Dark Energy Survey Year 1 Results: Cosmological Constraints from Cluster Abundances and Weak Lensing. *arXiv e-prints*, February 2020. URL https://arxiv.org/abs/2002.11124. _eprint: 2002.11124.

[49] T. E. Collett. The Population of Galaxy\ndashGalaxy Strong Lenses in Forthcoming Optical Imaging Surveys. *apj*, 811:20, September 2015. doi: 10.1088/0004-637X/811/1/20. _eprint: 1507.02657.

[50] T. E. Collett and S. D. Cunnington. Observational selection biases in time-delay strong lensing and their impact on cosmography. *mnras*, 462:3255–3264, November 2016. doi: 10.1093/mnras/stw1856. _eprint: 1605.08341.

[51] T. E. Collett, P. J. Marshall, M. W. Auger, S. Hilbert, S. H. Suyu, Z. Greene, T. Treu, C. D. Fassnacht, L. V. E. Koopmans, M. Bradač, and R. D. Blandford. Reconstructing the lensing mass in the Universe

from photometric catalogue data. *mnras*, 432:679–692, June 2013. doi: 10.1093/mnras/stt504. _eprint: 1303.6564.

[52] Stephane Colombi, Andrew H. Jaffe, Dmitri Novikov, and Christophe Pichon. Accurate estimators of power spectra in N-body simulations. *Mon. Not. Roy. Astron. Soc.*, 393:511, 2009. doi: 10.1111/j.1365-2966.2008.14176.x. _eprint: 0811.0313.

[53] William R. Coulton, Jia Liu, Ian G. McCarthy, and Ken Osato. Weak Lensing Minima and Peaks: Cosmological Constraints and the Impact of Baryons. *Mon. Not. Roy. Astron. Soc.*, 495(3):2531–2542, 2020. doi: 10.1093/mnras/staa1098. _eprint: 1910.04171.

[54] M. Crocce, S. Pueblas, and R. Scoccimarro. Transients from Initial Conditions in Cosmological Simulations. *Mon. Not. Roy. Astron. Soc.*, 373:369–381, 2006. doi: 10.1111/j.1365-2966.2006.11040.x. _eprint: astro-ph/0606505.

[55] Rocco D'Agostino and Rafael C. Nunes. Measurements of H_0 in modified gravity theories: The role of lensed quasars in the late-time Universe. *prd*, 101(10):103505, May 2020. doi: 10.1103/PhysRevD.101.103505. _eprint: 2002.06381.

[56] Christopher T. Davies, Marius Cautun, and Baojiu Li. Weak lensing by voids in weak lensing maps. *Mon. Not. Roy. Astron. Soc.*, 480(1):L101–L105, 2018. doi: 10.1093/mnrasl/sly135. _eprint: 1803.08717.

[57] Christopher T. Davies, Marius Cautun, and Baojiu Li. Cosmological test of gravity using weak lensing voids. *Mon. Not. Roy. Astron. Soc.*, 490(4):4907–4917, 2019. doi: 10.1093/mnras/stz2933. _eprint: 1907.06657.

[58] Christopher T. Davies, Marius Cautun, and Baojiu Li. The self similarity of weak lensing peaks. *Mon. Not. Roy. Astron. Soc.*, 488(4):5833–5851, 2019. doi: 10.1093/mnras/stz2157. _eprint: 1905.01710.

[59] Christopher T. Davies, Enrique Paillas, Marius Cautun, and Baojiu Li. Optimal void finders in weak lensing maps. 2020. _eprint: 2004.11387.

[60] Antonio De Felice and Shinji Tsujikawa. Cosmology of a covariant Galileon field. *Phys. Rev. Lett.*, 105: 111301, 2010. doi: 10.1103/PhysRevLett.105.111301. _eprint: 1007.2700.

[61] Antonio De Felice, Lavinia Heisenberg, Ryotaro Kase, Shinji Mukohyama, Shinji Tsujikawa, and Ying-li Zhang. Cosmology in generalized Proca theories. *JCAP*, 1606(06):048, 2016. doi: 10.1088/1475-7516/2016/06/048. _eprint: 1603.05806.

[62] Antonio De Felice, Lavinia Heisenberg, Ryotaro Kase, Shinji Mukohyama, Shinji Tsujikawa, and Ying-li Zhang. Effective gravitational couplings for cosmological perturbations in generalized Proca theories. *Phys. Rev. D*, 94(4):044024, 2016. doi: 10.1103/PhysRevD.94.044024. _eprint: 1605.05066.

[63] Antonio De Felice, Lavinia Heisenberg, Ryotaro Kase, Shinji Tsujikawa, Ying-li Zhang, and Gong-Bo Zhao. Screening fifth forces in generalized Proca theories. *Phys. Rev.*, D93(10):104016, 2016. doi: 10.1103/PhysRevD.93.104016. _eprint: 1602.00371.

[64] Antonio de Felice, Lavinia Heisenberg, and Shinji Tsujikawa. Observational constraints on generalized Proca theories. *Phys. Rev.*, D95(12):123540, 2017. doi: 10.1103/PhysRevD.95.123540. _eprint: 1703.09573.

[65] Antonio De Felice, Chao-Qiang Geng, Masroor C. Pookkillath, and Lu Yin. Reducing the $_0$ tension with generalized Proca theory. 2020. _eprint: 2002.06782.

[66] Claudia de Rham. Massive Gravity. *Living Rev. Rel.*, 17:7, 2014. doi: 10.12942/lrr-2014-7. _eprint: 1401.4173.

[67] Claudia de Rham, Scott Melville, Andrew J. Tolley, and Shuang-Yong Zhou. Positivity Bounds for Massive Spin-1 and Spin-2 Fields. *JHEP*, 03:182, 2019. doi: 10.1007/JHEP03(2019)182. _eprint: 1804.10624.

[68] C. Deffayet, S. Deser, and G. Esposito-Farese. Generalized Galileons: All scalar models whose curved background extensions maintain second-order field equations and stress-tensors. *Phys. Rev. D*, 80: 064015, 2009. doi: 10.1103/PhysRevD.80.064015. _eprint: 0906.1967.

[69] C. Deffayet, Gilles Esposito-Farese, and A. Vikman. Covariant Galileon. *Phys. Rev. D*, 79:084003, 2009. doi: 10.1103/PhysRevD.79.084003. _eprint: 0901.1314.

[70] C. Deffayet, Xian Gao, D.A. Steer, and G. Zahariade. From k-essence to generalised Galileons. *Phys. Rev. D*, 84:064039, 2011. doi: 10.1103/PhysRevD.84.064039. _eprint: 1103.3260.

[71] DESI Collaboration. The DESI Experiment Part I: Science,Targeting, and Survey Design. *arXiv:1611.00036 [astro-ph]*, December 2016. URL http://arxiv.org/abs/1611.00036. arXiv: 1611.00036.

[72] Vincent Desjacques, Donghui Jeong, and Fabian Schmidt. The Galaxy Power Spectrum and Bispectrum in Redshift Space. *JCAP*, 12:035, 2018. doi: 10.1088/1475-7516/2018/12/035. _eprint: 1806.04015.

[73] Suhail Dhawan, Saurabh W. Jha, and Bruno Leibundgut. Measuring the Hubble constant with Type Ia supernovae as near-infrared standard candles. *aap*, 609:A72, January 2018. doi: 10.1051/0004-6361/201731501. _eprint: 1707.00715.

[74] J. P. Dietrich and J. Hartlap. Cosmology with the shear-peak statistics. *Mon. Not. Roy. Astron. Soc.*, 402:1049, 2010. doi: 10.1111/j.1365-2966.2009.15948.x. _eprint: arXiv:0906.3512.

[75] G. Dobler, C. D. Fassnacht, T. Treu, P. Marshall, K. Liao, A. Hojjati, E. Linder, and N. Rumbaugh. Strong Lens Time Delay Challenge. I. Experimental Design. *apj*, 799:168, February 2015. doi: 10.1088/0004-637X/799/2/168.

[76] Gregory Dobler and Charles R. Keeton. Microlensing of Lensed Supernovae. *The Astrophysical Journal*, 653(2):1391–1399, December 2006. ISSN 0004-637X, 1538-4357. doi: 10.1086/508769. URL https://iopscience.iop.org/article/10.1086/508769.

[77] Alan R. Duffy, Joop Schaye, Scott T. Kay, and Claudio Dalla Vecchia. Dark matter halo concentrations in the Wilkinson Microwave Anisotropy Probe year 5 cosmology. *Mon. Not. Roy. Astron. Soc.*, 390:L64, 2008. doi: 10.1111/j.1745-3933.2008.00537.x. _eprint: 0804.2486.

[78] G.R. Dvali, Gregory Gabadadze, and Massimo Porrati. 4-D gravity on a brane in 5-D Minkowski space. *Phys. Lett. B*, 485:208–214, 2000. doi: 10.1016/S0370-2693(00)00669-9. _eprint: hep-th/0005016.

[79] Russell Eberhart and James Kennedy. Particle swarm optimization. In *Proceedings of the IEEE international conference on neural networks*, volume 4, pages 1942–1948, 1995.

[80] Alexander Eggemeier, Roman Scoccimarro, and Robert E. Smith. Bias Loop Corrections to the Galaxy Bispectrum. *Phys. Rev. D*, 99(12):123514, 2019. doi: 10.1103/PhysRevD.99.123514. _eprint: 1812.03208.

[81] A. Einstein. Die Grundlage der allgemeinen Relativitätstheorie. *Annalen der Physik*, 354(7):769–822, 1916. ISSN 00033804, 15213889. doi: 10.1002/andp.19163540702. URL https://onlinelibrary.wiley.com/doi/10.1002/andp.19163540702.

[82] Willem Elbers, Carlos S Frenk, Adrian Jenkins, Baojiu Li, and Silvia Pascoli. An optimal nonlinear method for simulating relic neutrinos. *Monthly Notices of the Royal Astronomical Society*, page stab2260, August 2021. ISSN 0035-8711, 1365-2966. doi: 10.1093/mnras/stab2260. URL https://academic.oup.com/mnras/advance-article/doi/10.1093/mnras/stab2260/6343051.

[83] S. M. Faber, C. N. A. Willmer, C. Wolf, D. C. Koo, B. J. Weiner, J. A. Newman, M. Im, A. L. Coil, C. Conroy, M. C. Cooper, M. Davis, D. P. Finkbeiner, B. F. Gerke, K. Gebhardt, E. J. Groth, P. Guhathakurta,

J. Harker, N. Kaiser, S. Kassin, M. Kleinheinrich, N. P. Konidaris, R. G. Kron, L. Lin, G. Luppino, D. S. Madgwick, K. Meisenheimer, K. G. Noeske, A. C. Phillips, V. L. Sarajedini, R. P. Schiavon, L. Simard, A. S. Szalay, N. P. Vogt, and R. Yan. Galaxy Luminosity Functions to z\raisebox-0.5ex\textasciitilde1 from DEEP2 and COMBO-17: Implications for Red Galaxy Formation. *apj*, 665(1):265–294, August 2007. doi: 10.1086/519294. _eprint: astro-ph/0506044.

[84] Bridget Falck, Kazuya Koyama, Gong-bo Zhao, and Baojiu Li. The Vainshtein Mechanism in the Cosmic Web. *JCAP*, 07:058, 2014. doi: 10.1088/1475-7516/2014/07/058. _eprint: 1404.2206.

[85] Bridget Falck, Kazuya Koyama, and Gong-Bo Zhao. Cosmic Web and Environmental Dependence of Screening: Vainshtein vs. Chameleon. *JCAP*, 07:049, 2015. doi: 10.1088/1475-7516/2015/07/049. _eprint: 1503.06673.

[86] Bridget Falck, Kazuya Koyama, Gong-Bo Zhao, and Marius Cautun. Using Voids to Unscreen Modified Gravity. *Mon. Not. Roy. Astron. Soc.*, 475(3):3262–3272, 2018. doi: 10.1093/mnras/stx3288. _eprint: 1704.08942.

[87] Pedro G. Ferreira. Cosmological Tests of Gravity. *Ann. Rev. Astron. Astrophys.*, 57:335–374, 2019. doi: 10.1146/annurev-astro-091918-104423. _eprint: 1902.10503.

[88] Matthew Fong, Miyoung Choi, Victoria Catlett, Brandyn Lee, Austin Peel, Rachel Bowyer, Lindsay J. King, and Ian G. McCarthy. The impact of baryonic physics and massive neutrinos on weak lensing peak statistics. *Mon. Not. Roy. Astron. Soc.*, 488(3):3340–3357, 2019. doi: 10.1093/mnras/stz1882. _eprint: 1907.03161.

[89] Daniel Foreman-Mackey. corner.py: Scatterplot matrices in Python. *The Journal of Open Source Software*, 1(2):24, June 2016. doi: 10.21105/joss.00024. URL https://doi.org/10.21105/joss.00024. Publisher: The Open Journal.

[90] Wendy L. Freedman, Barry F. Madore, Dylan Hatt, Taylor J. Hoyt, In Sung Jang, Rachael L. Beaton, Christopher R. Burns, Myung Gyoon Lee, Andrew J. Monson, Jillian R. Neeley, M. M. Phillips, Jeffrey A. Rich, and Mark Seibert. The Carnegie-Chicago Hubble Program. VIII. An Independent Determination of the Hubble Constant Based on the Tip of the Red Giant Branch. *apj*, 882(1):34, September 2019. doi: 10.3847/1538-4357/ab2f73. _eprint: 1907.05922.

[91] A. Friedmann. Über die Möglichkeit einer Welt mit konstanter negativer Krümmung des Raumes. *Zeitschrift für Physik*, 21(1):326–332, December 1924. ISSN 1434-6001, 1434-601X. doi: 10.1007/BF01328280. URL http://link.springer.com/10.1007/BF01328280.

[92] J. N. Fry. Statistics of voids in hierarchical universes. *The Astrophysical Journal*, 306:358, July 1986. ISSN 0004-637X, 1538-4357. doi: 10.1086/164348. URL http://adsabs.harvard.edu/doi/10.1086/164348.

[93] Raphaël Gavazzi, Tommaso Treu, Philip J. Marshall, Florence Brault, and Andrea Ruff. THE SL2S GALAXY-SCALE GRAVITATIONAL LENS SAMPLE. I. THE ALIGNMENT OF MASS AND LIGHT IN MASSIVE EARLY-TYPE GALAXIES AT z = 0.2-0.9. *The Astrophysical Journal*, 761(2):170, December 2012. ISSN 0004-637X, 1538-4357. doi: 10.1088/0004-637X/761/2/170. URL https://iopscience.iop.org/article/10.1088/0004-637X/761/2/170.

[94] Hector Gil-Marin, Fabian Schmidt, Wayne Hu, Raul Jimenez, and Licia Verde. The Bispectrum of f(R) Cosmologies. *JCAP*, 11:019, 2011. doi: 10.1088/1475-7516/2011/11/019. _eprint: 1109.2115.

[95] A. Goldstein and others. An Ordinary Short Gamma-Ray Burst with Extraordinary Implications: Fermi-GBM Detection of GRB 170817A. *Astrophys. J.*, 848(2):L14, 2017. doi: 10.3847/2041-8213/aa8f41. _eprint: 1710.05446.

[96] M.H. Goroff, Benjamin Grinstein, S.J. Rey, and Mark B. Wise. Coupling of Modes of Cosmological Mass Density Fluctuations. *Astrophys. J.*, 311:6–14, 1986. doi: 10.1086/164749.

[97] Z. S. Greene, S. H. Suyu, T. Treu, S. Hilbert, M. W. Auger, T. E. Collett, P. J. Marshall, C. D. Fassnacht, R. D. Blandford, M. Bradač, and L. V. E. Koopmans. Improving the Precision of Time-delay Cosmography with Observations of Galaxies along the Line of Sight. *apj*, 768:39, May 2013. doi: 10.1088/0004-637X/768/1/39. _eprint: 1303.3588.

[98] D. Gruen and others. Weak lensing by galaxy troughs in DES Science Verification data. *Mon. Not. Roy. Astron. Soc.*, 455(3):3367–3380, 2016. doi: 10.1093/mnras/stv2506. _eprint: 1507.05090.

[99] Suraj N. Gupta. Gravitation and Electromagnetism. *Phys. Rev.*, 96:1683–1685, 1954. doi: 10.1103/PhysRev.96.1683.

[100] Salman Habib, Adrian Pope, Hal Finkel, Nicholas Frontiere, Katrin Heitmann, David Daniel, Patricia Fasel, Vitali Morozov, George Zagaris, Tom Peterka, Venkatram Vishwanath, Zarija Lukić, Saba Sehrish, and Wei-keng Liao. HACC: Simulating sky surveys on state-of-the-art supercomputing architectures. *New Astronomy*, 42:49–65, January 2016. ISSN 13841076. doi: 10.1016/j.newast.2015.06.003. URL https://linkinghub.elsevier.com/retrieve/pii/S138410761500069X.

[101] ChangHoon Hahn, Francisco Villaescusa-Navarro, Emanuele Castorina, and Roman Scoccimarro.

Constraining M_ν with the bispectrum. Part I. Breaking parameter degeneracies. *JCAP*, 03:040, 2020. doi: 10.1088/1475-7516/2020/03/040. _eprint: 1909.11107.

[102] Nico Hamaus, P. M. Sutter, Guilhem Lavaux, and Benjamin D. Wandelt. Probing cosmology and gravity with redshift-space distortions around voids. *Journal of Cosmology and Astroparticle Physics*, 2015(11):036–036, November 2015. ISSN 1475-7516. doi: 10.1088/1475-7516/2015/11/036. URL http://arxiv.org/abs/1507.04363. arXiv: 1507.04363.

[103] Nico Hamaus, Alice Pisani, Paul M. Sutter, Guilhem Lavaux, Stéphanie Escoffier, Benjamin D. Wandelt, and Jochen Weller. Constraints on Cosmology and Gravity from the Dynamics of Voids. *Phys. Rev. Lett.*, 117(9):091302, 2016. doi: 10.1103/PhysRevLett.117.091302. _eprint: 1602.01784.

[104] Nico Hamaus, Alice Pisani, Jin-Ah Choi, Guilhem Lavaux, Benjamin D. Wandelt, and Jochen Wellera. Precision cosmology with voids in the final BOSS data. 2020. _eprint: 2007.07895.

[105] A. J. S. Hamilton. Linear Redshift Distortions: A Review. *Springer*, 231:185–275, 1998. doi: 10.1007/978-94-011-4960-0_17. ISBN: 978-94-010-6082-0.

[106] Nick Hand, Yu Feng, Florian Beutler, Yin Li, Chirag Modi, Uros Seljak, and Zachary Slepian. nbodykit: an open-source, massively parallel toolkit for large-scale structure. *Astron. J.*, 156(4):160, 2018. doi: 10.3847/1538-3881/aadae0. _eprint: 1712.05834.

[107] Ichihiko Hashimoto, Yann Rasera, and Atsushi Taruya. Precision cosmology with redshift-space bispectrum: a perturbation theory based model at one-loop order. *Phys. Rev. D*, 96(4):043526, 2017. doi: 10.1103/PhysRevD.96.043526. _eprint: 1705.02574.

[108] Lavinia Heisenberg. Generalization of the Proca Action. *J. Cosmo. Astropart. Phys.*, 1405:015, 2014. doi: 10.1088/1475-7516/2014/05/015. _eprint: 1402.7026.

[109] Lavinia Heisenberg. A systematic approach to generalisations of General Relativity and their cosmological implications. *Phys. Rept.*, 796:1–113, 2019. doi: 10.1016/j.physrep.2018.11.006. _eprint: 1807.01725.

[110] Lavinia Heisenberg and Matthias Bartelmann. Kinetic field theory applied to vector-tensor gravity. *Phys. Lett. B*, 796:59–64, 2019. doi: 10.1016/j.physletb.2019.07.004. _eprint: 1901.01041.

[111] Lavinia Heisenberg and Hector Villarrubia-Rojo. Proca in the sky. *Journal of Cosmology and Astroparticle Physics*, 2021(03):032, March 2021. ISSN 1475-7516. doi: 10.1088/1475-7516/2021/03/032. URL https://iopscience.iop.org/article/10.1088/1475-7516/2021/03/032.

[112] Lavinia Heisenberg, Ryotaro Kase, Masato Minamitsuji, and Shinji Tsujikawa. Black holes in vector-tensor theories. *J. Cosmo. Astropart. Phys.*, 1708(08):024, 2017. doi: 10.1088/1475-7516/2017/08/024. _eprint: 1706.05115.

[113] Katrin Heitmann, Hal Finkel, Adrian Pope, Vitali Morozov, Nicholas Frontiere, Salman Habib, Esteban Rangel, Thomas Uram, Danila Korytov, Hillary Child, Samuel Flender, Joe Insley, and Silvio Rizzi. The Outer Rim Simulation: A Path to Many-core Supercomputers. *\apjs*, 245(1):16, November 2019. doi: 10.3847/1538-4365/ab4da1. _eprint: 1904.11970.

[114] César Hernández-Aguayo, Christian Arnold, Baojiu Li, and Carlton M Baugh. Galaxy formation in the brane world I: overview and first results. *Monthly Notices of the Royal Astronomical Society*, 503(3):3867–3885, April 2021. ISSN 0035-8711, 1365-2966. doi: 10.1093/mnras/stab694. URL https://academic.oup.com/mnras/article/503/3/3867/6168396.

[115] Yuichi Higuchi and Masato Shirasaki. The imprint of $f(R)$ gravity on weak gravitational lensing – I. Connection between observables and large-scale structure. *Mon. Not. Roy. Astron. Soc.*, 459(3):2762–2776, 2016. doi: 10.1093/mnras/stw814. _eprint: 1603.01325.

[116] Chiaki Hikage and others. Cosmology from cosmic shear power spectra with Subaru Hyper Suprime-Cam first-year data. *Publ. Astron. Soc. Jap.*, 71(2):Publications of the Astronomical Society of Japan, Volume 71, Issue 2, April 2019, 43, https://doi.org/10.1093/pasj/psz010, 2019. doi: 10.1093/pasj/psz010. _eprint: 1809.09148.

[117] H. Hildebrandt and others. KiDS+VIKING-450: Cosmic shear tomography with optical and infrared data. *Astron. Astrophys.*, 633:A69, 2020. doi: 10.1051/0004-6361/201834878. _eprint: 1812.06076.

[118] G. W. Horndeski. Second-order scalar-tensor field equations in a four-dimensional space. *Int.J.Theor.Phys.*, 10:363, 1974.

[119] Bhuvnesh Jain and Ludovic Van Van Waerbeke. Statistics of dark matter halos from gravitational lensing. *Astrophys. J. Lett.*, 530:L1, 2000. doi: 10.1086/312480. _eprint: astro-ph/9910459.

[120] Elise Jennings. An improved model for the nonlinear velocity power spectrum. *Mon. Not. Roy. Astron. Soc.*, 427:L25–L29, 2012. doi: 10.1111/j.1745-3933.2012.01338.x. _eprint: 1207.1439.

[121] Nick Kaiser. Clustering in real space and in redshift space. *Monthly Notices of the Royal Astronomical Society*, 227(1):1–21, July 1987. ISSN 0035-8711, 1365-2966. doi: 10.1093/mnras/227.1.1. URL https://academic.oup.com/mnras/article-lookup/doi/10.1093/mnras/227.1.1.

[122] C. R. Keeton. A Catalog of Mass Models for Gravitational Lensing. *ArXiv Astrophysics e-prints*, February 2001. _eprint: astro-ph/0102341.

[123] Tsutomu Kobayashi, Masahide Yamaguchi, and Jun'ichi Yokoyama. Generalized G-inflation: Inflation with the most general second-order field equations. *Prog. Theor. Phys.*, 126:511–529, 2011. doi: 10.1143/PTP.126.511. _eprint: 1105.5723.

[124] L. V. E. Koopmans and C. D. Fassnacht. A Determination of H_0 with the CLASS Gravitational Lens B1608+656. II. Mass Models and the Hubble Constant from Lensing. *The Astrophysical Journal*, 527 (2):513–524, December 1999. ISSN 0004-637X, 1538-4357. doi: 10.1086/308120. URL https://iopscience.iop.org/article/10.1086/308120.

[125] L. V. E. Koopmans, T. Treu, A. S. Bolton, S. Burles, and L. A. Moustakas. The Sloan Lens ACS Survey. III. The Structure and Formation of Early-Type Galaxies and Their Evolution since $z \sim 1$. *\apj*, 649:599–615, October 2006. doi: 10.1086/505696. _eprint: astro-ph/0601628.

[126] R. Kormann, P. Schneider, and M. Bartelmann. Isothermal elliptical gravitational lens models. *\aap*, 284:285–299, April 1994.

[127] Danila Korytov, Andrew Hearin, Eve Kovacs, Patricia Larsen, Esteban Rangel, Joseph Hollowed, Andrew J. Benson, Katrin Heitmann, Yao-Yuan Mao, Anita Bahmanyar, Chihway Chang, Duncan Campbell, Joseph DeRose, Hal Finkel, Nicholas Frontiere, Eric Gawiser, Salman Habib, Benjamin Joachimi, François Lanusse, Nan Li, Rachel Mandelbaum, Christopher Morrison, Jeffrey A. Newman, Adrian Pope, Eli Rykoff, Melanie Simet, Chun-Hao To, Vinu Vikraman, Risa H. Wechsler, Martin White, and (The LSST Dark Energy Science Collaboration. CosmoDC2: A Synthetic Sky Catalog for Dark Energy Science with LSST. *\apjs*, 245(2):26, December 2019. doi: 10.3847/1538-4365/ab510c. _eprint: 1907.06530.

[128] Kazuya Koyama. Cosmological Tests of Modified Gravity. *Rept. Prog. Phys.*, 79(4):046902, 2016. doi: 10.1088/0034-4885/79/4/046902. _eprint: 1504.04623.

[129] Guilhem Lavaux and Benjamin D. Wandelt. PRECISION COSMOGRAPHY WITH STACKED VOIDS. *The Astrophysical Journal*, 754(2):109, August 2012. ISSN 0004-637X, 1538-4357. doi: 10.1088/0004-637X/754/2/109. URL https://iopscience.iop.org/article/10.1088/0004-637X/754/2/109.

[130] Jaehyun Lee, Jihye Shin, Owain N. Snaith, Yonghwi Kim, C. Gareth Few, Julien Devriendt, Yohan Dubois, Leah M. Cox, Sungwook E. Hong, Oh-Kyoung Kwon, Chan Park, Christophe Pichon, Juhan

Kim, Brad K. Gibson, and Changbom Park. The Horizon Run 5 Cosmological Hydrodynamical Simulation: Probing Galaxy Formation from Kilo- to Gigaparsec Scales. *The Astrophysical Journal*, 908(1):11, February 2021. ISSN 1538-4357. doi: 10.3847/1538-4357/abd08b. URL https://iopscience.iop.org/article/10.3847/1538-4357/abd08b.

[131] Antony Lewis and Anthony Challinor. *CAMB: Code for Anisotropies in the Microwave Background*. February 2011. _eprint: 1102.026.

[132] Baojiu Li. *Simulating Large-Scale Structure for Models of Cosmic Acceleration*. 2514-3433. IOP Publishing, 2018. ISBN 978-0-7503-1587-6. doi: 10.1088/978-0-7503-1587-6. URL http://dx.doi.org/10.1088/978-0-7503-1587-6.

[133] Baojiu Li and Hongsheng Zhao. Structure Formation by the Fifth Force III: Segregation of Baryons and Dark Matter. *Phys. Rev. D*, 81:104047, 2010. doi: 10.1103/PhysRevD.81.104047. _eprint: 1001.3152.

[134] Baojiu Li, Lindsay J. King, Gong-Bo Zhao, and HongSheng Zhao. A Semi-analytic Ray-tracing Algorithm for Weak Lensing. *Mon. Not. Roy. Astron. Soc.*, 415:881, 2011. doi: 10.1111/j.1365-2966.2011.18754.x. _eprint: 1012.1625.

[135] Baojiu Li, Gong-Bo Zhao, Romain Teyssier, and Kazuya Koyama. ECOSMOG: An Efficient Code for Simulating Modified Gravity. *J. Cosmo. Astropart. Phys.*, 1201:051, 2012. doi: 10.1088/1475-7516/2012/01/051. _eprint: 1110.1379.

[136] Baojiu Li, Alexandre Barreira, Carlton M. Baugh, Wojciech A. Hellwing, Kazuya Koyama, Silvia Pascoli, and Gong-Bo Zhao. Simulating the quartic Galileon gravity model on adaptively refined meshes. *JCAP*, 1311:012, 2013. doi: 10.1088/1475-7516/2013/11/012. _eprint: 1308.3491.

[137] Baojiu Li, Gong-Bo Zhao, and Kazuya Koyama. Exploring Vainshtein mechanism on adaptively refined meshes. *JCAP*, 1305:023, 2013. doi: 10.1088/1475-7516/2013/05/023. _eprint: 1303.0008.

[138] N. Li, M. D. Gladders, E. M. Rangel, M. K. Florian, L. E. Bleem, K. Heitmann, S. Habib, and P. Fasel. PICS: Simulations of Strong Gravitational Lensing in Galaxy Clusters. *apj*, 828:54, September 2016. doi: 10.3847/0004-637X/828/1/54. _eprint: 1511.03673.

[139] Zack Li, Jia Liu, José Manuel Zorrilla Matilla, and William R. Coulton. Constraining neutrino mass with tomographic weak lensing peak counts. *Phys. Rev. D*, 99(6):063527, 2019. doi: 10.1103/PhysRevD.99.063527. _eprint: 1810.01781.

[140] K. Liao, T. Treu, P. Marshall, C. D. Fassnacht, N. Rumbaugh, G. Dobler, A. Aghamousa, V. Bonvin, F. Courbin, A. Hojjati, N. Jackson, V. Kashyap, S. Rathna Kumar, E. Linder, K. Mandel, X.-L. Meng, G. Meylan, L. A. Moustakas, T. P. Prabhu, A. Romero-Wolf, A. Shafieloo, A. Siemiginowska, C. S. Stalin, H. Tak, M. Tewes, and D. van Dyk. Strong Lens Time Delay Challenge. II. Results of TDC1. *apj*, 800: 11, February 2015. doi: 10.1088/0004-637X/800/1/11. _eprint: 1409.1254.

[141] Jia Liu, J. Colin Hill, Blake D. Sherwin, Andrea Petri, Vanessa Böhm, and Zoltán Haiman. CMB lensing beyond the power spectrum: Cosmological constraints from the one-point probability distribution function and peak counts. *Phys. Rev. D*, 94(10):103501, 2016. doi: 10.1103/PhysRevD.94.103501. _eprint: 1608.03169.

[142] E. Macaulay, R. C. Nichol, D. Bacon, D. Brout, T. M. Davis, B. Zhang, B. A. Bassett, D. Scolnic, A. Möller, C. B. D'Andrea, S. R. Hinton, R. Kessler, A. G. Kim, J. Lasker, C. Lidman, M. Sako, M. Smith, M. Sullivan, T. M. C. Abbott, S. Allam, J. Annis, J. Asorey, S. Avila, K. Bechtol, D. Brooks, P. Brown, D. L. Burke, J. Calcino, A. Carnero Rosell, D. Carollo, M. Carrasco Kind, J. Carretero, F. J. Castander, T. Collett, M. Crocce, C. E. Cunha, L. N. da Costa, C. Davis, J. De Vicente, H. T. Diehl, P. Doel, A. Drlica-Wagner, T. F. Eifler, J. Estrada, A. E. Evrard, A. V. Filippenko, D. A. Finley, B. Flaugher, R. J. Foley, P. Fosalba, J. Frieman, L. Galbany, J. García-Bellido, E. Gaztanaga, K. Glazebrook, S. González-Gaitán, D. Gruen, R. A. Gruendl, J. Gschwend, G. Gutierrez, W. G. Hartley, D. L. Hollowood, K. Honscheid, J. K. Hoormann, B. Hoyle, D. Huterer, B. Jain, D. J. James, T. Jeltema, E. Kasai, E. Krause, K. Kuehn, N. Kuropatkin, O. Lahav, G. F. Lewis, T. S. Li, M. Lima, H. Lin, M. A. G. Maia, J. L. Marshall, P. Martini, R. Miquel, P. Nugent, A. Palmese, Y.-C. Pan, A. A. Plazas, A. K. Romer, A. Roodman, E. Sanchez, V. Scarpine, R. Schindler, M. Schubnell, S. Serrano, I. Sevilla-Noarbe, R. Sharp, M. Soares-Santos, F. Sobreira, N. E. Sommer, E. Suchyta, E. Swann, M. E. C. Swanson, G. Tarle, D. Thomas, R. C. Thomas, B. E. Tucker, S. A. Uddin, V. Vikram, A. R. Walker, P. Wiseman, and DES Collaboration. First cosmological results using Type Ia supernovae from the Dark Energy Survey: measurement of the Hubble constant. *mnras*, 486:2184–2196, June 2019. doi: 10.1093/mnras/stz978. _eprint: 1811.02376.

[143] Andrea V. Maccio', Aaron A. Dutton, Frank C. van den Bosch, Ben Moore, Doug Potter, and Joachim Stadel. Concentration, Spin and Shape of Dark Matter Haloes: Scatter and the Dependence on Mass and Environment. *Mon. Not. Roy. Astron. Soc.*, 378:55–71, 2007. doi: 10.1111/j.1365-2966.2007.11720.x. _eprint: astro-ph/0608157.

[144] Hugo Martel and Paul R. Shapiro. A convenient set of comoving cosmological variables and their

application. *Mon. Not. Roy. Astron. Soc.*, 297:467, 1998. doi: 10.1046/j.1365-8711.1998.01497.x. _eprint: astro-ph/9710119.

[145] Ian G. McCarthy, Joop Schaye, Simeon Bird, and Amandine M. C. Le Brun. The bahamas project: calibrated hydrodynamical simulations for large-scale structure cosmology. *Monthly Notices of the Royal Astronomical Society*, 465(3):2936–2965, March 2017. ISSN 0035-8711, 1365-2966. doi: 10.1093/mnras/stw2792. URL https://academic.oup.com/mnras/article-lookup/doi/10.1093/mnras/stw2792.

[146] C. McCully, C. R. Keeton, K. C. Wong, and A. I. Zabludoff. A new hybrid framework to efficiently model lines of sight to gravitational lenses. *mnras*, 443:3631–3642, October 2014. doi: 10.1093/mnras/stu1316. _eprint: 1401.0197.

[147] C. McCully, C. R. Keeton, K. C. Wong, and A. I. Zabludoff. Quantifying Environmental and Line-of-sight Effects in Models of Strong Gravitational Lens Systems. *apj*, 836:141, February 2017. doi: 10.3847/1538-4357/836/1/141. _eprint: 1601.05417.

[148] Myles A. Mitchell, Christian Arnold, Jian-hua He, and Baojiu Li. A general framework to test gravity using galaxy clusters II: A universal model for the halo concentration in $f(R)$ gravity. *Mon. Not. Roy. Astron. Soc.*, 487(1):1410–1425, 2019. doi: 10.1093/mnras/stz1389. _eprint: 1901.06392.

[149] Ivelina G. Momcheva, Kurtis A. Williams, Richard J. Cool, Charles R. Keeton, and Ann I. Zabludoff. A Spectroscopic Survey of the Fields of 28 Strong Gravitational Lenses. *apjs*, 219(2):29, August 2015. doi: 10.1088/0067-0049/219/2/29. _eprint: 1503.02074.

[150] Azadeh Moradinezhad Dizgah, Matteo Biagetti, Emiliano Sefusatti, Vincent Desjacques, and Jorge Noreña. Primordial Non-Gaussianity from Biased Tracers: Likelihood Analysis of Real-Space Power Spectrum and Bispectrum. 2020. _eprint: 2010.14523.

[151] A. More, A. Verma, P. J. Marshall, S. More, E. Baeten, J. Wilcox, C. Macmillan, C. Cornen, A. Kapadia, M. Parrish, C. Snyder, C. P. Davis, R. Gavazzi, C. J. Lintott, R. Simpson, D. Miller, A. M. Smith, E. Paget, P. Saha, R. Küng, and T. E. Collett. SPACE WARPS- II. New gravitational lens candidates from the CFHTLS discovered through citizen science. *mnras*, 455:1191–1210, January 2016. doi: 10.1093/mnras/stv1965. _eprint: 1504.05587.

[152] Dipak Munshi. The Integrated Bispectrum in Modified Gravity Theories. *JCAP*, 01:049, 2017. doi: 10.1088/1475-7516/2017/01/049. _eprint: 1610.02956.

[153] J. B. Muñoz and M. Kamionkowski. Large-distance lens uncertainties and time-delay measurements of H_0. *prd*, 96(10):103537, November 2017. doi: 10.1103/PhysRevD.96.103537. _eprint: 1708.08454.

[154] Shintaro Nakamura, Antonio De Felice, Ryotaro Kase, and Shinji Tsujikawa. Constraints on massive vector dark energy models from integrated Sachs-Wolfe-galaxy cross-correlations. *Phys. Rev.*, D99 (6):063533, 2019. doi: 10.1103/PhysRevD.99.063533. _eprint: 1811.07541.

[155] R. Narayan and M. Bartelmann. Lectures on Gravitational Lensing. *ArXiv Astrophysics e-prints*, June 1996. _eprint: astro-ph/9606001.

[156] Julio F. Navarro, Carlos S. Frenk, and Simon D.M. White. The Structure of cold dark matter halos. *Astrophys. J.*, 462:563–575, 1996. doi: 10.1086/177173. _eprint: astro-ph/9508025.

[157] Julio F. Navarro, Carlos S. Frenk, and Simon D.M. White. A Universal density profile from hierarchical clustering. *Astrophys. J.*, 490:493–508, 1997. doi: 10.1086/304888. _eprint: astro-ph/9611107.

[158] Angelo F. Neto, Liang Gao, Philip Bett, Shaun Cole, Julio F. Navarro, Carlos S. Frenk, Simon D.M. White, Volker Springel, and Adrian Jenkins. The statistics of lambda CDM Halo Concentrations. *Mon. Not. Roy. Astron. Soc.*, 381:1450–1462, 2007. doi: 10.1111/j.1365-2966.2007.12381.x. _eprint: 0706.2919.

[159] Elisabeth R. Newton, Philip J. Marshall, Tommaso Treu, Matthew W. Auger, Raphäel Gavazzi, Adam S. Bolton, Léon V. E. Koopmans, and Leonidas A. Moustakas. THE SLOAN LENS ACS SURVEY. XI. BEYOND HUBBLE RESOLUTION: SIZE, LUMINOSITY, AND STELLAR MASS OF COMPACT LENSED GALAXIES AT INTERMEDIATE REDSHIFT. *The Astrophysical Journal*, 734(2):104, June 2011. ISSN 0004-637X, 1538-4357. doi: 10.1088/0004-637X/734/2/104. URL https://iopscience.iop.org/article/10.1088/0004-637X/734/2/104.

[160] Alberto Nicolis, Riccardo Rattazzi, and Enrico Trincherini. The Galileon as a local modification of gravity. *Physical Review D*, D79(6):064036, 2009. ISSN 1550-7998, 1550-2368. doi: 10.1103/PhysRevD.79.064036. URL https://link.aps.org/doi/10.1103/PhysRevD.79.064036. _eprint: 0811.2197.

[161] Andrea Oddo, Emiliano Sefusatti, Cristiano Porciani, Pierluigi Monaco, and Ariel G. Sánchez. Toward a robust inference method for the galaxy bispectrum: likelihood function and model selection. *JCAP*, 03:056, 2020. doi: 10.1088/1475-7516/2020/03/056. _eprint: 1908.01774.

[162] M. Oguri and P. J. Marshall. Gravitationally lensed quasars and supernovae in future wide-field optical imaging surveys. *mnras*, 405:2579–2593, July 2010. doi: 10.1111/j.1365-2966.2010.16639.x. _eprint: 1001.2037.

[163] Masamune Oguri. Gravitational Lens Time Delays: A Statistical Assessment of Lens Model Dependences and Implications for the Global Hubble Constant. *The Astrophysical Journal*, 660(1):1–15, May 2007. ISSN 0004-637X, 1538-4357. doi: 10.1086/513093. URL https://iopscience.iop.org/article/10.1086/513093.

[164] Enrique Paillas, Marius Cautun, Baojiu Li, Yan-Chuan Cai, Nelson Padilla, Joaqu\'ın Armijo, and Sownak Bose. The Santiago–Harvard–Edinburgh–Durham void comparison II: unveiling the Vainshtein screening using weak lensing. *Mon. Not. Roy. Astron. Soc.*, 484(1):1149–1165, 2019. doi: 10.1093/mnras/stz022. _eprint: 1810.02864.

[165] Laura C. Parker, Henk Hoekstra, Michael J. Hudson, Ludovic van Waerbeke, and Yannick Mellier. The Masses and Shapes of Dark Matter Halos from Galaxy-Galaxy Lensing in the CFHT Legacy Survey. *apj*, 669(1):21–31, November 2007. doi: 10.1086/521541. _eprint: 0707.1698.

[166] John A. Peacock, Shaun Cole, Peder Norberg, Carlton M. Baugh, Joss Bland-Hawthorn, Terry Bridges, Russell D. Cannon, Matthew Colless, Chris Collins, Warrick Couch, Gavin Dalton, Kathryn Deeley, Roberto De Propris, Simon P. Driver, George Efstathiou, Richard S. Ellis, Carlos S. Frenk, Karl Glazebrook, Carole Jackson, Ofer Lahav, Ian Lewis, Stuart Lumsden, Steve Maddox, Will J. Percival, Bruce A. Peterson, Ian Price, Will Sutherland, and Keith Taylor. A measurement of the cosmological mass density from clustering in the 2dF Galaxy Redshift Survey. *Nature*, 410 (6825):169–173, March 2001. ISSN 0028-0836, 1476-4687. doi: 10.1038/35065528. URL http://www.nature.com/articles/35065528.

[167] P. J. E. Peebles. *The large-scale structure of the universe*. Princeton University Press, 1980. ISBN 978-0-691-20983-8. URL https://press.princeton.edu/books/paperback/9780691209838/the-large-scale-structure-of-the-universe.

[168] Simone Peirone, Noemi Frusciante, Bin Hu, Marco Raveri, and Alessandra Silvestri. Do current cosmological observations rule out all Covariant Galileons? *Phys. Rev. D*, 97(6):063518, 2018. doi: 10.1103/PhysRevD.97.063518. _eprint: 1711.04760.

[169] G. Pietrzyński, D. Graczyk, A. Gallenne, W. Gieren, I. B. Thompson, B. Pilecki, P. Karczmarek, M. Górski, K. Suchomska, M. Taormina, B. Zgirski, P. Wielgórski, Z. Ko\laczkowski, P. Konorski, S. Villanova, N. Nardetto, P. Kervella, F. Bresolin, R. P. Kudritzki, J. Storm, R. Smolec, and W. Narloch. A

distance to the Large Magellanic Cloud that is precise to one per cent. *nat*, 567(7747):200–203, March 2019. doi: 10.1038/s41586-019-0999-4. _eprint: 1903.08096.

[170] Annalisa Pillepich, Volker Springel, Dylan Nelson, Shy Genel, Jill Naiman, Rüdiger Pakmor, Lars Hernquist, Paul Torrey, Mark Vogelsberger, Rainer Weinberger, and Federico Marinacci. Simulating galaxy formation with the IllustrisTNG model. *Monthly Notices of the Royal Astronomical Society*, 473(3):4077–4106, January 2018. ISSN 0035-8711, 1365-2966. doi: 10.1093/mnras/stx2656. URL http://academic.oup.com/mnras/article/473/3/4077/4494369.

[171] Alice Pisani and others. Cosmic voids: a novel probe to shed light on our Universe. 2019. _eprint: 1903.05161.

[172] Alice Pisani, P.M. Sutter, Nico Hamaus, Esfandiar Alizadeh, Rahul Biswas, Benjamin D. Wandelt, and Christopher M. Hirata. Counting voids to probe dark energy. *Phys. Rev. D*, 92(8):083531, 2015. doi: 10.1103/PhysRevD.92.083531. _eprint: 1503.07690.

[173] Planck Collaboration, N. Aghanim, Y. Akrami, M. Ashdown, J. Aumont, C. Baccigalupi, M. Ballardini, A. J. Banday, R. B. Barreiro, N. Bartolo, S. Basak, R. Battye, K. Benabed, J.-P. Bernard, M. Bersanelli, P. Bielewicz, J. J. Bock, J. R. Bond, J. Borrill, F. R. Bouchet, F. Boulanger, M. Bucher, C. Burigana, R. C. Butler, E. Calabrese, J.-F. Cardoso, J. Carron, A. Challinor, H. C. Chiang, J. Chluba, L. P. L. Colombo, C. Combet, D. Contreras, B. P. Crill, F. Cuttaia, P. de Bernardis, G. de Zotti, J. Delabrouille, J.-M. Delouis, E. Di Valentino, J. M. Diego, O. Doré, M. Douspis, A. Ducout, X. Dupac, S. Dusini, G. Efstathiou, F. Elsner, T. A. Enßlin, H. K. Eriksen, Y. Fantaye, M. Farhang, J. Fergusson, R. Fernandez-Cobos, F. Finelli, F. Forastieri, M. Frailis, E. Franceschi, A. Frolov, S. Galeotta, S. Galli, K. Ganga, R. T. Génova-Santos, M. Gerbino, T. Ghosh, J. González-Nuevo, K. M. Górski, S. Gratton, A. Gruppuso, J. E. Gudmundsson, J. Hamann, W. Handley, D. Herranz, E. Hivon, Z. Huang, A. H. Jaffe, W. C. Jones, A. Karakci, E. Keihänen, R. Keskitalo, K. Kiiveri, J. Kim, T. S. Kisner, L. Knox, N. Krachmalnicoff, M. Kunz, H. Kurki-Suonio, G. Lagache, J.-M. Lamarre, A. Lasenby, M. Lattanzi, C. R. Lawrence, M. Le Jeune, P. Lemos, J. Lesgourgues, F. Levrier, A. Lewis, M. Liguori, P. B. Lilje, M. Lilley, V. Lindholm, M. López-Caniego, P. M. Lubin, Y.-Z. Ma, J. F. Macías-Pérez, G. Maggio, D. Maino, N. Mandolesi, A. Mangilli, A. Marcos-Caballero, M. Maris, P. G. Martin, M. Martinelli, E. Martínez-González, S. Matarrese, N. Mauri, J. D. McEwen, P. R. Meinhold, A. Melchiorri, A. Mennella, M. Migliaccio, M. Millea, S. Mitra, M.-A. Miville-Deschênes, D. Molinari, L. Montier, G. Morgante, A. Moss, P. Natoli, H. U. Nørgaard-Nielsen, L. Pagano, D. Paoletti, B. Partridge, G. Patanchon, H. V. Peiris, F. Perrotta, V. Pettorino, F. Piacentini, L. Polastri, G. Polenta, J.-L. Puget, J. P. Rachen, M. Reinecke, M. Remazeilles,

A. Renzi, G. Rocha, C. Rosset, G. Roudier, J. A. Rubiño-Martín, B. Ruiz-Granados, L. Salvati, M. Sandri, M. Savelainen, D. Scott, E. P. S. Shellard, C. Sirignano, G. Sirri, L. D. Spencer, R. Sunyaev, A.-S. Suur-Uski, J. A. Tauber, D. Tavagnacco, M. Tenti, L. Toffolatti, M. Tomasi, T. Trombetti, L. Valenziano, J. Valiviita, B. Van Tent, L. Vibert, P. Vielva, F. Villa, N. Vittorio, B. D. Wandelt, I. K. Wehus, M. White, S. D. M. White, A. Zacchei, and A. Zonca. Planck 2018 results. VI. Cosmological parameters. *arXiv e-prints*, July 2018. _eprint: 1807.06209.

[174] Erwin Platen, Rien Van De Weygaert, and Bernard J. T. Jones. A cosmic watershed: the WVF void detection technique. *Mon. Not. Roy. Astron. Soc.*, 380(2):551–570, 2007. ISSN 0035-8711. doi: 10.1111/j.1365-2966.2007.12125.x.

[175] Beth A. Reid and Martin White. Towards an accurate model of the redshift space clustering of halos in the quasilinear regime. *Mon. Not. Roy. Astron. Soc.*, 417:1913–1927, 2011. doi: 10.1111/j.1365-2966.2011.19379.x. _eprint: 1105.4165.

[176] Janina Renk, Miguel Zumalacárregui, Francesco Montanari, and Alexandre Barreira. Galileon gravity in light of ISW, CMB, BAO and H_0 data. *JCAP*, 10:020, 2017. doi: 10.1088/1475-7516/2017/10/020. _eprint: 1707.02263.

[177] A. G. Riess, S. Casertano, W. Yuan, L. M. Macri, and D. Scolnic. Large Magellanic Cloud Cepheid Standards Provide a 1% Foundation for the Determination of the Hubble Constant and Stronger Evidence for Physics beyond ΛCDM. *\apj*, 876:85, May 2019. doi: 10.3847/1538-4357/ab1422. _eprint: 1903.07603.

[178] Adam G. Riess, Lucas M. Macri, Samantha L. Hoffmann, Dan Scolnic, Stefano Casertano, Alexei V. Filippenko, Brad E. Tucker, Mark J. Reid, David O. Jones, Jeffrey M. Silverman, Ryan Chornock, Peter Challis, Wenlong Yuan, Peter J. Brown, and Ryan J. Foley. A 2.4% Determination of the Local Value of the Hubble Constant. *The Astrophysical Journal*, 826(1):56, July 2016. ISSN 1538-4357. doi: 10.3847/0004-637X/826/1/56. URL http://arxiv.org/abs/1604.01424. arXiv: 1604.01424.

[179] C. E. Rusu, C. D. Fassnacht, D. Sluse, S. Hilbert, K. C. Wong, K.-H. Huang, S. H. Suyu, T. E. Collett, P. J. Marshall, T. Treu, and L. V. E. Koopmans. H0LiCOW - III. Quantifying the effect of mass along the line of sight to the gravitational lens HE 0435-1223 through weighted galaxy counts\starf. *\mnras*, 467:4220–4242, June 2017. doi: 10.1093/mnras/stx285. _eprint: 1607.01047.

[180] Cristian E. Rusu, Kenneth C. Wong, Vivien Bonvin, Dominique Sluse, Sherry H. Suyu, Christopher D. Fassnacht, James H. H. Chan, Stefan Hilbert, Matthew W. Auger, Alessandro Sonnenfeld, Simon

Birrer, Frederic Courbin, Tommaso Treu, Geoff C. F. Chen, Aleksi Halkola, Léon V. E. Koopmans, Philip J. Marshall, and Anowar J. Shajib. H0LiCOW XII. Lens mass model of WFI2033-4723 and blind measurement of its time-delay distance and H_0. *mnras*, 498(1):1440–1468, October 2020. doi: 10.1093/mnras/stz3451. _eprint: 1905.09338.

[181] Simon Saunders, Joseph Silk, John D. Barrow, and Khalil Chamcham. *The Philosophy of Cosmology*. Cambridge University Press, 2017. ISBN 978-1-107-14539-9. doi: 10.1017/9781316535783.

[182] Abraham Savitzky and Marcel JE Golay. Smoothing and differentiation of data by simplified least squares procedures. *Analytical chemistry*, 36(8):1627–1639, 1964. Publisher: ACS Publications.

[183] P. Schneider. *Gravitational lenses*. 1999.

[184] P. Schneider and D. Sluse. Mass-sheet degeneracy, power-law models and external convergence: Impact on the determination of the Hubble constant from gravitational lensing. *aap*, 559:A37, November 2013. doi: 10.1051/0004-6361/201321882. _eprint: 1306.0901.

[185] Peter Schneider, Jürgen Ehlers, and Emilio E. Falco. *Gravitational Lenses*. 1992. doi: 10.1007/978-3-662-03758-4.

[186] Roman Scoccimarro. Redshift-space distortions, pairwise velocities and nonlinearities. *Phys. Rev. D*, 70:083007, 2004. doi: 10.1103/PhysRevD.70.083007. _eprint: astro-ph/0407214.

[187] Roman Scoccimarro. Fast Estimators for Redshift-Space Clustering. *Phys. Rev. D*, 92(8):083532, 2015. doi: 10.1103/PhysRevD.92.083532. _eprint: 1506.02729.

[188] Roman Scoccimarro, Stephane Colombi, James N. Fry, Joshua A. Frieman, Eric Hivon, and Adrian Melott. Nonlinear evolution of the bispectrum of cosmological perturbations. *Astrophys. J.*, 496:586, 1998. doi: 10.1086/305399. _eprint: astro-ph/9704075.

[189] Emiliano Sefusatti, Martin Crocce, Roman Scoccimarro, and Hugh Couchman. Accurate Estimators of Correlation Functions in Fourier Space. *Mon. Not. Roy. Astron. Soc.*, 460(4):3624–3636, 2016. doi: 10.1093/mnras/stw1229. _eprint: 1512.07295.

[190] Mauro Sereno and Danuta Paraficz. Hubble constant and dark energy inferred from free-form determined time delay distances. *mnras*, 437(1):600–605, January 2014. doi: 10.1093/mnras/stt1938. _eprint: 1310.2251.

[191] A. J. Shajib, S. Birrer, T. Treu, A. Agnello, E. J. Buckley-Geer, J. H. H. Chan, L. Christensen, C. Lemon, H. Lin, M. Millon, J. Poh, C. E. Rusu, D. Sluse, C. Spiniello, G. C. F. Chen, T. Collett, F. Courbin, C. D.

Fassnacht, J. Frieman, A. Galan, D. Gilman, A. More, T. Anguita, M. W. Auger, V. Bonvin, R. McMahon, G. Meylan, K. C. Wong, T. M. C. Abbott, J. Annis, S. Avila, K. Bechtol, D. Brooks, D. Brout, D. L. Burke, A. Carnero Rosell, M. Carrasco Kind, J. Carretero, F. J. Castander, M. Costanzi, L. N. da Costa, J. De Vicente, S. Desai, J. P. Dietrich, P. Doel, A. Drlica-Wagner, A. E. Evrard, D. A. Finley, B. Flaugher, P. Fosalba, J. García-Bellido, D. W. Gerdes, D. Gruen, R. A. Gruendl, J. Gschwend, G. Gutierrez, D. L. Hollowood, K. Honscheid, D. Huterer, D. J. James, T. Jeltema, E. Krause, N. Kuropatkin, T. S. Li, M. Lima, N. MacCrann, M. A. G. Maia, J. L. Marshall, P. Melchior, R. Miquel, R. L. C. Ogando, A. Palmese, F. Paz-Chinchón, A. A. Plazas, A. K. Romer, A. Roodman, M. Sako, E. Sanchez, B. Santiago, V. Scarpine, M. Schubnell, D. Scolnic, S. Serrano, I. Sevilla-Noarbe, M. Smith, M. Soares-Santos, E. Suchyta, G. Tarle, D. Thomas, A. R. Walker, and Y. Zhang. STRIDES: A 3.9 per cent measurement of the Hubble constant from the strong lens system DES J0408-5354. *arXiv e-prints*, page arXiv:1910.06306, October 2019. _eprint: 1910.06306.

[192] Masato Shirasaki, Takahiro Nishimichi, Baojiu Li, and Yuichi Higuchi. The imprint of f(R) gravity on weak gravitational lensing – II. Information content in cosmic shear statistics. *Mon. Not. Roy. Astron. Soc.*, 466(2):2402–2417, 2017. doi: 10.1093/mnras/stw3254. _eprint: 1610.03600.

[193] Y. Shu, A. S. Bolton, S. Mao, C. S. Kochanek, I. Pérez-Fournon, M. Oguri, A. D. Montero-Dorta, M. A. Cornachione, R. Marques-Chaves, Z. Zheng, J. R. Brownstein, and B. Ménard. The BOSS Emission-line Lens Survey. IV. Smooth Lens Models for the BELLS GALLERY Sample. *apj*, 833:264, December 2016. doi: 10.3847/1538-4357/833/2/264. _eprint: 1608.08707.

[194] Yiping Shu, Joel R. Brownstein, Adam S. Bolton, Léon V. E. Koopmans, Tommaso Treu, Antonio D. Montero-Dorta, Matthew W. Auger, Oliver Czoske, Raphaël Gavazzi, Philip J. Marshall, and Leonidas A. Moustakas. The Sloan Lens ACS Survey. XIII. Discovery of 40 New Galaxy-scale Strong Lenses. *The Astrophysical Journal*, 851(1):48, December 2017. ISSN 1538-4357. doi: 10.3847/1538-4357/aa9794. URL https://iopscience.iop.org/article/10.3847/1538-4357/aa9794.

[195] D. Sluse, A. Sonnenfeld, N. Rumbaugh, C. E. Rusu, C. D. Fassnacht, T. Treu, S. H. Suyu, K. C. Wong, M. W. Auger, V. Bonvin, T. Collett, F. Courbin, S. Hilbert, L. V. E. Koopmans, P. J. Marshall, G. Meylan, C. Spiniello, and M. Tewes. H0LiCOW - II. Spectroscopic survey and galaxy-group identification of the strong gravitational lens system HE 0435-1223. *mnras*, 470(4):4838–4857, October 2017. doi: 10.1093/mnras/stx1484. _eprint: 1607.00382.

[196] Alessandro Sonnenfeld, Tommaso Treu, Philip J. Marshall, Sherry H. Suyu, Raphaël Gavazzi, Matthew W. Auger, and Carlo Nipoti. THE SL2S GALAXY-SCALE LENS SAMPLE. V. DARK MATTER

HALOS AND STELLAR IMF OF MASSIVE EARLY-TYPE GALAXIES OUT TO REDSHIFT 0.8. *The Astrophysical Journal*, 800(2):94, February 2015. ISSN 1538-4357. doi: 10.1088/0004-637X/800/2/94. URL https://iopscience.iop.org/article/10.1088/0004-637X/800/2/94.

[197] Volker Springel. E pur si muove: Galilean-invariant cosmological hydrodynamical simulations on a moving mesh. *Monthly Notices of the Royal Astronomical Society*, 401(2):791–851, January 2010. ISSN 00358711, 13652966. doi: 10.1111/j.1365-2966.2009.15715.x. URL https://academic.oup.com/mnras/article-lookup/doi/10.1111/j.1365-2966.2009.15715.x.

[198] Volker Springel, Simon D.M. White, Giuseppe Tormen, and Guinevere Kauffmann. Populating a cluster of galaxies. 1. Results at z = 0. *Mon. Not. Roy. Astron. Soc.*, 328:726, 2001. doi: 10.1046/j.1365-8711.2001.04912.x. _eprint: astro-ph/0012055.

[199] S. H. Suyu, P. J. Marshall, M. W. Auger, S. Hilbert, R. D. Blandford, L. V. E. Koopmans, C. D. Fassnacht, and T. Treu. Dissecting the Gravitational lens B1608+656. II. Precision Measurements of the Hubble Constant, Spatial Curvature, and the Dark Energy Equation of State. *The Astrophysical Journal*, 711:201–221, March 2010. ISSN 0004-637X, 1538-4357. doi: 10.1088/0004-637X/711/1/201. URL https://iopscience.iop.org/article/10.1088/0004-637X/711/1/201. _eprint: 0910.2773.

[200] S. H. Suyu, M. W. Auger, S. Hilbert, P. J. Marshall, M. Tewes, T. Treu, C. D. Fassnacht, L. V. E. Koopmans, D. Sluse, R. D. Blandford, F. Courbin, and G. Meylan. Two Accurate Time-delay Distances from Strong Lensing: Implications for Cosmology. *apj*, 766:70, April 2013. doi: 10.1088/0004-637X/766/2/70. _eprint: 1208.6010.

[201] S. H. Suyu, T. Treu, S. Hilbert, A. Sonnenfeld, M. W. Auger, R. D. Blandford, T. Collett, F. Courbin, C. D. Fassnacht, L. V. E. Koopmans, P. J. Marshall, G. Meylan, C. Spiniello, and M. Tewes. Cosmology from Gravitational Lens Time Delays and Planck Data. *apjl*, 788:L35, June 2014. doi: 10.1088/2041-8205/788/2/L35. _eprint: 1306.4732.

[202] S. H. Suyu, V. Bonvin, F. Courbin, C. D. Fassnacht, C. E. Rusu, D. Sluse, T. Treu, K. C. Wong, M. W. Auger, X. Ding, S. Hilbert, P. J. Marshall, N. Rumbaugh, A. Sonnenfeld, M. Tewes, O. Tihhonova, A. Agnello, R. D. Blandford, G. C.-F. Chen, T. Collett, L. V. E. Koopmans, K. Liao, G. Meylan, and C. Spiniello. H0LiCOW - I. H_0 Lenses in COSMOGRAIL's Wellspring: program overview. *mnras*, 468:2590–2604, July 2017. doi: 10.1093/mnras/stx483. _eprint: 1607.00017.

[203] A. S. Tagore, D. J. Barnes, N. Jackson, S. T. Kay, M. Schaller, J. Schaye, and T. Theuns. Reducing biases on H_0 measurements using strong lensing and galaxy dynamics: results from the EAGLE simulation. *mnras*, 474:3403–3422, March 2018. doi: 10.1093/mnras/stx2965. _eprint: 1706.07733.

[204] Atsushi Taruya, Takahiro Nishimichi, and Shun Saito. Baryon Acoustic Oscillations in 2D: Modeling Redshift-space Power Spectrum from Perturbation Theory. *Phys. Rev. D*, 82:063522, 2010. doi: 10.1103/PhysRevD.82.063522. _eprint: 1006.0699.

[205] Romain Teyssier. Cosmological hydrodynamics with adaptive mesh refinement: a new high resolution code called ramses. *Astron. Astrophys.*, 385:337–364, 2002. doi: 10.1051/0004-6361:20011817. _eprint: astro-ph/0111367.

[206] The Euclid Collaboration. Euclid Definition Study Report. Technical report, arXiv, October 2011. URL http://arxiv.org/abs/1110.3193.

[207] The LSST Collaboration. LSST: From Science Drivers to Reference Design and Anticipated Data Products. *The Astrophysical Journal*, 873(2):111, March 2019. ISSN 1538-4357. doi: 10.3847/1538-4357/ab042c. URL https://iopscience.iop.org/article/10.3847/1538-4357/ab042c.

[208] Tom Theuns, Aidan Chalk, Matthieu Schaller, and Pedro Gonnet. SWIFT: task-based hydrodynamics and gravity for cosmological simulations. *arXiv:1508.00115 [astro-ph]*, August 2015. URL http://arxiv.org/abs/1508.00115. arXiv: 1508.00115.

[209] S. S. Tie and C. S. Kochanek. Microlensing makes lensed quasar time delays significantly time variable. *mnras*, 473:80–90, January 2018. doi: 10.1093/mnras/stx2348. _eprint: 1707.01908.

[210] O. Tihhonova, F. Courbin, D. Harvey, S. Hilbert, C. E. Rusu, C. D. Fassnacht, V. Bonvin, P. J. Marshall, G. Meylan, D. Sluse, S. H. Suyu, T. Treu, and K. C. Wong. H0LiCOW VIII. A weak-lensing measurement of the external convergence in the field of the lensed quasar HE 0435-1223. *mnras*, 477(4):5657–5669, July 2018. doi: 10.1093/mnras/sty1040. _eprint: 1711.08804.

[211] T. Treu and L. V. E. Koopmans. The internal structure of the lens PG1115+080: breaking degeneracies in the value of the Hubble constant. *Monthly Notices of the Royal Astronomical Society*, 337(2): L6–L10, September 2002. ISSN 0035-8711, 1365-2966. doi: 10.1046/j.1365-8711.2002.06107.x. URL https://academic.oup.com/mnras/article-lookup/doi/10.1046/j.1365-8711.2002.06107.x.

[212] M.A. Troxel and others. Dark Energy Survey Year 1 results: Cosmological constraints from cosmic shear. *Phys. Rev. D*, 98(4):043528, 2018. doi: 10.1103/PhysRevD.98.043528. _eprint: 1708.01538.

[213] A. Vainshtein. To the problem of nonvanishing gravitation mass. *Phys. Lett. B*, 39:393, 1972.

[214] Rien van de Weygaert and Erwin Platen. Cosmic Voids: Structure, Dynamics and Galaxies. *International Journal of Modern Physics: Conference Series*, 1:41, 2011. doi: 10.1142/S2010194511000092. _eprint: arXiv:0912.2997.

[215] Licia Verde and others. Tensions between the Early and the Late Universe. *Nature Astronomy*, 3: 891–895, 2019. doi: 10.1038/s41550-019-0902-0. _eprint: 1907.10625.

[216] Francisco Villaescusa-Navarro, ChangHoon Hahn, Elena Massara, Arka Banerjee, Ana Maria Delgado, Doogesh Kodi Ramanah, Tom Charnock, Elena Giusarma, Yin Li, Erwan Allys, Antoine Brochard, Cora Uhlemann, Chi-Ting Chiang, Siyu He, Alice Pisani, Andrej Obuljen, Yu Feng, Emanuele Castorina, Gabriella Contardo, Christina D. Kreisch, Andrina Nicola, Justin Alsing, Roman Scoccimarro, Licia Verde, Matteo Viel, Shirley Ho, Stephane Mallat, Benjamin Wandelt, and David N. Spergel. The Quijote Simulations. *The Astrophysical Journal Supplement Series*, 250(1):2, August 2020. ISSN 1538-4365. doi: 10.3847/1538-4365/ab9d82. URL https://iopscience.iop.org/article/10.3847/1538-4365/ab9d82.

[217] Jenny Wagner. Generalised model-independent characterisation of strong gravitational lenses. IV. Formalism-intrinsic degeneracies. *aap*, 620:A86, December 2018. doi: 10.1051/0004-6361/201834218. _eprint: 1809.03505.

[218] Steven Weinberg. Photons and gravitons in perturbation theory: Derivation of Maxwell's and Einstein's equations. *Phys. Rev.*, 138:B988–B1002, 1965. doi: 10.1103/PhysRev.138.B988.

[219] Rainer Weinberger, Volker Springel, Lars Hernquist, Annalisa Pillepich, Federico Marinacci, Rüdiger Pakmor, Dylan Nelson, Shy Genel, Mark Vogelsberger, Jill Naiman, and Paul Torrey. Simulating galaxy formation with black hole driven thermal and kinetic feedback. *Monthly Notices of the Royal Astronomical Society*, 465(3):3291–3308, March 2017. ISSN 0035-8711, 1365-2966. doi: 10.1093/mnras/stw2944. URL https://academic.oup.com/mnras/article-lookup/doi/10.1093/mnras/stw2944.

[220] O. Wertz, B. Orthen, and P. Schneider. Ambiguities in gravitational lens models: impact on time delays of the source position transformation. *aap*, 617:A140, October 2018. doi: 10.1051/0004-6361/201732240. _eprint: 1712.05033.

[221] Martin J. White and Wayne Hu. A New algorithm for computing statistics of weak lensing by large scale structure. *Astrophys. J.*, 537:1–11, 2000. doi: 10.1086/309009. _eprint: astro-ph/9909165.

[222] Simon D. M. White. The hierarchy of correlation functions and its relation to other measures of galaxy clustering. *Monthly Notices of the Royal Astronomical Society*, 186(2):145–154, February 1979. ISSN 0035-8711, 1365-2966. doi: 10.1093/mnras/186.2.145. URL https://academic.oup.com/mnras/article-lookup/doi/10.1093/mnras/186.2.145.

[223] Clifford M. Will. The Confrontation between General Relativity and Experiment. *Living Reviews in Relativity*, 17(1):4, December 2014. ISSN 2367-3613, 1433-8351. doi: 10.12942/lrr-2014-4. URL http://link.springer.com/10.12942/lrr-2014-4.

[224] Hans A. Winther and Pedro G. Ferreira. Vainshtein mechanism beyond the quasistatic approximation. *Phys. Rev.*, D92:064005, 2015. doi: 10.1103/PhysRevD.92.064005. _eprint: 1505.03539.

[225] K. C. Wong, A. Sonnenfeld, J. H. H. Chan, C. E. Rusu, M. Tanaka, A. T. Jaelani, C.-H. Lee, A. More, M. Oguri, S. H. Suyu, and Y. Komiyama. Survey of Gravitationally Lensed Objects in HSC Imaging (SuGOHI). II. Environments and Line-of-Sight Structure of Strong Gravitational Lens Galaxies to z \tilde 0.8. *apj*, 867:107, November 2018. doi: 10.3847/1538-4357/aae381. _eprint: 1809.07341.

[226] Kenneth C. Wong, Charles R. Keeton, Kurtis A. Williams, Ivelina G. Momcheva, and Ann I. Zabludoff. The Effect of Environment on Shear in Strong Gravitational Lenses. *apj*, 726(2):84, January 2011. doi: 10.1088/0004-637X/726/2/84. _eprint: 1011.2504.

[227] Kenneth C. Wong, Sherry H. Suyu, Matthew W. Auger, Vivien Bonvin, Frederic Courbin, Christopher D. Fassnacht, Aleksi Halkola, Cristian E. Rusu, Dominique Sluse, Alessand ro Sonnenfeld, Tommaso Treu, Thomas E. Collett, Stefan Hilbert, Leon V. E. Koopmans, Philip J. Marshall, and Nicholas Rumbaugh. H0LiCOW - IV. Lens mass model of HE 0435-1223 and blind measurement of its time-delay distance for cosmology. *mnras*, 465(4):4895–4913, March 2017. doi: 10.1093/mnras/stw3077. _eprint: 1607.01403.

[228] Kenneth C. Wong, Sherry H. Suyu, Geoff C. F. Chen, Cristian E. Rusu, Martin Millon, Dominique Sluse, Vivien Bonvin, Christopher D. Fassnacht, Stefan Taubenberger, Matthew W. Auger, Simon Birrer, James H. H. Chan, Frederic Courbin, Stefan Hilbert, Olga Tihhonova, Tommaso Treu, Adriano Agnello, Xuheng Ding, Inh Jee, Eiichiro Komatsu, Anowar J. Shajib, Alessandro Sonnenfeld, Roger D. Bland ford, Leon V. E. Koopmans, Philip J. Marshall, and Georges Meylan. H0LiCOW XIII. A 2.4% measurement of $_0$ from lensed quasars: 5.3σ tension between early and late-Universe probes. *arXiv e-prints*, page arXiv:1907.04869, July 2019. _eprint: 1907.04869.

[229] D. Xu, D. Sluse, P. Schneider, V. Springel, M. Vogelsberger, D. Nelson, and L. Hernquist. Lens galaxies

in the Illustris simulation: power-law models and the bias of the Hubble constant from time delays. *mnras*, 456:739–755, February 2016. doi: 10.1093/mnras/stv2708. _eprint: 1507.07937.

[230] Wenlong Yuan, Adam G. Riess, Lucas M. Macri, Stefano Casertano, and Daniel M. Scolnic. Consistent Calibration of the Tip of the Red Giant Branch in the Large Magellanic Cloud on the Hubble Space Telescope Photometric System and a Redetermination of the Hubble Constant. *apj*, 886(1):61, November 2019. doi: 10.3847/1538-4357/ab4bc9. _eprint: 1908.00993.

[231] Pengjie Zhang, Michele Liguori, Rachel Bean, and Scott Dodelson. Probing Gravity at Cosmological Scales by Measurements which Test the Relationship between Gravitational Lensing and Matter Overdensity. *Phys. Rev. Lett.*, 99:141302, 2007. doi: 10.1103/PhysRevLett.99.141302. _eprint: 0704.1932.

[232] Ivaylo Zlatev, Limin Wang, and Paul J. Steinhardt. Quintessence, Cosmic Coincidence, and the Cosmological Constant. *Physical Review Letters*, 82(5):896–899, February 1999. ISSN 0031-9007, 1079-7114. doi: 10.1103/PhysRevLett.82.896. URL https://link.aps.org/doi/10.1103/PhysRevLett.82.896.